Institute of Thermal Technology
Faculty of Energy and Environmental Engineering
Silesian University of Technology

Enhancement of Monte Carlo Technique in Absorbing/Emitting Radiating Media for CFD applications

Author:
Paweł Kuczyński

Supervisor:
Ryszard Białecki

Co-supervisor:
Gabriel Węcel

Gliwice 2016

Acknowledgements

The work of this thesis could not be completed without huge amount of help I have received from a number of people. First of all I would like to thank my supervisor - Professor Ryszard Białecki for agreeing to supervise and coordinate the thesis, his knowledge, encouragement, support, optimism and patience.

Also, I would like to thank my co-supervisor Ph.D. Gabriel Węcel whose thesis served as a valuable source of information and ideas, a bunch of which is used within the present work.

I would like to express my gratitude to Ph.D. Tomasz Golec and Ph.D. Bartosz Świątkowski for their encouragement to start writing the thesis. They created an environment, in which I was equipped with all the tools and resources needed to finish this work.

Hours spent on discussions with Ph.D. Robert Lewtak played a stimulating and motivating role during radiation model development. M.Sc. Krzysztof Strug was always willing to help with problems concerning Linux operating system.

Ph.D. Jacek Widuch's broad knowledge in the field of parallel computing has been invaluable.

I owe thanks to Ph.D. Paweł Kozołub for his help with C++ programming within OpenFOAM.

The final demonstration of radiation model capabilities would not be possible without huge amount of work done by Ph.D. Sławomir Sładek, who incorporated the radiation model into his OpenFOAM code and finished numerical simulation of coal combustion in a test rig.

Support of Ph.D. Łukasz Piechowicz and M.Sc. Andrzej Miliszewski from Seco/Warwick Europe S.A. in the field of pit furnaces construction and operation is greatly appreciated.

This research was partially sponsored by the National Research and Development Centre of Poland through the Strategic Program *'Advanced technologies of energy generation'*, Research Task 2: 'Development of oxyfuel combustion technologies for pulverized and fluidized coal-fired boilers integrated with the carbon capture and storage technology', Grant No. SP/E/2/666420/10.

Finally, I wish to thank my wife Magdalena for her love, understanding and support.

Contents

List of symbols

Latin

a	weighting factor, $-$
A	surface area, m^2
b	radiosity - wall outgoing radiative heat flux, W/m^2
c	speed of light in medium, m/s
c_0	speed of light in vacuum, $2.998 \times 10^8\, m/s$
c_p	specific isobaric heat, $J/(kgK)$
C	cell center
$\mathbf{C}(u)$	parametric NURBS curve
d_p	particle diameter, m
$\mathbf{d}$	bundle direction vector
D	mass diffusion coefficient, m^2/s
D_{ij}	radiation distribution factor, $-$
$\mathbf{D}$	radiation distribution factor matrix
e^r	radiative energy flux, W/m^2
e_b	blackbody emissive power, W/m^2
e_{ph}	photon energy, J
E	activation energy, constant in Arrhenius expression, $J/kmol$
E^r	radiative energy, J
E_p	radiative energy emission by particles, W/m^3
f	user-defined surface flatness criterion, $-$
F	momentum source term, N/m^3; view factor, $-$
F_D	drag coefficient, $-$
g	artificial wavenumber, $-$; Earth gravity, $9.81\, m/s^2$
G	incident radiation, W/m^2
h	specific enthalpy, J/kg; convective heat transfer coefficient, $W/(m^2K)$
h^0	enthalpy of formation, J/kg
h_P	Planck's constant, $6.626 \times 10^{-34}\, Js$
H	total enthalpy, J/kg
i	surface irradiation, W/m^2
I	radiation intensity, $W/(m^2sr)$
I_b	radiation intensity of a blackbody, $W/(m^2sr)$
J	diffusive mass flux, $kg/(m^2s)$

$\mathbf{J}$	Jacobi matrix
k	specific turbulent kinetic energy, m^2/s^2; thermal conductivity, $W/(mK)$
k_B	Boltzmann constant, $1.381 \times 10^{-23}\, J/K$
L	length, m
m	mass, kg; number of discrete directions, $-$
M_r	molar fraction ratio of H_2O to CO_2 (p_{H2O}/p_CO2), $-$
n	index of refraction, $-$
$\mathbf{n}$	surface unit normal vector
N	order of method, $-$; number of rays, $-$
$N_{i,p}$	normalized B-spline basis functions of degree p
OF	ortho-Cartesian boundary cell overlap factor, $-$
p	degree of B-spline in u direction, $-$; surface flatness, $-$; pressure, atm
P_l	associated Legendre polynomial
Pr	Prandtl number, $-$
$\mathbf{P}$	control point
q	degree of B-spline in v direction, $-$
q^r	radiative heat flux, W/m^2
q^r_v	radiative heat source or sink, W/m^3
Q^r	radiative heat rate, W
r_s	specularity ratio, $-$
$\mathbf{r}$	position vector
R	production rate due to reaction, $kg/(m^3 s)$; random number $\in [0, 1)$
$R_{i,p}$	rational basis function
Re	Reynolds number, $-$
s	distance, m
s_A	stoichiometric coefficient of species A, $-$
s_t	speedup, -
$\mathbf{s}, \mathbf{s}'$	direction vectors
S	surface area, m^2; domain boundary
S_m	mass source, kg/m^3
$\mathbf{S}$	parametric NURBS surface
$\mathbf{S}_u$, $\mathbf{S}_v$	partial derivatives of NURBS surface in u and v direction
Sc	Schmidt number, $-$
t	time, s; line parameter, $-$

$\mathbf{t}$	surface tangent unit vector
T	temperature, K
T_r	radiation temperature, K
u	NURBS surface parameter, $-$
u_i	i-th component of velocity vector, m/s; knot value, $-$
$\mathbf{U}$	knot vector
v	NURBS surface parameter, $-$
V	cell volume, m^3
x	particle size parameter, $-$
x_i	Cartesian coordinate
Y	mass fraction, $-$
Y_l	spherical harmonics
z	molar fraction, $-$

Greek

α	absorptivity, $-$
δ_{ij}	Kronecker delta, $-$
ϵ	emissivity, $-$; turbulent dissipation rate, m^2/s^3; convergence threshold, $-$
λ	wavelength, m
κ	absorption coefficient, $1/m^2$
μ	dynamic viscosity, $kg/(m^2s^2)$
ν	frequency, $1/s$
Ω	solid angle, sr; computational domain
π	plane
ϕ	azimuthal angle, rad
ψ	arbitrary scalar value
ρ	in section 2.1.3 reflectivity, $-$; in section 2.2.1 density, kg/m^3
σ	Stefan-Boltzmann constant, $5.6696 \times 10^{-8}\, W/(m^2K^4)$
$\sigma_k, \sigma_\epsilon$	turbulent Prandtl numbers, $-$
τ	stress tensor, $kg/(m^2s^3)$; transmissivity, $-$
θ	polar angle, rad

Subscripts

0	vacuum; initial value
∞	far field
a	absorbed
A	species
b	blackbody
d	diffuse
D	drag
e	emitted, execution (in chapter 6)
eff	effective
g	gray gas
i	index
in	incident
j	index
kin	kinetic
λ	spectral
m	medium
max	maximum
min	minimum
out	outgoing
p	particle; parametric
P	product
ph	photon
r	radiation
R	reactant
ref	reference
rp	between origin and destination points
s	specular
t	turbulent
u	in u parametric direction
v	volume; in v parametric direction
w	at wall

Superscripts

avg	average
CFD	on dense convective mesh
h	in homogeneous coordinate system
r	radiative

Abbreviations

BEM	boundary element method
BVH	bounding volumes hierarchy
CAD	computer aided design
CFD	computational fluid dynamics
CVM	control volume method
DNS	direct numerical simulation
DO	discrete ordinates
DT	discrete transfer
FSK	full-spectrum k-distribution
GPU	graphics process unit
LES	large eddy simulation
MC	Monte-Carlo
MCRT	Monte-Carlo Ray Tracing
MPI	Message Passing Interface
NURBS	non-uniform rational basis spline
RANS	Reynolds-averaged Navier-Stokes
RDF	radiation distribution factor
RNG	random number generator
RTE	radiation transport equation
S2S	surface-to-surface
SIMD	single instruction multiple data

Chapter 1

Introduction

1.1 Motivation of the present study

Mathematical modelling is a widespread tool used by engineers and researches, providing a cost-effective and convenient way to tackle practical problems. The commercial packages have a variety of models available and can deal with a range of different phenomena. The simulation can give an engineer a valuable insight into the problem at hand, allowing to better understand the phenomena and to avoid possible mistakes. The stated above benefits, together with the rapid growth of computational power of modern computers, made the mathematical modelling very popular in the design, reliability estimation, research and other processes.

In the last decade of the previous century a number of codes were developed and then integrated into comprehensive commercial packages, which can deal with multi-physics phenomena. At that time, most of the effort was put into the stability and efficiency of the models. Although big improvements were done in the field of the hardware, the possibilities of speeding up the simulations by increasing the frequency of the processor are almost exhausted. Currently, the appearance of multi-core processors and clouds of interconnected computers opened the door to parallel programming. Another state-of-the art technique of parallel computing originates from the computer graphics community and makes use of graphical processor units.

The field of new models development was somewhat neglected by commercial packages developers, in spite of the recent advances in computer capabilities. Nevertheless, the progress in computer power makes it possible to introduce mathematical models, whose usage was previously limited, because of long computing times and storage reqiurement. It is also worth to mention,

that the code of the models implemented the commercial packages cannot be readily modified. Thus, open-source packages have emerged, as a market response to the needs of the users, who frequently modify the code in order to test new solutions, or simply suit their needs. Open-source packages serve as a convenient tool for researchers. Moreover, relatively high prices of commercial codes should not be overlooked when discussing the motivation of using their open-source counterparts.

Thermal radiation is a dominant heat transfer mode at elevated temperatures. Therefore, it is crucial in environments encountered in industrial furnaces, combustion systems, heating equipment, rocket plumes, etc. Radiative heat transfer influences the gas and particle phases and also affects the combustion chemistry. The difficulties arising when modelling radiative heat transfer stem from the fact, that it is a long-distance and potentially all-to-all phenomenon, contrary to convection or heat conduction, which can be treated as local phenomena. The complexity is fully reflected in the mathematical description of the radiation transport, which is described by an integro-differential equation. The level of complexity is elevated by the radiative properties of medium, which are irregular functions of temperature, wavelength and gas composition.

The models for solving radiation heat transfer problems available in commercial CFD packages are often based upon many simplifications which limit their usage or generate solutions with hard-to-control errors. Moreover, the treatment of boundary conditions of special types (specular reflections, collimated beams) and material properties (non-diffusive surfaces, anisotropic radiation) is limited or even impossible to account for within those models.

All the above reasons make the Monte Carlo a promising tool for solving the heat radiation problems. Not only can it treat the radiation transfer without many simplifications present in other techniques, but also is capable of generating benchmark solutions. This is the only method capable of dealing with radiative heat transfer problem of arbitrary level of complexity justified by physics. The usage of the Monte Carlo in engineering applications was limited, since its computer implementations resulted in excessively long computing times. Therefore, the computational efficiency of the method is of great importance. It should be emphasized, that Monte Carlo can be efficiently parallelized. This feature in the advent of easy access to large computer clusters and graphical processor units significantly reduces the computation time.

1.2 Earlier studies

1.2.1 Monte Carlo Method history

Historically, the statistical sampling technique, also named Monte Carlo, was developed for the purposes of Manhattan Project during World War II in Los Alamos Laboratory [62]. Stanisław Ulam, Enrico Fermi, John von Neumann and Nicholas Metropolis used the method to create histories of life of neutrons during fission. According to those researchers, the process of fission can be modelled by tracing a large, but finite, number of neutrons and analyse the state of atoms the neutrons can interact with. The specific events in the process like emission, absorption of the neutron, direction of emission or reflection, change of energy state etc. are determined by random sampling from a known probability density function. Since then the field of Monte Carlo application has grown and now include evaluation of multidimensional integrals [62], rendering in 3D graphics, predicting the illumination [59, 60], radio-waves propagation [113], radiation transport or generation of semi-exact solutions to problems that have no analytical solution [62] - to name only a few. When it comes to thermal radiation heat transfer, Monte Carlo was first used in early 1960' by Fleck and later by Howell and Perlmutter [37, 52, 53, 54]. The recent contributions to the enhancement of MC technique are due to the computer graphics community [1, 30, 41, 94]. In this branch of engineering, MC is used mainly for rendering of 3D scenes.

1.2.2 Monte Carlo in radiative heat transfer

Since the radiation mode of heat transfer predominates in high temperatures, the fields of application of radiation models usually converge to the problems in which high temperature is present. There exist a number of numerical methods capable of solving radiation problems, including Surface to Surface (S2S) [50, 81], Zonal [49, 51], Spherical Harmonics (P_N) [6, 48, 58, 70, 71], Discrete Ordinates (DO) [35, 36, 122, 123], Boundary Elements Method (BEM) [7, 8, 9, 10, 131] and Discrete Transfer (DT) [22, 24, 72]. Each of these methods is described in some detail in chapter 3. Monte Carlo has a number of distinctive features, that in some cases can make it preferable to the methods mentioned earlier. Monte Carlo method is not prone to the ray effect, as it is the case in DO [23, 81] and DT methods. The code of Monte Carlo technique can be kept relatively simple, yet capable of solving problems with some

specific boundary conditions (specular reflections, collimated rays) or detailed material properties (non-diffusive surfaces, radiation anisotropy). It stands in contrast with S2S and P_N methods, for which the coding and solution efforts rise drastically together with the problem complexity. Moreover, the core of Monte Carlo, the ray tracing procedure, is a very good candidate to parallel programming, described in details in section 1.2.5.

Monte Carlo Ray Tracing was applied to radiation heat transfer among surfaces by F. J. Nevárez-Ayala in FELIX code [87] and by C. Zeeb in MONT3D code [138, 139]. The technique was also used in combustion simulations to determine the effects of radiation-turbulence interactions. Different turbulence models were employed, namely direct numerical simulation (DNS) [26, 137], Reynolds-averaged Navier-Stokes (RANS) [110] and large-eddy simulation (LES) [56, 111, 141].

Monte Carlo method was used to simulate the behaviour of the scattering medium [115, 120] by exploring Mie theory. In those cases the ray direction can be influenced by the presence of particles. In his work, Trivic [121] used different method of incorporating the particles into Monte Carlo simulation. The particles are treated as a gray gas of equivalent absorptivity. Thus, the ray direction can not be changed due to ray-particle interaction. However, the presence of particles is seen in the form of higher gas absorption coefficient and consequently as a higher absorption probability. The main shortcoming of Trivic's approach is to assume the particles have the same temperature as the surrounding medium. Such an approach may result in high inaccuracy in the case of coal combustion systems, in which the temperature of coal particles significantly differs from the gas they are suspended in.

When it comes to the simulation of practical systems, Monte Carlo method was used to predict radiative heat transfer in coal-fired boilers in AIOLOS code [64, 104] and flame modelling [110, 111, 117, 141].

1.2.3 Ray tracing on coarse meshes

The core of Monte Carlo technique is the procedure of ray tracing, in which the most time consuming part is the routine of ray-boundary intersection [1, 43, 76, 109, 138, 139]. In the case of non-participating medium, the radiative heat fluxes at boundary walls are of interest, thus the ray has to intersect only real boundaries of the domain. More complicated case is an optically active medium, for which the volumetric heat sources or sinks are also to be defined. The volumetric heat sources or sinks correspond to the net radiative energy

emitted or absorbed by the medium. In order to find the ray absorption point, the information about the length of the ray within the medium is needed. Thus, the intersections of the ray and the boundaries of inner volumetric cells are to be defined as well. In the thesis, the main goal is to implement Monte Carlo in an optically active medium.

Space traversal techniques help to reduce the number of ray-boundary intersection tests, increasing the efficiency of a ray tracer. In the finite volume approach the computational domain is to be discretized by an introduction of a set of volumetric cells. The most straightforward implementation of Monte Carlo technique is to trace the rays on the original convective mesh. In this case, during the ray tracing the space is traversed volume-by-volume [77], resulting in prohibitively long computation times. However, it should be noticed that the characteristic dimension of the radiation is considerably larger than that of turbulence or convection. Therefore, the usage of coarse mesh, build on the basis of fine convective mesh, for solving the radiative heat transfer is a natural step towards reducing the computational intensity of the ray tracing algorithm. The idea of using coarse ortho-Cartesian mesh was presented in G. Węcel Ph.D. thesis [131]. Later, this concept was also used by I. Hunsaker [56]. The present thesis makes use of the same idea.

The reason why a regular ortho-Cartesian mesh was chosen for ray tracing is that, the volume elements are always axis-aligned cuboids and the procedure of finding the ray-cell intersection is fast and simple to implement [4, 12, 39, 40, 131]. The model presented in the thesis implements uniform ortho-Cartesian mesh, in which the ray is traced cell-by-cell and traverses the space linearly in time. Similar concepts has been presented in the literature such as uniform space division [139] and volume-by-volume advancement [77] methods but not with the boundary description by NURBS surfaces. It should be emphasized that in the case of non-participating medium the proposed method may not be optimal one in comparison with other space subdivision methods like octrees, BSP-trees, KD-trees or bounding volume hierarchy (BVH). In those approaches the space can be traversed faster than linearly in time. More information about the mentioned above methods can be found in the literature [4, 39, 40, 42, 57]. However, in the case of participating medium, the space subdivision method directly influences the size of volume elements in which the medium properties are averaged. In general, the mesh resolution should be fine enough to adequately account for the changes in medium properties. Moreover, the position of zones to be refined is not known a-priori.

Therefore, the idea of a regular ortho-Cartesian mesh was chosen instead of other space subdivision techniques mentioned before. G. Węcel used the ortho-Cartesian mesh with varying cell sizing [131]. However, in his implementation, it was not possible to locally refine the mesh. The idea of hierarchical mesh presented in the thesis is a solution to this problem.

1.2.4 Boundary description

The mathematical description of 3D geometry can be a challenging task, especially when it comes to complicated shapes. The simplest way to describe the 3D surface is to express it as a finite set of triangular or quadrilateral surfaces [138]. By doing so, the user has to accept its shortcomings in the form of relatively large memory consumption and limited accuracy when the surface is not planar. The usage of polynomials is a more elaborated way of 3D geometry description. Polynomials are smooth and have a compact form. However, they are proven to be unstable to floating point operations, since their coefficients can attain very large or small values [31, 96]. In computer graphics it is also important to have a possibility of local geometry modification, which is hard to achieve using polynomials. The stated above shortcomings can be successfully circumvented by using a special form of the mathematical description of boundaries, namely the parametric non-uniform rational basis spline (NURBS) surfaces.

In order to specify the boundaries of the enclosure, NURBS surfaces were chosen because of a few reasons. They are able to describe shapes of high complexity, use little of computer memory, are stable to floating point operations and are widely used in computer aided design (CAD) programs and computer graphics [31, 95, 96]. Moreover, there exist efficient algorithms for finding ray-NURBS surface intersection. Most of these algorithms were developed for the purposes of surfaces visualization and rendering in computer graphics.

According to Pabst [91], the algorithms for finding ray-parametric surface intersection can be classified as follows: subdivision, numerical, algebraic and Bézier Clipping.

Subdivision-based algorithms make use of convex hull property of parametric surfaces [102, 136]. The surface is tested for the intersection with ray and in the case of success it is subdivided. The process is repeated until no hit is reported or the surface is smaller than prescribed threshold and therefore is assumed to adequately approximate the real intersection point.

The core of numerical algorithms is the iterative Newton's method characterized by quadratic convergence rate, provided it has a good initial guess. The algorithm was first used in the context of finding ray-parametric surface intersection by Toth [119]. The initial guesses for Newton's method were obtained from the interval analysis of the surface. Other authors [2, 41, 76, 91] used hierarchies of axis aligned bounding boxes to properly initialize Newton's method and to limit the number of ray-surface intersection tests, but they implemented different algorithms for bounding box creation.

Algebraic method for ray-parametric surface intersection was first demonstrated by Kajiya [61]. The method requires finding the roots of 18th-degree polynomial and is limited to 3-rd order surfaces without possibility to extend it to arbitrary NURBS surfaces making its application impractical.

The Bézier Clipping algorithm for ray-patch intersection was introduced by Nishita [86] and it can be thought of as an integration of subdivision-based and numerical algorithms. The method utilizes convex hull property of parametric patches to determine parts of surface that cannot contain an intersection point. The algorithm has better convergence than subdivision-based algorithms and was improved by Efremov [30]. Wang [125] improved the performance of ray-parametric patch intersection algorithm for coherent rays by combining Newton's and Bézier Clipping methods.

From the algorithms presented above only Newton's and Bézier Clipping methods are fast enough to be implemented in ray tracing. Newton's method has an advantage over the Bézier Clipping, as it is not limited only to Bézier patches and therefore this technique was used in this work.

1.2.5 Parallel ray tracing

Monte Carlo method requires tracing a huge number of rays in order to get an accurate solution. It is considered a good candidate for parallel computation, since the tracing procedure of a single ray does not require any information about the fate of other rays [136, 138]. Therefore, the natural way to speed-up the calculations is to use multi-processor machines. The reason for resorting to parallel computing is even more obvious, as the possibilities of improving the frequency of a single processor have almost reached the limit. The problem of parallelization of Monte Carlo ray tracing radiation models is addressed in works [21, 33, 56, 75, 79, 98, 127, 135], which report a good scaling of the ray tracing algorithm.

Single-instruction multiple-data stream (SIMD) machines were used in first attempts of parallelization of Monte Carlo method. In this kind of architecture the group of rays is passed to the processors at one time. After every ray from the group is absorbed the new set of rays can be worked on. This led to poor scalability, since in general the ray path lengths are different and some processors may idle, waiting for the termination of the last ray. The way to overcome the problem is to generate new rays as soon as one of them was terminated [45].

The state-of-the-art technique, originating from computer graphics community, uses graphics process units (GPUs) for parallel ray tracing. A single GPU has a shared memory and is composed of hundreds of cores, allowing to trace hundreds of rays simultaneously. The technique proved to be very efficient, as it allowed for the real-time rendering of 3D scenes in computer graphics [1, 91, 103]. Moreover, Despres run Monte Carlo ray tracing on an nVidia 7600 GS GPU and showed speedup of 6 in comparison with Xeon 2.4 GHz CPU [27].

Due to the fact, that the field of parallel computing is relatively young, the programming standards of common C++ language lag behind. Thus, the correct implementation of parallel code is a challenging task, in which the programmer has to take into account the configuration of the computer or computer network and the type of hardware. The codes with GPU-enhanced processing are developed using libraries specific for a given GPU vendor, like nVidia CUDA C/C++ [89]. For so called distributed-memory multiprocessors, networks of workstations and combinations of those, the most popular programming technique is Message Passing Interface (MPI) [85]. In this standard, multiple copies of a program cooperate with each other by exchanging the data. In order to force a single, sequential program to include parallel portions of the code (multi-threading or farming), OpenMP library was introduced [16]. It is a gentle modification of C, C++ programs and thus is relatively easy in implementation. It is also possible to stitch MPI and OpenMP together into one hybrid parallel program [135].

In order to achieve good scaling, the inter-processor communication should be minimised. In CFD applications, the common procedure is to decompose the computational domain into fragments corresponding to different processors. Then MPI is used in order to allow data exchange between the processors. The domain decomposition is a good strategy in the case of CFD calculations, where all the phenomena have local character (fluid flow, turbulence, conduc-

tion, combustion). However, radiation is potentially all-to-all phenomena, in which the interaction occurs on a long distances. Therefore, there are two main strategies for parallel treatment of Monte Carlo technique applied to radiation heat transfer. The first is the domain decomposition, which requires passing the rays between processors owing their part of the domain [135]. The second idea is to create a local copy of a mesh, that can be used individually by each processor, avoiding data exchange [56]. The latter idea is better, when the ray tracing is done on coarse mesh of relatively low size. This topic was not covered within the thesis, but rather is described here in order to point out the direction for further research.

1.3 Objectives

The main objective of the thesis is to develop Monte Carlo Ray Tracing method able of solving conjugate heat transfer problems in domains of arbitrary shapes, in the presence of non-gray gases and solid particles.

The stated above objective is to be realized, by dealing with the following partial problems:

- Develop the system for ray tracing on hierarchical ortho-Cartesian meshes with the geometry description in the form of NURBS surfaces.
- Implement the code within the open-source package OpenFOAM.
- Verify the technique using benchmark solutions.
- Prove the concept of using coarse meshes in the radiative analysis.
- Enhance the numerical efficiency of the method by
  - introducing coarse ortho-Cartesian mesh,
  - implementation of parallel ray tracing.
- Extend the applicability range of the MCRT method to include
  - non-gray properties of gases,
  - influence of solid particles suspended in the fluid.
- Compare Monte Carlo method with Discrete Ordinates.

Chapter 2

Mathematical models

2.1 Radiative heat transfer

This section describes basic laws and definitions that are associated with heat radiation. The purpose is to introduce the terminology and to give a general overview of the subject matter. A detailed description of the radiative heat transfer theory can be found in textbooks [51, 81, 108].

Radiative heat transfer and *thermal radiation* terms are frequently used to describe the phenomena of heat transfer caused by emission and absorption of electromagnetic waves or photons. There exist two theories describing the behaviour of photons: electromagnetic wave theory and quantum mechanics. Neither of these approaches is capable to fully explain all phenomena that are observed. This fact is commonly known as the wave-particle duality and the solution is to use both theories interchangeably, depending on the case at hand.

As in each mode of heat transfer, the driving force of radiation is the temperature difference. What distinguishes radiation from conduction and convection is that in simpler cases the heat transfer rates are proportional to the difference in temperature to the fourth power. Therefore, the radiative heat transfer mode becomes dominant at high temperatures.

In general all atoms emit radiative energy in the form of waves (photons) when their temperature is above absolute zero. As explained by quantum mechanics theory, atoms and molecules, undergo transitions from one energy state to another which is connected with the emission or absorption of energy in the form of photons. Photons propagate in vacuum with the speed of light c_0, which equals to $2.998 \times 10^8\ m/s$. In the case of other media, the propagation

speed c is expressed by introducing the index of refraction n:

$$c = \frac{c_0}{n}. \tag{2.1}$$

The value of refraction index depends on the type of medium. For most gases $n \simeq 1$ and thus its influence can be neglected. On the other hand, the refractive index for liquids and semi-transparent solids is much higher than one and in this case it should be taken into account (eg. for glass $n \simeq 1.55$).

The electromagnetic wave (or photon) is described by means of its velocity c, wavelength λ and frequency ν, coupled by equation:

$$c = \lambda\nu. \tag{2.2}$$

According to quantum mechanics, every photon has a discrete amount of energy e_{ph} expressed by means of Planck's constant h_P:

$$e_{ph} = h_P\nu. \tag{2.3}$$

The range of wavelength spectrum of electromagnetic waves is broad and varies from order of couple hundred of meters (radio waves) to less than 10^{-14} meters (γ rays). The wavelength range characteristic to thermal radiation spans from 0.1 to 100 μm and is limited to waves emitted by a medium only due to its temperature. Therefore, the region corresponding to thermal radiation ranges from long-wave portion of the ultraviolet, through the visible light up to the mid-infrared (Fig. 2.1) [81].

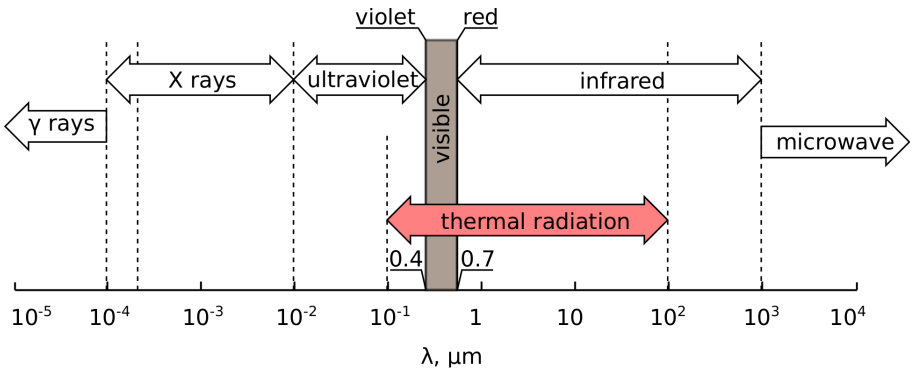

Figure 2.1: Electromagnetic wave spectrum.

In order to solve engineering problems one has to consider the interaction of incident radiant energy with matter. The problems involve emission and absorption of radiation by solid surfaces, partially transmitting media such as gases and clouds of suspended particles. All the material properties required by

the radiative heat transfer equations may depend on the wavelengths of radiant energy. It is customary to name the quantities related to a given wavelength as *spectral (monochromatic)* and those concerning the whole spectrum as *total (panchromatic)*. The first group of quantities is denoted by a subscript λ.

2.1.1 Blackbody radiation

A *blackbody* is defined as a perfect absorber of thermal radiation, which means it absorbs all incident radiation from all directions and at all wavelengths. In thermodynamic equilibrium, blackbody must radiate away as much energy as it absorbs, thus it was found that it is also a perfect isotropic emitter [108]. The amount of energy a blackbody emits at a given temperature T and wavelength λ is called the *spectral blackbody emissive power* and can be determined according to *Planck's law* (Fig. 2.2):

$$e_{b\lambda}(T,\lambda) = \frac{2\pi h_P c_0^2}{n^2\lambda^5\left[e^{(h_P c_0/n\lambda k_B T)}-1\right]}, \tag{2.4}$$

where $h_P = 6.626 \times 10^{-34}$ Js is Planck's constant, n is refractive index, c_0 is speed of light in vacuum, $k_B = 1.381 \times 10^{-23}$ J/K is Boltzmann constant. After introducing constants $C_1 = h_P {c_0}^2$ and $C_2 = h_P c_0/k_B$ the equation 2.4 can be simplified to

$$e_{b\lambda}(T,\lambda) = \frac{2\pi C_1}{n^2\lambda^5\left[e^{(C_2/n\lambda T)}-1\right]}. \tag{2.5}$$

According to equations (2.4), (2.5), the overall level of emission rises with increasing temperature, while the wavelength of maximum emission moves towards shorter wavelengths. The wavelength of maximum emission at a given temperature can be found from equation, known as *Wien displacement law*:

$$\lambda_{max} = \frac{C_3}{nT}, \tag{2.6}$$

where $C_3 = 2897.8$ μmK. *Total blackbody emissive power* is the energy flux emitted by a blackbody within all wavelengths (W/m^2). It can be calculated from the *Stefan-Boltzmann law*:

$$e_b(T) = \int_0^\infty e_{b\lambda}(T,\lambda)d\lambda = n^2\sigma T^4, \tag{2.7}$$

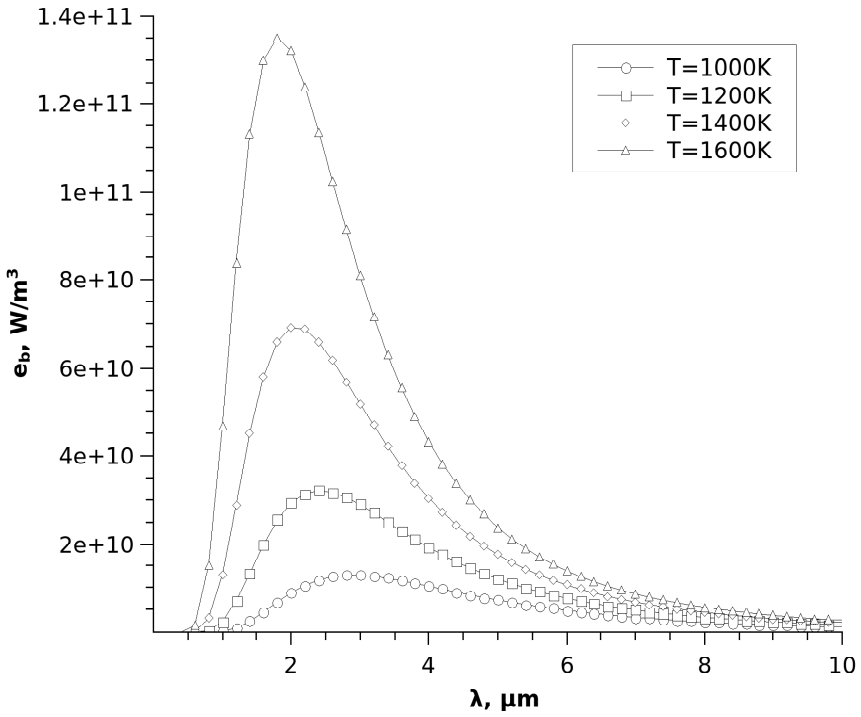

Figure 2.2: Spectral blackbody emissive power for various temperatures.

where σ is *Stefan-Boltzmann constant* defined as

$$\sigma = \frac{2C_1\pi^5}{15C_2^4} = 5.6696 \cdot 10^{-8}\ W/m^2K^4. \tag{2.8}$$

The blackbody emissive power in the wavelength range λ_1, λ_2 is

$$e_{b,\lambda_1-\lambda_2} = \int_{\lambda_1}^{\lambda_2} e_{b\lambda}(T,\lambda)d\lambda = \int_{\lambda_1}^{\lambda_2} \frac{2\pi C_1}{n^2\lambda^5\left[e^{(C_2/n\lambda T)}-1\right]}d\lambda. \tag{2.9}$$

In order to compute integral (2.9) one can use tables or Wiebelt's approximation, both returning $f(n\lambda T)$, which is the fraction of total blackbody emissive power in the wavelength interval from 0 to arbitrary value of λ for a given value of $n\lambda T$. Then

$$e_{b,\lambda_1-\lambda_2} = [f(n\lambda_2 T) - f(n\lambda_1 T)]n^2\sigma T^4. \tag{2.10}$$

2.1.2 Intensity of radiation

The *radiative energy flux* (W/m^2) is defined as spectral radiative energy E^r_λ transferred through differential surface area dS in time:

$$e^r_\lambda = \frac{E^r_\lambda}{dS\,dt}. \tag{2.11}$$

The radiation emitted in a given direction is defined in terms of the *intensity*. Intensity of radiation is the spectral radiative energy flux transferred within an infinitesimal solid angle $d\Omega$ centered around a given direction (Fig. 2.3) and is given by equation

$$I_\lambda = \frac{de^r_\lambda}{\cos\phi\, d\Omega} = \frac{d^3E^r_\lambda}{dS\cos\phi\, d\Omega\, dt}, \tag{2.12}$$

where ϕ is the angle between the differential surface normal and incoming intensity direction vectors. The units of the intensity are $W/(m^2\,sr)$, where sr is called steradian and is a unit of solid angle $d\Omega$. After integrating over entire

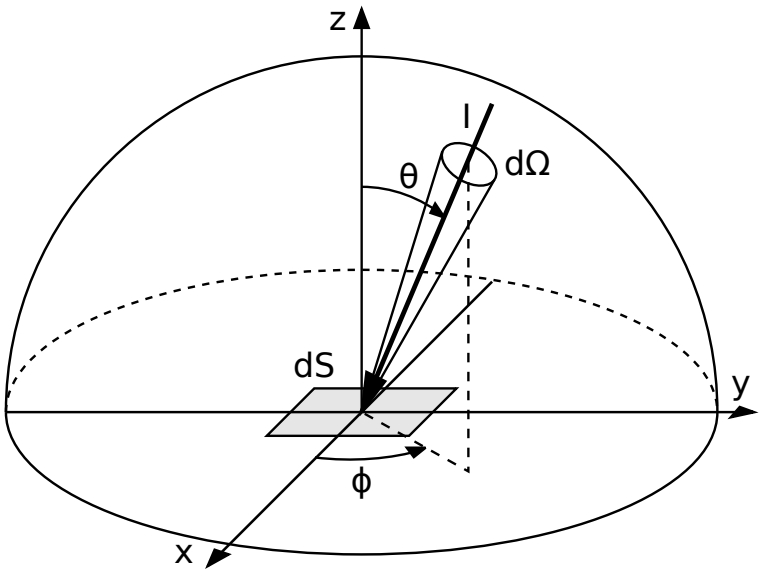

Figure 2.3: Intensity of radiation I travelling along direction, defined by polar θ and azimuthal ϕ angles in an infinitesimal solid angle $d\Omega$, centered around that direction and striking differential surface dS.

spectrum, one can find total intensity of radiation:

$$I = \int_0^\infty I_\lambda\, d\lambda. \tag{2.13}$$

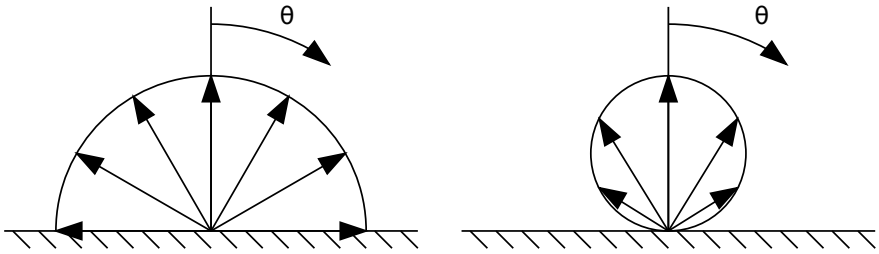

(a) intensity (b) directional emissive power

Figure 2.4: Angular dependence of blackbody intensity and blackbody directional emissive power.

It is proven [108] that intensity of radiation from a blackbody is independent of the direction of emission (Fig. 2.4). Surfaces that do not have directional dependence of radiative properties are called *diffuse*. In order to obtain the radiative energy flux at a given surface, the normal component of the radiation intensity should be integrated over a hemisphere

$$e^r = \int_{2\pi} I \cos\phi \, d\Omega. \tag{2.14}$$

The differential solid angle is related to the polar and azimuthal angles by

$$d\Omega = \sin\phi \, d\phi \, d\theta. \tag{2.15}$$

Inserting equation (2.15) into (2.1.2) yields for diffuse surfaces

$$e^r = I \int_{\theta=0}^{2\pi} \int_{\phi=0}^{\pi/2} \cos\phi \sin\phi \, d\phi \, d\theta = \pi I. \tag{2.16}$$

The above equation is also valid for the blackbody

$$e_b^r = \pi I_b. \tag{2.17}$$

Radiative energy flux from a finite solid angle is defined by $\theta \in < \theta_1, \theta_2 >$ and $\phi \in < \phi_1, \phi_2 >$

$$e^r = I \int_{\theta_1}^{\theta_2} \int_{\phi_1}^{\phi_2} \cos\phi \sin\phi \, d\phi \, d\theta = \frac{1}{2} I \left(\sin\theta_2{}^2 - \sin\theta_1{}^2 \right) (\phi_2 - \phi_1). \tag{2.18}$$

2.1.3 Radiation between surfaces

Unlike their thermo-physical counterparts, radiative properties of materials are in general a function of wavelength. Materials whose properties do not change with wavelength are called *gray*. This assumption greatly simplifies the analysis and it is accepted in most engineering applications. Thus, most problems considered in the present work are analysed for the gray bodies.

When the beam of radiation strikes a surface of a body, it can be absorbed, reflected or transmitted. The material is called *opaque* if no electromagnetic wave can penetrate through it. Most solids absorb the radiation within a very thin surface layer, thus no radiative energy transmission occurs (Fig. 2.5).

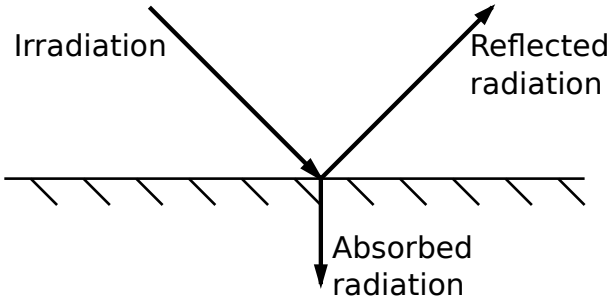

Figure 2.5: Absorption and reflection by a surface.

In section 2.1.1 the blackbody was defined as a perfect emitter and absorber of radiant energy. The behaviour of real surfaces deviates from that of blackbody, but their properties are defined by means of the respective blackbody counterparts. Therefore, the fraction of blackbody emission emitted by a real surface of the same temperature is termed *emissivity* ϵ. By analogy, the *absorptivity* α is the fraction of blackbody radiation absorbed by a real surface. According to the *Kirchhoff's Law*, when local thermodynamic equilibrium is assumed, the surface absorptivity equals to emissivity, for both total and spectral cases

$$\alpha = \epsilon; \alpha_\lambda = \epsilon_\lambda. \tag{2.19}$$

Since not all radiation incoming at the real surface is absorbed, a part of it should be reflected, in order to fulfil the balance of energy. The ability of the surface to reflect the radiation is called *reflectivity* ρ and can be determined from the equation

$$\rho = 1 - \alpha = 1 - \epsilon. \tag{2.20}$$

For real surfaces, the direction of radiation beam after being reflected is strongly dependent upon the angle of incidence. The most accurate is bidirectional reflectivity model, but such approach requires detailed material data, acquiring

of which is cumbersome and not always possible. Instead, the model applied in the current work treats the reflectivity as a sum of specular (or *mirror-like*) ρ_s and diffuse ρ_d components:

$$\rho = \rho_s + \rho_d. \tag{2.21}$$

The diffuse reflection is such, that all directions from a hemisphere above the reflection point are equally probable. In the case of specular reflection, the new direction of the beam lies symmetrically on the opposite side of the surface normal at the point of reflection. The ratio of the specular component of reflectivity to the overall reflectivity is given by *specularity ratio*

$$r_s = \frac{\rho_s}{\rho} = \frac{\rho_s}{\rho_s + \rho_d}. \tag{2.22}$$

2.1.4 Radiation in absorbing emitting media

The medium is called *transparent* if it does not interact with radiation. On the other hand, if the interaction occurs, the medium is termed *semitransparent* and this is the case for a number of media encountered in practical problems.

The interactions between medium and radiation include attenuation and augmentation of the radiation intensity along a specific path. The attenuation is caused by absorption of radiative energy by molecules and/or by scattering. Consequently, the augmentation occurs when a molecule releases energy by emission of a photon and/or by scattering. The term *scattering* refers to the interaction of electromagnetic waves with small particles (fly ash, fog, etc.) and denotes a change of a direction in which a photon travels by one of three mechanisms - diffraction, reflection or refraction. As a consequence, the intensity of radiation in a given direction can also be amplified or attenuated by means of inscattered and outscattered rays respectively.

The interaction between electromagnetic waves and particles, suspended within a gaseous phase, depends on the dimension of the particles with respect to radiation wavelength and is expressed by means of *size parameter*

$$x = \frac{\pi d_p}{\lambda}, \tag{2.23}$$

where d_p is effective particle diameter. There are three regimes of interaction, in which different theories are applied:

i) $x \ll 1$ - Rayleigh scattering,

ii) $x \simeq 1$ - Mie scattering,

iii) $x \gg 1$ - the particle surface can be treated as an ordinary surface subject to geometric optics.

The problems covered by the thesis include the combustion of pulverized coal inside a chamber. The coal particles are assumed to be ideal spheres, of diameters in the range of $d_p \in (10, 2000)\,\mu m$, which corresponds to the particle diameters encountered in industrial furnaces. The thermal radiation wavelengths are in the range of $\lambda \in (0.1, 100)\,\mu m$. As a consequence, the values of the size parameter x change from order of one up to order of tens of thousands and in prevailing majority of cases $x \gg 1$. Therefore, it was assumed in the thesis, that radiation particles interaction can be described by means of geometric optics. Moreover, the surface of coal particles is very rough and irregular, thus its absorptivity is close to 1. It implies, that the radiation scattering due to the presence of particles can be neglected and another method for interaction of particles with radiation can be introduced.

The method of particle radiation interaction used in the thesis assumes, that a cloud of particles is treated as an additional gray gas absorbing and emitting the radiation. Therefore, the scattering effects on particles are not considered within the thesis. However, it should be emphasized that Monte Carlo ray tracing method is capable of including scattering effects [74, 81, 108]. The topic of coupling between radiation and particles is presented in details in section 4.1.2.

Kirchhoff's Law for media states, that at every point the ability of the medium to absorb and emit radiation must be equal. The properties of medium describing its ability to absorb and emit radiation are expressed by means of *absorption* and *emission coefficients*. These coefficients are equal upon the restrictions given by *Kirchhoff's Law*.

The change of radiation intensity due to absorption when passing through a semitransparent medium of thickness ds is

$$dI_a = -\kappa I ds, \tag{2.24}$$

where κ is absorption coefficient and I is the incoming intensity. The absorbed portion of the radiation intensity on the path $0 \rightarrow s$ can also be defined in

terms of *absorptivity* α:

$$\alpha \equiv \frac{I(0) - I(s)}{I(0)} = 1 - \exp\left(-\int_0^s \kappa \, ds\right), \tag{2.25}$$

where $I(0), I(s)$ are respectively the intensities at the beginning and at the end of the path s.

The intensity emitted along a differential path is

$$dI_e = \kappa I_b \, ds, \tag{2.26}$$

where I_b is the blackbody intensity. Equations (2.24) and (2.26) can be formulated in terms of spectral variables by appending subscript λ to intensities and absorption coefficient.

2.1.5 Radiative heat transfer equation

The change of total radiation intensity of the ray along a given direction and in the given location within a semitransparent emitting and absorbing medium is governed by the equation

$$\frac{dI}{ds} = \mathbf{s} \cdot \nabla I = \kappa I_b(T_m) - \kappa I, \tag{2.27}$$

where κ is absorption coefficient, I is intensity of incoming radiation, I_b is emitted radiation and T_m denotes the temperature of the medium. Equation (2.27) is called the *differential form of the directional equation of radiative transfer* and is also valid for spectral quantities.

Equation (2.27) is subject to boundary condition

$$I(\mathbf{r_w}, \mathbf{s}) = \epsilon(\mathbf{r_w}) I_b(\mathbf{r_w}) + \frac{1 - \epsilon(\mathbf{r_w})}{\pi} \int_{\mathbf{n}\cdot\mathbf{s}'<0} I(\mathbf{r_w}, \mathbf{s}') |\mathbf{n} \cdot \mathbf{s}'| \, d\Omega', \tag{2.28}$$

where $\mathbf{r_w}$ is a location at the wall, $\mathbf{n}$ denotes surface normal unit vector pointing into the domain and making an angle θ' with an arbitrary direction $\mathbf{s}'$, such that $\cos\theta' = \mathbf{n} \cdot \mathbf{s}'$.

The solution of RTE (2.27) yields the radiation intensity field I at any point and any direction of the domain. Subsequently, the radiation intensity field can

be used to determine the radiative heat flux vector according to equation

$$\mathbf{q} = \int_{4\pi} I(\mathbf{s})\mathbf{s}\, d\Omega. \tag{2.29}$$

The radiative heat flux in the direction of the vector n is:

$$q^r = \mathbf{q} \cdot \mathbf{n} = \int_{4\pi} I(\mathbf{s})\mathbf{n} \cdot \mathbf{s}\, d\Omega. \tag{2.30}$$

The radiative heat source/sink due to absorption and emission within the participating medium is obtained by integrating the equation of radiative transfer (2.27) over all solid angles

$$q_v^r = \nabla \cdot \mathbf{q} = \int_{4\pi} \kappa I_b\, d\Omega - \int_{4\pi} \kappa I\, d\Omega = 4\kappa\sigma T^4 - \kappa G, \tag{2.31}$$

where G is called *incident radiation* and equals to

$$G = \int_{4\pi} I\, d\Omega. \tag{2.32}$$

2.1.6 Radiative properties of gases and their approximations

The gray gas assumption, i.e. wavelength independent radiative properties of gas, can deteriorate the accuracy of radiative heat transfer predictions. In the case of the model, which is meant to provide benchmark solutions, the ability to deal with real gas properties is crucial.

The gas can be seen as a composition of molecules, atoms, ions and free electrons. According to quantum mechanics, the molecule is a system of atoms, that has a discrete set of energy states, composed of electronic, rotational and vibrational modes. The transitions between discrete energy states are connected with absorption/emission of photons. Since energy states have discrete values, so are the photon energies and wavelengths, according to the equation (2.3). Consequently, the gas absorption and emission coefficients are highly oscillating functions of wavelength in the form of a sequence of very narrow spectral lines. Closely spaced spectral lines form bands. The width of spectral lines depend on various broadening effects, which in turn are correlated to gas temperature, pressure and composition.

For the temperature levels encountered in most engineering applications, gas mixtures emit/absorb energy of wavelengths corresponding to vibration-rotation bands. Bands connected to electronic transitions play an important role in higher temperatures (above several thousand K). Vibration-rotation bands have the biggest width for triatomic molecules, among which CO_2 and H_2O are of special interest, since they are frequently present in significant amounts in most engineering problems.

Since the real behaviour of the gases is far from gray-gas assumption, their radiative properties should be modelled in more detailed way. There are several methods of modelling spectral properties of gases, which include:

1. Line-by-line,
2. Narrow-band,
3. Wide-band,
4. k-distribution,
5. Weighted Sum of Gray Gases.

Line-by-line

Line-by-line method is considered to be the most accurate. Simultaneously, it is the most time consuming technique, which makes it impractical for engineering calculations. The method uses databases of high-resolution line spectra for different molecules and their mixtures at various temperatures. The databases are known as HITRAN [100] and HITEMP [101]. In this method, the radiative absorption is determined by integrating over all lines with contributions within the band.

Narrow-band

Narrow-band models use simplifications to ease the spectral integration over a given bandwidth. The simplifications concern mainly the shape of the line structure. Within the narrow-band models, one can distinguish between *the Elsasser*, *the Goody* and *the Malkmus* models. The differences are their assumed distributions of line spacing, shape and intensity. More information can be found in [28, 44].

Wide-band

By analogy, the wide-band model spans over an entire vibration-rotation band.

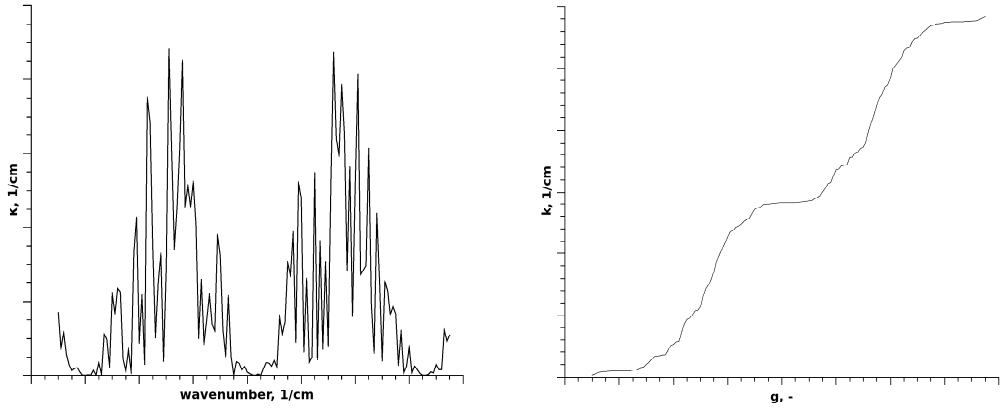

(a) κ versus wavenumber (b) $\kappa - g$ distribution

Figure 2.6: Reordering of the absorption coefficient κ vs. wavenumber function in order to form the κ-distribution in g-space.

In practice, to predict the radiative behaviour of gases and to derive the relations for wide-band models, theoretical quantum mechanics can be used, as was done by Grief [20, 55]. Another approach was presented by Edwards and Menard [28] who modelled a band of rotation lines and introduced the exponential wide band model. The model was verified against a large dataset and presented in publications [29, 134]. It was proven to yield results of very good agreement with experimental data.

k-distribution

The idea behind the k-distribution method is to avoid laborious integration over the narrow spectral intervals (Fig. 2.6a) by replacing it by the integration over the normalized artificial wavenumber g. In order to achieve it, the absorption coefficient is reordered to form a monotonic absorption coefficient cumulative distribution function versus normalized artificial wavenumber g (Fig. 2.6b). Then, the smoothly varying function is used to calculate the spectral property dependence in the radiative transfer relations. As a consequence of reordering, the number of points required for integration is much less than in the case of original dependence of the absorption coefficient and wavenumber. The name of the method comes from the nomenclature used in the field of meteorology, where k stands for the absorption coefficient.

Standard k-distribution method was found to be inefficient in cases of non-homogeneous gas compositions or temperatures across the domain. The correlated k-distribution (c-k method) overcomes the limitations of the standard model [44, 67, 99, 112, 141]. The most recent works of Modest, Zhang and Wang [83, 84, 126, 140] resulted in an introduction of full-spectrum k-distribution

(FSK) method, which is in fact a variant of c-k method. The authors claim, that the technique is an exact method for a correlated absorption coefficient, utilizing a continuous k-distribution over the whole spectrum and allowing usage of a quadrature scheme of arbitrary order. The experimental data for the absorption coefficient was taken from HITEMP [101] for H_2O and CDSD [116] for CO_2 species.

Weighted Sum of Gray Gases

WSGG model was developed by Hottel [51] for the purpose of its implementation in zonal method. Its main advantage, being a good compromise between accuracy and computational time, made it one of the most widely used in engineering problems [82, 108].

Although some researchers used more accurate modelling of radiative gas properties in their ray tracing algorithms (c-k [117, 141]), none of them can be easily used in engineering problems due to prohibitively long computational time. This is caused by the fact, that spectral properties of the gases have to be randomly sampled by statistically meaningful number of rays. The stated above advantage was also the main reason why WSGG was employed within the present work.

The theoretical background of the model is covered by this paragraph following the approach used by G. Węcel works [130, 131, 132, 133]. The numerical implementation inside Monte Carlo Ray Tracing model is described in chapter 4.9. Finally, section 6.3 presents practical example.

$\star \star \star$

The total absorptivity (equal to emissivity) of the gas is defined as

$$\alpha = \epsilon = 1 - \tau = 1 - e^{\int_s \kappa ds}. \tag{2.33}$$

In accordance to paper of G. Wecel [132], total emissivity of $H_2O - CO_2$ mixture is calculated by

$$\epsilon = \sum_{i=0}^{N_g} a_i \left(1 - e^{-\kappa_i p_t (z_C + z_H) s}\right), \tag{2.34}$$

where $N_g, a, \kappa, p_t, z_C, z_H, s$ are the number of gray gases in the model, the weighting factor, the absorption coefficient, total pressure of the mixture, molar fraction of CO_2 and H_2O and path length, respectively. In the present

formulation of WSGGM four gray gases $N_g = 4$ with a transparent gas ($i = 0$) are used. The weighting factors are positive and sum-up to unity

$$\sum_{i=0}^{N_g} a_i = 1.0, \quad a_i >= 0. \tag{2.35}$$

For the transparent gas ($i = 0$)

$$a_0 = 1 - \sum_{i=1}^{N_g} a_i. \tag{2.36}$$

The physical meaning of weighting factor is the following. It is the portion of black body energy associated with the given component gas of the spectral regions in which the absorption coefficient is close to κ_k (cf. Fig. 2.7). The

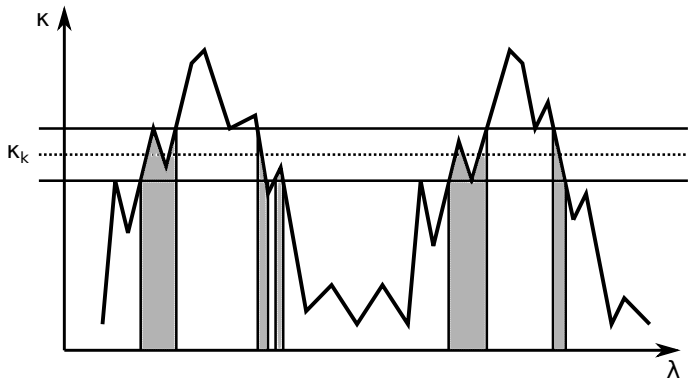

Figure 2.7: Definition of weighting factors a_k as a portion of spectral energy distribution [51].

weighting factors are polynomial functions of temperature and molar fraction ratio

$$a_i = \sum_{j=0}^{4} b_{i,j} T_r^j, \quad a_i >= 0, \tag{2.37}$$

where T_r is normalized temperature defined as $T_r = T/T_{ref}$. Reference temperature is set to be $T_r = 1200K$. The $b_{i,j}$ coefficient is a polynomial function of molar fraction ratio of H_2O to CO_2 $M_r = p_{H2O}\ p_{CO2}$

$$b_{i,j} = \sum_{k=0}^{4} C_{i,j,k} M_r^k. \tag{2.38}$$

The absorption coefficient of a single gray gas i is

$$\kappa_i = \sum_{k=0}^{4} d_{i,k} M_r^k. \tag{2.39}$$

The WSGGM coefficients C and d are found by least-square surface fitting to the data generated using HITEMP 2010 spectroscopic database. The model coefficients for a $CO_2 - H_2O$ mixture for molar fraction ratio $M_r \in (0.01, 4.00)$, temperature $T \in (300, 2400)$ K and pressure-path length product $p_t s \in (0.01, 60)$ atm were reported in paper [132] and used within the thesis.

2.2 Computational fluid dynamics

The purpose of this section is to give a brief description of the mathematical models dealing with mass, momentum and energy transfer, that are connected to fluid flow. In the present work, the open-source computational fluid dynamics (CFD) package OpenFOAM [90] was used. Within the package, all the equations are already implemented and the author's role was only to modify the radiation model, visible in the overall energy balance equation as an energy source term. It should be kept in mind, that the models presented within the current section are limited to those, directly used in the problems addressed by the thesis. Therefore, all the models being outside the scope of the thesis were omitted.

2.2.1 Flow field

Mass Conservation

The mass conservation equation or continuity equation has the following form

$$\frac{\partial \rho}{\partial t} + \frac{\partial}{\partial x_i}(\rho u_i) = S_m, \tag{2.40}$$

where: ρ is fluid density, u_i is velocity in i-th direction, S_m is the mass source. In the case of species transport, the continuity equation reads

$$\frac{\partial \rho Y_A}{\partial t} + \frac{\partial}{\partial x_i}(\rho u_i Y_A) = -\frac{\partial}{\partial x_i} J_{A,i} + R_A + S_{m,A}, \tag{2.41}$$

where: Y_A is mass fraction of species A, R_A is the production rate of species A due to reaction, $S_{m,A}$ is the mass source of species A due to devolatilization or evaporation and $J_{A,i}$ is the diffusion mass flux of species A. The diffusion mass flux in the case of laminar flow regime, is described by Fick's Law:

$$J_{A,i} = -\rho D_{A,m} \frac{\partial Y_A}{\partial x_i}, \quad i = 1, 2, 3; \tag{2.42}$$

where $D_{A,m}$ is diffusion coefficient of species A in the mixture.

Momentum Conservation

The momentum conservation law is described by Navier-Stokes equation of the form:

$$\frac{\partial}{\partial t}\left(\rho u_i\right) + \frac{\partial}{\partial x_j}\left(\rho u_i u_j\right) = -\frac{\partial p}{\partial x_i} + \frac{\partial \tau_{ij}}{\partial x_j} + \rho g_i + F_i, \tag{2.43}$$

where p denotes static pressure, τ_{ij} is stress tensor, g_i is gravitational acceleration, F_i is the momentum source term, eg. due to the presence of particulate matter and its interaction with continuous phase.

The stress tensor is determined from the following relation

$$\tau_{ij} = \left[\mu\frac{\partial u_i}{\partial x_j} + \frac{\partial u_j}{\partial x_i}\right] - \frac{2}{3}\mu\frac{\partial u_l}{\partial x_l}\delta_{ij}, \tag{2.44}$$

where μ is molecular dynamic viscosity, δ_{ij} is Kronecker delta.

2.2.2 Heat transfer

The main equation describing heat transfer is called the energy conservation equation. In the case of flows involving multi-species transport and including chemical reactions, the equation is given by:

$$\frac{\partial}{\partial t}(\rho H) + \frac{\partial}{\partial x_i}(u_i(\rho H)) = \frac{\partial}{\partial x_i}(k + k_t)\frac{\partial T}{\partial x_i} - \frac{\partial}{\partial x_i}\sum_A h_A J_A + \frac{\partial}{\partial x_i}(\tau_{ij})_{\text{eff}} u_j + S_h, \tag{2.45}$$

where H is total specific enthalpy, k, k_t are thermal and turbulent conductivities, h_A denotes sensible specific enthalpy of species A, J_A is diffusion flux of species A, $(\tau_{ij})_{\text{eff}}$ is effective stress tensor, S_h is the volumetric heat source, defined as

$$S_h = S_{h,r} + S_{h,p} + S_{h,react}, \tag{2.46}$$

where $S_{h,r}, S_{h,p}, S_{h,react}$ are respectively the volumetric heat sources due to radiation, particles and reactions. $S_{h,r}$ is defined by equations (4.19) or (4.38), $S_{h,p}$ by (2.62) and $S_{h,react}$ by (2.69), (2.76). The total enthalpy H is a sum of sensible enthalpy and kinetic energy

$$H = h + \frac{u_i^2}{2}. \tag{2.47}$$

The sensible enthalpy h in the case of multiple species transport is

$$h = \sum_A Y_A h_A, \tag{2.48}$$

where Y_A denotes the mass fraction of species A in the mixture and h_A is the sensible specific enthalpy of species A, which is given by

$$h_A = h_A^0 + \int_{T_{ref,A}}^{T} c_{p,A} dT, \tag{2.49}$$

where $c_{p,A}$ is specific isobaric heat of species A, $T_{ref,A}$ is the reference temperature of species A, at which the formation enthalpy h_A^0 has been determined.

2.2.3 Turbulence

The characteristic feature of the turbulent flows is the presence of eddies of different dimensions and time constants. The biggest eddies have dimensions close to the dimensions of the main flow, while the smallest ones are responsible for kinetic energy dissipation and its transformation to heat. The presence of eddies inside the flow results in the fluctuations of local flow velocity. In theory, it is possible to take into account all the sizes and time constants of vortex structures without resorting to any simplifications. This approach to flow and turbulence modelling is known as direct numerical simulation (DNS). The computational cost of this technique increases with the third power of the turbulent Reynolds number Re_t^3, which excludes its application in most engineering problems. Therefore, other models describing turbulence were developed, one of which is Reynolds averaging technique.

The Reynolds averaging model uses time averaged form of equations (2.40) and (2.43). In the turbulent flow, every parameter ψ (arbitrary scalar) can be decomposed into mean (time-averaged) and fluctuating components:

$$\psi_i = \overline{\psi_i} + \psi_i', \tag{2.50}$$

where $\overline{\psi}$ is mean component of the parameter ψ and ψ' is fluctuating component.
Analogously, the velocity can be written as

$$u_i = \overline{u_i} + u_i'. \tag{2.51}$$

According to Reynolds, the continuity and momentum conservation equations can be rewritten in terms of time averaged velocities as:

$$\frac{\partial \rho}{\partial t} + \frac{\partial}{\partial x_i}\left(\rho \overline{u_i}\right) = 0, \tag{2.52}$$

$$\begin{array}{l} \frac{\partial}{\partial t}\left(\rho \overline{u_i}\right) + \frac{\partial}{\partial x_j}\left(\rho \overline{u_i u_j}\right) = \\ -\frac{\partial \overline{p}}{\partial x_i} + \frac{\partial}{\partial x_j}\left[\mu\left(\frac{\overline{u_i}}{x_j} + \frac{\overline{u_j}}{x_i} - \frac{2}{3}\delta_{ij}\frac{\overline{u_l}}{\overline{x_l}}\right)\right] + \frac{\partial}{\partial x_j}\left(-\rho \overline{u_i' u_j'}\right), \end{array} \tag{2.53}$$

where $\left(-\rho \overline{u_i' u_j'}\right)$ is Reynolds stresses term. Equation (2.53) is commonly known as Reynolds-averaged Navier-Stokes (RANS) equation.
In general, the Reynolds stresses term is not known. Therefore, to find a solution to equation (2.53), the Boussinesq hypothesis is employed, due to which:

$$-\rho \overline{u_i' u_j'} = \mu_t\left(\frac{\partial \overline{u_i}}{\partial x_i} + \frac{\partial \overline{u_j}}{\partial x_i}\right) - \frac{2}{3}\left(\rho k + \mu_t \frac{\partial \overline{u_i}}{\partial x_i}\right)\delta_{ij}, \tag{2.54}$$

where μ_t is turbulent viscosity and k denotes turbulent kinetic energy.

In order to determine the turbulent kinetic energy, the $k-\epsilon$ model was introduced [68]. The model was named after the two equations, in which the main variables are k - turbulent kinetic energy and ϵ - turbulence dissipation rate. The equations have the following form:

$$\rho \frac{Dk}{Dt} = \frac{\partial}{\partial x_j}\left(\left(\mu + \frac{\mu_t}{\sigma_k}\right)\frac{\partial k}{\partial x_j}\right) + G_k + G_b - \rho\epsilon - Y_M + S_k \tag{2.55}$$

and

$$\rho \frac{D\epsilon}{Dt} = \frac{\partial}{\partial x_j}\left(\left(\mu + \frac{\mu_t}{\sigma_\epsilon}\right)\frac{\partial \epsilon}{\partial x_j}\right) + C_{1\epsilon}\frac{\epsilon}{k}(G_k + C_{3\epsilon}G_b) - C_{2\epsilon}\rho\frac{\epsilon^2}{k} + S_\epsilon, \tag{2.56}$$

where: G_k, G_b are the generation of turbulent kinetic energy due to the mean velocity gradients and buoyancy respectively, Y_M is fluctuating dilatation dissipation, $C_{1\epsilon}, C_{2\epsilon}, C_{3\epsilon}$ are empirical constants, $\sigma_k, \sigma_\epsilon$ are turbulent Prandtl numbers, determined experimentally, S_k, S_ϵ are user defined source terms. The turbulent viscosity μ_t from equation (2.54) is determined from the equation

$$\mu_t = \rho C_\mu \frac{k^2}{\epsilon}. \tag{2.57}$$

2.2.4 Dispersed phase

The multiphase flow of particles immersed in the fluid was modelled using *Euler-Lagrange* approach. The main idea is is to treat the fluid phase as a continuum, whose motion is governed by Navier-Stokes equation (2.43). The dispersed phase is composed of a large set of independent particles. The motion of the dispersed phase is determined by tracking a representative number of particles through the pre-calculated flow field. The two phases are interconnected by exchange of momentum, mass and energy (Fig. 2.8). The model assumes, that particle-particle interactions can be neglected, which is true for a low volume fraction occupied by the discrete phase. In the pulverized coal combustion, where concentrations of coal are in most cases $< 1\,kg/m^3$, the volume fraction of particles in the fluid are < 0.1. Therefore, the model can be applied to the pulverized coal combustion.

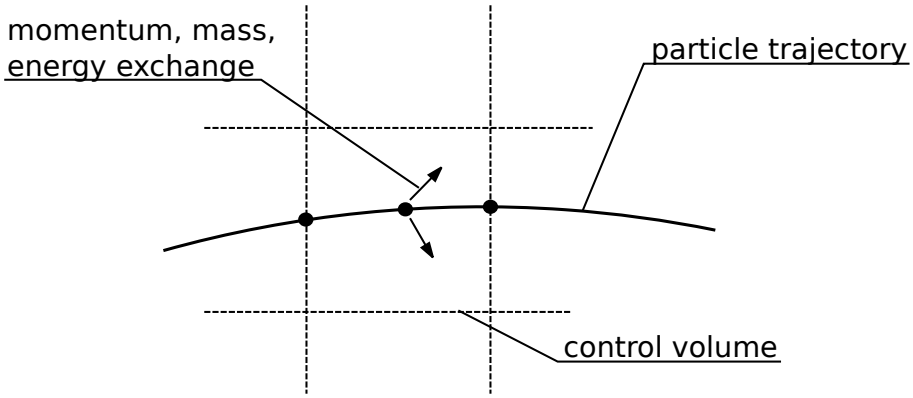

Figure 2.8: Particle trajectory.

Dispersed phase motion

The particle trajectory is determined by integrating the equation of force balance on the particle:

$$\frac{du_p}{dt} = F_D(\overrightarrow{u} - \overrightarrow{u_p}) + \frac{\overrightarrow{g}(\rho_p - \rho)}{\rho_p} + \overrightarrow{F}, \tag{2.58}$$

where u_p, u are particle and fluid velocities, ρ_p, ρ are particle and fluid densities, F_D is drag coefficient, $\overrightarrow{g}$ is gravitational acceleration vector and $\overrightarrow{F}$ is an acceleration vector due to the presence of additional phenomena like e.g. thermophoresis, Brownian effects or Saffman's lift forces.

Dispersed phase heat transfer

The energy balance of the particle has the following form:

$$m_p c_p \frac{dT_p}{dt} = hA_p(T_\infty - T_p) + \epsilon_p A_p \sigma (T_r^4 - T_p^4), \tag{2.59}$$

where $m_p, c_p, T_p, A_p, \epsilon_p$ are the particle mass, heat capacity, temperature, surface area and emissivity, respectively, T_∞ denotes local temperature of the fluid, σ is Stefan-Boltzmann constant and T_r is radiation temperature, defined by

$$T_r = \left(\frac{G}{4\sigma}\right)^{1/4}. \tag{2.60}$$

Symbol G denotes the incident radiation in W/m^2, which is computed using equation (2.32). The convective heat transfer coefficient h is computed using Ranz-Marshall correlation:

$$Nu = \frac{hd_p}{k_\infty} = 2.0 + 0.6\, Re_d^{1/2}\, Pr^{1/3}, \tag{2.61}$$

where d_p is particle diameter, k_∞ is thermal conductivity of the fluid, Re_d is Reynolds number based on particle diameter and the relative velocity, Pr is Prandtl number of the fluid ($c_p\mu/k_\infty$).

The volumetric heat source in equation (2.45) due to the presence of particles is

$$S_{h,p} = -hA_p(T_\infty - T_p). \tag{2.62}$$

2.2.5 Reacting flow

One of the examples covered in the thesis is pulverized coal combustion in a chamber (sec. 6.3). In this case, modelling of both homogeneous and heterogeneous reactions is necessary.

The source of species A due to reactions is a sum of contributions from all chemical reactions in which the species is involved

$$R_A = \sum_k^{K_R} R_{A,k}, \tag{2.63}$$

where K_R is the number of reactions and $R_{A,k}$ is the production rate of species A due to $k-th$ reaction.

Homogeneous reactions

In order to determine the rate of production due to reactions between gaseous species finite-rate/eddy-dissipation model is employed. The idea of the method is to upgrade diffusion driven model of Magnussen [73] with reaction kinetics based on Arrhenius-type expression. In this model the rate of production of species A due to reaction is given by the smallest value calculated from three expressions:

$$R_A = s_A \min(R_{A,R}; R_{A,P}; R_{A,kin}), \tag{2.64}$$

where s_A is stoichiometric coefficient of species A, $R_{A,R}, R_{A,P}, R_{A,kin}$ are respectively the production rates of species A obtained from mixing rates of reactants R, product species P and from kinetics of reaction.

The mixing rates can be determined from

$$R_{A,R} = 4M_A\rho\frac{\epsilon}{k}\min\left(\frac{Y_R}{\nu_R M_R}\right), \tag{2.65}$$

$$R_{A,P} = 2M_A\rho\frac{\epsilon}{k}\frac{\sum\limits_P Y_P}{\sum\limits_P \nu_P M_P}, \tag{2.66}$$

where: M_A, M_R, M_P are molar weights of A, reactants and product species, ϵ is turbulent kinetic energy dissipation rate, k is kinetic energy, Y_R and Y_P are mass fractions of reagent and product species, ν_R, ν_P are stoichiometric coefficients of reactants and product species, respectively.

Kinetic rate of reaction is calculated from

$$R_{A,kin} = k_r M_A \prod_{j=1}^{n}\left(\frac{Y_j\rho}{M_j}\right)^{\eta_{j,P}+\eta_{j,R}}, \tag{2.67}$$

$$k_r = B_0 e^{-E/RT}, \tag{2.68}$$

where $\eta_{j,P}, \eta_{j,R}$ are the exponents of j species in products and in reactants, B_0 is pre-exponential coefficient, E is activation energy.

The occurrence of reactions inside the flow is accompanied by heat generation and consumption. This heat is accounted for in the energy balance equation (2.45) in the form of source term:

$$S_{h,react} = \sum_A \left[h_A^0 + \int\limits_{T_{ref,A}}^{T} c_{p,A}dT\right] R_A, \tag{2.69}$$

where $T_{ref,A}$ is the reference temperature of species A, at which the formation enthalpy of species A, h_A^0, has been determined.

Char combustion - kinetic diffusion model

In the kinetic diffusion char combustion model reaction rate depends on kinetics and on diffusion rate [14, 34]. It is assumed that CO_2 is the only product of the reaction. The char reaction rate is determined from:

$$-\frac{dm_p}{dt} = A_p \frac{\rho M R T Y_{O2}}{M_{O2}} \frac{D_0 R_k}{R_k + D_0}, \tag{2.70}$$

where Y_{O2} is oxygen mass fraction in the gaseous phase surrounding the particle, M_{O2} is molar weight of oxygen, D_0 is oxygen diffusion rate, R_k is reaction rate. The diffusion rate of oxygen and reaction rate are given by:

$$D_0 = B_1 \frac{[0.5(T_p + T)]^{0.75}}{d_p}, \tag{2.71}$$

$$R_k = B_2 e^{E/RT_p}, \tag{2.72}$$

where B_1 is diffusion constant, B_2 is pre-exponential coefficient, E is activation energy.

In the case of char combustion in oxygen-enriched environment, multi-reaction combustion model is implemented. It consists of three global reactions:

$$C(s) + \frac{1}{2}O_2 \rightarrow CO, \tag{2.73}$$

$$C(s) + CO_2 \rightarrow 2CO, \tag{2.74}$$

$$C(s) + H_2O \rightarrow CO + H_2. \tag{2.75}$$

The rate of each reaction is determined in accordance with kinetic-diffusion model (equations (2.70), (2.71) and (2.72)). The mass loss of char is a sum of contributions from each reaction.

The heat released due to the presence of surface reactions can be determined from energy balance using enthalpies of formation of reactant species:

$$S_{h,react} = m_{\mathrm{CO}} h^0_{\mathrm{CO}} - m_{\mathrm{C}} h^0_{\mathrm{C}} - m_{\mathrm{CO2}} h^0_{\mathrm{CO2}} - m_{\mathrm{H2O}} h^0_{\mathrm{H2O}}. \tag{2.76}$$

Chapter 3

Numerical methods of solving heat radiation problems

The chapter deals with the brief description of models used in radiative heat transfer in participating media. For each method, a set refences is given, which allows the reader to deepen the knowledge in a particular subject.

In the process of MCRT model development, which is a main goal of the thesis, *surface to surface* (S2S) model was used. This method is dedicated to radiation transfer in non-participating medium and for the sake of completeness its description can be found in appendix A.

3.1 Zonal method

The zonal method is an extension of the net exchange method, covered in appendix A. It was developed by Hottel and Cohen [49] for an absorbing, emitting, non-scattering gray gas with constant absorption coefficient and later upgraded by Hottel and Sarofim [51] to include variable absorption coefficient and isotropic scattering.

In order to find a solution to radiative heat exchange problem, i.e. to find radiative heat fluxes at the enclosure walls and radiative heat sources/sinks within participating medium, the enclosure boundary is divided into N surface areas and the medium into K volume elements. Within each element the surface or medium parameters (temperature, surface absorptivity or medium absorption coefficient) are kept constant.

The method employs the concept of *direct exchange areas* between respective elements. In the following derivations it is assumed that medium has uniform constant absorption coefficient and is non-scattering. The *surface-*

to-surface direct exchange area, $\overline{s_i s_j}$ (Fig. 3.1a) is defined by equations

$$Q^r_{ij} = \overline{s_i s_j}\, q^r_{out,i}, \tag{3.1}$$

$$\overline{s_i s_j} = \int_{A_i}\int_{A_j} e^{-\kappa|\mathbf{r}_i\mathbf{r}_j|}\,\frac{\cos\theta_i\cos\theta_j}{\pi|\mathbf{r}_i\mathbf{r}_j|^2}\,dA_j\,dA_i, \tag{3.2}$$

where Q^r_{ij} is the total heat coming from zone i that travels directly (without reflections) to zone j; $q^r_{out,i}$ is radiosity of surface i (sum of emitted and reflected radiative heat flux); dA_i, dA_j are differential areas; κ is absorption coefficient; θ_i, θ_j are the angles between surface normal vectors $\mathbf{n}_i$, $\mathbf{n}_j$ and vector connecting elements $\mathbf{r}_i\mathbf{r}_j$; $|\mathbf{r}_i\mathbf{r}_j|$ is the distance between elements.
The *volume-to-surface direct exchange area*, $\overline{g_i s_j}$ (Fig. 3.1b) is defined by equations

$$Q^r_{ij} = \overline{g_i s_j}\, e_{b,i}, \tag{3.3}$$

$$\overline{g_i s_j} = \int_{V_i}\int_{A_j} e^{-\kappa|\mathbf{r}_i\mathbf{r}_j|}\,\frac{\cos\theta_j}{\pi|\mathbf{r}_i\mathbf{r}_j|^2}\,\kappa\,dA_j\,dV_i, \tag{3.4}$$

where dV_i is differential volume element, $e_{b,i}$ is blackbody emissive power of element i.
The *volume-to-volume direct exchange area*, $\overline{g_i g_j}$ (Fig. 3.1c) is defined by equations

$$Q^r_{ij} = \overline{g_i g_j}\, e_{b,i}, \tag{3.5}$$

$$\overline{g_i g_j} = \int_{V_i}\int_{V_j} e^{-\kappa|\mathbf{r}_i\mathbf{r}_j|}\,\frac{\kappa^2}{\pi|\mathbf{r}_i\mathbf{r}_j|^2}\,dV_j\,dV_i. \tag{3.6}$$

The *reciprocity* equations for direct exchange areas are

$$\overline{s_i s_j} = \overline{s_j s_i}, \quad \overline{g_i s_j} = \overline{s_j g_i}, \quad \overline{g_i g_j} = \overline{g_j g_i}. \tag{3.7}$$

Moreover, the following summation relations hold

$$\sum_{j=1}^{N}\overline{s_j s_i} + \sum_{k=1}^{K}\overline{g_k s_i} = A_i, \quad 1 \le i \le N, \tag{3.8}$$

$$\sum_{j=1}^{N}\overline{s_j g_i} + \sum_{k=1}^{K}\overline{g_k g_i} = 4\kappa V_i, \quad 1 \le i \le K. \tag{3.9}$$

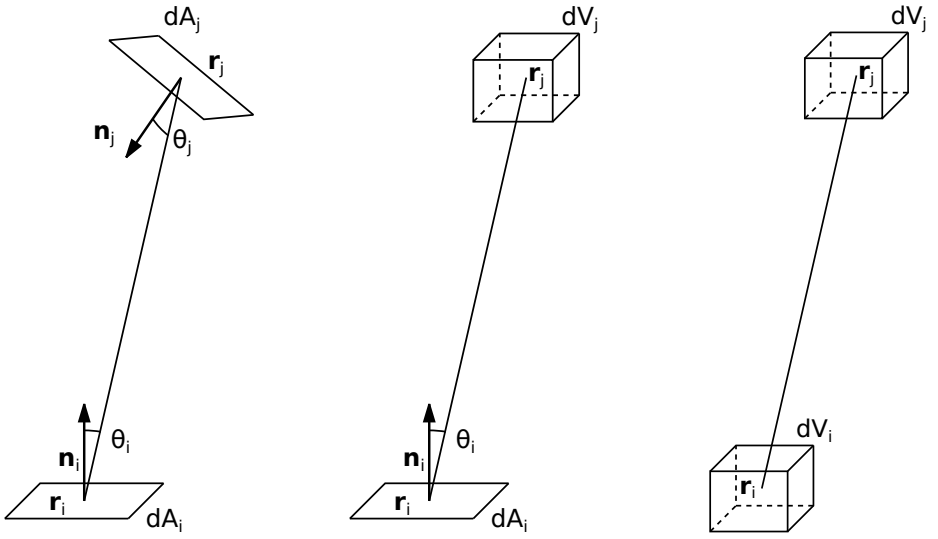

(a) Surface-Surface (b) Surface-Volume (c) Volume-Volume

Figure 3.1: Radiative exchange between differential elements of different type.

Writing an energy balance for surface zone i yields

$$Q_i^r = A_i q_i^r = A_i(q_{out,i}^r - q_{in,i}^r) = A_i \epsilon_i \left(e_{b,i} - q_{in,i}^r\right), \tag{3.10}$$

$$\begin{aligned} Q_i^r &= \sum_{j=1}^{N} \overline{s_j s_i} \left(q_{out,i}^r - q_{out,j}^r\right) + \sum_{k=1}^{K} \left(q_{in,i}^r - e_{b,k}\right) \\ &= \epsilon_i \left(A_i e_{b,i} - \sum_{j=1}^{N} \overline{s_j s_i}\, q_{out,j}^r - \sum_{k=1}^{K} \overline{g_k s_i}\, e_{b,k} \right), \quad 1 \le i \le N. \end{aligned} \tag{3.11}$$

Analogously, an energy balance for volume element i yields

$$Q_{v,i}^r = V_i q_{v,i}^r = \kappa V_i (4e_{b,i} - G_i), \tag{3.12}$$

$$\begin{aligned} Q_{v,i}^r &= \sum_{j=1}^{N} \overline{s_j g_i} \left(e_{b,i} - q_{out,j}^r\right) + \sum_{k=1}^{K} \overline{g_k g_i} \left(e_{b,i} - e_{b,k}\right) \\ &= 4\kappa V_i e_{b,i} - \sum_{j=1}^{N} \overline{s_j g_i}\, q_{out,j}^r - \sum_{k=1}^{K} \overline{g_k g_i}\, e_{b,k}, \quad 1 \le i \le K. \end{aligned} \tag{3.13}$$

In the case of known temperature field in the whole domain and by using equation (A.9) to express net heat at wall elements Q^r by means of radiosity, equations (3.11), (3.13) form a system of $N + K$ equations with unknown surface radiosities q_{out}^r and unknown net heat at volume elements Q_v^r. In order

to find the unknown variables a set of linear algebraic equations needs to be solved. In the case, the temperatures of the domain are unknown, they are to be determined iteratively and the matrix inversion is to be done every iteration.

The equations of the zonal method can be simplified to the case of non-participating medium, and in this particular case the method is similar to the net exchange method described in appendix A.

⋆ ⋆ ⋆

The zonal method suffers from main drawback, being the computationally intensive determination of direct exchange areas. A variant of the method used the concept of total exchange areas, which can be calculated using direct exchange areas [49, 51, 88]. Upon the assumption that gas and surface absorption properties do not vary with temperature and composition, direct exchange areas can be calculated once for a given case. Although the computation of total exchange areas is more involved than direct exchange areas, it can shorten the overall simulation time. The benefits of this approach are especially visible in the case of conjugate heat transfer, where the temperatures of surface and volume elements can change and the solution is obtained in an iterative manner.

3.2 Boundary Element

The *Boundary Element Method* (BEM) in the application to radiation heat transfer problems was proposed by R. Białecki in [7] and developed in later works [8, 9, 10]. In his Ph.D. thesis [131], G. Węcel improved the method and applied it to conjugate heat transfer problems, including the simulations of Czochralski crystal growth process and natural gas combustion [12, 13, 128, 129]. The method has common roots with Hottel's zonal method and Finite Element Method, which in turn can be viewed as a variants of the weighted residuals methods.

The main idea behind BEM is to transform the original differential RTE (2.27) into an equivalent form of an integral equation:

$$I(\mathbf{p}) = I(\mathbf{r})\tau(\mathbf{r},\mathbf{p}) + \int\limits_{L_{rp}} \kappa(\mathbf{r}')I_b\left[T_m(\mathbf{r}')\right]\tau(\mathbf{r}',\mathbf{p})dL_{rp}(\mathbf{r}'), \tag{3.14}$$

where L_{rp} denotes the line of sight between origin $\mathbf{r}$ and destination $\mathbf{p}$ points, $\tau(\mathbf{r},\mathbf{p}), \tau(\mathbf{r}',\mathbf{p})$ are transmissivities, defined as a fraction of energy leaving the

origin point and reaching the destination point.
As a result of the transformation, the dimensionality of the problem is reduced. This can be achieved, since the integration over the enclosure volume is replaced by an equivalent integration along a radiative path times an integration over the enclosure boundary. In the next step, the radiative transfer equation (3.14) is solved by dividing the enclosure boundary into surface and volume elements. In each volume element, the temperature and the absorption coefficient of the medium are assumed uniform. At boundaries, the blackbody emissive power and the radiative heat flux are approximated using shape functions. In order to determine the unknown transmissivities in equation (3.14), the ray tracing is performed. The resulting set of algebraic equations is solved by means of the weighted residuals method [8]. Due to the introduction of shape functions, approximating the radiative heat fluxes at boundaries, the radiative energy balance is not fulfilled. The discrepancy (residuum) is minimized by forcing it to vanish at selected set of nodes. This procedure is commonly known as nodal collocation.

⋆ ⋆ ⋆

BEM can be treated as a generalization of S2S and Zonal methods assuming the trial functions and weighted functions are constant in each boundary element and vanish to zero outside it. BEM can also be interpreted as Galerkin solution to radiative transfer equation. Since the weighted functions have a form of Dirac delta, BEM method can be classified as a collocation method [7, 8].

BEM proved to be more efficient than Monte Carlo and Discrete Transfer techniques, however it was much slower than Discrete Ordinates [131]. During the development stage of coupling BEM with CFD code, Węcel came to the conclusion, that applying the method to the same numerical grid as used for convective problems can lead to prohibitively long computational times. To mitigate the problem, he introduced coarse Cartesian structured meshes on which the radiative solution was obtained. Subsequently the solution was transferred onto the convective mesh. Using the coarse meshes allowed BEM achieving computational times comparable with DO method. Contrary to DT and DO methods, BEM is not prone to ray effect.

3.3 Spherical harmonics - P_N approximation

The P_N method solves RTE (2.27) using its approximation in the form of a set of simultaneous partial differential equations. The approach was first introduced by Jeans [58] in the early 20th century to model the heat transfer in stars. Cheng [19] upgraded the method to the three-dimensional case. More information about the enhancements of the method can be found in articles [6, 48, 70, 71].

In order to develop the P_N method, the radiation intensity at a given location $\mathbf{r}$ and direction $\mathbf{s}$ is expressed in terms of Fourier series as

$$I(\mathbf{r},\mathbf{s}) = \sum_{l=0}^{\infty} \sum_{m=-l}^{l} I_l^m(\mathbf{r}) Y_l^m(\mathbf{s}), \tag{3.15}$$

where $I_l^m(\mathbf{r})$ are coefficients and $Y_l^m(\mathbf{s})$ are *spherical harmonics*, defined by

$$Y_l^m(\mathbf{s}) = (-1)^{(m+|m|)/2} \left[\frac{(l-|m|)!}{(l+|m|)!}\right]^{1/2} e^{im\phi} P_l^{|m|}(\cos\theta), \tag{3.16}$$

where θ, ϕ are polar and azimuthal angels defining the direction s, $i = \sqrt{-1}$ thus $e^{im\phi}$ provides the harmonics $\cos m\phi, \sin m\phi$, $P_l^{|m|}(\cos\theta)$ are associated Legendre polynomials of degree l and order m.

The spherical harmonics approximation is exact, when the number of terms in Fourier series of equation (3.15) is infinite, i.e. when $l \to \infty$. In practice, the series is truncated after a given number of terms. The highest value for l retained, N, defines the method name and order. The most common approximations are called P_1 and P_3, arisen from retaining terms of l less or equal to 1 and 3 respectively.

The coefficients $I_l^m(\mathbf{r})$ of equation (3.15) are not known and must be evaluated in order to determine $I(\mathbf{r},\mathbf{s})$. To achieve this, the so called *moment equations* are generated by multiplying the intensity in a given location by powers of the direction cosines and then integrating over all solid angles. Then the local intensity from equation (3.15) is substituted into the moment equations, forming a set of algebraic equations. Solving the set of equations yields the representation of the local intensity in terms of moments, which are function of location only.

The next step of the method is to determine the moments of intensity. This is done by generating *moment differential equations* from the RTE (2.27), written in terms of optical coordinate, by multiplying the equation by powers of

the direction cosines and then integrating over all solid angles. This procedure leads to a set of partial differential equations with unknown moments of intensity. Once the moments are determined, the radiation intensity in a given location and its angular variation can be evaluated and the problem is solved.

⋆ ⋆ ⋆

The P_1-approximation gained popularity because of its relative simplicity and compatibility of the solution methods for sets of partial differential equations, already available in CFD codes for equations describing flow and/or heat transfer. It should be emphasized, that the results predicted by P_1-approximation can be far from accurate, especially in optically thin media with strong anisotropy in radiation intensity in the case of geometries with large aspect ratios [81]. The solution accuracy can be improved by increasing the order of approximation. However, this requires a solution of much larger set of partial differential equations, thus much bigger computation effort [80].

3.4 Discrete Ordinates - S_N approximation

The *Discrete Ordinates* (DO) can be classified as a particular case of *flux method*, which simplifies the directional variation of the radiation intensity. The basic version of the flux method, introduced independently by Schuster [105] and Schwarzschild [106], solves the radiation problem in one direction only and is commonly known as *two-flux method*. Extending the two-flux model into two- and three-dimensional problems gives four- and six-flux models respectively [17]. In the methods described above, the directions in which the radiation transport equation is solved are the same as the axes of Cartesian coordinate system.

DO method in its current form was developed by Fiveland [35, 36] and Truelove [122, 123], whose works allowed for its implementation to arbitrary geometries and to absorbing, emitting and scattering media.

DO method solves RTE (2.27) with boundary condition defined by (2.28) in an arbitrary number m of discrete directions S, dividing the entire solid angle into finite solid angles. DO is also termed as S_N method, in which N denotes the order of method, given by

$$m = N(N+2) \tag{3.17}$$

in the case of three-dimensional formulation. Each discrete direction corresponds to a centreline of a differential solid angle. The finite solid angles do not overlap and in each of them the radiation intensity is assumed to be uniform. The computational domain is subdivided into a finite number of elements and directional RTE (2.27) is formulated for each discrete direction. Subsequently, the equations are discretized spatially using finite difference schemes and form a system of partial differential equations. The radiative heat fluxes and heat sources are determined by integration over the entire solid angle at each surface (2.30) and volume element (2.31). The integration over the solid angle employs numerical quadratures.

⋆ ⋆ ⋆

DO method is one of the most popular methods for solving radiative heat transfer problems in engineering applications due to its capabilities and ease of implementation, especially for coupled radiative and convective heat transfer. The capabilities include absorbing, emitting media, anisotropic scattering and diffusely, specularly reflecting walls. Moreover, the arbitrary level of the solution accuracy can be achieved by controlling the number of discrete directions.

The drawbacks of the method include the iterative character of the solution, even when all the temperatures in the domain are known. Also, the computational effort needed grows with the number of discrete directions and there is no procedure of determining the optimal number of discrete directions. The discrete ordinates method is known to be prone to so called *ray effect*, connected to the angular discretization of RTE [23]. The ray effect is visible especially in the cases of hot spots either in the medium or at the boundary surfaces. The radiative energy from such spots is transmitted mainly in the discrete directions, thus the reported values of radiative heat fluxes and heat sources at locations distant form hot spots can be far from exact.

Moreover, there exist *false scattering* effect, also known as *false diffusion* [23, 92]. This effect occurs due to the finite size of the control volumes and to the fact, that in general the mesh is not aligned with the ordinates, in which one solves the RTE. Thus, the solutions that should have a sharp step, exhibit a smoothed slope. The negative consequences of the false diffusion effect can be mitigated by increasing either the number of control volumes inside the mesh or the order of spatial discretization. It should be emphasized, that the ray effect and the false diffusion tend to minimize each others' negative effects.

The topic is covered in more details in section 6.2, where the solution generated by DO model is compared with Monte Carlo.

3.5 Discrete Transfer

The *Discrete Transfer* (DT) method was developed by Lockwood and Shah [72] in order to implement the radiation heat transfer mode into codes for combustion and flow. Later it was improved by [22, 24]. The method exhibits features encountered in Hottel zonal, Monte Carlo and flux methods. It is built on the concept of solving the radiation transfer equation for representative rays in the domain.

The procedure starts with the subdivision of the computational domain into volume and surface elements. For each element the parameters of the surface and volume are assumed to be uniform. Then, the hemisphere above each surface element is subdivided into a finite number of non-overlapping differential solid angles, in which the radiation intensity is uniform. Subsequently, the rays are traced from the surface elements in the directions corresponding to the centres of the differential solid angles. Therefore, unlike in the Monte Carlo method, the ray directions are set in advance, not randomly chosen. During the tracing procedure, the ray passes through the volume cells, in which the radiation intensity behaves accordingly to equation (2.27) i.e., it is attenuated by absorption and amplified by emission of the medium. The ray is traced until it hits another surface element. The radiative heat sources in volume cells are computed by summing up the contributions from all rays passing through a given volume cell. Analogously, the irradiation of the surface element is a sum of contributions from rays that hit a given surface element.

⋆ ⋆ ⋆

Since DT method uses the ray tracing procedure in predefined directions, it is prone to the *ray effect*, similar to DO method. On the other hand, the rays are traced only from boundaries of the domain, therefore the computational time is reduced compared to Monte Carlo model. The accuracy of the solution can be adjusted by modifying the number of rays traced, although it should be stressed, that the number of rays greatly influences the computational time. Analogously to DO method the number of rays traced is to be set intuitively.

3.6 Monte Carlo Ray Tracing

The statistical sampling technique, also named Monte Carlo, was developed for the purposes of Manhattan Project during World War II in Los Alamos Laboratory [62]. Stanisław Ulam, Enrico Fermi, John von Neumann and Nicholas Metropolis used the method to create histories of life of neutrons during fission. In the field of thermal radiation heat transfer, Monte Carlo was first used in early 1960' by Fleck and later by Howell and Perlmutter [37, 52, 53, 54].

The radiation can be viewed as an energy transport by photons (also termed energy bundles or rays). The main idea behind Monte Carlo is to trace a meaningful number of photons from their emission to the absorption point getting an insight into the phenomenon. The behaviour of photons i.e., the emission from surface, gas, direction of emission, their interaction with semitransparent medium, particles or walls, are defined by random sampling with known probability density functions. The statistical component of the method is reflected in its name, as Monte Carlo is a district of Monaco, famous of gambling and casinos.

In the following, the variants of Monte Carlo Ray Tracing are described, including *standard ray tracing, energy partitioning, forward* and *backward*.

In the Monte Carlo method the computational domain is subdivided into a finite number of surface and volume elements. Inside each element, the radiative properties of the medium or surface are assumed to be uniform. Subsequently, the radiative energy balance is determined by registering the fate of energy bundles emitted from each surface or volume element. In general, there are two approaches to the Monte Carlo Ray Tracing technique [33, 81]. In one of them, called *standard ray tracing*, the absorption-free path of the bundle is determined randomly. When the bundle passes though subsequent volume cells, its absorption-free and real travel paths are updated. The bundle is absorbed within the current volume element, as soon as its real path is greater than absorption-free path. When the bundle reaches the wall it can be absorbed with a certain probability at the corresponding surface element. Upon the absorption, the whole energy carried by a photon is assigned to the element at which absorption occurred. The different approach is presented by *energy partitioning* variant of Monte Carlo. In this variant of the method, during the emission the bundle is assigned an initial energy. As a consequence of passing through volume cells and of reflecting from walls, the bundle energy decays. The tracing stops when the energy of the bundle is smaller than the prescribed threshold. A word of comment is necessary here. The main difference between

standard ray tracing and energy partitioning variants of the method is that the latter is proven to be more efficient in the case of optically thick and optically thin media [33, 81, 124]. In the former variant however, the reciprocity equations can be used (described in Chapter 4). After the ray tracing is completed, the radiative heat fluxes at walls and volumetric heat sources in the medium are computed. The accuracy of the method is influenced by the number of rays traced as well as the resolution of spatial discretization of the computational domain.

The described above Monte Carlo Ray Tracing procedure, together with its two variants, is known as *forward*. The method is commonly used in the classes of problems, where the information about the whole radiation field is required. However, in the case only the information about the intensity hitting a small point of the domain or over a small range of solid angles is of interest (radiation detector, collimated rays), the forward Monte Carlo can be very inefficient. For those special cases, the so called *backward* (*reverse*) Monte Carlo can be employed. The approach is based on the idea, that a solution of directional RTE in a given direction and boundary condition can be found from the solution to a simpler problem defined in an opposite direction and different boundary condition. Thus, instead of tracing rays from all the elements defining an enclosure and registering those which hit the small radiation detector, the solution procedure simplifies to follow the rays emitted from the detector. In some cases the usage of the method can result in tremendous savings of CPU time. More details about the method can be found in [56, 81, 114].

The scope of the thesis is the forward Monte Carlo Ray Tracing method in its standard variant. Chapter 4 is devoted to the application of this method in the code of OpenFOAM.

Chapter 4

Monte Carlo Ray Tracing application to radiative heat transfer

The chapter presents a system for Monte Carlo ray tracing (MCRT) utilizing coarse hierarchical ortho-Cartesian mesh which is created based upon convective computational fluid dynamics (CFD) mesh. Parametric non-uniform rational basis spline (NURBS) surfaces [31, 96] are used to define the enclosure boundaries. The procedures of ray-surface intersection and the random selection of emission points from the NURBS surface are described in details. The radiation transport is solved on the coarse mesh and the solution is interpolated onto the underlying dense convective mesh. The model accounts for the radiation in absorbing and emitting gases and the presence of particles. The code is designed as an add-on to open-source program OpenFOAM [90].

The mathematical models described in chapter 2 are already implemented inside the open-source package OpenFOAM. The package solves the governing equations of mass, momentum, energy and radiation transfer in the fluid using the *control volume method* (CVM). The solution involves the discretization of the underlying equations in order to form a system of partial differential equations. The implementation of MCRT model was realized by adding a new radiation model to the existing structure of the package. Since MCRT solves the radiation transport described by an integral equation on meshes of different resolution, the procedure of coupling between the conductive and convective heat transfer within the fluid is also developed. The radiation problem is solved assuming that the temperature field at the boundary and inside the medium is known. In practice, the temperature field is obtained from CFD analysis

(equation (2.45)). Then, the radiative heat fluxes and volumetric heat sources are computed. Since they influence the temperature field of the fluid, the final solution is to be obtained in the iterative manner.

The equations governing the radiative heat transfer for MCRT method are derived according to the *Net Exchange Formulation*. It is similar to the formulations of S2S and Zonal models, presented in appendix A and section 3.1. Moreover, the variant of MCRT model described in the present chapter is termed as *standard* and *forward* technique (cf. section 3.6).

4.1 Governing equations

4.1.1 Absorbing and emitting medium

This section presents the derivation of radiative heat flux at the wall and volumetric heat source and sink in absorbing and emitting medium in the absence of particles.

Suppose that the domain is divided into n elements, of which $i \in [1, N]$ are surface elements and $i \in [N+1, n]$ are volume elements (Fig. 4.1). The radiation distribution factor (RDF) is defined as [74]

$$D_{ij} = \frac{E^r_{ij}}{E^r_{e,i}} \simeq \frac{N_{ij}}{N_i}, \tag{4.1}$$

where E^r_{ij} is the fraction of the radiative energy emitted by element i and absorbed in element j, $E^r_{e,i}$ is the radiative energy emitted from element i, N_{ij} is the number of rays emitted from element i and absorbed in element j including reflections and the presence of semitransparent medium, N_i is the total number of rays emitted from element i.

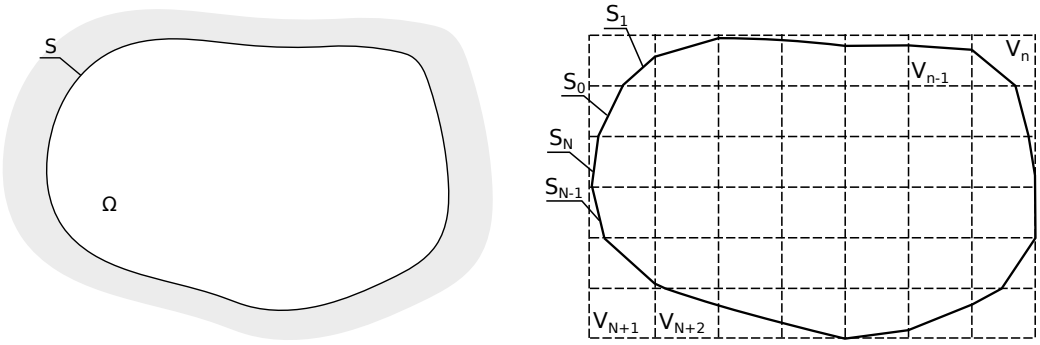

(a) Before discretization (b) After discretization

Figure 4.1: The discretization of the domain into a finite number of surface S and volume elements Ω.

The radiative energy emitted by surface or volume element equals to

$$E^r_{e,i} = \begin{cases} \epsilon_i A_i e_{b,i} & , 1 \leqslant i \leqslant N, \\ 4\pi\kappa_i V_i I_{b,i} & , N+1 \leqslant i \leqslant n. \end{cases} \tag{4.2}$$

Rearranging equation (4.1)

$$E^r_{ij} = E^r_{e,i} D_{ij} \tag{4.3}$$

and using (4.2) yields:

$$E^r_{ij} = \begin{cases} \epsilon_i A_i e_{b,i} D_{ij} & , 1 \leqslant i \leqslant N, \\ 4\pi\kappa_i V_i I_{b,i} D_{ij} & , N+1 \leqslant i \leqslant n. \end{cases} \tag{4.4}$$

Making the energy balance, the net radiative heat from element i is

$$Q^r_i = E^r_{e,i} - E^r_{a,i}, \tag{4.5}$$

where $E_{a,i}$ is the radiative energy absorbed by element i.
The radiative energy absorbed by surface or volume element i is expressed as a sum of contributions from all surface and volume elements:

$$E^r_{a,i} = \sum_{j=1}^{N} E^r_{ji} + \sum_{j=N+1}^{n} E^r_{ji}. \tag{4.6}$$

Using equation (4.4) yields

$$E^r_{a,i} = \sum_{j=1}^{N} \epsilon_j A_j e_{b,j} D_{ji} + 4\pi \sum_{j=N+1}^{n} \kappa_j V_j I_{b,j} D_{ji} \quad , 1 \leqslant i \leqslant n. \tag{4.7}$$

Inserting (4.2) and (4.7) into equation (4.5):

$$Q^r_i = \begin{cases} \epsilon_i A_i e_{b,i} - \sum\limits_{j=1}^{N} \epsilon_j A_j e_{b,j} D_{ji} - 4\pi \sum\limits_{j=N+1}^{n} \kappa_j V_j I_{b,j} D_{ji} & , 1 \leqslant i \leqslant N, \\ 4\pi\kappa_i V_i I_{b,i} - \sum\limits_{j=1}^{N} \epsilon_j A_j e_{b,j} D_{ji} & \\ \qquad\qquad -4\pi \sum\limits_{j=N+1}^{n} \kappa_j V_j I_{b,j} D_{ji} & , N+1 \leqslant i \leqslant n. \end{cases} \tag{4.8}$$

The reciprocity equations between respective pairs of elements are [74]

$$\kappa_i V_i D_{ij} = \kappa_j V_j D_{ji}, \quad \text{(volume-volume)}, \tag{4.9}$$

$$\epsilon_i A_i D_{ij} = 4\kappa_j V_j D_{ji}, \quad \text{(surface-volume)}, \tag{4.10}$$

$$4\kappa_i V_i D_{ij} = \epsilon_j A_j D_{ji}, \quad \text{(volume-surface)}, \tag{4.11}$$

$$\epsilon_i A_i D_{ij} = \epsilon_j A_j D_{ji}, \quad \text{(surface-surface)}. \tag{4.12}$$

The derivation of the reciprocity equations (4.9) to (4.12) is presented in appendix B.1. Making use of the reciprocity equations, equation (4.8) becomes

$$Q_i^r = \begin{cases} \epsilon_i A_i e_{b,i} - \sum_{j=1}^{N} \epsilon_i A_i e_{b,j} D_{ij} - \sum_{j=N+1}^{n} \pi \epsilon_i A_i e_{b,j} / \pi D_{ij} & , 1 \leqslant i \leqslant N, \\ 4\pi\kappa_i V_i e_{b,i}/\pi - \sum_{j=1}^{N} 4\kappa_i V_i e_{b,j} D_{ij} & \\ \qquad - \sum_{j=N+1}^{n} 4\pi\kappa_i V_i e_{b,j}/\pi D_{ij} & , N+1 \leqslant i \leqslant n. \end{cases} \tag{4.13}$$

The net radiative heat flux from i-th surface element, q_i^r, and the volumetric heat source and sink due to radiation absorption and emission from i-th volume element, $q_{v,i}^r$, are

$$q_i^r = \frac{Q_i^r}{A_i} \quad , 1 \leqslant i \leqslant N, \tag{4.14}$$

$$q_{v,i}^r = \frac{Q_i^r}{V_i} \quad , N+1 \leqslant i \leqslant n. \tag{4.15}$$

$$q_i^r = \frac{1}{A_i} \left\{ \epsilon_i A_i e_{b,i} - \epsilon_i A_i \sum_{j=1}^{N} e_{b,j} D_{ij} - \epsilon_i A_i \sum_{j=N+1}^{n} e_{b,j} D_{ij} \right\}, 1 \leqslant i \leqslant N. \tag{4.16}$$

$$q_{v,i}^r = \frac{1}{V_i} \left\{ 4\kappa_i V_i e_{b,i} - 4\kappa_i V_i \sum_{j=1}^{N} e_{b,j} D_{ij} - 4\kappa_i V_i \sum_{j=N+1}^{n} e_{b,j} D_{ij} \right\}, N+1 \leqslant i \leqslant n. \tag{4.17}$$

Finally

$$q_i^r = \epsilon_i e_{b,i} - \epsilon_i \sum_{j=1}^{n} e_{b,j} D_{ij}, \quad 1 \leqslant i \leqslant N, \tag{4.18}$$

$$q_{v,i}^r = 4\kappa_i e_{b,i} - 4\kappa_i \sum_{j=1}^{n} e_{b,j} D_{ij}, \quad N+1 \leqslant i \leqslant n, \tag{4.19}$$

where the sum over j encloses both surface and volume elements.

4.1.2 Absorbing and emitting medium with particles

This section presents the derivation of radiative heat flux at the wall and volumetric heat source and sink in absorbing and emitting medium in the presence of particles. The particles are assumed to be spherical in shape.

Suppose that the domain is divided into n elements, of which $i \in [1, N]$ are surface elements and $i \in [N+1, n]$ are volume elements (Fig. 4.1). The radiation distribution factor is defined as

$$D_{ij} = \frac{E^r_{ij}}{E^r_{e,i}} \simeq \frac{N_{ij}}{N_i}, \tag{4.20}$$

where E^r_{ij} is the fraction of the radiative energy emitted by element i and absorbed in element j, $E^r_{e,i}$ is the radiative energy emitted from element i, N_{ij} is the number of rays emitted from element i and absorbed in element j including reflections, the presence of semitransparent medium and particles, N_i is the total number of rays emitted from element i. The radiative energy emitted by surface or volume element equals to

$$E^r_{e,i} = \begin{cases} \epsilon_i A_i e_{b,i} & , 1 \leqslant i \leqslant N, \\ 4\pi\kappa_i V_i I_{b,i} + 4\pi V_i E_{p,i} & , N+1 \leqslant i \leqslant n. \end{cases} \tag{4.21}$$

where $E_{p,i}$ is the radiative energy emission term due to the presence of particles in volume element i. It is defined by

$$E_{p,i} = \sum_{m=1}^{M} \epsilon_{p,m} A_{pc,m} \frac{\sigma T^4_{p,m}}{\pi V_i} = \sum_{m=1}^{M} \epsilon_{p,m} \frac{\pi d^2_{p,m}}{4} \frac{\sigma T^4_{p,m}}{\pi V_i}, \tag{4.22}$$

where M is the number of particles in the volume V_i; ϵ_p, A_{pc}, T_p, d_p are respectively emissivity, the cross-section area and temperature of the particle. After rearranging equation (4.20)

$$E^r_{ij} = E^r_{e,i} D_{ij}, \tag{4.23}$$

and using (4.21) yields:

$$E^r_{ij} = \begin{cases} \epsilon_i A_i e_{b,i} D_{ij} & , 1 \leqslant i \leqslant N, \\ \left(4\pi\kappa_i V_i I_{b,i} + 4\pi V_i E_{p,i}\right) D_{ij} & , N+1 \leqslant i \leqslant n, \end{cases} \tag{4.24}$$

Making the energy balance, the net radiative heat from element i is

$$Q_i^r = E_{e,i}^r - E_{a,i}^r, \tag{4.25}$$

where $E_{a,i}$ is the radiative energy absorbed by element i.
The radiative energy absorbed by surface or volume element i is expressed as a sum of contributions from all surface and volume elements:

$$E_{a,i}^r = \sum_{j=1}^{N} E_{ji}^r + \sum_{j=N+1}^{n} E_{ji}^r. \tag{4.26}$$

Using equation (4.24) yields

$$E_{a,i}^r = \sum_{j=1}^{N} \epsilon_j A_j e_{b,j} D_{ji} + 4\pi \sum_{j=N+1}^{n} \kappa_j V_j I_{b,j} D_{ji} + 4\pi \sum_{j=N+1}^{n} V_j E_{p,j} D_{ji} \quad , 1 \leqslant i \leqslant n. \tag{4.27}$$

Inserting (4.21) and (4.27) into equation (4.25):

$$Q_i^r = \begin{cases} \epsilon_i A_i e_{b,i} - \sum_{j=1}^{N} \epsilon_j A_j e_{b,j} D_{ji} - 4\pi \sum_{j=N+1}^{n} \kappa_j V_j I_{b,j} D_{ji} \\ \qquad\qquad -4\pi \sum_{j=N+1}^{n} V_j E_{p,j} D_{ji} \qquad , 1 \leqslant i \leqslant N, \\ 4\pi\kappa_i V_i I_{b,i} + 4\pi V_i E_{p,i} - \sum_{j=1}^{N} \epsilon_j A_j e_{b,j} D_{ji} \\ \qquad -4\pi \sum_{j=N+1}^{n} \kappa_j V_j I_{b,j} D_{ji} - 4\pi \sum_{j=N+1}^{n} V_j E_{p,j} D_{ji} \quad , N+1 \leqslant i \leqslant n. \end{cases} \tag{4.28}$$

The reciprocity equations between respective pairs of elements are [74]

$$(\kappa_i + \kappa_{p,i})\, V_i D_{ij} = (\kappa_j + \kappa_{p,j})\, V_j D_{ji}, \quad \text{(volume-volume)}, \tag{4.29}$$

$$\epsilon_i A_i D_{ij} = 4\,(\kappa_j + \kappa_{p,j})\, V_j D_{ji}, \quad \text{(surface-volume)}, \tag{4.30}$$

$$4\,(\kappa_i + \kappa_{p,i})\, V_i D_{ij} = \epsilon_j A_j D_{ji}, \quad \text{(volume-surface)}, \tag{4.31}$$

$$\epsilon_i A_i D_{ij} = \epsilon_j A_j D_{ji}, \quad \text{(surface-surface)}, \tag{4.32}$$

where $\kappa_{p,i}$ is particles equivalent absorption coefficient defined as

$$\kappa_{p,i} = \sum_{m=1}^{M} \epsilon_{p,m} \frac{\pi d_{p,m}^2}{4\, V_i}. \tag{4.33}$$

The derivation of the reciprocity equations (4.29) to (4.32) is presented in appendix B.2. Making use of the reciprocity equations, equation (4.28) becomes

$$Q_i^r = \begin{cases} \epsilon_i A_i e_{b,i} - \sum_{j=1}^{N} \epsilon_i A_i e_{b,j} D_{ij} \\ \quad - \sum_{j=N+1}^{n} 4V_j \left(\kappa_j e_{b,j} + \pi E_{p,j}\right) \frac{\epsilon_i A_i D_{ij}}{4V_j(\kappa_j + \kappa_{p,j})} & , 1 \leqslant i \leqslant N, \\ 4\kappa_i V_i e_{b,i} + 4\pi V_i E_{p,i} - \sum_{j=1}^{N} 4(\kappa_i + \kappa_{p,i}) V_i e_{b,j} D_{ij} \\ \quad - \sum_{j=N+1}^{n} 4(\kappa_j e_{b,j} + \pi E_{p,j}) \frac{\kappa_i + \kappa_{p,i}}{\kappa_j + \kappa_{p,j}} V_i D_{ij} & , N+1 \leqslant i \leqslant n. \end{cases} \tag{4.34}$$

The net radiative heat flux from i-th surface element, q_i^r, and the volumetric heat source and sink due to radiation absorption and emission from i-th volume element, $q_{v,i}^r$, are

$$q_i^r = \frac{Q_i^r}{A_i} \quad , 1 \leqslant i \leqslant N, \tag{4.35}$$

$$q_{v,i}^r = \frac{Q_i^r}{V_i} \quad , N+1 \leqslant i \leqslant n. \tag{4.36}$$

Finally

$$\begin{aligned} q_i^r = \epsilon_i e_{b,i} - \sum_{j=1}^{N} \epsilon_i e_{b,j} D_{ij} + \\ - \sum_{j=N+1}^{n} \frac{\kappa_j e_{b,j} + \pi E_{p,j}}{(\kappa_j + \kappa_{p,j})} \epsilon_i D_{ij} \quad , 1 \leqslant i \leqslant N, \end{aligned} \tag{4.37}$$

$$\begin{aligned} q_{v,i}^r = 4(\kappa_i e_{b,i} + \pi E_{p,i}) - \sum_{j=1}^{N} 4(\kappa_i + \kappa_{p,i}) e_{b,j} D_{ij} \\ - \sum_{j=N+1}^{n} 4(\kappa_j e_{b,j} + \pi E_{p,j}) \frac{\kappa_i + \kappa_{p,i}}{\kappa_j + \kappa_{p,j}} D_{ij} \quad , N+1 \leqslant i \leqslant n. \end{aligned} \tag{4.38}$$

4.1.3 Non-participating medium

In the case of non-participating medium only the radiative heat fluxes at boundary walls are of interest as the volumetric heat sources are by definition zero. For the sake of compactness, the derivation of the equation is not reproduced here, but it is analogous to those presented in previous sections 4.1.1 and 4.1.2. The relation for radiative heat flux at wall can be obtained from equation (4.18), where the summation concerns only surface elements. Suppose that the boundary of the domain is divided into n surface elements.

Then the radiative heat flux at surface element i is:

$$q_i^r = \epsilon_i e_{b,i} - \epsilon_i \sum_{j=1}^{n} e_{b,j} D_{ij}, \quad 1 \leqslant i \leqslant n. \tag{4.39}$$

$\star \star \star$

The most general relationships for the wall radiative heat flux and volumetric heat source/sink are equations (4.37) and (4.38) respectively. However it should be noticed, that by setting the terms related to the presence of the particles to zero, i.e. $\kappa_p = 0$ and $E_p = 0$, equations (4.18), (4.19) are obtained. Similarly, by setting the gas absorption coefficient to zero ($\kappa = 0$), equations (4.18), (4.19) simplify to equation (4.39).

4.2 Radiation distribution factors

The ray tracing procedure used for calculating the values of radiation distribution factors (RDFs) is the core of MCRT method. All the governing equations of MCRT method (4.18), (4.19), (4.37), (4.38) and (4.39) make use of RDFs D_{ij}. It should be pointed out here, that although the notation for the RDFs in the equations from chapter 4.1 is identical, their physical meaning differs between sections 4.1.1, 4.1.2, 4.1.3. The most general definition of the RDF under the consideration is the one from section 4.1.2, since it accounts for the presence of semitransparent medium and particles.

The RDFs are estimated by registration of absorption points of energy bundles, that are emitted from each surface and volume element i and followed taking into account reflections, presence of semitransparent medium and particles, according to [74]

$$D_{ij} \cong \frac{N_{ij}}{N_i}, \tag{4.40}$$

where N_{ij} is the number of energy bundles emitted from element i and absorbed in element j, N_i denotes the total number of energy bundles emitted from element i. The radiation distribution factors are computed for every surface and volume element inside the domain and they form two dimensional radiation distribution factor matrix $\mathbf{D}$ (Fig. 4.2). In the case of participating medium, there exist four kinds of RDFs:

- surface - surface,
- surface - volume,

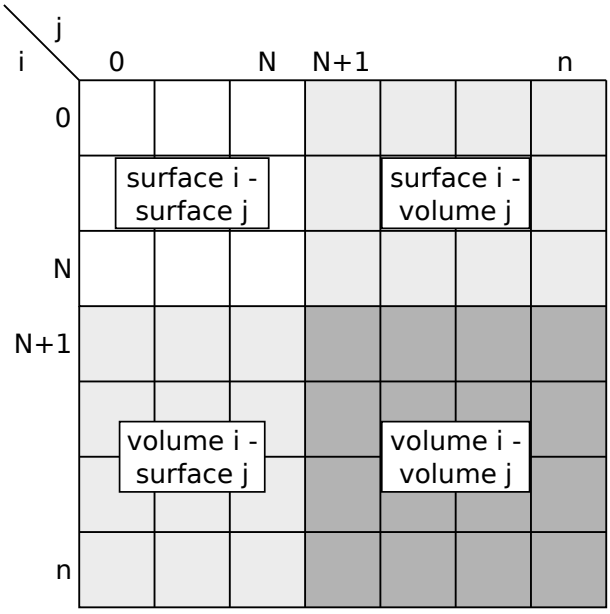

Figure 4.2: The radiation distribution factor matrix **D** and its entries corresponding to various combinations of surface and volume elements.

- volume - surface,
- volume - volume.

The distinction between those types of RDFs is important during the derivation of governing equations and the usage of reciprocity equations, which was done in section 4.1 of this chapter. The elements of the **D** matrix have the following properties:

1. Conservation of energy

$$\sum_{j=1}^{n} D_{ij} = 1.0, \qquad 1 \leqslant i \leqslant n, \tag{4.41}$$

2. Reciprocity
   - non-participating medium: eqn (4.12),
   - participating medium: eqns (4.9), (4.10), (4.11), (4.12),
   - participating medium with particles: eqns (4.29), (4.30), (4.31), (4.32).

A word of comment is necessary here. Since the ray tracing procedure involves the emission of rays from subsequent surface and volume elements denoted by index i and the absorption in elements denoted by index j, the energy conservation law (4.41) is not fulfilled. To be more precise, it is fulfilled

by summing up the elements from rows of matrix **D**, but not in columns. Thus, in the standard formulation of Monte Carlo ray tracing (cf. section 3.6), the usage of reciprocity equations is crucial, as it guarantees the energy conservation in the governing equations for wall heat fluxes and volumetric heat sources (4.18), (4.19), (4.37), (4.38) and (4.39). In other words, if an equation uses the RDFs from a single row, the energy conservation is guaranteed, otherwise it is not. In the case, the reciprocity equations are not known, it is still possible to derive the relations for wall heat fluxes and volumetric heat sources, but the **D** matrix smoothing algorithm ought to be used. Such algorithms are described in [25, 69].

A major advantage of the distribution factor approach presented by Mahan [74] is that the distribution factors are calculated independently from their subsequent use. In the case, the radiative properties of the surface and/or gas are independent of the temperature and composition, the **D** matrix needs to be computed only once. Therefore, the influence of different temperature or heat flux distributions on the enclosure walls can be evaluated without recomputing the distribution factors each time, i.e. without repeating computationally expensive ray tracing procedure.

4.3 Hierarchical ortho-Cartesian mesh

The most time consuming part of MCRT method is the ray tracing procedure used for the determination of elements of RDF matrix, as was underlined in section 4.2. In order to speed up the tracing of rays, the concept of *hierarchical ortho-Cartesian mesh* is introduced. The main idea is to create a regular, coarse, ortho-Cartesian mesh (*Uniform Spatial Division* [139]) on which the radiation heat transfer is solved and which communicates with the underlying convective mesh. The ortho-Cartesian mesh cells are therefore cuboids with all walls parallel to the planes of global coordinate system. The mesh can be considered as uniform, since the height, width and depth of the cells are constant throughout the whole mesh. The communication between both meshes is assured by the fact that every ortho-Cartesian cell contains a list of CFD cells. A given CFD cell belongs to ortho-Cartesian cell if its center is inside the ortho-Cartesian cell. Depending on the type and the number of CFD cells on the list the ortho-Cartesian cells are classified as follows (cf. Fig. 4.3):

- *active* - when the list is not empty,

- *boundary* - when at least one CFD cell from the list is a boundary cell,
- *inactive* - when the list is empty.

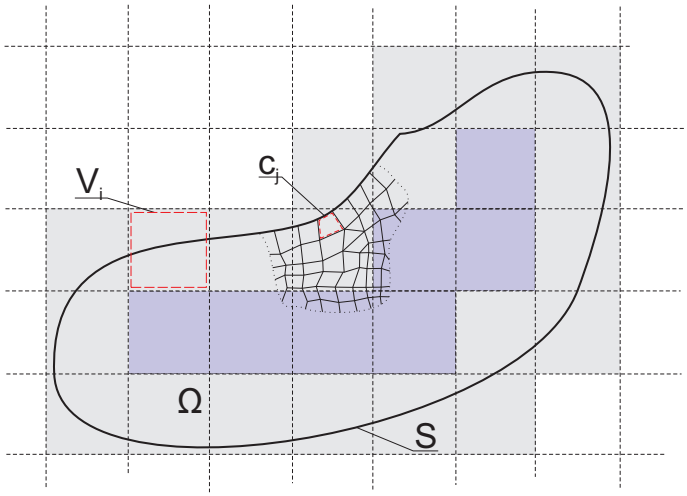

Figure 4.3: Ortho-Cartesian mesh cells (V_i) created on the basis of convective mesh cells (c_j). Dark colour - active inner cells, bright colour - active boundary cells (containing boundary S of domain Ω), white colour - inactive cells.

The classification of the ortho-Cartesian mesh cells is important, since the ray tracing is to be done only for active cells. Boundary cells are special kind of cells, as they contain the surfaces that bound the enclosure. In the thesis the parametric non-uniform rational basis spline (NURBS) surfaces were chosen for the description of boundaries. The details concerning the topic of boundary description are presented in section 4.4. As a consequence of the introduction of the coarse mesh, the number of elements (both surface and volume), for which the ray tracing needs to be performed, significantly reduces. During the ray tracing, one active cell corresponds to one volume element. On the other hand, one surface element placed in one boundary cell can be composed of a set of NURBS surfaces (at least one).

The results of the numerical simulation are strongly influenced by the resolution of the mesh. In the case of radiative analysis, the mesh should be refined in the zones, where the strong gradients of emissive power of the medium and enclosure surfaces are expected. The gradients of emissive power are caused by the spatial variation of the radiative properties and temperautre of the medium and surface. Therefore, it is of great importance to deliver the functionality of the mesh resolution control to the user. In the case of ortho-Cartesian mesh employed in the thesis, the resolution control is realized by means of:

1. global mesh resolution,

2. local refinement regions,

together forming a *mesh hierarchy* (Fig. 4.4).

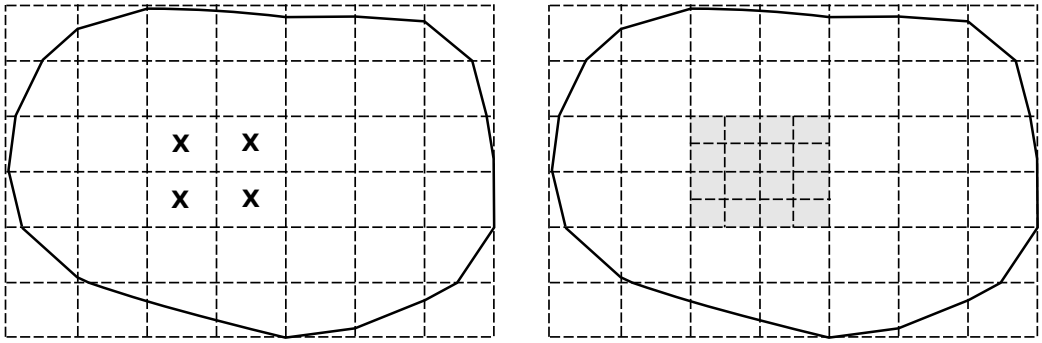

Figure 4.4: Ortho-Cartesian mesh before and after refinement: (a) four cells from 0-th level marked to be refined (**X**), (b) mesh after refinement with some 1-st level cells (gray).

The 0-th level of the mesh hierarchy is composed of the cells, formed by the division of the domain using X, Y, Z global resolution. In the next step, some cells from 0-th level can be marked to be refined by defining refinement regions. As a consequence, the marked cells are further divided into eight (in 3D) smaller uniform cells, which are placed in 1-st level of the mesh hierarchy. In theory, it is possible to extend the mesh hierarchy beyond 1-st level. However, in the thesis the depth of mesh hierarchy was limited to two levels: 0-th and 1-st.

Mesh refinement using the hierarchy is very efficient in terms of overall mesh size. The refinement is local and does not influence the resolution of the mesh outside the area of interest, as it is the case in non-hierarchical mesh (Fig. 4.5). It should be noticed, that mesh refinement can be also realized by varying cell size.

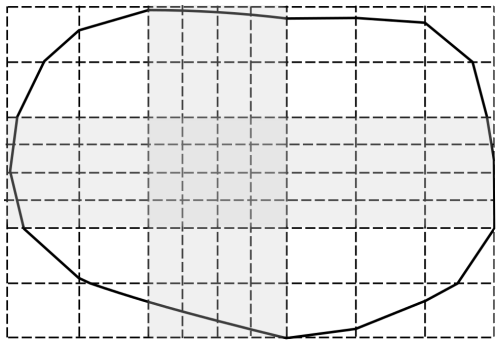

Figure 4.5: Ortho-Cartesian mesh refined without using mesh hierarchy.

4.4 Description of boundaries on ortho-Cartesian mesh

The computational domain consists of its bounding surfaces and the medium filling-up the interior. In the case of radiative analysis, the surfaces bound the entire domain and together form an enclosure. Thus, the enclosure bounding surfaces can represent real walls, inlets or outlets. The domain can be properly described by means of bounding surfaces only, provided the convention of their normal vector direction with respect to the interior is established. In the current work, it was assumed that the surface normal vectors point *outwards* the valid domain (Fig. 4.6).

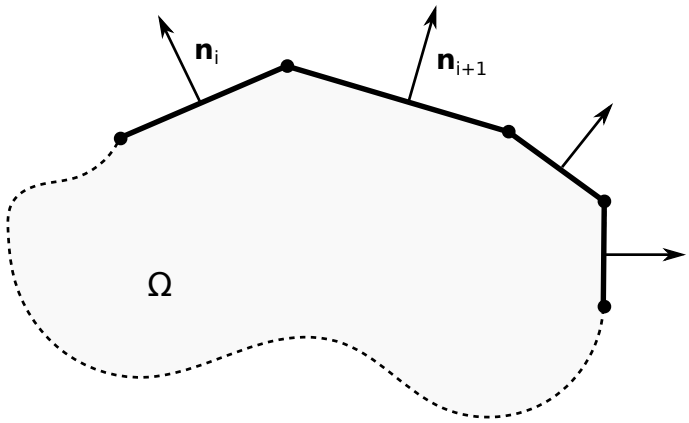

Figure 4.6: Surface normal vectors **n** at boundaries pointing outwards the domain Ω.

It has been already emphasized in section 1.2.4, that the mathematical description of 3D geometry can be a challenging task, especially for geometries of complicated shapes. The simplest way to describe the 3D surface is to express it as a finite set of triangular or quadrilateral surfaces [138]. By doing so, the user has to accept the shortcomings of this approach in the form of relatively large memory demand and limited accuracy for not planar surfaces. The usage of polynomials is a more elaborated way of 3D geometry description. Polynomials are smooth and have a compact form, however they are unstable to floating point operations, since their coefficients can attain very large or small values [31, 95, 96]. In computer graphics it is also important to have a possibility to locally modify the geometry, which is difficult to achieve using polynomials. The stated above shortcomings can be avoided by using a special form of the mathematical description of boundaries, namely the parametric non-uniform rational b-spline (NURBS) surfaces.

In the thesis, NURBS surfaces were chosen to define the boundaries of the enclosure because of a few reasons. NURBS surfaces can describe shapes of high complexity, use little of computer memory, are stable to floating point operations and are widely used in CAD programs and computer graphics (Fig. 4.7) [31, 95, 96]. Moreover, there exist efficient algorithms for finding ray-NURBS surface intersection, most of which were developed for the purposes of surfaces visualization and rendering in computer graphics. More information about those algorithms is presented in sections 1.2.4 and 4.4.2. A brief theoretical background of NURBS curves and surfaces is presented in appendix C. A thorough discussion of the subject can be found in monographs [31, 96].

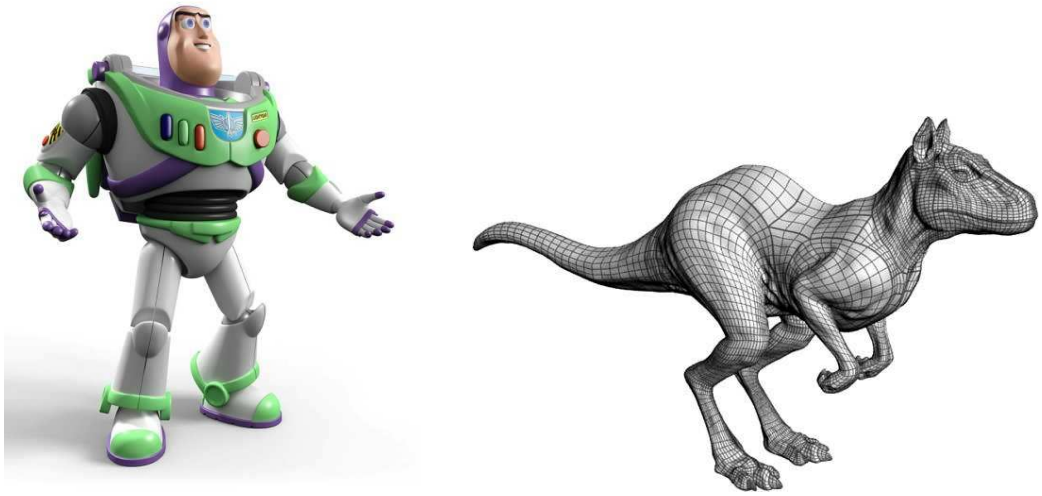

(a) source: *www.pixar.com* (b) source: *www.ruiztaravillo.wordpress.com*

Figure 4.7: Examples of NURBS surfaces used in computer graphics.

4.4.1 Generation of NURBS surfaces

Since NURBS surfaces describe the boundaries, it is natural, that they are inside boundary cells of ortho-Cartesian mesh (cf. section 4.3). Those cells are special ones, because each of them contains surface elements that describe the enclosure geometry. It is assumed that each boundary cell contains exactly one surface element, which in turn consists of many NURBS surfaces (at least one). Therefore, the enclosure boundary is approximated by a set of NURBS surfaces.

At first NURBS surfaces of order 3 are created using method of squared distance minimization and boundary points extracted from CFD cells belonging to ortho-Cartesian boundary cells. After the surface *flattening* procedure (see sect. 4.4.2.1) some of the surfaces are divided and therefore one surface element

can consist of more than one surface. NURBS surfaces of order 3 are flexible enough to express most of complex shapes adequately and the surface evaluation time is acceptable. This is confirmed by the fact that the surfaces of 3-rd order are widely used in computer graphics and CAD programs [31, 96]. The algorithms for NURBS surface creation from unorganized cloud of points and for surface evaluation were taken from *Point Cloud Library* [93]. The boundary CFD cells for boundary points extraction are selected using ortho-Cartesian cells overlapping (Fig. 4.8). The cells overlapping is defined by parameter OF according to equation

$$OF = \frac{(dx' - dx)}{2dx} = \frac{(dy' - dy)}{2dy} = \frac{(dz' - dz)}{2dz}, \tag{4.42}$$

where dx, dy and dx', dy' are ortho-Cartesian cell dimensions before and after introduction of cells overlapping. The value of OF parameter is defined by the user and usually is set to $0.15 - 0.25$.

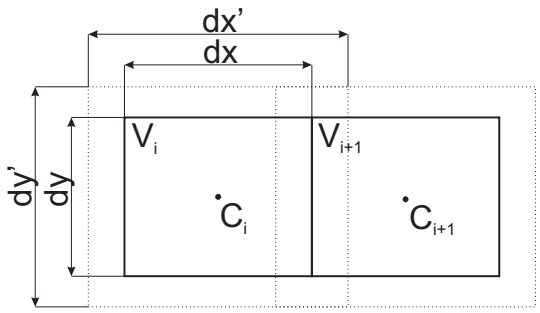

Figure 4.8: Overlapping of ortho-Cartesian cells (V) in order to extract boundary points for NURBS surface creation. dx, dy and dx', dy' - cell dimensions before and after introduction of cell overlapping, C - cell center.

The idea of ortho-Cartesian boundary cells overlapping was introduced in order to assure the boundaries are water-tight and to avoid creation of NURBS surfaces from too few points. In the neighbouring cells the generation of NURBS surfaces runs independently, thus the transitions between the surfaces from cell-to-cell can be far from smooth and frequently may contain gaps. As a consequence, during the ray-tracing some of the rays can escape the enclosure, causing non-physical behaviour.

Fig. 4.9 depicts the steps involved in the procedure of NURBS surface generation. In each ortho-Cartesian boundary cell, a list of boundary convective mesh cells is created. A convective cell c belongs to a given ortho-Cartesian cell V when its center $\mathbf{P}^c$ is inside this cell, accounting for cells overlapping. Then, the boundary points $\mathbf{P}^b$ are extracted from the boundary convective

cells. Finally, the NURBS surface **S** is generated on the basis of boundary points using squared distance minimization. An example of surface fitting to a set of points is presented in Fig. 4.10.

⋆ ⋆ ⋆

A word of comment is appropriate here. During the preliminary stage of the program development a different approach for a generation of NURBS surfaces was considered. The 3D geometry was generated using a standard program (Gambit, Ansys Design Modeller) and saved in standard IGES format. Then, NURBS surfaces were extracted from the IGES file directly. However, instead of uniform surface description using NURBS, the IGES file contains the geometry described by many forms of surfaces like planes, surfaces of revolution and others. Translating all the possible types of surfaces into NURBS was prohibitively labourious task. Moreover, NURBS surfaces from IGES have a general form of trimmed parametric surfaces (C.3). The need for surface trimming adds one more level of complexity to the boundaries description. Due to the encountered problems, the idea to read NURBS surfaces directly from geometry file was abandoned. Despite all the issues stated above, the idea is worth exploring, because it can greatly reduce the time of ortho-Cartesian mesh preparation stage and reduce the number of NURBS surfaces used.

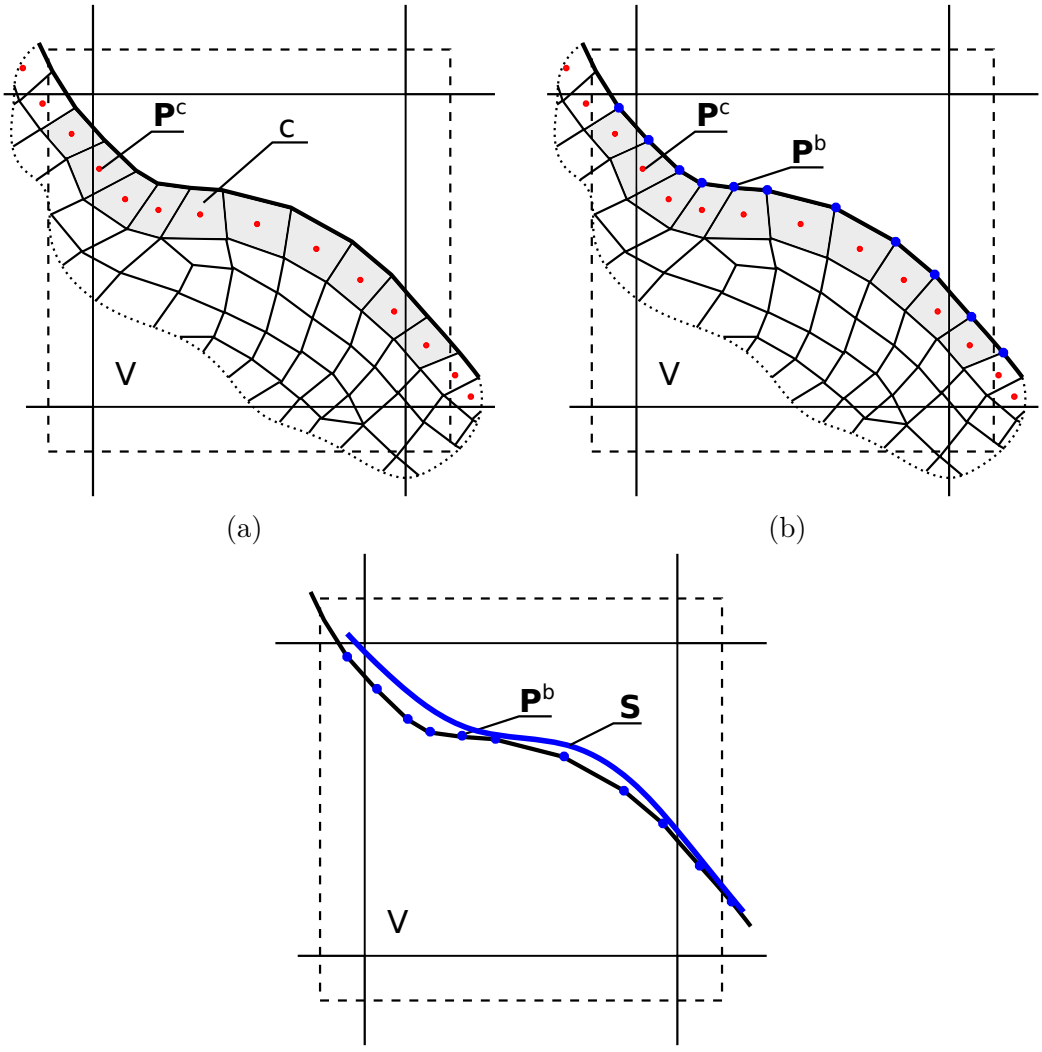

Figure 4.9: Steps of NURBS surface $\mathbf{S}$ generation out of boundary boundary points belonging to ortho-Cartesian cell. c, V denote convective and ortho-Cartesian mesh cells, $\mathbf{P}^c$ are convective cell centres, $\mathbf{P}^b$ are boundary points. Convective cells c marked gray are boundary cells selected to belong to a given ortho-Cartesian cell V using cell overlapping.

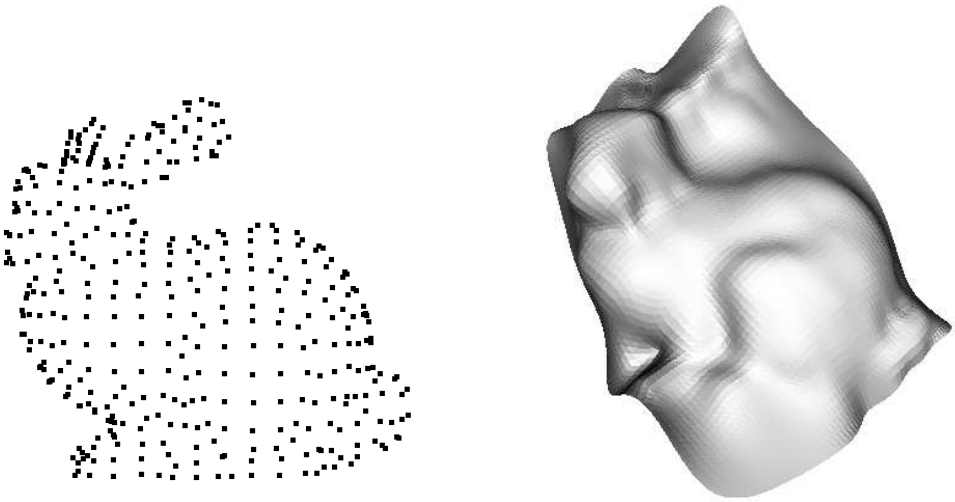

(a) set of points (b) NURBS surface

Figure 4.10: Stanford bunny - an example of NURBS surface created on the basis of a set of points [93].

4.4.2 Intersection of rays and NURBS surfaces

In the preceding section 4.4.1, the generation of a single NURBS surface was introduced. The discussion about the available methods for ray-tracing NURBS surfaces was presented in section 1.2.4. In the thesis, Newton's method for ray-NURBS surface has been choosen.

Starting from the emission point, the ray is followed cell-by-cell. The procedure for finding the ray-surface intersection point is triggered when the ray hits the boundary cell of ortho-Cartesian mesh. The procedure comprises of two main steps: iterative Newton's method and bounding volume hierarchy for proper initialization. Newton's method has been proposed by [61], later developed by [76] and is described in details in appendix D. It has a quadratic convergence rate provided it was given an initial guess $\mathbf{u_0} = \{u_0, v_0\}$ that is close enough to the solution. The proper initial guess for Newton's method is assured by the procedure of ray traversing the hierarchy of bounding boxes. The method requires computation of the directional derivatives of the surface at a given point, therefore the surface has to be differentiable in the considered domain.

4.4.2.1 Bounding Volume Hierarchy

Newton's method for finding ray-surface intersection point is computationally expensive since it requires multiple evaluation of the surface point and surface derivatives. Therefore it is important to avoid ray-surface intersection test whenever possible. Additionally, Newton's method needs a good initial guess $\mathbf{u_0} = \{u_0, v_0\}$, which should be closer to the real solution for considerably curved surfaces.

Stated above requirements are met using *bounding volume hierarchy* (BVH) described by Martin in [76]. Generally, the hierarchy consists of root, internal and leaf nodes. The root node is the highest level node containing the other ones, internal nodes are in the middle of each branch of the hierarchy. Leaf nodes are placed only at the lowest level of each hierarchy branch and are assigned an initial point for Newton's iteration (Fig. 4.11). Bounding volumes are more associated with the objects they are actually bounding and have a tendency to bound them tightly, contrary to the volumes created by other techniques like octrees, BSP-trees, KD-trees in which the space is divided using top-down approach. For bounding volumes axis-aligned bounding boxes were chosen i.e., the walls of the boxes are parallel to the planes of global coordinate

system. Such definition produces a very efficient ray-box intersection algorithm introduced by Kay [63] and mentioned later by Smits [109]. Axis-aligned boxes can also nicely bound flat parts of the surface which is often the case, as shown later in chapter 5.

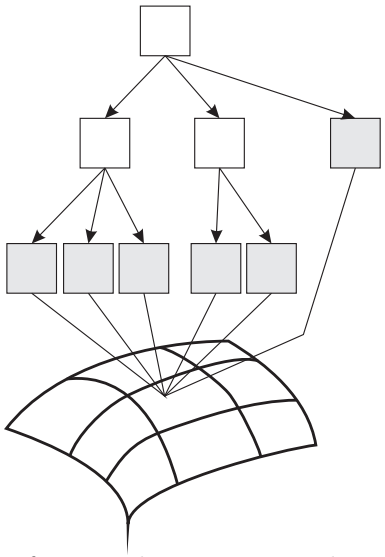

Figure 4.11: An example of BVH that is assigned to a single NURBS surface. Leaf nodes (grey) contain an initial point for Newton's iteration.

In order to construct the BVH, the leaf nodes are created using Abert's method [1, 2] and then placed into the hierarchy using Goldsmith-Salmon algorithm [43]. During the placement of leaf nodes into the hierarchy, the other nodes (root and internal) are created. In Abert's method, the leaf nodes are created using the concept of surface flatness criterion p. It can be considered as a parameter measuring how flat is the surface under the consideration. It is defined as

$$p = \prod_{i=1}^{7} \mathbf{n}_i \cdot \mathbf{n}_{i+1}, \tag{4.43}$$

where $\mathbf{n}_i$ are surface normal vectors evaluated at eight points shown in Fig. 4.12.

A surface is considered to be perfectly flat if $p = 1$. For $p > f$ a leaf bounding box is created by taking x, y, z coordinates of four points corresponding to four limiting vertices of the parametric domain. The initial point for Newton's iteration is the arithmetic mean of the limiting values of the parametric domain. If $p \leqslant f$ the surface is divided in half of its parametric domain. The process is recursively repeated till all subsurfaces fulfil the flatness criterion. Parameter $f \in [0, 1]$ is set empirically and usually equals to $0.8 - 0.9$. In the case $p < 0$, the surface is also subdivided in half of its parametric domain.

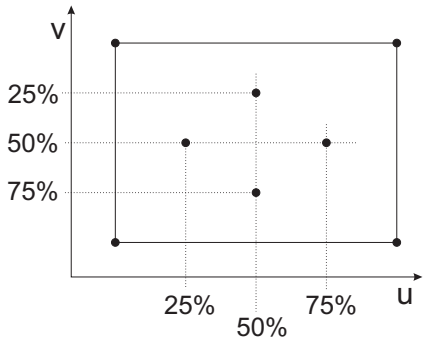

Figure 4.12: Eight surface sampling points (black dots) used for the evaluation of surface flatness criterion p.

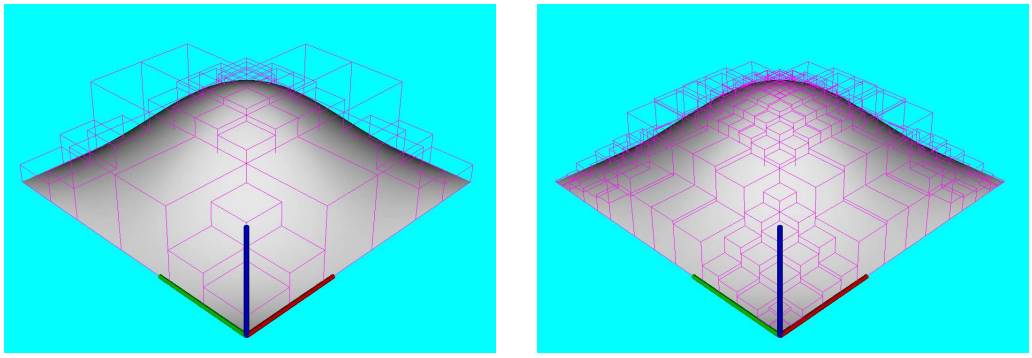

(a) $f = 0.8$ (b) $f = 0.95$

Figure 4.13: Leaf bounding boxes for NURBS surface, created based on different surface flatness criterion f.

Different approach was presented by Martin [76]. In his work, the curvature-based refinement was used to divide the surface into *almost flat* Bézier patches and convex hull property was employed to create bounding boxes. As well as Abert, Martin used heuristics to estimate the curvature of the surface but in his case the division of one segment causes analogical divisions in neighbouring segments. Thus the method can lead to unnecessary divisions of the base surface. Heuristics developed by Abert is more versatile, because it takes into account surface curvature in both directions (u and v) simultaneously and does not require so many divisions as Martin's approach. Moreover, using convex hull property in the case of NURBS surfaces to create bounding boxes leads to inefficiencies, as was shown by Abert [1]. Taking into account the above reasons, Abert's method was used. Examples of leaf bounding boxes created for two values of f parameter are shown in Fig. 4.13.

By taking f parameter closer to 1 the parts of surfaces inside bounding boxes are *more flat*. As a consequence higher number of bounding boxes is created leading to bigger hierarchy tree, higher memory consumption and slower ray traversal through the hierarchy. On the other hand, Newton's iteration is

likely to converge faster. By providing an initial point from BVH created with the $f = 0.8 - 0.9$, the method usually converges after 3-4 iterations.

After computing all the leaf bounding boxes the BVH is created using Goldsmith-Salmon algorithm [43]. The measure of quality for the hierarchy is the average time needed for a ray to traverse the hierarchy. The principle of the algorithm is to put the leaf nodes into the hierarchy tree one-by-one and to search the tree for optimum insertion place which is determined by the minimization of tree cost function. The algorithm allows to create *almost optimal* hierarchy tree with the computational cost of order $n \log(n)$, where n denotes the number of leaf nodes. An example of BVH is shown in Fig. 4.11.

In order to efficiently store and traverse the BVH a depth-first order array of bounding box objects with skip-pointer mechanism was used (Fig. 4.14). If the ray-box intersection test was successful, the next box to test is the subsequent element of the array. Otherwise, the box to test is determined by a skip-pointer mechanism which tells how many elements in front of the current element of the array should be omitted. The advantages of such representation of the hierarchy are efficient use of the computer memory (no empty elements), limited to the minimum the amount of information stored in one element and no need for using recursive function calls during the hierarchy traversal [109].

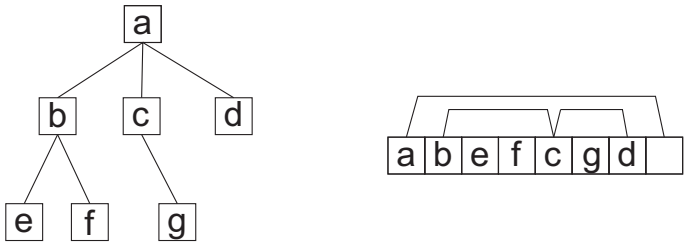

Figure 4.14: BVH representations. Left: using pointers to child nodes, right: depth-first order array with skip-pointer mechanism.

It is important to note, that if the value of surface flatness criterion parameter f is set low, it is more probable for Newton's method to converge to improper point or even diverge. In this case the ray can travel to inactive ortho-Cartesian cell and escape from the enclosure producing non physical result. It does not terminate the code execution, simply the traced ray is neglected. It should be kept in mind that the value of f parameter is a compromise between the speed the ray traverses through BVH and the number of rays that can escape from the enclosure.

4.4.3 Bundle emission point at NURBS surface

An important step in MCRT method is determination of bundle emission point. In the case of emitting and absorbing media, the bundle can originate from both surface and volume elements. Current section presents only the procedure of finding the bundle emission point from the surface element or, more precisely, NURBS surfaces. The emission from volume elements is addressed in section 4.5.

The emission points should have uniform distribution across the surface, because the amount of energy emitted from the surface of constant temperature is proportional to its area. Algorithm that is capable of drawing random points on any parametric surface with uniform distribution was described by Kopytov in his works [65, 66].

A parametric surface $\mathbf{S}(u, v)$ is defined in parametric domain $\Omega_p : \{u_1 \leqslant u \leqslant u_2; v_1 \leqslant v \leqslant v_2\}$. The joint probability distribution function of parameters u and v - $f(u, v)$ is to be determined. This function corresponds to the uniform point distribution in 3d-space. In the case of uniform distribution of points on the surface, the probability of point A being on the small fragment of surface $\Delta\mathbf{S}$ equals to

$$P\left(A \in \Delta\mathbf{S}\right) = \frac{\Delta\mathbf{S}}{\mathbf{S}}, \tag{4.44}$$

where

$$\Delta\mathbf{S} = \sqrt{EG - F^2}\,\Delta u \Delta v, \tag{4.45}$$

$$\mathbf{S} = \iint\limits_{\Omega_p} \sqrt{EG - F^2}\,du dv. \tag{4.46}$$

E, F, G are coefficients of First Fundamental Form of the surface $\mathbf{S}$:

$$E = \mathbf{S}_u \cdot \mathbf{S}_u, \tag{4.47}$$

$$F = \mathbf{S}_u \cdot \mathbf{S}_v, \tag{4.48}$$

$$G = \mathbf{S}_v \cdot \mathbf{S}_v. \tag{4.49}$$

Inserting equations (4.45) and (4.46) into (4.43) leads to

$$P\left(A \in \Delta\mathbf{S}\right) = \frac{\sqrt{EG - F^2}\,\Delta u \Delta v}{\iint\limits_{\Omega_p} \sqrt{EG - F^2}\,du dv}. \tag{4.50}$$

On the other hand, probability of point A being on the surface fragment $\Delta\mathbf{S}$ equals to

$$P\left(A \in \Delta\mathbf{S}\right) = f(u,v)\,\Delta u \Delta v. \tag{4.51}$$

Comparing the equations (4.50) and (4.51) the expression for unknown joint probability distribution function is found

$$f(u,v) = \frac{\sqrt{EG - F^2}}{\iint\limits_{\Omega_p} \sqrt{EG - F^2}\,dudv}. \tag{4.52}$$

The function $f(u,v)$ is proportional to $\sqrt{EG - F^2}$.

The dependencies derived above are used in the algorithm for drawing random points on parametric surface with uniform distribution in 3d-space:

1. Determine the maximum of the function $f_{\max} = \max\sqrt{EG - F^2}$ in domain Ω_p.

2. Generate two random numbers R_u and R_v from $[0,1)$ interval and scale them to the size of the domain Ω_p by computing parameters u_0, v_0

$$u_0 = (u_2 - u_1)\cdot R_u + u_1, \quad v_0 = (v_2 - v_1)\cdot R_v + v_1, \tag{4.53}$$

   where u_1, u_2, v_1, v_2 are local parameters bounding valid surface domain Ω_p.

3. Check the condition

$$f_{\max} R < f(u_0, v_0), \tag{4.54}$$

   where R - random number from $[0,1)$ interval. If the condition is fulfilled the point $\mathbf{S}(u_0, v_0)$ is accepted, otherwise it is rejected.

4. Repeat steps 2, 3 till required number of points on the surface $\mathbf{S}$ is achieved.

An example of 10k random point locations on NURBS surface sampled with uniform distribution is shown in Fig. 4.15.

The algorithm described above is applicable to one surface only, thus it needs upgrading to account for many surfaces, as it is the case for some of the boundary cells of ortho-Cartesian mesh. If a boundary cell contains more than one NURBS surface, the surface is chosen randomly with probability proportional to its area. Kopytov's algorithm is used to draw a single emission point from this surface and then the point is tested if it lies inside the boundaries

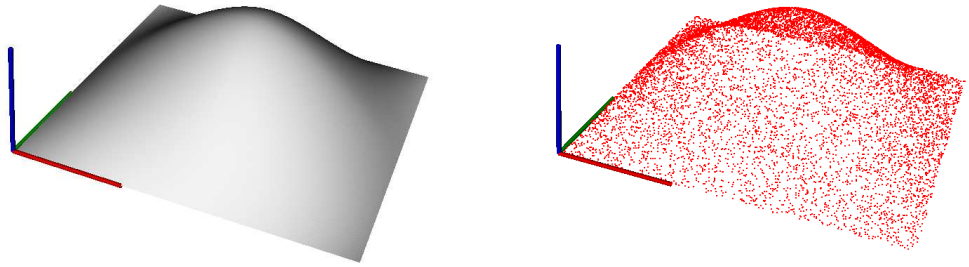

(a) (b)

Figure 4.15: 10k random points lying on NURBS surface sampled with uniform distribution.

of ortho-Cartesian cell. If it does, it is accepted as an emission point for new energy bundle, otherwise the procedure is repeated.

4.5 Ray tracing procedure

The aim of this section is to present the ray tracing algorithm, which is the crucial part of MCRT method and during of which the values of radiation distribution factors D_{ij} are determined.

Up to this moment, among the issues covered by the current chapter were the ortho-Cartesian mesh and the description of boundaries in the form of NURBS surfaces. These are the elements of the system, needed for practical tracing the rays. Since the radiation problem is solved on the coarse ortho-Cartesian mesh, this mesh has to be created before. After the radiation model is invoked by the CFD program, the check is performed whether the model runs for the first time (Fig. 4.16). If it does, then the preprocessing stage begins, which is done once for the whole simulation. The preprocessing stage involves initialization of RDF matrix $\mathbf{D}$ and generation and initialization of ortho-Cartesian mesh. As soon as the preprocessing stage is finished, the $\mathbf{D}$ matrix is to be read from file. If the file is not present, then the loop over surface and volume elements is executed. For each element the ray tracing procedure starts in order to compute new values of $\mathbf{D}$ matrix entries. After the values of RDFs are known, radiative heat fluxes q^r and heat sources or sinks q_v^r are evaluated and interpolated onto the underlying convective mesh. The data exchange between meshes is the topic of section 4.6.

In the case the radiation model runs for the next time, the radiative properties of the medium and surfaces are updated. If the absorption coefficient of

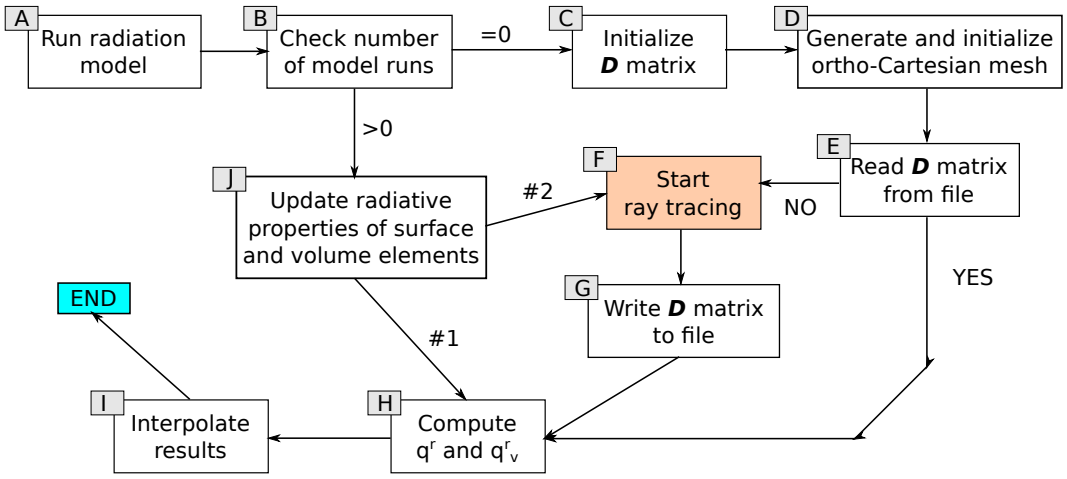

Figure 4.16: Stages of MCRT model.

the medium is constant with the changes of temperature and/or gas composition and so is the emissivity of surfaces, then there is no need to recompute the **D** matrix. This situation corresponds to path #1 shown in Fig. 4.16. Otherwise, the ray tracing procedure is to be repeated, following path #2. It should be emphasized here, that the assumption of invariant radiative properties of the medium and surfaces with respect to temperature can greatly shorten the simulation time, by avoiding computationally expensive ray tracing procedure.

The ortho-Cartesian mesh initialization stage has the following steps:

- establish mesh resolution and refinement regions,
- assign cells from convective mesh to the ortho-Cartesian cells,
- classify cells to be: active, inactive, boundary,
- in each boundary cell select boundary points and use them to span NURBS surface,
- orient NURBS surfaces, so that their normal vectors point outwards the domain,
- create BVH for each NURBS surface,
- initialize radiative properties of medium and boundaries.

⋆ ⋆ ⋆

Once the preprocessing stage is accomplished, the ray tracing procedure is invoked. For each surface and volume element, a fixed number of rays is released

and followed until absorption. In the following, the ray tracing procedure employed in the thesis is described in details, beginning with the flowchart (Fig. 4.17).

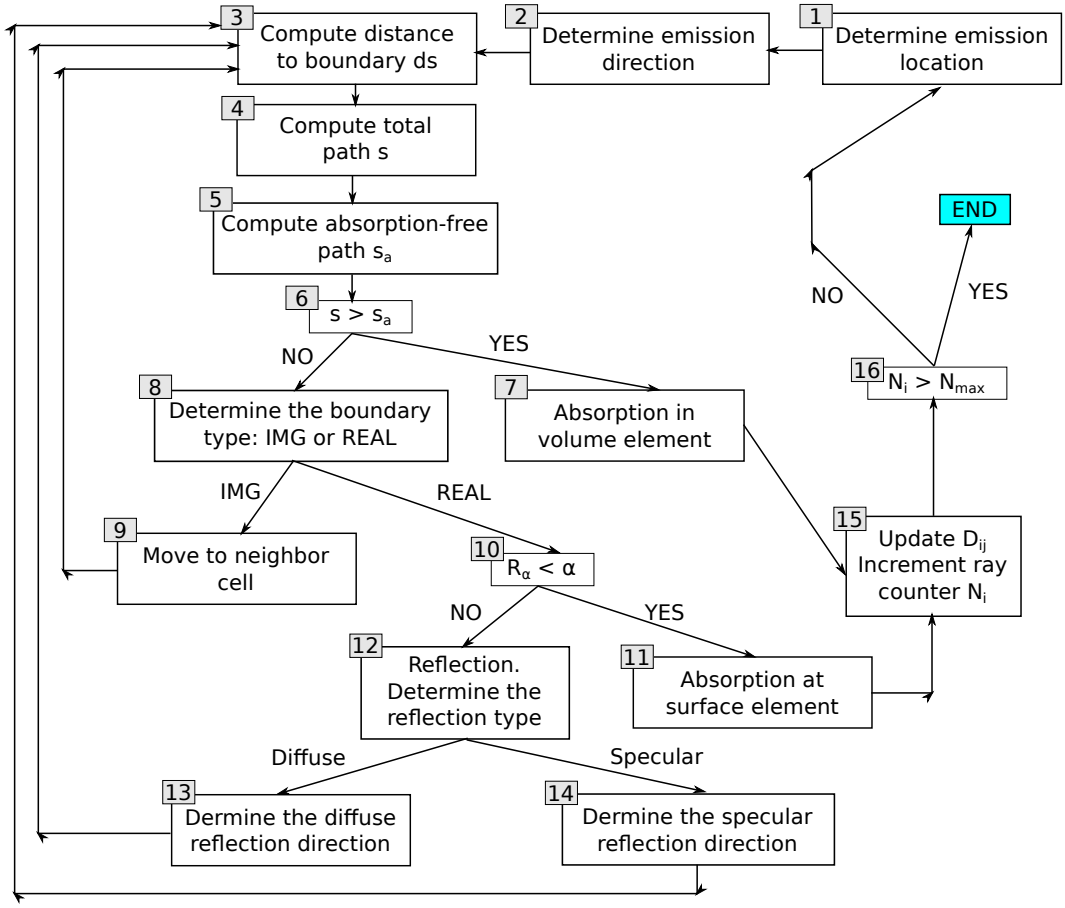

Figure 4.17: The logic flowchart of the ray tracing procedure used in MCRT method in participating medium.

The steps numbering corresponds to the one introduced in Fig. 4.17.

Step #1

The procedure of determining the ray emission point depends on the type of element of ortho-Cartesian mesh:

Surface - the emission point is found using procedure described in section 4.4.3.

Inner Volume - the emission point is found by drawing three random numbers R_x, R_y, R_z from $[0, 1)$ interval, forming vector $\mathbf{R}_x = \{R_x, R_y, R_z\}$ and inserting it into

$$\mathbf{r}_0 = \mathbf{C} + (\mathbf{R}_x - 0.5)\mathbf{dx}, \tag{4.55}$$

where $\mathbf{C}$ is ortho-Cartesian cell center vector, $\mathbf{dx}$ = dx, dy, dz denote cell dimensions vector.

Boundary Volume - the candidate for an emission point ($\mathbf{r}_0^c$) is found from equation (4.55). Then, the condition whether the candidate point lies within the valid domain is checked. If it does, it is accepted, if not another candidate point is drawn. The checking procedure makes use of boundary faces obtained from boundary convective cells belonging to a given ortho-Cartesian cell (Fig. 4.18). Those faces have normal vectors $\mathbf{n}_f$ pointing outwards the domain. In a loop over N boundary faces, the vector $\mathbf{v} = \mathbf{r}_0^c - \mathbf{C}_f$ is created and its direction is compared with the face normal vector $\mathbf{n}_f$. If only for one face the direction of both vectors $\mathbf{v}$ and $\mathbf{n}_f$ is the same, the candidate point is rejected, otherwise it is accepted.

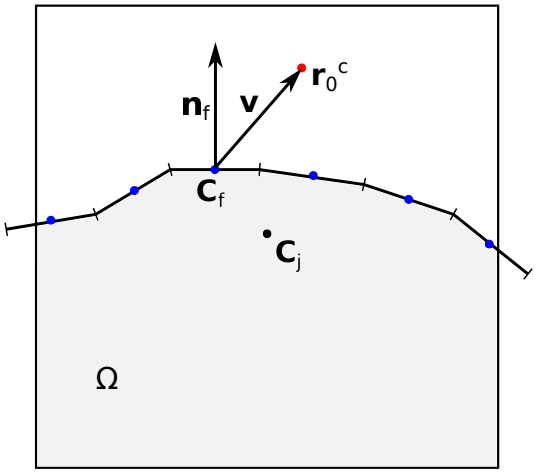

Figure 4.18: A candidate emission point $\mathbf{r}_0^c$ from volume cell being tested whether it lies within valid domain Ω. The test involves checking the direction of vector $\mathbf{v} = \mathbf{r}_0^c - \mathbf{C}_f$ with respect to each face normal vector $\mathbf{n}_f$. $\mathbf{C}_f$ denotes boundary face center, $\mathbf{C}_j$ is center of ortho-Cartesian cell.

Step #2

The procedure of determining the emission direction depends on the type of element of ortho-Cartesian mesh [74]:

Surface - for diffuse surfaces, the emission direction $\mathbf{d}$ is defined by polar and azimuthal angles $\phi \in [0, 2\pi)$ and $\theta \in [0, \frac{1}{2}\pi)$ (Fig. 4.20 *a)*):

$$\phi = 2\pi R_\phi, \tag{4.56}$$

$$\theta = \arcsin(\sqrt{R_\theta}), \tag{4.57}$$

where R_ϕ and R_θ are random numbers from $[0, 1)$ interval. Angles ϕ and θ form a hemisphere above the surface emission point in the opposite direction of surface normal vector $\mathbf{n}$. In order to transform the ray direction into global coordinate system, the following equation is used

$$\mathbf{d} = -\mathbf{n}\cos(\theta) + \mathbf{t}_1 \sin(\theta)\cos(\phi) + \mathbf{t}_2 \sin(\theta)\cos(\phi), \tag{4.58}$$

where $\mathbf{t}_1$, $\mathbf{t}_2$ are unit tangent vectors of the surface at emission point.

Volume - the emission direction $\mathbf{d}$ is defined by polar and azimuthal angles $\phi \in [0, 2\pi)$ and $\theta \in [0, \pi)$

$$\phi = 2\pi R_\phi, \tag{4.59}$$

$$\theta = \arccos(2R_\theta - 1), \tag{4.60}$$

The transformation to global coordinate system gives:

$$\mathbf{d} = \mathbf{n}_x \cos(\theta) + \mathbf{n}_y \sin(\theta)\cos(\phi) + \mathbf{n}_z \sin(\theta)\cos(\phi), \tag{4.61}$$

where $\mathbf{n}_x$, $\mathbf{n}_y$, $\mathbf{n}_z$ are unit vectors parallel to the axes of global coordinate system.

Steps #3, #4, #5, #6

Within current ortho-Cartesian cell, denoted by index k, a distance to the nearest boundary ds_k is computed (Fig. 4.19). The boundary is understood to be a plane bounding the cell (imaginary surface) or surface being a portion of the enclosure (real surface). Then, the values of total s and absorption-free s_a paths are evaluated using the recursive relations:

$$s_k = \begin{cases} 0, & k = 0, \\ s_{k-1} + ds_k, & k > 0, \end{cases} \tag{4.62}$$

$$s_{a,k} = \begin{cases} s^*_{a,k}, & k = 0, \\ \frac{s_{k-1} s_{a,k-1} + ds_k s^*_{a,k}}{s_{k-1} + ds_k}, & k > 0, \end{cases} \tag{4.63}$$

where

$$s^*_{a,k} = -\frac{1}{\kappa_{t,k}} \ln(1 - R_a), \tag{4.64}$$

R_a is a random number from $[0, 1)$ interval, which should be drawn only once per one ray. $s^*_{a,k}$ is absorption-free path computed on the basis of total ab-

sorption coefficient $\kappa_{t,k}$, defined as a sum of gas κ_k and particle equivalent $\kappa_{p,k}$ absorption coefficients:

$$\kappa_{t,k} = \kappa_k + \kappa_{p,k}. \tag{4.65}$$

The particle equivalent absorption coefficient can be determined from equation (4.33).

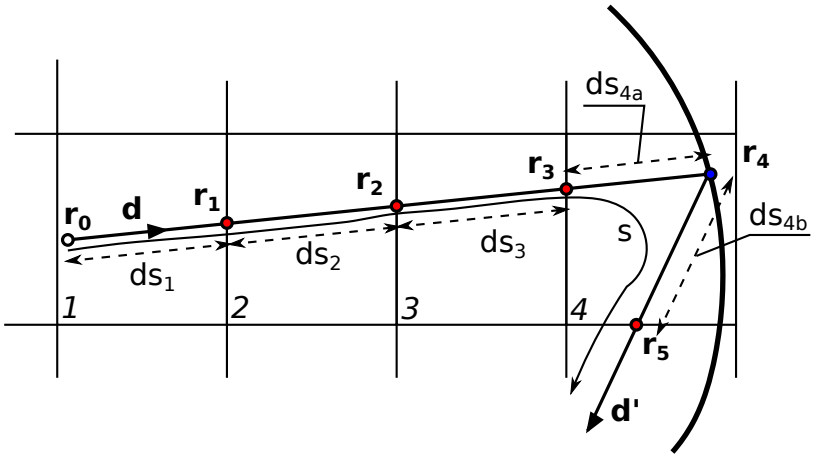

Figure 4.19: Updates of ray total path s using path increments ds during tracing on ortho-Cartesian mesh. Red and blue points are ray-imaginary and ray-real surface intersections respectively.

During the computation of the distance to the boundary ds an information of the type of current ortho-Cartesian cell is used (Fig. 4.3). In the case, the ray is within an active boundary cell, the intersection algorithm has to take into account the fact, that the intersection point can be imaginary - with cell bounding plane, or real one - with enclosure wall. Moreover, the ray can have more than one intersection point with NURBS surface. All possible ray-NURBS surface intersection points are found during BVH traversal in which, provided the ray hits leaf node, the iterative Newton's procedure is launched (sec. 4.4.2). The hierarchy is traversed till its end, because finding one ray-surface intersection point does not guarantee it is correct and unique one. After BVH traversal is completed the list of all possible intersection points, imaginary and real, is created. The task of the interrogation algorithm is to choose the closest point to the ray origin that is within current ortho-Cartesian cell.

Another issue worth mentioning is the minimum distance of the intersection point from the bundle emission or reflection point $L_{\min}$. It was noted that some intersection points were found exactly in the emission/reflection point. It is caused by the fact that after emission or reflection the ray is inside the boundary cell and the procedure of finding intersection point is automatically

triggered. After introducing $L_{\min}$ parameter the ray is forced to travel at least this distance before intersection is reported. The value of the $L_{\min}$ parameter is set by the user and it should be equal to several percent of mean linear dimension of ortho-Cartesian cell.

Setting proper values of NURBS surface flatness criterion f and $L_{\min}$ parameters is crucial for good performance of ray tracer.

Step #7

In the case $s > s_a$ is true, the ray is absorbed in current volume element.

Steps #8, #9

In the case $s > s_a$ is not true, the ray is not absorbed within the volume. Thus, the type of the boundary should be checked in order to determine if the ray hits the real surface being a fragment of an enclosure walls or just crosses the cell boundary plane (cf. Fig. 4.19). If the latter is true, the ray moves to the neighbouring ortho-Cartesian cell.

Steps #10, #11

The ray hits a real surface, being a fragment of an enclosure walls. It is absorbed at the surface element if the following is true

$$R_\alpha < \alpha, \tag{4.66}$$

where R_α is random number from $[0, 1)$ interval, α is wall absorptivity at a surface element. Otherwise, the ray is reflected.

Step #12

The ray is reflected and the program has to determine the type of reflection, which can be either diffuse or specular. The reflective properties of boundary surfaces are described by means of specularity ratio: $r_s = \rho_s/(\rho_s + \rho_d)$. It can be interpreted as a probability the ray is reflected in a specular way. Therefore reflection is specular if

$$R_s < r_s, \tag{4.67}$$

where R_s is a random number from $[0, 1)$ interval. Otherwise, the reflection is diffuse.

Steps #13, #14

The direction of diffuse reflection (Fig. 4.20(a)) is computed in exactly the same manner as for diffuse emission from surface (Step #2). In the case of

specular reflection (Fig. 4.20(b)), new direction is

$$\mathbf{d}' = \mathbf{d} - 2\,(\mathbf{d} \cdot \mathbf{n})\,\mathbf{n}, \tag{4.68}$$

where $\mathbf{d}$ is ray direction before reflection.

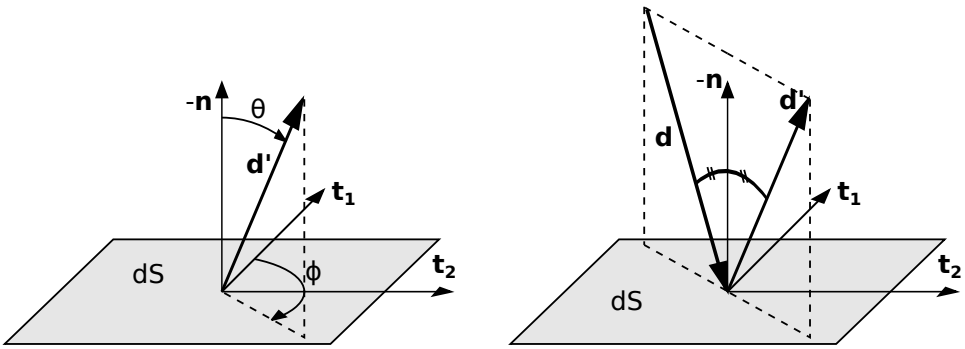

(a) Diffuse reflection (b) Specular reflection

Figure 4.20: Types of ray reflection from differential surface dS. θ, ϕ are polar and azimuthal angles, $\mathbf{n}$, $\mathbf{t}_1$, $\mathbf{t}_2$ are surface normal and tangent vectors, $\mathbf{d}$, $\mathbf{d}'$ are ray direction vectors before and after reflection.

Steps #15, #16

Knowing the indices of elements from which the bundle was emitted (i) and at which was absorbed (j), the corresponding entry of $\mathbf{D}$ matrix is updated and the bundle counter N_i is incremented. If the total number of bundles traced exceeds the maximum defined by the user, i.e. $N_i > N_{\max}$, then the ray tracing for a given element ends and the program goes to next element. The procedure is repeated till all surface and volume elements are visited.

4.6 Data exchange between convective and ortho-Cartesian meshes

The radiative heat transfer problem is solved on coarse ortho-Cartesian mesh, which is build on the basis of the underlying convective mesh. Therefore, the two-way communication between both meshes is necessary in order to provide appropriate data transfer.

The parameters needed for performing radiative analysis and which are transferred from convective onto ortho-Cartesian mesh include:

- surface properties:
  - T - temperature,

  - α - absorptivity,
  - r_s - specularity ratio,
- medium properties:
  - T_m - temperature,
  - κ - absorption coefficient,
  - composition,
- particle properties:
  - κ_p - particles equivalent absorption coefficient,
  - E_p - radiative energy emission due to the presence of particles.

The transfer of parameters is achieved by surface and volume weighted averaging applied to surface and volume parameters respectively. Suppose that N convective cells belong to a given ortho-Cartesian cell, then an average value of volume parameter is

$$\psi_m^{\text{avg}} = \frac{\sum_{i=0}^{N} \psi_{m,i} V_i^{\text{CFD}}}{\sum_{i=0}^{N} V_i^{\text{CFD}}}, \tag{4.69}$$

where V_i^{CFD} is convective cell volume. Analogously, for parameters defined on surface:

$$\psi_w^{\text{avg}} = \frac{\sum_{i=0}^{M} \psi_{w,i} A_i^{\text{CFD}}}{\sum_{i=0}^{M} A_i^{\text{CFD}}}, \tag{4.70}$$

where M is the number of convective boundary faces in a given ortho-Cartesian cell and A_i^{CFD} denotes the face area.

Since the radiative energy emitted by an arbitrary element is proportional to the temperature to the fourth power (for the case of gray media), thus the temperature field is a special kind of filed variables, which should be averaged in a different manner:

$$T_m^{\text{avg}} = \sqrt[4]{\frac{\sum_{i=0}^{N} T_{m,i}^4 V_i^{\text{CFD}}}{\sum_{i=0}^{N} V_i^{\text{CFD}}}}, \tag{4.71}$$

$$T_w^{\text{avg}} = \sqrt[4]{\frac{\sum_{i=0}^{M} T_{w,i}^4 A_i^{\text{CFD}}}{\sum_{i=0}^{M} A_i^{\text{CFD}}}}, \tag{4.72}$$

where T_m, T_w are medium and wall temperatures.

$\star \star \star$

The results of radiative analysis, i.e. heat fluxes on walls q^r and heat sources or sinks in medium q_v^r are obtained on the ortho-Cartesian mesh. Those quantities are assigned to the centres of ortho-Cartesian cells and are to be transferred onto the underlying convective mesh. The linear interpolation scheme was employed in the thesis.

Let ψ denote continuous scalar field, whose values are given at discrete locations corresponding to the centres $\mathbf{C}$ of ortho-Cartesian mesh. Then, the value of the scalar in an arbitrary location $\mathbf{r}$ within the domain and within a cuboid defined by eight nearest cell centres $\mathbf{C}_l$ (Fig. 4.21), is computed as

$$\psi(\mathbf{r}) = \sum_{l=0}^{7} L_l(\mathbf{r})\, \psi(\mathbf{C}_l), \tag{4.73}$$

where $L_l(\mathbf{r})$ is an interpolant defined by

$$L_l(\mathbf{r}) = \prod_{i=0}^{2} S_{l,i}(r_i), \tag{4.74}$$

in which

$$S_{l,i}(r_i) = \begin{cases} 1 - t_i(r_i), & C_{l,i} \leqslant r_i, \\ t_i(r_i), & r_i < C_{l,i} \end{cases} \tag{4.75}$$

for $i = 0, 1, 2$ and

$$t_i(r_i) = \frac{r_i - C_{0,i}}{d\mathbf{x}_i}, \quad i = 0, 1, 2, \tag{4.76}$$

where $d\mathbf{x} = \{dx, dy, dz\}$ are ortho-Cartesian cell dimensions.

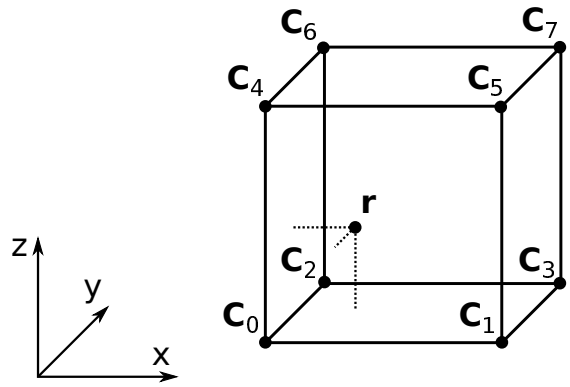

Figure 4.21: The numbering convention for the nearest cell centres $\mathbf{C}$, which define cuboid enclosing a given location $\mathbf{r}$.

4.7 Parallel ray tracing

The section presents the enhancements of the ray tracer code by implementing parallel computing using OpenMP library. The topic of parallel computing in Monte Carlo ray tracing has been also described in some detail in section 1.2.5.

The core of parallel computing is to divide the task at hand into smaller problems and to distribute them among multiple processors [3]. Ideally, this process can result in the reduction of wall-time (speedup) that is proportional to the number of processors used. However, it is a rare case in reality. The speedup is degraded by the time spend on passing the information between processors and by idle processor time, caused by waiting for other processors to finish their tasks. In order to keep the speedup as high as possible, the programmer should design a code in a manner, that guarantees a given processor has an easy access to all the data it needs to complete the task. Also, he should take care of the proper load balancing, i.e. distribute the load equally between processors.

The most populat techniques used for parallel computing are:

- graphics process units (GPUs),
- distributed-memory multiprocessors,
- shared-memory multiprocessors.

Although the usage of GPU proved to be very efficient in parallel ray tracing, this approach was not employed in the thesis. The main reason behind such a decision are hardware limitations. The codes with GPU-enhanced processing are developed using libraries, which are specific for a given GPU vendor (nVidia CUDA C/C++ [89]) and severely limit code portability.

For the case of distributed-memory applications the programming standard of Message Passing Interface (MPI) is employed [85]. In spite of very high potential, the idea of using MPI in the thesis was abandoned due to relatively complex programming and difficulties with data sharing between processors. The implementation of MPI standard in CFD computations is a complicated task, since it involves the domain decomposition and was beyond the scope of the thesis. It should be noted, that the domain decomposition is a good strategy for processes that exhibit local behaviour - fluid flow, thermal conduction, convection, etc. However, thermal radiation is potentially all-to-all phenomenon, in which the interaction between the elements occurs on long distances. Thus, employing the domain decomposition in the form met in CFD applications is

very inefficient, since it will involve exchanging large data pieces during the ray tracing.

In shared-memory applications, OpenMP library is a well suited tool for code parallelism [16]. It allows for multi threading, i.e. the existence of multiple threads within a single process. The threads are executed independently and share the process resources. The method gives reasonable speedup for moderate number of processors. Moreover, implementation of OpenMP library into the serial code is relatively simple. Taking all its benefits into account, it was used in the thesis.

OpenMP allows to use two main ways for load balancing - static and dynamic. Static load balancing distributes the load once, at the beginning of the computation. Thus, in the case the problem is not divided into equal parts, it can generate an uneven load distribution among the processors and lower the performance. In the dynamic load balancing, the work is divided into chunks, which are assigned to the processors dynamically, i.e. as soon as they finish their current task. Since the ray paths can have different lengths, the dynamic load balancing scheme is favourable over the static one [46] and was used within the code.

⋆ ⋆ ⋆

In the case of Monte Carlo method applied to thermal radiation problems, the computational domain is divided into surface and volume elements. In order to compute the values of RDF matrix, a ray tracing (cf. Fig. 4.17) is performed for each of those elements individually. Thus, there is a loop over the elements inside the code and this loop has been parallelized using OpenMP. It should be noted that during the tracing of a single ray, the information about other rays is not needed. Thus, tracing a single ray (or a number of rays) is an independent task, that can be performed by a single processor.

The performance of the parallel code is measured using *speedup*, defined as

$$s_t = \frac{t_1}{t_n}, \tag{4.77}$$

where t_1, t_n are the program execution times on one and n-threads respectively and *efficiency*

$$\eta = \frac{t_1}{n\, t_n}. \tag{4.78}$$

The results of the test, run on the eight-processor shared-memory 2x4 Intel Xeon 2.33 GHz machine, are shown in Fig. 4.22, 4.23. In the test, the computer

time spent only on ray tracing procedure was measured, as this part of the code is parallelized. The time does not include the preprocessing stage. The results are compared with an ideal case corresponding to linear speedup and maximum efficiency equal to 1.0.

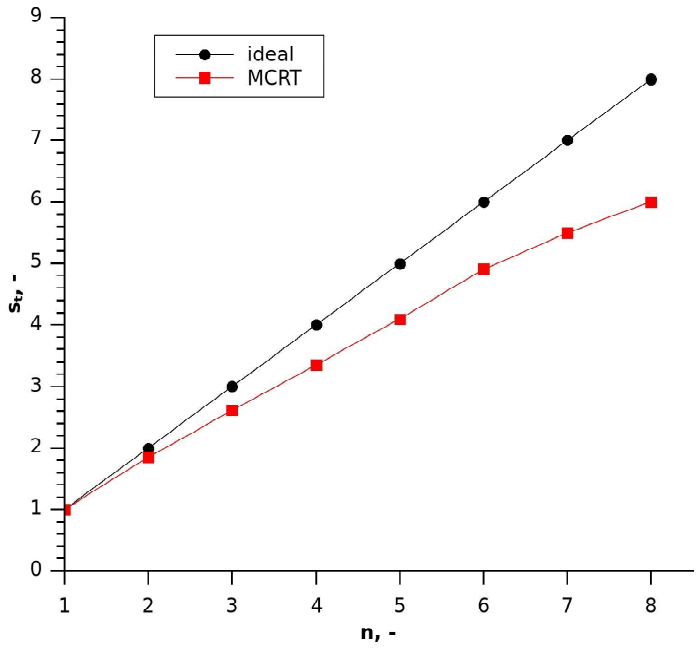

Figure 4.22: Speedup of parallel ray tracing code as a function of number of threads for MCRT and an ideal linear cases.

The results prove that Monte Carlo ray tracing is a good candidate for parallel computations, because the usage of additional processors significantly reduces the run time. However, the efficiency drops with the number of threads involved in the computations to the value of 0.8 for 6 threads. Increasing the number of threads above 6 causes the efficiency to decrease even more to the value of 0.75. The scaling for moderate numbers of threads for Monte Carlo code should be close to an ideal one, i.e. its efficiency should be close to 1.0. Lower efficiencies achieved by the code employed in the thesis are caused by the fact, that the code was not optimized for parallel computing. The code utilizes container classes that are based on iterators instead of indices. Such container classes are not designed to efficiently cooperate with OpenMP library. Therefore, some time is consumed to access the data stored within those containers. Moreover, on the eight-processor machine some computational resources are wasted to maintain the operating system and auxiliary programs. Thus, setting the number of threads close to the number of processors does not result in as efficient speedup as for the lower numbers of threads.

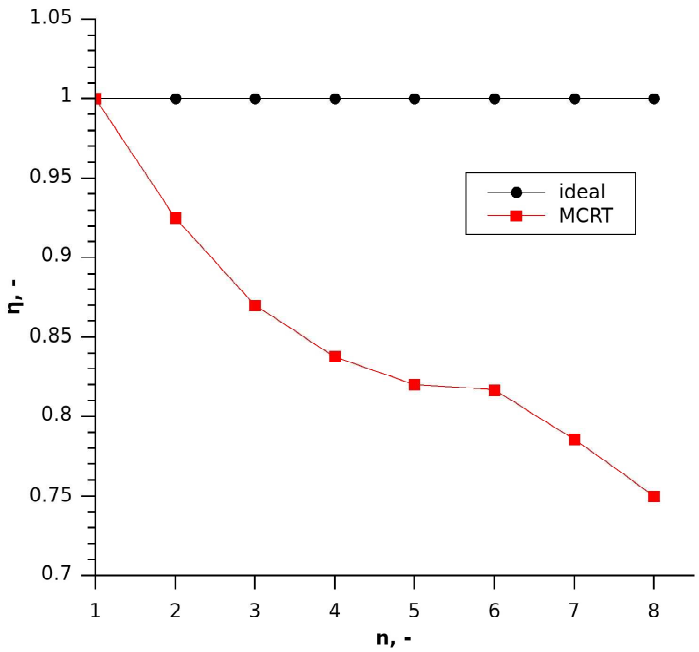

Figure 4.23: Efficiency of parallel ray tracing code as a function of number of threads for MCRT and an ideal linear cases.

OpenMP library has its shortcomings in the form of usage limited to shared memory machines, which excludes massive parallelism. Thus, for future work it is recommended to employ MPI standard. However in this case, the issue of minimizing the data exchange between processors, i.e. avoiding passing of the rays between processors should be solved.

Similar attempts were made by Hunsaker in his Ph.D. thesis [56]. The idea employed in his thesis was called adaptive focus mesh refinement, or data onion. Each processor is handed a fully resolved version of a subset of the domain and a coarsened version of the remainder of the domain. Then the rays are traced by each processor on such simplified domain, thus avoiding passing the rays between processors. The approach produced the results of poor accuracy, the cause of which has not been clarified by the author.

4.8 Ray tracing on ortho-Cartesian vs. standard meshes

The goal of the section is to show the benefits of using ortho-Cartesian mesh for ray tracing. The comparison is done between MCRT model described in the thesis, working on coarse ortho-Cartesian mesh in emitting and absorbing medium, and the most crude implementation of Monte Carlo, in which the rays

are traced from every volume and boundary face of standard dense convective mesh. Since the crude implementation of Monte Carlo is not available, the following considerations are purely theoretical and should be treated as an estimate.

In the following, two cases from chapter 5 are analysed, namely:

1. BTC 1 - Well-stirred combustion chamber,
2. BTC 2 - Non-isothermal gray medium.

The summary of the meshes for both cases is shown in Tab. 4.1.

Table 4.1: The summary of dense convective and coarse ortho-Cartesian meshes for considered cases, denoted by superscripts c and oC. N_v, N_s, N_{nurbs}, N_{BV} are the number of volume cells, boundary surfaces, NURBS surfaces and total number of bounding volumes respectively.

$Case$	N_v^c	N_s^c	N_v^{oC}	N_s^{oC}	N_{nurbs}^{oC}	N_{BV}^{oC}
BTC 1	23 600	5 520	1 536	744	1 152	2 784
BTC 2	117 800	14 356	2 640	1 184	1 598	8 150

During the comparison of the ray tracing methods mentioned at the beginning of this section, one has to take into account the following issues:

- total number of surface and volume elements,
- the presence of bounding volume hierarchy in the case of otho-Cartesian mesh,
- the differences in geometrical description of volume elements between ortho-Cartesian and convective meshes.

The main advantage of using ortho-Cartesian mesh over standard one is much lower number of surface and volume elements the rays are to be traced from. Thus, the total number of rays, expressed as

$$n_r = N_r(N_s + N_v), \tag{4.79}$$

where N_r is the number of rays per one element (surface or volume), N_s, N_v are the number of surface and volume elements, is also heavily reduced. Tab. 4.2 shows estimates of total number of rays traced for both versions of Monte Carlo model, assuming $N_r = 100k$ rays released from one element. The results prove that using ortho-Cartesian mesh significantly reduces the total number

Table 4.2: Total number of rays traced n_r for both versions of Monte Carlo model and speedup (last column) obtained using ortho-Cartesian mesh instead of convective one.

Case	N_r	n_r^c	n_r^{oC}	n_r^c/n_r^{oC}
BTC 1	100 000	2 912.0 M	228.0 M	12.8
BTC 2	100 000	13 215.6 M	382.4 M	34.6

of rays. The speedup, caused by avoiding tracing of some rays and defined as n_r^c/n_r^{oC}, depends on the case at hand and can be as high as 35.

The presence of bounding volumes hierarchy reduces the potential speedup resulting from the reduction of elements. During the tracing of rays on ortho-Cartesian mesh, the ray has to be intersected with some of the volumes from the hierarchy. Under the assumption that the ray is tested for intersection with every fourth bounding volume, the speedup is estimated to be 9.8 and 22.6 for BTC1 and BTC2 respectively.

The last point in the current discussion is the difference in geometrical description of volume elements between both considered meshes. In the case of ortho-Cartesian mesh it is guaranteed, that every volume is defined by six planes parallel to the planes of global coordinate system. When the ray traverses the mesh, three ray-plane intersection points are found (ray direction is known and only three planes from six can be selected) and the closest point lying in front of the ray origin is accepted, allowing for finding the neighbour cell. However, in the standard mesh composed of hexahedral elements, there is no guarantee that for each of six faces defined by four vertices each of those vertices lies on the same plane. This fact has been pointed out by G. Wecel in his Ph.D. thesis [131] and has its consequences. Namely, each of six faces has to be divided into two triangles and twelve ray-plane intersection points are found. For further calculations the closest point lying on the triangular face is accepted. As a consequence, two times more ray-intersection points have to be computed together with one check if point is within triangle. Thus, it can be concluded, that traversing a standard mesh is around four times slower than ortho-Cartesian one.

Summarizing, the speedup resulting from using ortho-Cartesian mesh is estimated to be 40 and 90 for BTC1 and BTC2 respectively. It is eveident, that reported value of speed-up is greater for the case where the difference between ortho-Cartesian and CFD cells is bigger. The ratio between number of CFD and ortho-Cartesian cells is 16 and 45 for BTC1 and BTC2 respectively.

It should be kept in mind, that by using ortho-Cartesian mesh the quality of the solution is sacrificed to the potential speedup in computational time. This topic is covered in details in section 5.1.2.

4.9 Treatment of non-gray gases in Monte Carlo technique

Within the current thesis, radiative properties of non-gray gases in Monte Carlo model were accounted for using WSGGM described in some details in section 2.1.6. Theoretical background of WSGGM is fully covered by works of G. Węcel [130, 131, 132, 133].

In the case of WSGGM, fractions of blackbody emissive power, radiative heat flux and radiative heat source corresponding to k-th gas are defined by means of weighting factors a_k:

$$e_{b,k} = a_k e_b, \tag{4.80}$$

$$q^r_k = a_k q^r, \tag{4.81}$$

$$q^r_{v,k} = a_k q^r_v. \tag{4.82}$$

These fractions satisfy relationships

$$\sum_{k=0}^{N_g} e_{b,k} = e_b; \quad \sum_{k=0}^{N_g} q^r_k = q^r; \quad \sum_{k=0}^{N_g} q^r_{v,k} = q^r_v. \tag{4.83}$$

Using (4.80), (4.81) and (4.82) equations for radiative heat flux (4.37) and volumetric heat source due to emission or absorption in medium and particles (4.38) in element i can be rewritten in the following form

$$\begin{aligned} q^r_i = \sum_{k=0}^{N_g} \Bigg[& \epsilon_i e_{b,i} a_{i,k} - \sum_{j=1}^{N} \epsilon_i e_{b,j} D_{ij,k} a_{j,k} \\ & - \sum_{j=N+1}^{n} \frac{\kappa_{j,k} e_{b,j} + \pi E_{p,j}}{\kappa_{j,k} + \kappa_{p,j}} \epsilon_i D_{ij,k} a_{j,k} \Bigg] \quad , 1 \leqslant i \leqslant N, \end{aligned} \tag{4.84}$$

$$\begin{aligned} q^r_{v,i} = \sum_{k=0}^{N_g} \Bigg[& 4(\kappa_{i,k} e_{b,i} + \pi E_{p,i}) a_{i,k} - \sum_{j=1}^{N} 4(\kappa_{i,k} + \kappa_{p,i}) e_{b,j} D_{ij,k} a_{j,k} \\ & - \sum_{j=N+1}^{n} 4(\kappa_{j,k} e_{b,j} + \pi E_{p,j}) \frac{\kappa_{i,k} + \kappa_{p,i}}{\kappa_{j,k} + \kappa_{p,j}} D_{ij,k} a_{j,k} \Bigg] \quad , N+1 \leqslant i \leqslant n, \end{aligned} \tag{4.85}$$

where: k, N_g, a_k $D_{ij,k}$ denote gray gas index ($k = 0$ is transparent one), weighting factor, number of gray gases ($N_g = 4$) and one element of RDF matrix $\mathbf{D}$. a_k and κ_k values are computed following procedure from section 2.1.6 and using data reported by Węcel in paper [132]. It is important to emphasize, that there is a need to determine five $\mathbf{D}$ matrices, one for each gas, including transparent one. Therefore, the penalty for taking into account non-gray properties of gases is, as expected, a higher computational cost.

Chapter 5

Verification of the radiation model

The chapter presents MCRT cases used for verification, classified into two main groups: non-participating (sec. 5.1) and absorbing and emitting (sec. 5.2) media.

The reason for such a division lies in the history of MCRT model development. The development was divided into the stages, which was possible due to the relative easiness of code implementation. The code boasts the same structure for both variants - non-participating and semitransparent media. Firstly, the system for ray-tracing using otho-Cartesian mesh using NURBS surfaces for the boundaries description was implemented. At that stage, the absorption and emission of the ray inside semitransparent medium was not allowed. Without the allowance for ray absorption and emission inside the medium, the model solves the surface-to-surface radiation problems. The importance of this stage of the model development should not be underestimated, since the majority of the procedures tested here are used later in the upgraded version of the model. Secondly, the model was upgraded to take into account the absorbing and emitting medium, for which the test cases are described in section 5.2.

5.1 Non-participating medium

5.1.1 View factor

MCRT model was used to estimate value of the view factor for two parallel rectangular plates of sides equal to X and Y. Surfaces lay in front of each other at a distance of L. The exact value of the view factor was calculated using an

expression from the book [15]

$$F_{ij} = \frac{2}{\pi \bar{X}\bar{Y}} \left\{ \ln \left[\frac{(1+\bar{X}^2)(1+\bar{Y}^2)}{1+\bar{X}^2+\bar{Y}^2} \right]^{1/2} + \bar{X}(1+\bar{Y}^2)^{1/2} \tan^{-1} \frac{\bar{X}}{(1+\bar{Y}^2)^{1/2}} \right\} + \frac{2}{\pi \bar{X}\bar{Y}} \left\{ \bar{Y}(1+\bar{X}^2)^{1/2} \tan^{-1} \frac{\bar{Y}}{(1+\bar{X}^2)^{1/2}} - \bar{X} \tan^{-1} \bar{X} - \bar{Y} \tan^{-1} \bar{Y} \right\}, \tag{5.1}$$

where $\bar{X} = X/L, \bar{Y} = Y/L$. By setting the values $X = Y = 1/3\,m$ and $L = 1\,m$ the exact value of $F_{ij}^{exact} = 0.0329714$.

During the simulation rays were traced from the surface of one plate and hits were reported when rays arrived at the second plate. Using the number of hits reported N_{ij} and total number of rays traced N_i the view factor F_{ij} can be estimated using equation (4.40), repeated here for convenience: $F_{ij} = D_{ij} \cong \frac{N_{ij}}{N_i}$. For a given total number of rays traced N_{rays} 10 tests were performed for different seeds of random number generator (RNG). It allowed to determine mean value $F_{ij}^{estimate}$, standard deviation s_{10} and relative error ϵ for the view factor. The results are listed in Tab. 5.1 and shown on graph in Fig. 5.1.

Table 5.1: Results of simulation of view factor estimate. Values computed on the basis of 10 runs with different RNG seeds.

N_{rays}, -	F_{ij}^{exact}, -	$F_{ij}^{estimate}$, -	s_{10}, -	ϵ, %
100	0.0329714	0.038	0.02638	15.25
1000	0.0329714	0.0341	0.00370	3.42
10000	0.0329714	0.03289	0.00151	0.25
100000	0.0329714	0.033063	0.00043	0.24
1000000	0.0329714	0.0328263	0.00018	0.22

The results show that:

1. The estimated value of view factor tends to exact value with the increasing number of rays traced.

2. The value of standard deviation for 10 samples decreases proportionally to the value of the expression $\sqrt{N_{rays}}$.

3. Relative error tends to 0 for a large number of rays traced.

4. The mean value of the view factor for a given number of rays, should tend to the exact value for the increasing number of tests performed. In other words, performing 10 tests with 100 rays traced, should give the

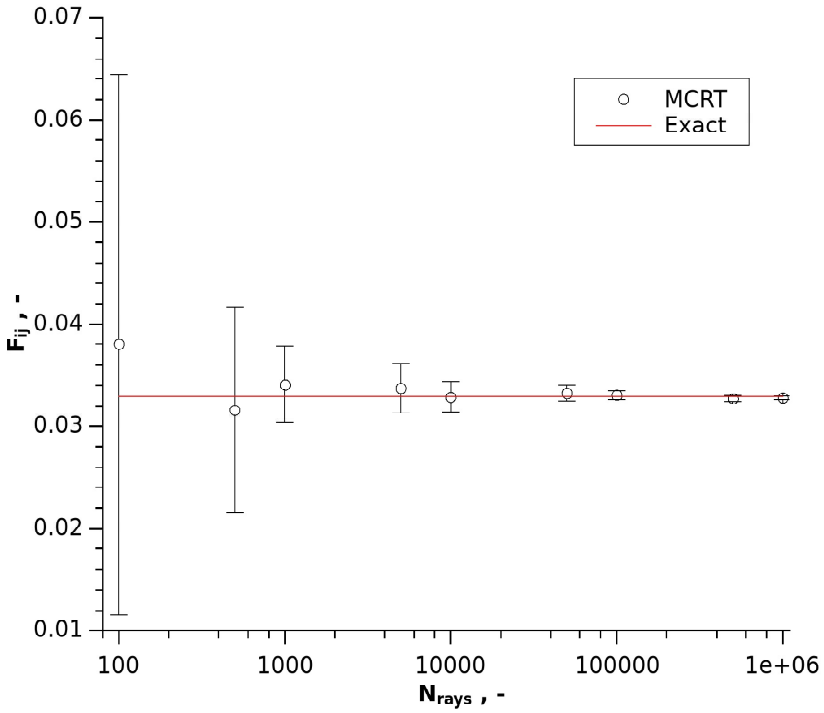

Figure 5.1: View factor estimates F_{ij} for two parallel plates computed on the basis of 10 tests with various RNG seeds done with MCRT model for different number of rays traced N_{rays} and compared with exact value [15]. Vertical bars denote standard deviation of the sampling set.

result similar to 1 test with 1000 rays. However, in the second case, the information about the standard deviation is lost.

The results proved a proper behaviour of the MCRT model with respect to computation of the view factor.

5.1.2 The cube

In this test the results obtained by surface-to-surface (S2S) Ansys Fluent [5] and OpenFOAM MCRT models are compared on the geometry of cube that has edges equal to 1 m (Fig. 5.2). The details of the S2S model are described in appendix A.

Fixed temperature boundary conditions are listed in Tab. 5.2, in which $T(r)$ (in K) defines a temperature profile on the wall

$$T(r) = \begin{cases} (T_0 - T_1) \cdot \cos^2(\frac{\pi}{2r_{max}} \cdot r) + T_1, & \text{if } r < r_{max}, \\ T_1, & \text{otherwise,} \end{cases} \tag{5.2}$$

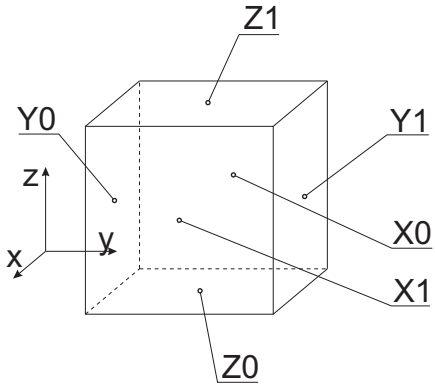

Figure 5.2: The geometry of 1m cube with names of boundary walls.

where: $r = \sqrt{p_i - p_0}$ - distance between the center of the cell boundary wall p_i and the center of *Z0* wall p_0, $T_0 = 500\,K$, $T_1 = 300\,K$ - maximum and minimum temperature, $r_{max} = 0.4\,m$ - radius of influence. $T(r)$ function guarantees temperature continuity on the boundary walls. The walls are diffuse with constant value of absorptivity, equal to 1.

Table 5.2: Boundary conditions - temperature and absorptivity at the walls.

Wall name	*T, K*	α, -
X0, X1, Y0, Y1, Z1	300	1
Z0	$T(r)$	1

CFD mesh consists of 125000 cells which corresponds to uniform x, y, z resolution of 50. MCRT model was run 5 times for different RNG seeds for each otho-Cartesian mesh resolutions M_{res} equal to 10, 20 and 40. The number of rays traced from one surface element was set to 10000.

Table 5.3: Balance of radiative heat fluxes (W) at cube walls for S2S and MCRT models. In the case of MCRT model the results are average values of 5 runs for different RNG seeds.

Model	M_{res}	*X0*	*X1*	*Y0*	*Y1*	*Z0*	*Z1*	*Net*
MCRT	10	-60.72	-61.20	-59.38	-62.08	314.02	-71.78	-1.13
MCRT	20	-61.59	-63.05	-62.40	-63.32	323.43	-77.09	-4.03
MCRT	40	-62.58	-62.04	-62.39	-62.94	325.85	-76.55	-0.65
S2S	-	-62.76	-62.75	-62.77	-62.76	326.53	-75.52	-0.03

Table 5.3 shows balances of radiative heat fluxes computed by S2S model and MCRT for three ortho-Cartesian mesh resolutions. The results produced by MCRT model follow S2S results and are closer to them for greater ortho-Cartesian mesh resolution. The balance of radiative heat fluxes for the entire enclosure should be equal to zero. In the case of MCRT model the unbalance

is greater than for S2S model, but the Monte Carlo results converge with the increase of mesh resolution. The unbalance is caused by uncertainties in computation of radiation distribution factors. The uncertainties can be lowered either by increasing the number of energy bundles traced, or by smoothing the distribution factor matrix. The smoothing procedure causes the elements of distribution factor matrix to fulfil energy conservation and reciprocity rules, described in details in section 4.2. Current version of MCRT model has not the smoothing procedure implemented.

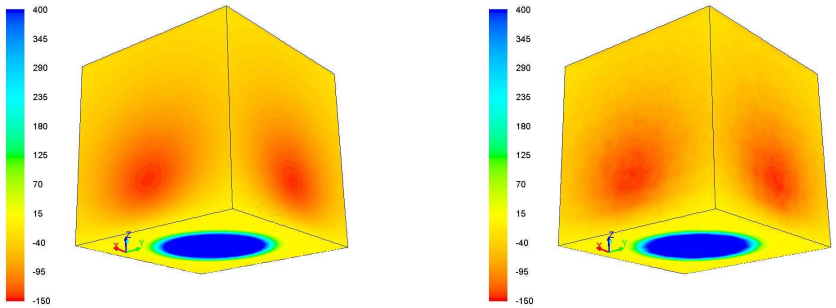

(a) S2S

(b) MCRT $M_{res} = 40$

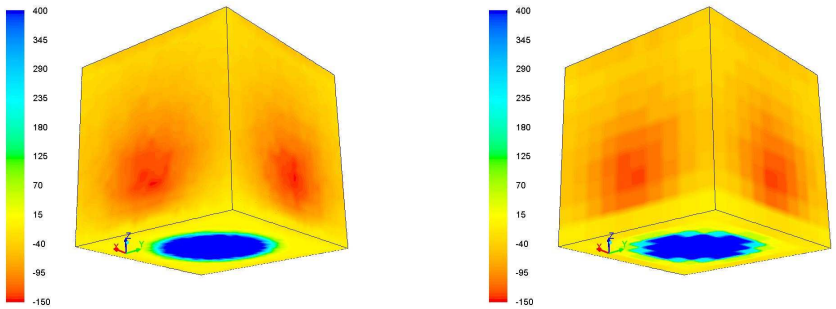

(c) MCRT $M_{res} = 20$

(d) MCRT $M_{res} = 10$

Figure 5.3: The influence of ortho-Cartesian mesh resolution on the radiative heat fluxes (W/m^2) on the walls.

Fig. 5.3 shows the influence of ortho-Cartesian mesh resolution M_{res} on the radiative heat fluxes. Increasing the resolution causes the solution to be more smooth and to approach the reference solution of S2S model. Moreover, the lower the resolution, the bigger the difference between extreme values of radiative heat flux reported by S2S and MCRT models. This fact is caused by the temperature averaging inside the ortho-Cartesian cells and it is important, since the radiative heat flux is proportional to the fourth power of temperature. Similar conclusions can be drawn by analysing Fig. 5.4, in which radiative heat fluxes along a symmetry line of wall *Z0* were presented.

In order to measure how the solution of MCRT model deviates from the accurate solution of S2S model the radiative heat fluxes on the line of symmetry

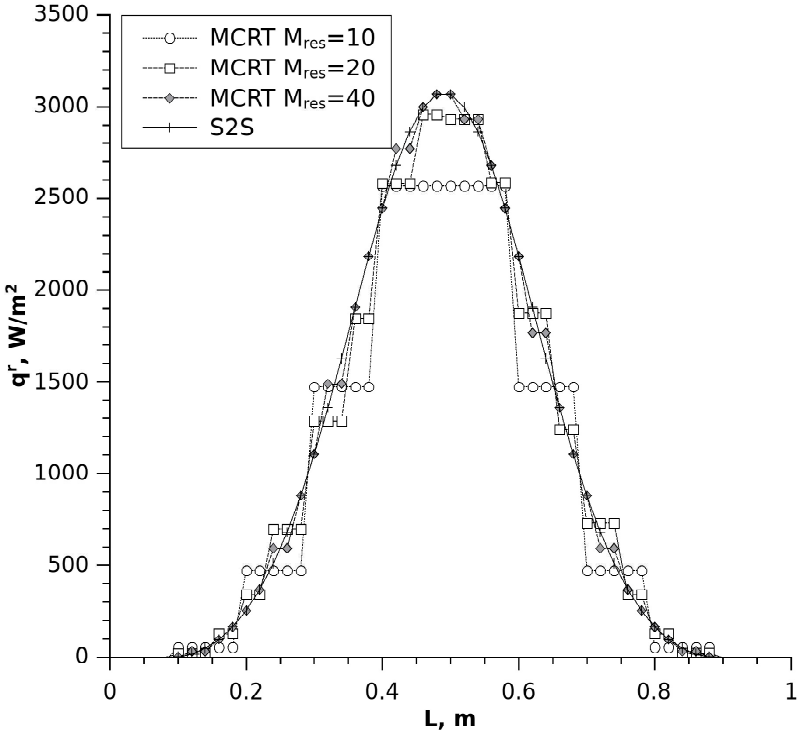

Figure 5.4: Radiative heat flux along the symmetry line of *Z0* wall for different resolutions of MCRT and S2S model.

of *X0* wall were extracted and compared using *p-norms*. The norms are defined as follows

$$||\mathbf{x}||_p = \left(|x_1|^p + |x_2|^p + ... + |x_n|^p\right)^{1/p}, \tag{5.3}$$

$$||\mathbf{x}||_\infty = \max\left\{|x_1|, |x_2|, ..., |x_n|\right\}, \tag{5.4}$$

where: $p = 1, 2$, $x_i = x_i^{S2S} - x_i^{MCRT}$.

The results are summarized in Tab. 5.4. Increasing the ortho-Cartesian mesh resolution two times causes the norms to decrease by a factor of two and to improve the accuracy of MCRT model. It should be noted that the resolution of ortho-Cartesian mesh can not be greater than the resolution of CFD mesh.

Table 5.4: The influence of ortho-Cartesian mesh resolution M_{res} on the deviation of heat fluxes on the symmetry line of *X0* wall obtained using MCRT model from S2S solution.

M_{res}	$\|\|\mathbf{x}\|\|_\infty$	$\|\|\mathbf{x}\|\|_1$	$\|\|\mathbf{x}\|\|_2$
10	11.9	239.3	39.4
20	9.4	130.2	24.3
40	3.4	59.3	10.7

5.2 Absorbing and emitting gray medium

The section covers the verification of MCRT model applied to absorbing and emitting gray medium. The verification of the model has been done by using the benchmark solutions obtained by several research institutions obtained with different techniques. The benchmark solutions were generated within the Radiarare Network of research institutions [47] and also has been used by G. Węcel in his work on BEM method [131].

The goal of Radiarare project was to establish a set of benchmark test cases (BTC). Subsequently, those cases are used in verification of various radiation heat transfer models. In all tests the temperatures of the walls and the medium were known, therefore the radiative analysis was uncoupled from the energy conservation for the fluid. Moreover, the medium and the walls were treated as gray.

The results were obtained by the following partners of the Radiarare Network:

- ENEL Produzione - Research (ENEL), Pisa, Italy;
  Discrete Transfer Method (DTM) and Discrete Ordinates Method (DOM)
- Lehrsthul fuer Stroemungsmechanik (LSTM), Erlangen, Germany;
  Monte-Carlo Method (MC);
- Instituto Superiori Tecnico (IST), Lisbon, Portugal;
  Discrete Transfer Method (DTM) and Discrete Ordinates Method (DOM)
- International Flame Research Foundation (IFRF), Ijmuiden, The Netherlands;
  Boundary Element Method (BEM)

Moreover, the results obtained by G. Węcel during his work on Boundary Element Method [131] are added for a reference:

- Institute of Thermal Technology (ITT), Silesian University of Technology, Gliwice, Poland;
  Boundary Element Method (BEM)

A detailed description of the models is covered in chapter 3. The naming convention for the respective models is summarized in Tab. 5.5.

The set of benchmark test cases consists of:

Table 5.5: The naming convention for the models used in verification procedure.

Abbrev.	*Institution*	*Model*
LSTM MC	Lehrsthul fuer Stroemungsmechanik, Germany	Monte Carlo
IST DOM	Instituto Superiori Tecnico, Portugal	Discrete Ordinates
IST DTM	Instituto Superiori Tecnico, Portugal	Discrete Transfer
Enel DOM	ENEL Produzione - Research, Italy	Discrete Ordinates
Enel DTM	ENEL Produzione - Research, Italy	Discrete Transfer
IFRF BEM	International Flame Research Foundation, The Netherlands	Boundary Element
ITC BEM	Institute of Thermal Technology, Poland	Boundary Element, *BERTA* code
ITC MC	Institute of Thermal Techno logy, Poland	Monte Carlo

- **BTC 1**

  Well-stirred combustion chamber with prescribed uniform temperatures of the medium, uniform wall emissivities and uniform wall temperatures.

- **BTC 2**

  Non-isothermal gray medium with prescribed uniform wall emissivities and a distribution of the wall and medium temperatures.

5.2.1 Well-stirred combustion chamber

Case set-up

The test case simulates a rectangular combustion chamber of dimensions 1m x 1m x 3m, presented in Fig. 5.5. Well-stirred assumption implies, that the temperature and absorption coefficient of the medium are uniform across the enclosure. Also the temperature and emissivity of walls are uniform. The walls have lower temperature than gas, thus they can be regarded as a heat sink. The radiative properties of both walls and medium are gray. The geometry of the chamber was simplified, including the burner inlet and the flue gas outlet, placed at the front and back walls of the chamber. The boundary conditions for the case are summarized in Tab. 5.6.

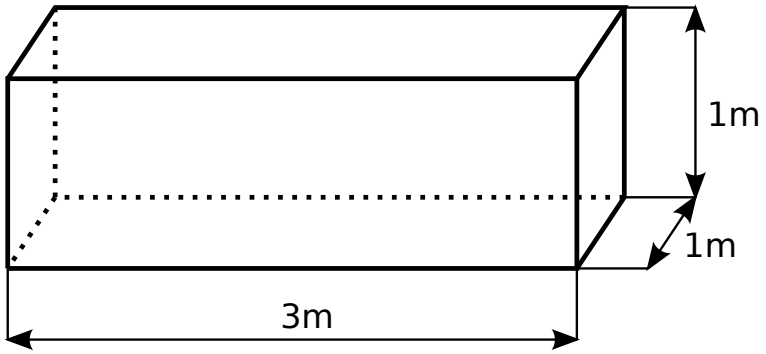

Figure 5.5: Geometry of benchmark case 1 - Well-stirred combustion chamber.

Table 5.6: Boundary conditions for BTC 1.

Parameter	*Value*	*Units*
Wall temperature	1000	$°C$
Wall emissivity	0.5; 0.8	$-$
Gas temperature	1500	$°C$
Gas absorption coeff.	0.1	m^{-1}

Results

CFD mesh resolution for this case is set to 20 x 20 x 60 corresponding to 24k of CFD cells. The resolution of ortho-Cartesian mesh for radiative analysis, created on the basis of CFD mesh, is 8 x 8 x 24 yielding 1536 cells. The number of rays traced from one volume or surface element is 1 million for ITT MC model.

The case was run two times with different wall emissivities ϵ, equal to 0.5 and 0.8. The output of the radiative analysis are the net heat fluxes at walls q^r. The surface irradiation (or the incident heat flux) i can be calculated from

the equation

$$q^r = \epsilon(i - e_b), \tag{5.5}$$

where e_b is the blackbody emissive power at the wall temperature.

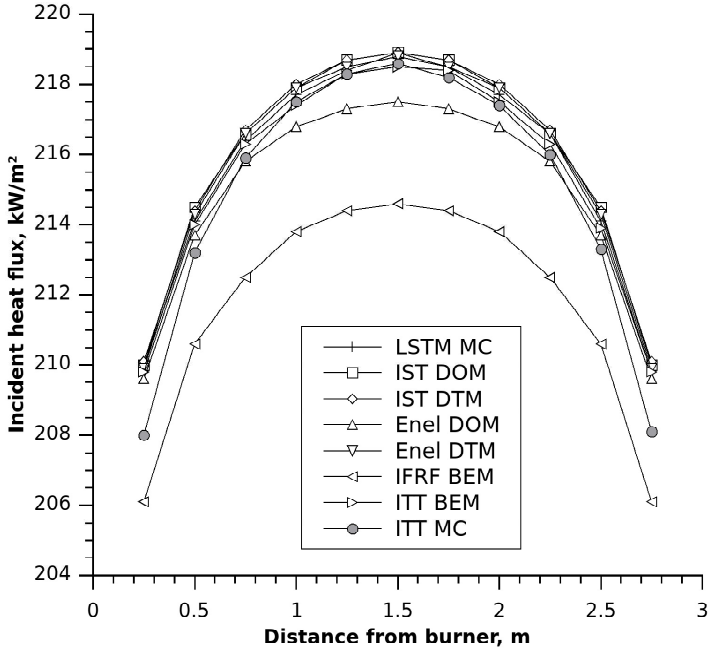

Figure 5.6: Comparison of the incident heat flux along the longer symmetry axis of chamber side wall obtained using different models; $\epsilon = 0.5$.

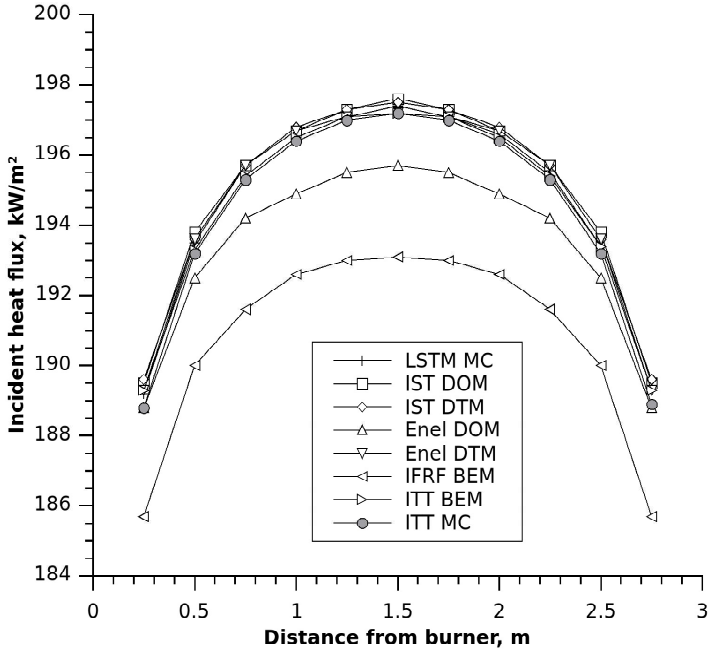

Figure 5.7: Comparison of the incident heat flux along the longer symmetry axis of chamber side wall obtained using different models; $\epsilon = 0.8$.

The comparison of incident heat flux along the longer axis of symmetry of the chamber side wall obtained using different models is shown in Fig. 5.6 and

Fig. 5.7 for cases of wall emissivity equal to $\epsilon = 0.5$ and $\epsilon = 0.8$ respectively. The results of ITT MC model show very good agreement with the results of most of the other methods. The observable differences are $< 0.5\,\%$. It should be noted, that the results of IFRF BEM method differ the most from other models. This fact can be explained by the simplified integration routines and ray tracing procedures employed in the code [78].

5.2.2 Non-isothermal gray medium

Case set-up

The test case simulates a cylindrical combustion chamber of length 3m and radius 0.5m, presented in Fig. 5.8. The chamber is axially fired and symmetrically cooled. The walls have uniform emissivity and the gas filling-up the enclosure has uniform absorption coefficient. The temperature of the gas and the walls is given by a location-dependent function $T(\mathbf{p})$, that simulates a flame from a burner, installed axially at the front wall of the chamber. The geometrical details of the burner as well as outlet were omitted for simplicity. The boundary conditions are summarized in Tab. 5.7.

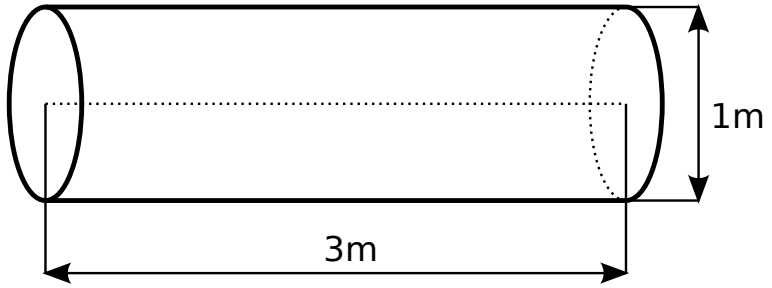

Figure 5.8: Geometry of benchmark case 2 - Non-isothermal gray medium.

Table 5.7: Boundary conditions for BTC 2.

Parameter	*Value*	*Units*
Wall temperature	$T(\mathbf{p})$	$^{\circ}C$
Wall emissivity	0.7	$-$
Gas temperature	$T(\mathbf{p})$	$^{\circ}C$
Gas absorption coeff.	0.1	m^{-1}

The temperature distribution of both the gas and the walls $T(\mathbf{p})$ (in $^\circ C$) across the enclosure is given by the following equations

$$T(\mathbf{p}) = T_0(\mathbf{p}) + (T_a - T_0(\mathbf{p}))g(\mathbf{p}), \tag{5.6}$$

$$T_0(\mathbf{p}) = \frac{T_1}{2}\left(1 + \frac{1}{2R}\sqrt{x^2+y^2}\right), \tag{5.7}$$

$$g(\mathbf{p}) = \frac{L}{z}\exp\left[-m_0 - \frac{1}{2}\left(\left(\frac{\ln(z/L)+m_0}{s}\right)^2 + \frac{x^2+y^2}{(\sigma R)^2}\right)\right], \tag{5.8}$$

where T_a is the maximum temperature of the flame, x, y, z are Cartesian coordinates, R, L denotes the chamber radius and length, m_0, s are the parameters of the flame position along z-axis, σ is flame width parameter and T_1 is temperature at $x = y = z = 0$.

The temperature distribution function $T(\mathbf{p})$ is symmetrical with respect to the chamber axis. The temperature profile along the axis of symmetry has the following properties: at $z = 0$ the temperature equals to T_0, then it reaches a maximum and finally decreases at the cold end of the furnace. Along the radius of the chamber, the temperature follows a Gaussian profile.

The parameters necessary to determine the temperature profile are given in Tab. 5.8. The simulations were performed for two kinds of flames: short and long, corresponding to the values of m_0 parameter equal to 0.75 and 0.25 respectively (cf. Fig. 5.9).

Table 5.8: Boundary conditions for BTC 2.

Parameter	*Value*	*Units*
T_1	1200	$^\circ C$
T_a	1800	$^\circ C$
m_0	0.75 (*short flame*)	–
	0.25 (*long flame*)	–
s	1	–
σ	0.375	–

Results

CFD mesh size for this case is 100k of CFD cells. The resolution of ortho-Cartesian mesh for radiative analysis, created on the basis of CFD mesh, is 10 x 10 x 30 yielding 3000 cells. The number of rays traced from one volume or surface element is 1 million for ITT MC model.

The case was run two times with different temperature profiles, corresponding to short ($m_0 = 0.75$) and long ($m_0 = 0.25$) flames. The output of the radiative analysis are the net heat fluxes at walls q^r.

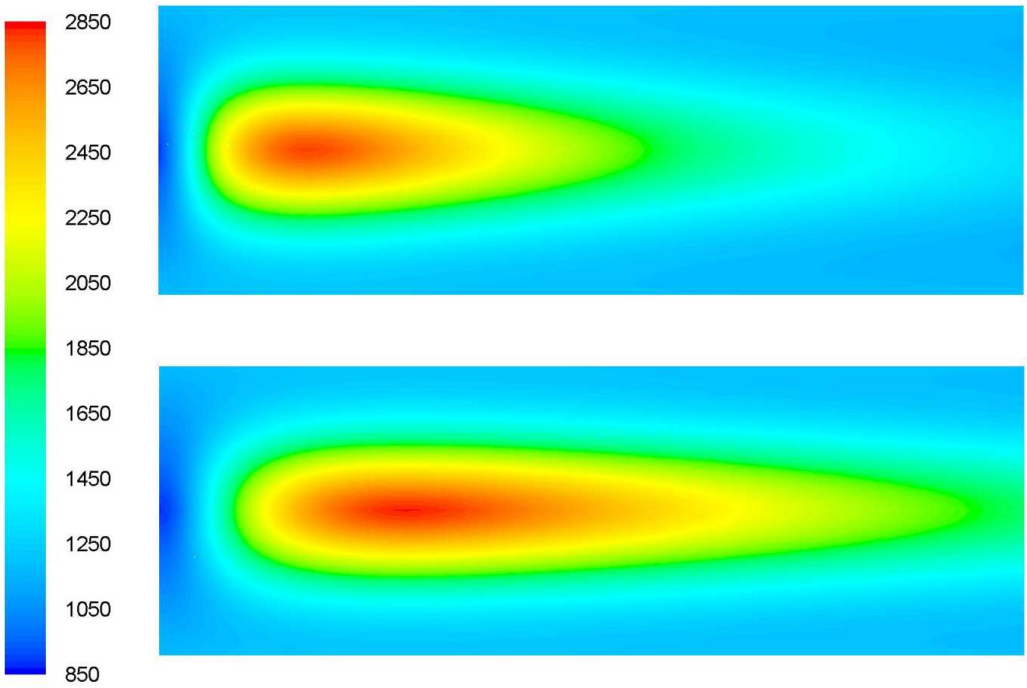

Figure 5.9: Temperature profiles (K) in the plane of symmetry of the chamber. Above: short flame, $m_0 = 0.75$, below: long flame $m_0 = 0.25$.

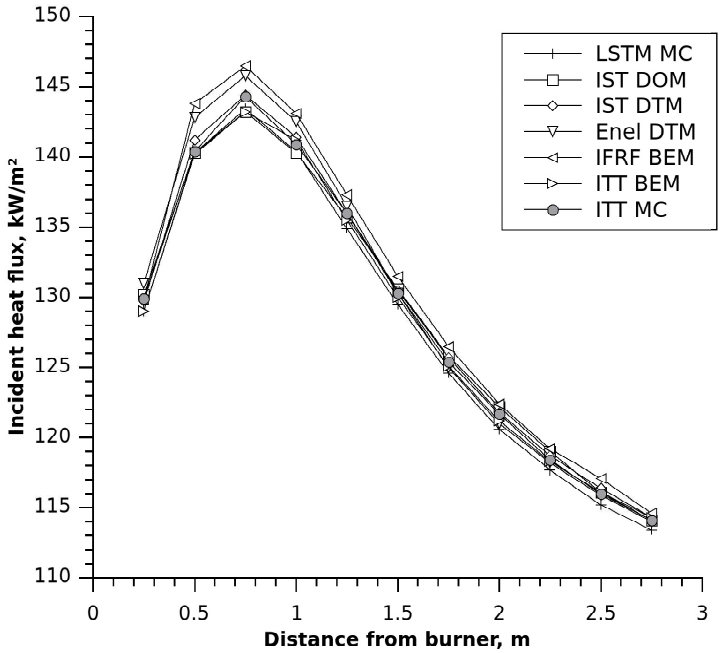

Figure 5.10: Comparison of the incident heat flux along the chamber side wall obtained using different models; short flame, $m_0 = 0.75$.

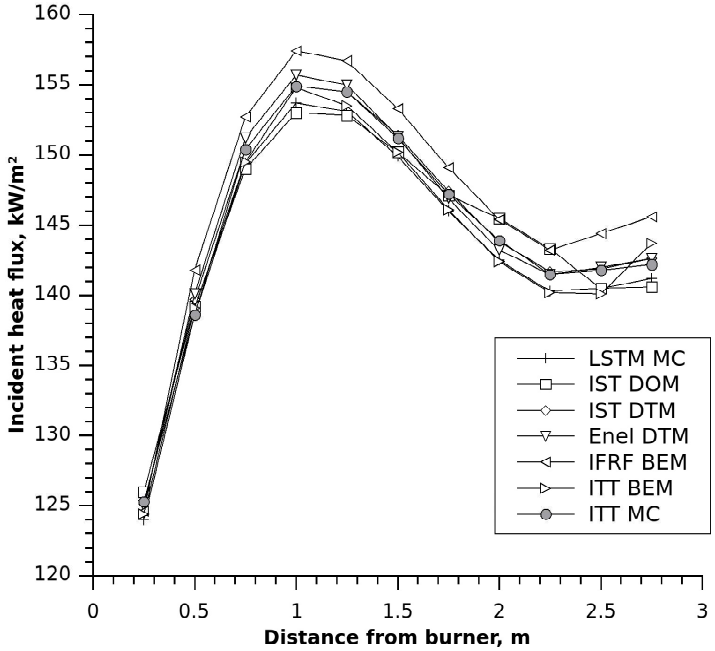

Figure 5.11: Comparison of the incident heat flux along the chamber side wall obtained using different models; long flame, $m_0 = 0.25$.

The comparison of incident heat flux along the chamber side wall obtained using different models is shown in Fig. 5.10 and Fig. 5.11 for cases of short and long flame temperature profiles. The results of ITT MC model show very good agreement with the results of most of the other methods. The observable differences are $< 1.5\,\%$.

5.3 Absorbing and emitting non-gray medium

The section deals with verification of MCRT model with implemented WSGGM to take into account non-gray properties of gases. As a benchmark rectangular combustion chamber with oxygen-fired flame [97] was selected.

Case set-up

The geometry of the combustion chamber has dimensions 2 x 2 x 4m and is filled with a gas mixture surrounded by cold black walls at $T_w = 300K$. Inside the chamber, the total pressure equals to 1 bar and the gas mixture is composed of (molar fractions) 85% CO_2, 10% H_2O and 5% of other gas neutral to radiation heat transfer.

The temperature distribution inside the chamber is given by

$$T = (T_c - T_e)f(r/R) + T_e, \tag{5.9}$$

where: T_e is temperature at the end of the chamber, i.e. $z = 4m$ and equals $800K$, T_c is centerline temperature:

$$T_c(z) = \begin{cases} 400 + z/0.375 \cdot (1800 - 400), & \text{if } 0 \leq z < 0.375, \\ 1903.5 - z/(4 - 0.375) \cdot (1800 - 800), & \text{otherwise.} \end{cases} \tag{5.10}$$

Function $f(r/R)$ is defined as

$$f(r/R) = 1 - 3(r/R)^2 + 2(r/R)^3, \tag{5.11}$$

where r and R denote the shortest distance of a point from centerline and radius equal to $1m$. Temperature distribution described above resembles the temperature field of a flame.

Results

The CFD mesh for ITT MC consisted of 128k cells, while the resolution of uniform ortho-Cartesian mesh was 17 x 17 x 34, yielding 9826 cells. Calculations were done releasing 100k bundles from one element. The results were compared to benchmark solutions of Porter [97] and Bordbar [132]. Authors of the first benchmark used ray tracing and statistical narrow-band model for calculating radiative properties of gases and solved the problem on 17 x 17 x 24 grid. The concentration of grid points was greater in the vicinity of temperature peak at $z = 0.375m$. The solution of Bordbar was generated with the zonal approach and WSGG model for radiative gas properties on uniform cubical mesh, which had resolution of 17 x 17 x 34 points. The comparison of the results being radiative heat flux and radiative heat source term is shown in Fig. 5.12 and 5.13 respectively.

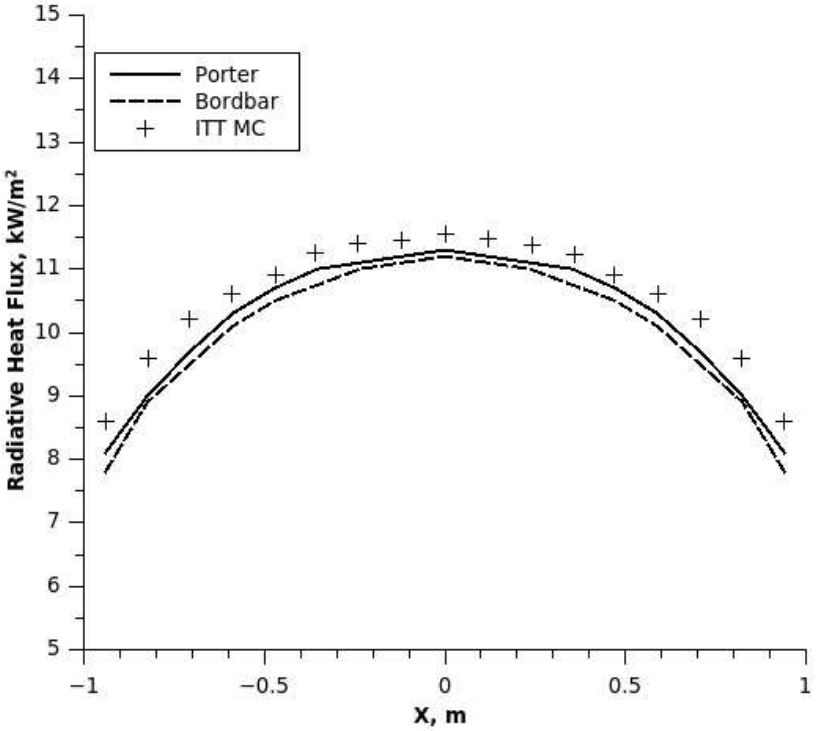

Figure 5.12: Comparison of the radiative heat flux along the centerline of $z = 4m$ wall.

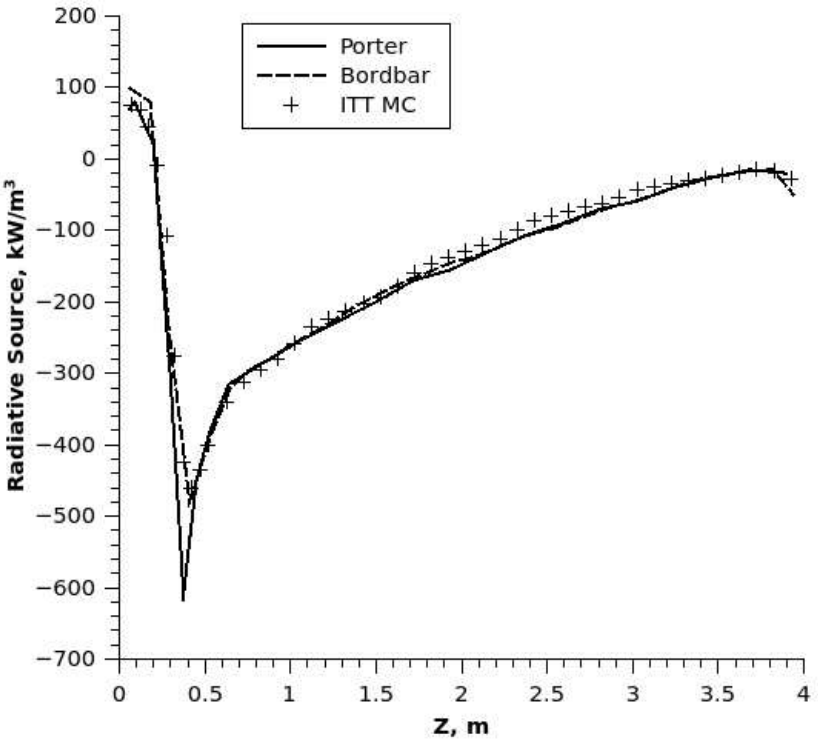

Figure 5.13: Comparison of the radiative heat source term along the centerline of the chamber.

The results show good agreement of ITT MC model with the benchmark solutions of Porter and Bordbar. The difference in radiative heat source term

along the centerline reported by the present model and benchmarks is $\leq 5\%$ in all the regions except zone near $z = 0.375m$, where the temperature peak is present.

The radiative heat flux along the centerline of $z = 4m$ wall shown by ITT MC model is close to benchmark solution of Porter with accuracy of $\leq 5\%$.

$\star \star \star$

The cases presented in this chapter served as a perfect tool for checking the code of Monte Carlo method. The results show very good agreement with benchmark solutions in all cases, therefore **the model can be considered as verified**.

Chapter 6

Applications

The chapter presents the practical applications of MCRT model on the example of a few cases. The first part of the chapter covers non-participating medium, while the second - semitransparent medium.

6.1 Non-participating medium - pit furnace

MCRT model was used for simulation of pit furnace performance. It is a perfect example of conjugate heat transfer, since the simulation involved all the modes of heat transfer - convection, conduction and radiation.

Pit furnaces are used (among other processes) for nitriding process of metal parts, such as connecting-rods, gear wheels, sleeves, housings etc. As a result of nitriding, a coating is created on the outer surface of the material. The coating has high hardness and good anti-wear properties. The nitriding process is operated in controlled atmosphere of 20% ammonia, 80% nitrogen mixture and in temperatures between 753 and 973 K. Depending on the required thickness of coating and the type of material, the whole process can last from several hours to couple of days. The simulation covered steady-state stage of the nitriding process.

The cross-section of the cylindrical pit furnace in the vertical plane of symmetry of real furnace is shown in Fig. 6.1. Fig. 6.2 presents the details of the geometrical model, created for the simulation purpose. The cylindrical chamber *14* of the pit furnace has a working space of dimensions: base diameter ϕ 600 mm, height 900 mm and is closed by a removable lid at the top. The sides of the chamber are covered by electric heaters *1-10* which have a maximum power of 40 kW. The furnace is insulated by bricks *12* and ceramic blankets *15*. Steel legs *11* reinforce the furnace base on which a steel shaft *13* is placed.

Ammonia/nitrogen mixture flows to the chamber through inlet *18* and escapes through outlet *16*. The mixing fan shaft *17* is placed in the center of the lid.

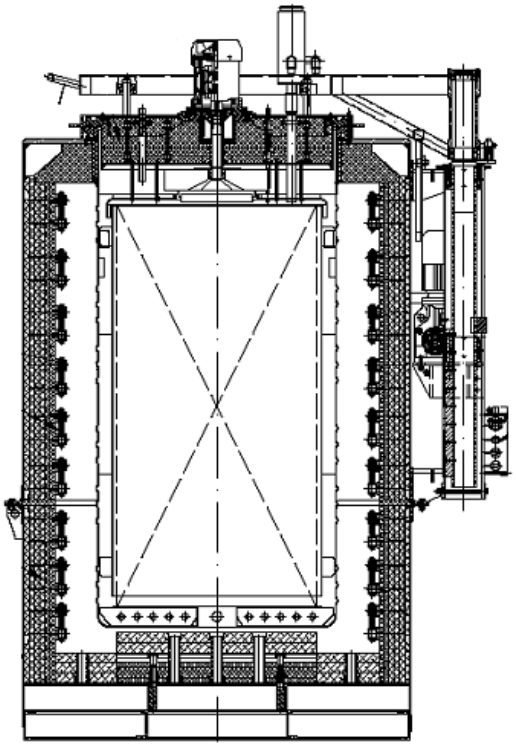

Figure 6.1: Cross-section of the cylindrical pit furnace in the vertical plane of symmetry. Courtesy of *Seco/Warwick Group* [107].

It should be noted that during the creation of geometrical model of the furnace certain simplifications and assumptions were made including:

- placing heaters inside the insulation,
- neglecting the presence of the gas-tight retort,
- neglecting the presence of the fan.

In practice, the furnace load is placed inside the gas-tight retort which prevents the heaters to have contact with nitriding atmosphere. The usage of the fan causes the atmosphere and its temperature to be more uniform inside the retort, especially in the neighbourhood of surfaces undergoing nitrification which influence the quality of the process. It should be kept in mind that the introduced simplifications influence the flow of the nitriding mixture inside the chamber. However, they do not change the overall energy balance of the system and are not crucial for testing the MCRT radiation model. Because of the low optical thickness of the medium inside the chamber, the absorption/emission properties of ammonia/nitrogen mixture were neglected.

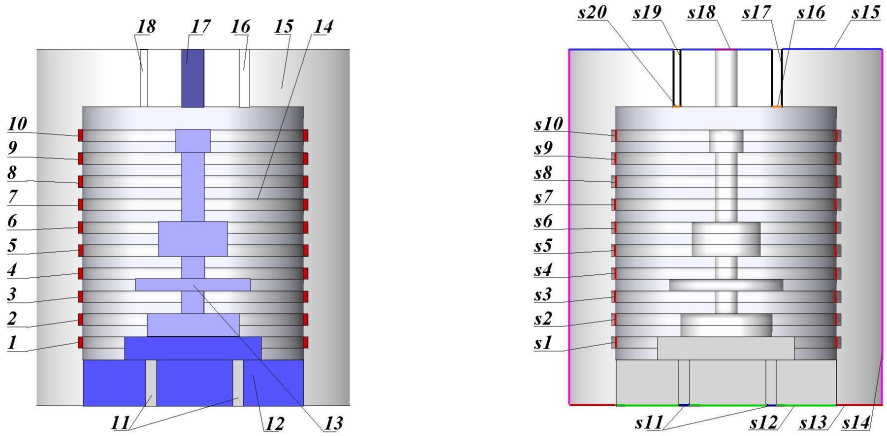

Figure 6.2: Cylindrical furnace cross-section through vertical plane of symmetry. *1-10* - electric heaters, *11* - steel legs, *12* - insulating brick, *13* - shaft, *14* - chamber, *15* - insulating ceramic blankets, *16* - outlet, *17* - fan shaft, *18* - inlet, *s1-s10* - inner surfaces of electric heaters, *s11* - bottom surf. of steel legs, *s12* - bottom surf. of insulating brick, *s13, s14, s15* - bottom/side/top surf. of insulating blanket, *s16, s20* - outlet/inlet, *s17, s19* - outlet/inlet pipes walls, *s18* - top surf. of fan shaft. The furnace data acquired from *Seco/Warwick Group* [107].

Selected boundary conditions are named in Fig. 6.2 and listed in Tab. 6.1. Material properties are shown in Tab. 6.2. The emissivity of all walls inside the furnace chamber was set to 1. The simulation was run for two radiation models MCRT and S2S for comparison. The resolution of ortho-Cartesian mesh was set to 20 x 20 x 22 and the number if rays released from each surface element was 10k.

Results

As a result of the simulation, temperatures and radiative heat fluxes within the chamber were determined and overall energy balance of the furnace was calculated. Fig. 6.3(a) shows the resulting temperature profile in the plane of symmetry. The detailed inspection of the profile reveals the existence of thermal bridges, created by fan shaft and steel legs. Also the cold stream of ammonia/nitrogen mixture, close to the inlet is visible. Fig. 6.3(b) shows the radiative heat fluxes on the sides of the chamber. Although the duty of each heater is the same, their radiant power differs significantly. This fact is caused by the different temperatures of the heaters. The heaters *1* and *10* have the lowest temperature and corresponding radiant power. The temperature and radiative heat flux profiles on the surface of nitriding object are shown in Fig.

Table 6.1: Boundary conditions for the case of pit furnace. Names correspond to the numeration introduced in Fig. 6.2.

Name	*BC type*	*Property*	*Units*	*Value*
s11, s12, s13,	wall natural	T_{ext}	K	300
s14, s15, s18	convection	h_{ext}	W/m^2K	5
s16	pressure outlet	p	Pa	0
s20	velocity inlet	v	m/s	0.0853
		$\dot{V}$	l/min	10
		T	K	300
s17, s19	wall	q	W/m^2	0
1 - 10	volume	q_v	W/m^3	130 000

T_{ext} - external free-stream temperature, h_{ext} - external heat transfer coefficient, p - pressure, v - velocity, $\dot{V}$ - volumetric flow rate, T - temperature, q - surface heat flux, q_v - volumetric heat source.

Table 6.2: Material properties used in the simulation. Volumes numbering corresponds to the one introduced in Fig. 6.2.

Material	*Volumes*	$k, W/mK$	$\rho, kg/m^3$	$c_p, J/kgK$
steel	11, 13, 17	58.00	7800	600
insulating blanket	15	0.20	70	970
insulating brick	12	0.14	480	1050
heaters rod	1 - 10	80.00	8000	450

k - heat conductivity, ρ - density, c_p - heat capacity.

6.4. The temperature on the shaft equals to 967 ± 4K and its range is too wide to assure the quality of the process. The non-uniform temperature is caused by the cold stream of ammonia/nitrogen mixture and exposure to the low-temperature side of fan shaft. The uniformity of the temperature distribution (and simultaneously nitrogen concentration) can be improved by using fan and gas flow-distribution equipment. Moreover, the electric power input for each heater should be adjusted in order to maintain uniform temperature across the chamber.

The overall energy balance for the furnace is shown in Tab. 6.3. In order to maintain the required temperature inside the chamber in steady state, only 10% of maximum heaters duty is needed. It is clear that most of the heat is lost through the insulation and metal parts and only a small percent ($< 4\%$) by hot exhaust gases. Mean temperature outside the side insulation is 382 K which is too high for people who operate the furnace. Additional cooling device should be installed in order to avoid contact with hot surfaces.

The comparison of radiative heat flux, mean temperature on selected walls and heat fluxes from Tab. 6.3 done for MCRT and S2S models shows good

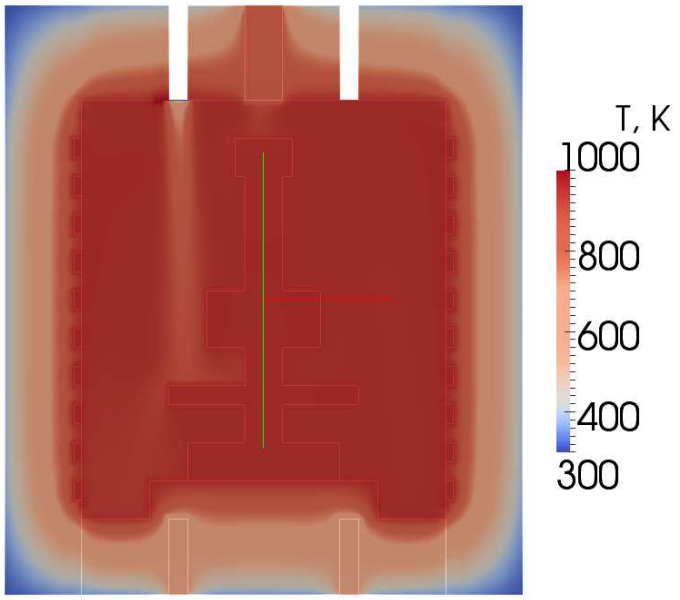

(a)

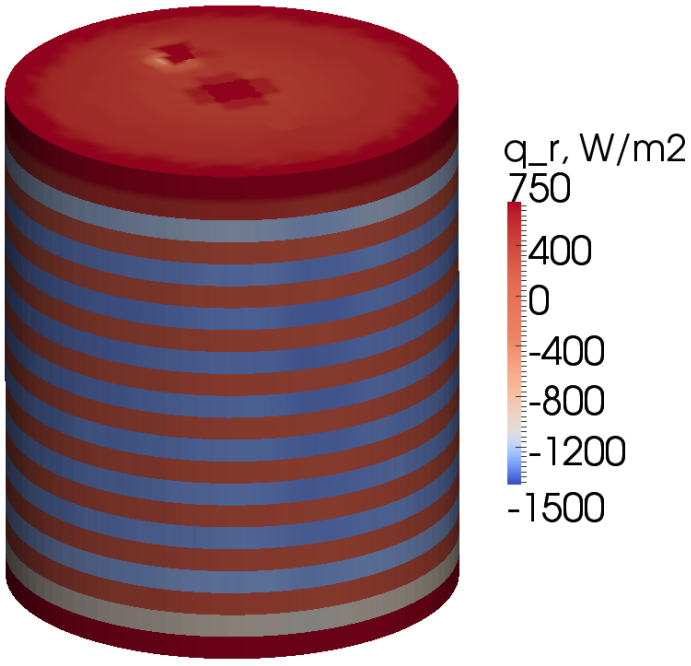

(b)

Figure 6.3: (a) Temperature profile (K) in furnace cross-section through vertical plane of symmetry. (b) Radiative heat flux (W/m^2) on the outer sides of cylindrical chamber.

agreement and the unbalance of the radiative heat fluxes is $< 0.7\%$. The differences are caused mainly by the temperature averaging inside ortho-Cartesian cells done in MCRT model.

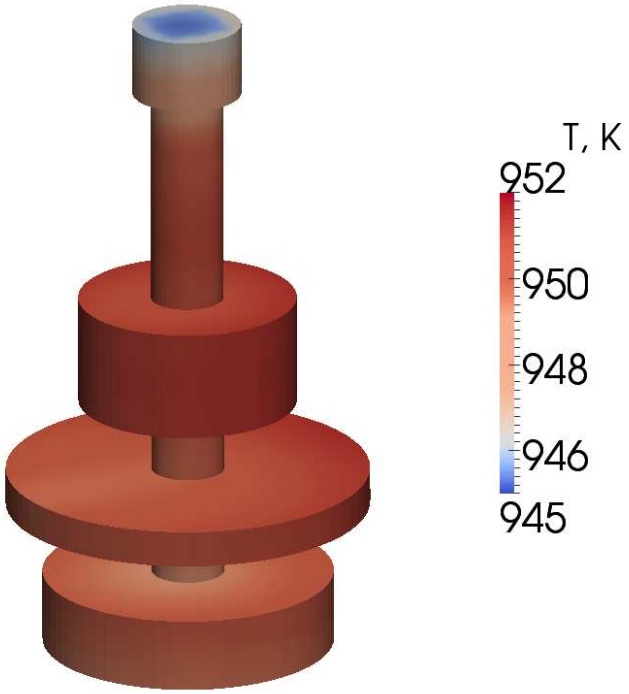

(a)

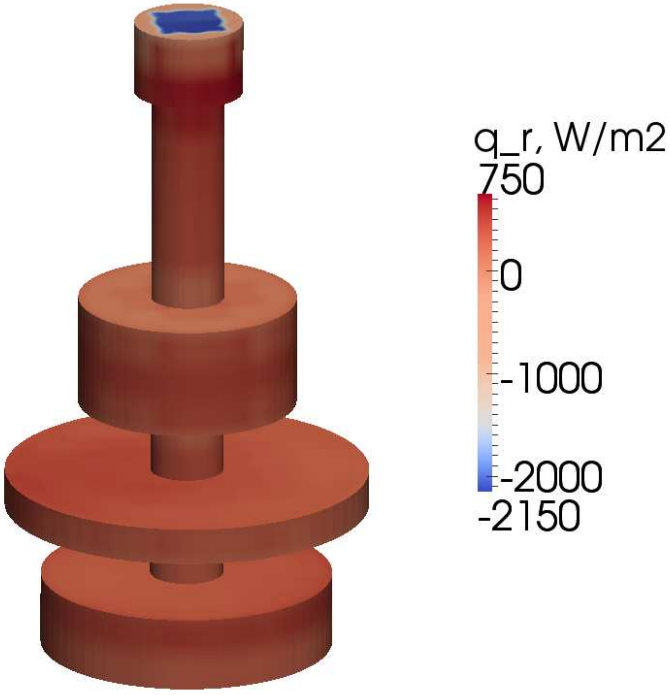

(b)

Figure 6.4: (a) Temperature (K) and (b) radiative heat flux (W/m^2) profiles on the outer surface of the shaft.

Table 6.3: Overall energy balance of the furnace for MCRT and S2S models. Surface names correspond to the ones introduced in Fig. 6.2.

Surfaces	Q_{MCRT}, W	Q_{S2S}, W
s11, s12, s13	-508	-522
s14	-2761	-2766
s15, s17, s18, s19	-489	-469
s16, s20	-79	-108
H_{gas}	-137	-136
$Q_{heaters}$	4000	4000
Net	-26	1

6.2 Absorbing/emitting medium - cylindrical comb. chamber

The issue of ray effect has been already introduced in chapter 3 together with the description of radiation models. The ray effect is an inherent feature of discrete ordinates and discrete transfer methods. The current section deals only with DO (also named S_N), as this method is widely used to solve many engineering problems, while the former is regarded as obsolete.

The ray effect is the deterioration of the solution of the radiative transfer equation (2.27) caused by the angular discretization [23]. In the case of DO model, it manifests itself in transferring the radiation preferably in the directions resulting from the angular discretization. The ray effect is visible especially in the cases of hot spots either in the medium or at the boundary surfaces. The radiative energy from such spots is transmitted mainly in the discrete directions, thus the reported values of radiative heat fluxes and heat sources at locations distant form hot spots can be far from exact.

Since the solution of the directional RTE is realized on the finite volume mesh, there exists another effect, known as false scattering or false diffusion [23, 92]. This effect occurs due to the spatial discretization of RTE and also due to the fact, that in general the mesh is not aligned with the ordinates, in which RTE is solved. Thus, the solutions that should have a sharp step, exhibit a smoothed slope. The negative consequences of the false diffusion effect can be mitigated by increasing either the number of control volumes inside the mesh or the order of spatial discretization. The ray effect and the false diffusion tend to minimize each others' negative effects, which is proven in the following.

Current section involves comparisons of solutions obtained by DO model for varying resolution of angular discretization, which is related to the order of the method N by equation (3.17), repeated here for convenience:

$$m = N(N + 2), \tag{6.1}$$

where m is the number of discrete directions. Table 6.4 shows the order of S_N method and corresponding number of discrete directions. In general, the order N can attain values that are not integers but it was rounded to the closest integer value for simplicity.

Table 6.4: Order of DO method N and corresponding number of discrete directions m in the case of 3D.

Notation	N	m
S_2	2	8
S_5	5	32
S_{10}	10	128
S_{16}	16	288
S_{25}	25	648
S_{27}	27	800

The existence of ray and false diffusion effects is shown on an example of cylindrical combustion chamber. In those examples the radiation heat transfer is computed using MCRT and DO models. Moreover, in DO model the influence of varying resolution of the angular discretization and the order of spatial discretization on the solution is analysed.

6.2.1 Case set-up

The geometry and setup of the case is the same as for the case of non-isothermal medium from section 5.2.2. The case simulates a cylindrical combustion chamber of length $3\,m$ and diameter $1\,m$ (cf. Fig. 6.5). The walls have uniform

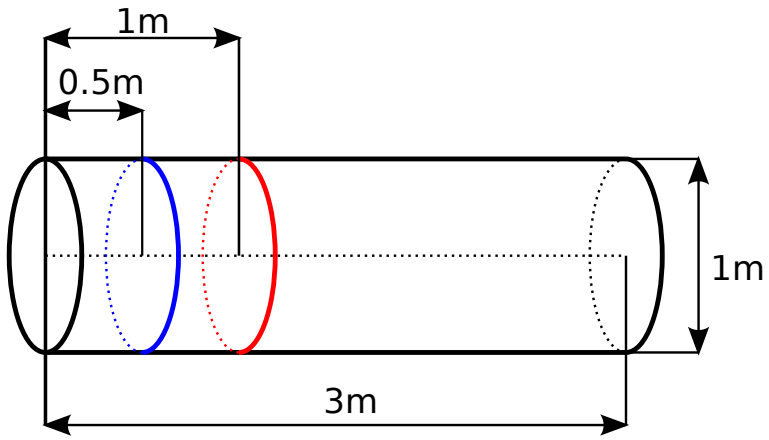

Figure 6.5: Geometry of cylindrical combustion chamber with two sampling lines on the circumference of the chamber side wall, located $0.5\,m$ and $1.0\,m$ from the front wall.

emissivity equal to 0.7, the gas has uniform absorption coefficient of $0.1\,m^{-1}$. The temperature distribution of both the gas and the walls is given by function $T(\mathbf{p})$ in $°C$, defined by equations (5.6), (5.7) and (5.8). The parameters for the proper calculation of the temperature profile are: $T_1 = 1200\,°C$, $T_a = 1800\,°C$, $m_0 = 0.75$, $s = 1$, $\sigma = 0.375$ and they correspond to the short flame profile (cf.

Fig. 5.9). The results for DO model are generated on fine CFD mesh of size 100k cells. The resolution of coarse ortho-Cartesian mesh for MCRT model is 10 x 10 x 30, yielding 3k cells.

6.2.2 Results

In order to visualize the ray effect, the case was run using DO (S_N) model with different parameters and the results were compared with MCRT model. The abbreviations of the models and their settings are the following:

1. $S_5 - 1^{st}O$: coarse angular resolution and 1^{st} order spatial discretization,
2. $S_{16} - 1^{st}O$: fine angular resolution and 1^{st} order spatial discretization,
3. $S_5 - 2^{nd}O$: coarse angular resolution and 2^{nd} order spatial discretization,
4. $S_{16} - 2^{nd}O$: fine angular resolution and 2^{st} order spatial discretization,
5. MCRT $N = X$: Monte Carlo ray tracing with the number of rays released from one element equal to X.

The results are the incident heat fluxes reported at walls (Fig. 6.6) and also along two sampling lines located on the circumference of the chamber at distances $z = 0.5\,m$ (Fig. 6.7, 6.9) and $z = 1.0\,m$ (Fig. 6.8, 6.10) from front wall. The mean value of the incident heat flux on the sampling lines and deviations from the mean for all considered models are summarized in Tab. 6.5. In order to measure the deviations form the mean p-norms are employed, given by equations (5.3) and (5.4).

Table 6.5: Mean value of the incident heat flux $\overline{i}$, kW/m^2 on sampling lines and deviations from the mean expressed in the form of p-norms.

Model	$\overline{i}$	$\|\|i\|\|_1$	$\|\|i\|\|_2$	$\|\|i\|\|_\infty$	$\frac{\|\|i\|\|_\infty}{\overline{i}}$
$z = 0.5\,m$	kW/m^2	kW/m^2	kW/m^2	kW/m^2	%
$S_5 - 1^{st}O$	141.5	125.6	15.0	3.4	2.4
$S_{16} - 1^{st}O$	141.5	107.1	11.3	2.0	1.4
$S_5 - 2^{nd}O$	142.2	485.5	48.2	6.6	4.6
$S_{16} - 2^{nd}O$	141.0	4.7	0.5	0.1	0.1
MCRT $N = 1k$	139.8	213.3	26.1	7.2	5.2
MCRT $N = 10k$	141.1	98.0	11.1	2.9	2.1
MCRT $N = 100k$	141.1	29.8	3.5	0.9	0.6
MCRT $N = 1M$	141.2	11.2	1.9	0.5	0.4
$z = 1.0\,m$					
$S_5 - 1^{st}O$	140.1	109.6	13.8	3.6	2.5
$S_{16} - 1^{st}O$	141.0	89.1	9.4	1.6	1.1
$S_5 - 2^{nd}O$	139.6	388.1	38.4	5.4	3.8
$S_{16} - 2^{nd}O$	141.2	3.8	0.4	0.1	0.1
MCRT $N = 1k$	142.0	215.7	24.1	5.3	3.7
MCRT $N = 10k$	141.7	66.5	7.8	1.9	1.3
MCRT $N = 100k$	141.4	27.6	3.2	0.8	0.6
MCRT $N = 1M$	141.4	13.6	1.6	0.5	0.4

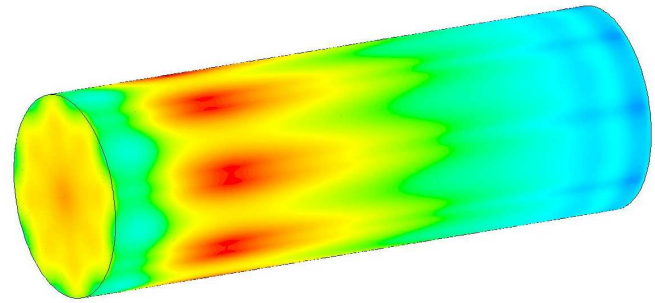

(a) $S_5 - 2^{nd}$

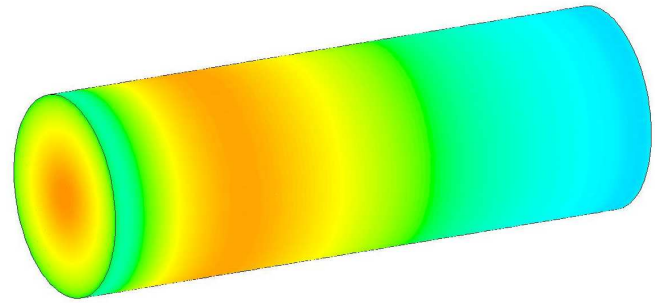

(b) $S_6 - 2^{nd}$

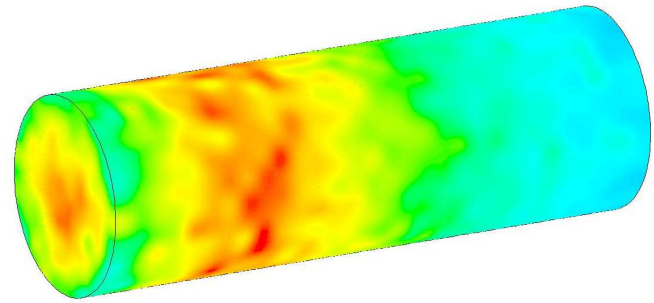

(c) MCRT $N = 1k$

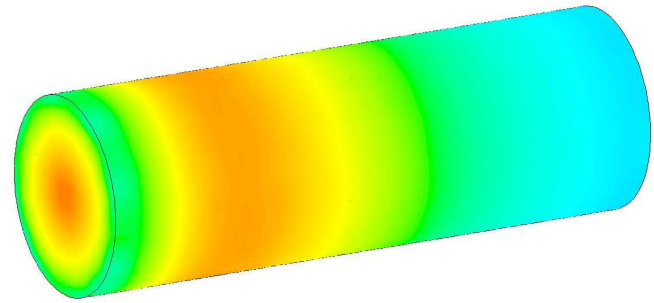

(d) MCRT $N = 1M$

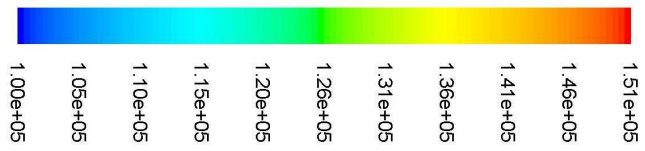

Figure 6.6: Wall incident heat flux (W/m^2) obtained using selected models.

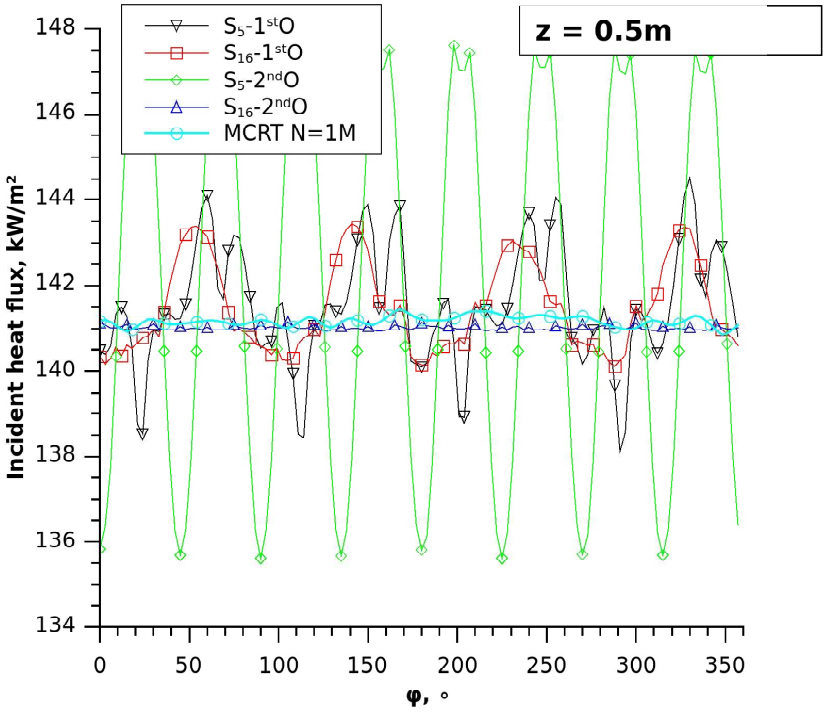

Figure 6.7: Surface incident heat flux along the sampling line. The line is located on the circumference of the chamber side wall and at distance $0.5\,m$ from burner.

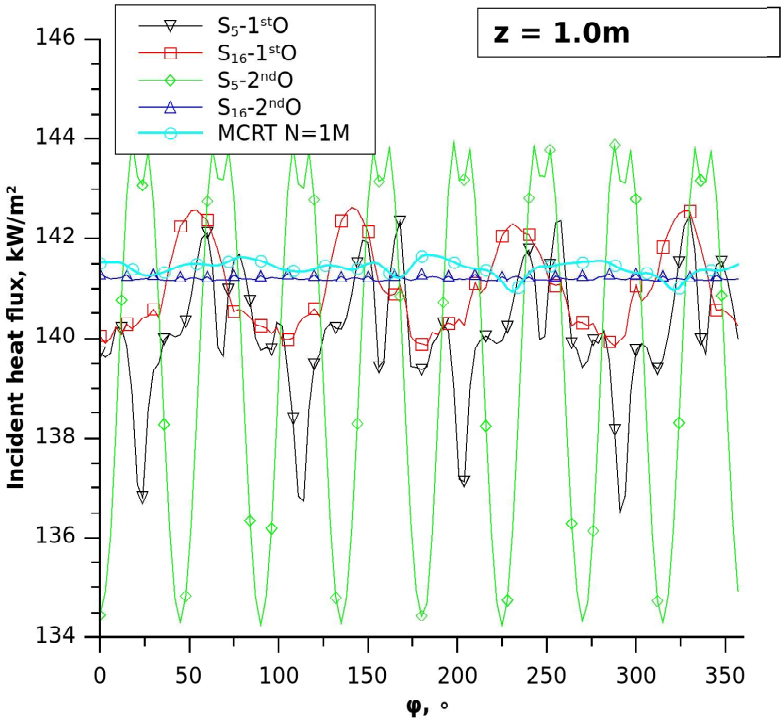

Figure 6.8: Surface incident heat flux along the sampling line. The line is located on the circumference of the chamber side wall and at distance $1.0\,m$ from burner.

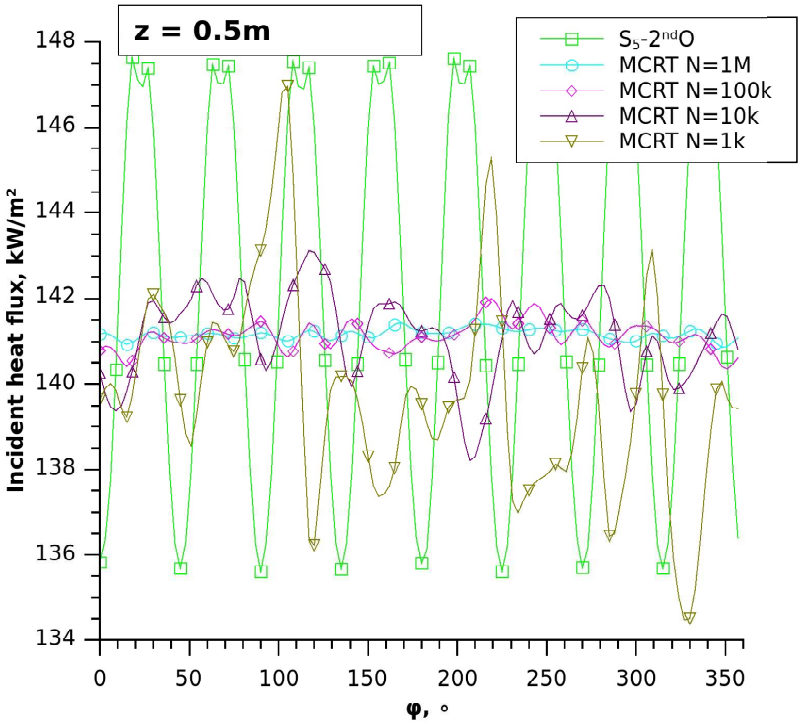

Figure 6.9: Surface incident heat flux along the sampling line. The line is located on the circumference of the chamber side wall and at distance $0.5\,m$ from burner.

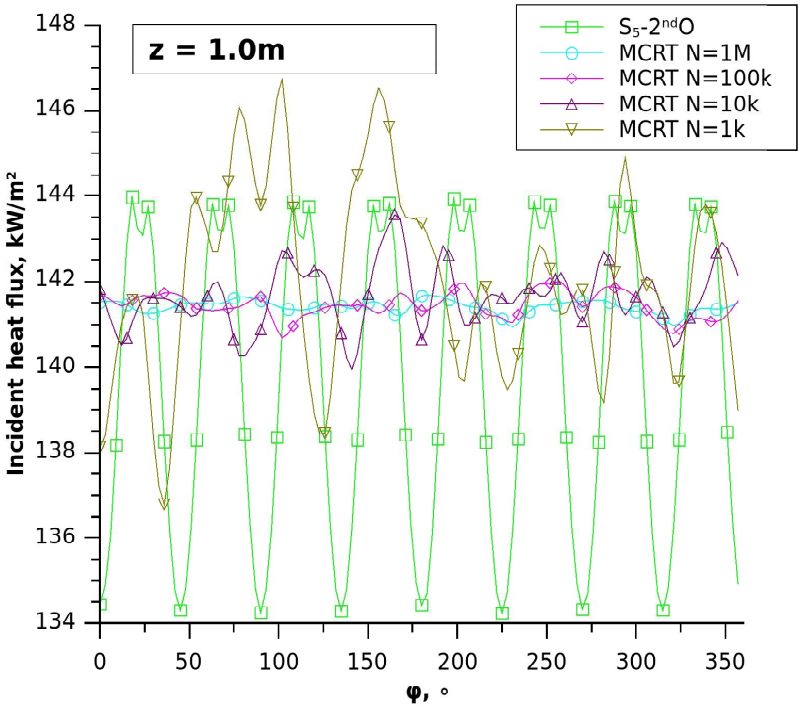

Figure 6.10: Surface incident heat flux along the sampling line. The line is located on the circumference of the chamber side wall and at distance $1.0\,m$ from burner.

The geometry of the chamber is axis-symmetrical and so is the temperature profile defined by function $T(\mathbf{p})$. Therefore, the values of the incident heat flux, reported along sampling lines $z = 0.5\,m$ and $z = 1.0\,m$ are expected to be uniform - however they are not. Analysing the results from Figs 6.6, 6.7, 6.8 and Tab. 6.5 it is clear, that the solution generated by DO model oscillates around mean value. The solution oscillations can not be eliminated only by increasing the method's order, i.e. increasing the number of ordinates, which is proven by comparing $S_5 - 1^{st}O$ and $S_{16} - 1^{st}O$. It is also not possible to achieve smoother solution only by setting higher order of spatial discretization: solutions of $S_5 - 1^{st}O$ and $S_5 - 2^{nd}O$. In those cases, the maximum relative difference of the reported incident heat flux has risen from 2.4% to 4.6% of the mean value for $z = 0.5\,m$ line. The only way to improve the quality of the solution is to increase both the number of ordinates and the order of spatial discretization ($S_{16} - 2^{nd}O$). The findings are consistent with the conclusions presented in paper by Coelho [23] and prove the existence of ray and false diffusion effects.

MCRT method is not prone to the ray effect, since the directions in which the rays are emitted cover the entire solid angle, not its discrete values. The reported oscillations result from the statistical nature of the model and depend on the number of rays N traced from one element. It has been shown in section 5.1.1, that the standard deviation of the solution from the mean value decreases proportionally to $\sqrt{N}$. The influence of the number of rays released from one element on the solution quality can be seen in Fig. 6.6 (c), (d) and Figs 6.9, 6.10 and compared using data from Tab. 6.5. As a consequence of the statistical nature of MC, its solution is characterized by irregular oscillations, which stands in contrast with regular oscillations of DO.

In order to provide quantitative information how much the values deviate from the mean value p-norms are used. By analysing Tab. 6.5 it can be concluded, that the solution generated by MCRT $N = 1k$ model has the quality falling between $S_5 - 1^{st}O$ and $S_5 - 2^{nd}O$, whereas the quality of MCRT $N = 10k$ model is similar to $S_{16} - 1^{st}O$. From the models of the best quality MCRT $N = 100k$, MCRT $N = 1M$ and $S_{16} - 2^{nd}O$ are comparable. The mean value of irradiation along sampling lines for MCRT models with lower number of rays per element, is close to quasi exact value obtained by MCRT $N = 1M$. The differences are $< 0.3\%$. What is remarkable, MCRT $N = 100k$ and MCRT $N = 1M$ produce the results of almost the same accuracy.

The quasi exact value of mean incident heat flux at sampling lines, $\overline{i}$, can be taken from the solutions of the highest order methods - MCRT $N = 1M$ and $S_{16} - 2^{nd}O$ (Tab. 6.5). The mean values reported by lower order methods differ from the quasi exact values by no more than 1%. In the quasi exact solution $\overline{i}_{z=0.5m} < \overline{i}_{z=1.0m}$, which is not the case for lower order DO models $S_5 - 1^{st}O$, $S_{16} - 1^{st}O$ and $S_5 - 2^{nd}O$. However, for all MCRT models, the tendency is the same as for quasi exact solution.

6.2.3 Comparison of execution time

The goal of this paragraph is to provide the information about the execution time of MCRT and DO models. The models are run on the same case, which is cylindrical combustion chamber and for which the temperature field across the domain is given. The presented comparison is done under the following assumptions:

- radiative properties of gas and walls are temperature independent,
- DO model runs on 8 threads,
- DO model convergence threshold $\epsilon = 1e - 6$,
- MCRT Ray Tracing procedure runs on 8 threads,
- MCRT pre- and post-processing stages run on 1 thread.

The whole MCRT model code is not run in parallel, only the ray tracing procedure is parallelized using OpenMP library (section 4.7). However, for the purpose of comparison, the real execution time of pre- and post-processing stages for MCRT model is divided by speedup reported for 8-processor machine, i.e. the value of 6 (cf Fig. 4.22).

Fig. 6.11 shows time needed by the considered models to generate converged solution. The auxiliary data, i.e. the number of DO iterations till convergence and time of pre- and post-processing stages of MCRT model, is presented in Fig. 6.12.

Before analysing the results, it is worth to rcall a few details concerning the used models. DO and MCRT models are very different in their architectures and solution techniques. DO uses standard dense convective mesh and iterative solution of the system of discretized differential equations, while MCRT creates coarse ortho-Cartesian mesh (pre-processing), traces the rays and interpolates the results back onto the convective mesh (post-processing). The pre-processing

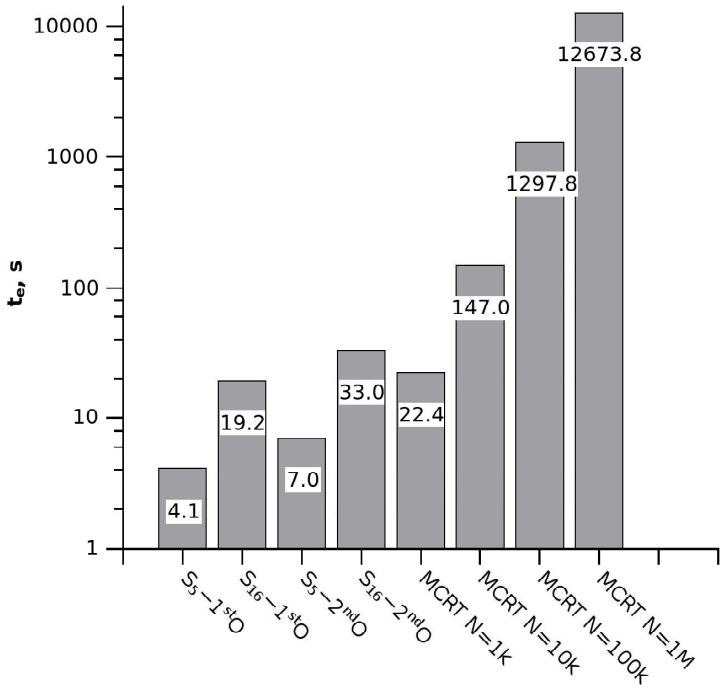

Figure 6.11: Execution time needed to obtain converged solution to radiation problem for considered models.

stage of MCRT model is executed only once. It needs to be emphasized, that in the case of temperature independent radiative properties, the ray tracing, i.e. the determination of radiation distribution factors (RDF) matrix, is also done only once per simulation. Thus, if the temperature distribution inside the domain changes, MCRT model can use previously calculated values of RDF matrix. This is not the case for DO model, for which the solution is found exclusively by iteratively.

Analysing the results, execution time of getting the radiative solution for a known temperature field, measured for all DO models is shorter than for almost all MCRT cases. The exception is MCRT $N = 1k$, which has execution time comparable to high order $S_{16} - 2^{nd}O$ model. Comparing pairs of models of similar accuracy, using MCRT instead of DO increased the solution time:

- 6 times for MCRT $N = 1k$ and $S_5 - 1^{st}O$,
- 8 times for MCRT $N = 10k$ and $S_{16} - 1^{st}O$,
- 39 times for MCRT $N = 100k$ and $S_{16} - 2^{nd}O$,
- 384 times for MCRT $N = 1M$ and $S_{16} - 2^{nd}O$.

This example shows the level of computational effort needed by MCRT method, even when run on coarse ortho-Cartesian mesh, which reduces the number of

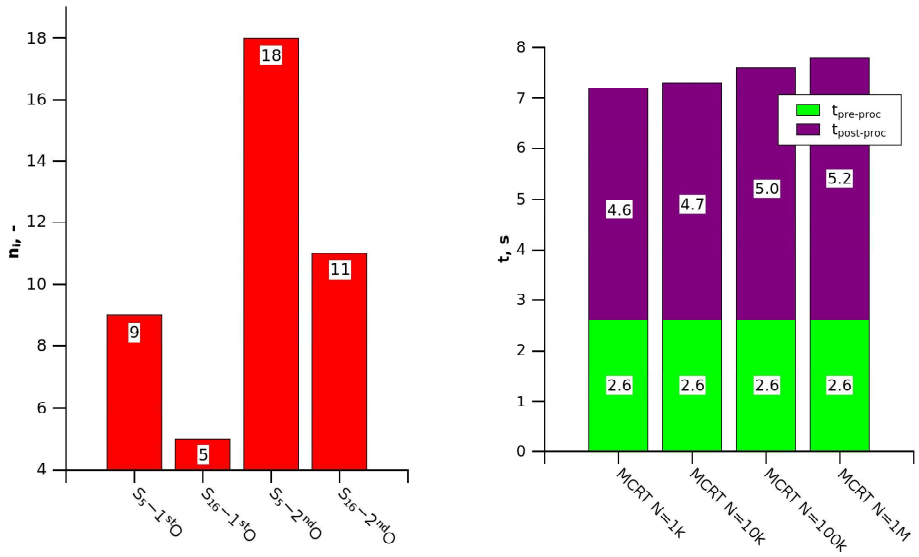

(a) Number of iterations till convergence at threshold $\epsilon = 1e - 6$.

(b) Time of pre- and post-processing.

Figure 6.12: Auxiliary data for DO and MCRT models.

cells from 100k to 3k.

Taking into the consideration MCRT models, the ray tracing procedure takes the majority of computational resources. The pre-processing stage takes the same time $t_{pre-proc} = 2.6\,s$ for all models, regardless the varying number of rays released. Similar situation is for the post-processing stage, for which $t_{post-proc} \simeq 5.0\,s$ (Fig. 6.12 (b)). Pre- and post-processing stages use rather small portion of the overall execution time, which varies from 34% for MCRT $N = 1k$, 5% for MCRT $N = 10k$, to 0.05% for MCRT $N = 1M$. The ray tracing time rises proportionally to the number of rays released from one element.

The number of iterations needed for DO models to achieve converged solution is shown in Fig. 6.12 (a). In general, models using second order spatial discretization converge slower than their first order counterparts. However, the better angular discretization, the lower number of iterations required to obtain the solution.

⋆ ⋆ ⋆

The purpose of this paragraph is to investigate under which circumstances MCRT model can give better performance than DO. The comparison of execution time between DO and MCRT models in the case of known temperature field proved the latter to be computationally expensive. However, known tem-

perature field across the domain is rarely the case. In most practical engineering problems the temperature distribution is determined iteratively by solving the energy equation coupled with flow, turbulence, presence of reactions etc. The radiation model is run typically once per 10 or 20 flow iterations. MCRT model can benefit from such situation, assuming the absorption coeffcient of gases and wall radiative properties are temperature independent. In this case, the ray tracing and pre-processing are done only once at the beginning of the simulation.

The radiation iteration n_r is understood as a one radiation model run, which is activated every 10 or 20 flow iterations and is not the same as the iteration within DO model. For the purpose of the analysis let us assume, that the time needed by DO model to achieve converged solution does not depend on the radiation iteration (n_r). The assumption is not always true. During the solution the temperature field converge to a certain state, thus the changes of the temperature field are the smaller the greater is the number of iterations. In such situation DO model should converge faster than reported for the fist radiation iteration. Such behaviour of the model is accounted for by introducing the speedup of convergence for DO model:

$$s_t^{DO} = t_{e,0}^{DO}/t_{e,n_r}^{DO}, \tag{6.2}$$

where t_{e,n_r}^{DO} is DO model execution time for a given radiation iteration n_r and $t_{e,0}^{DO}$ is DO model execution time for the first radiation iteration and is taken from Fig. 6.11. Since the speedup s_t^{DO} depends on the simulation, for the purpose of analysis its value was assumed to be equal to 1.25.

The total execution time of radiation model (i.e. the sum of radiation model execution time for all radiation iterations) for both DO and MCRT can be expressed by functions of the number of radiation iterations n_r:

$$t^{DO}(n_r) = n_r t_{e,0}^{DO}/s_t^{DO}, \tag{6.3}$$

$$t^{MC}(n_r) = t_{pre-proc} + t_{RT} + n_r t_{post-proc}. \tag{6.4}$$

The values of $t_{e,0}^{DO}$, $t_{pre-proc}$, t_{RT} and $t_{post-proc}$ are taken from Fig. 6.11 Fig. 6.12 to construct chart from Fig. 6.13.

The following pairs of models of similar accuracy were considered:

1. MCRT $N = 10k$ and $S_{16} - 1^{st}O$,
2. MCRT $N = 100k$ and $S_{16} - 2^{nd}O$,

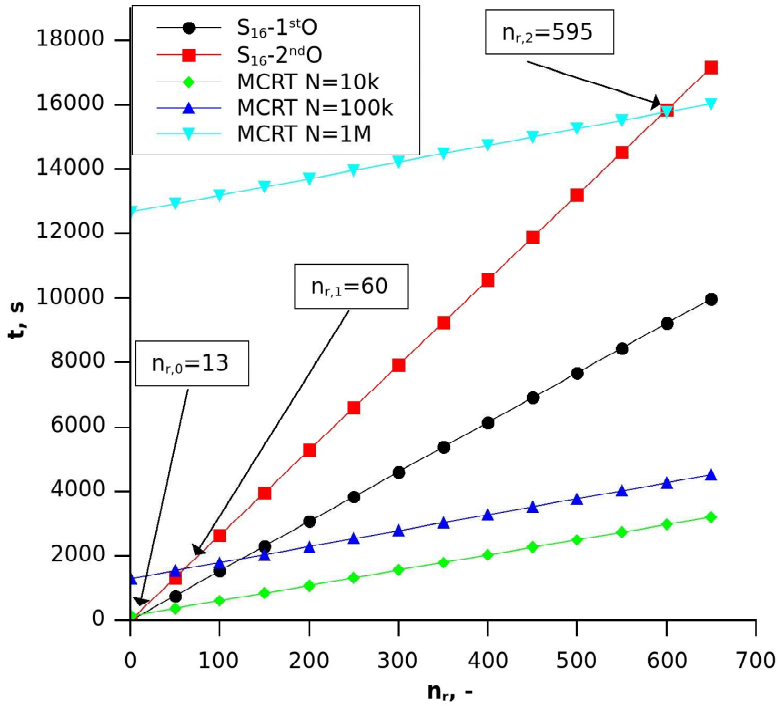

Figure 6.13: Total execution time of radiation model as a function of radiation iterations n_r. $n_{r,0}$ is the number of iterations at which MCRT $N = 10k$ becomes more efficient than $S_{16} - 1^{st}O$; $n_{r,1}$ corresponds to MCRT $N = 100k$ and $S_{16} - 2^{nd}O$; $n_{r,2}$ corresponds to MCRT $N = 1M$ and $S_{16} - 2^{nd}O$

3. MCRT $N = 1M$ and $S_{16} - 2^{nd}O$.

As has already been discussed in section 6.2.2 MCRT $N = 100k$ and MCRT $N = 1M$ models produce the results of comparable accuracy, however their execution time is much different.

Fig. 6.13 shows total execution time of considered models as a function of the number of radiation model iterations n_r. The intersection of the lines with vertical axis shows the time needed for preparing the model. For MCRT models the time covers pre processing and ray tracing stages. In the case of DO, those stages are not present.

The slope of the lines corresponds to the time needed by a given model to generate converged solution. For DO the slope depends strongly on the order of spatial discretization, contrary to MCRT, for which the slope is the same for all models. The most important conclusion, is that the time needed by MCRT models to generate subsequent radiation solutions is much less than for DO models. Comparing models of the similar solution accuracy, the minimum number of radiation iterations n_r justifying the usage of MCRT model instead of DO is

- $n_{r,0} = 13$ for MCRT $N = 10k$ and $S_{16} - 1^{st}O$,

- $n_{r,1} = 60$ for MCRT $N = 100k$ and $S_{16} - 2^{nd}O$,
- $n_{r,2} = 595$ for MCRT $N = 1M$ and $S_{16} - 2^{nd}O$.

It should be emphasized here, that MCRT model has not been professionally optimized, as is commercial DO Fluent. Thus, the results of computational time for MCRT model shown above, are expected to be better after code optimisation.

In the case of complex system modelling, involving the solution of flow and energy equations with the presence of turbulence, reactions, particles and radiation, the number of flow iterations needed to achieve converged solution is of order $10^3 - 10^4$. If the radiation transport is updated every 10 flow iterations, is gives the total number of radiation model runs of order $10^2 - 10^3$. Therefore, using MCRT model instead of DO can save the time especially for the cases, when

- the radiative properties of gases and walls are temperature independent,
- there is significant number of radiation iterations expected,
- the solution free of ray-effect is desired.

6.2.4 Local mesh refinement

This section shows the importance of ortho-Cartesian mesh resolution. The case of non-isothermal gray medium has been computed using locally refined mesh. All the cells whose centers lie inside bounding box defined by x-y-z points $p_{min} = \{-0.2, -0.2, 0.4\}$ and $p_{max} = \{0.2, 0.2, 1.2\}$ were divided into eight smaller cells. The refinement region conincides with the region of the highest temperature and is marked in Fig. 6.15 b).

Fig. 6.14 shows radiative heat source term on the axis of symmetry of the chamber for case without and with mesh refinement. Fig. 6.15 depicts coutourplots of the scalar variable on the symmetry plane.

The solution generated using locally refined mesh can be treated as more accurate. The differences in reported values of radiative heat soure term are $< 16\%$ and thus are signifficant. The reason behind it is that smaller volumetric cells better reflect local temperature profile. The higher the local temperature gradient, the denser should be the mesh. This observation coincides with conclusions from section 5.1.2, in which the ortho-Cartesian mesh resolution was changed and influenced the quality of the solution. However, in that case the mesh refinement was not local, but covered all the cells.

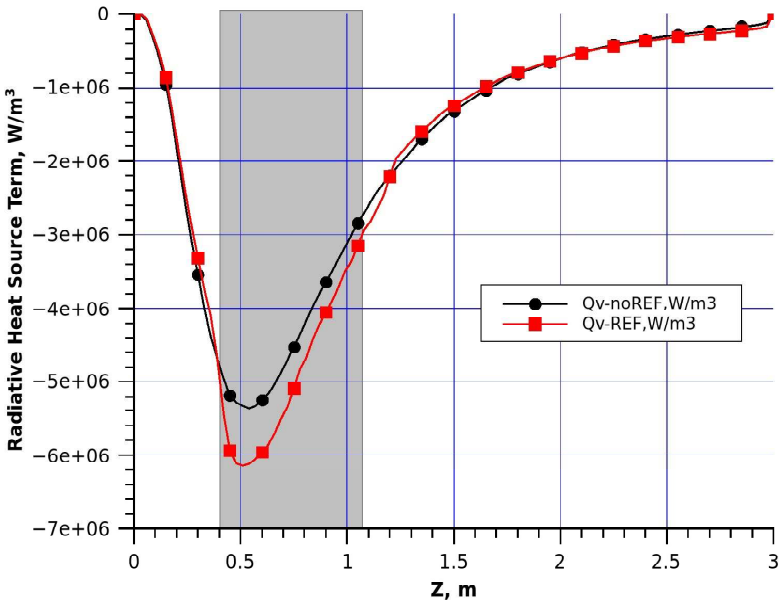

Figure 6.14: Values of radiative heat source term on chamber axis of symmetry. Gray rectangle marks the zone of local ortho-Cartesian mesh refinement.

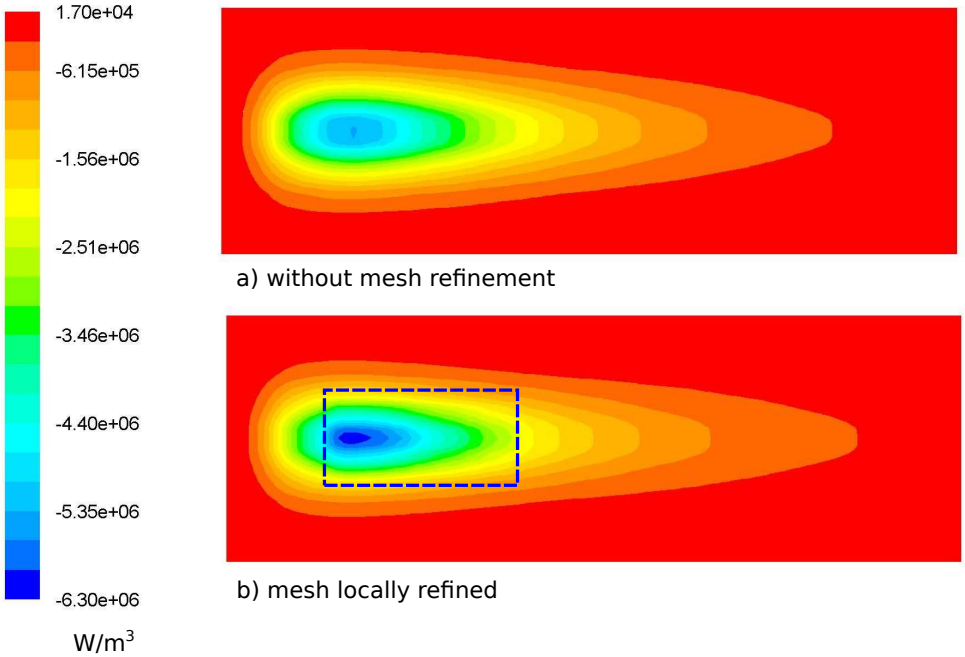

Figure 6.15: Contourplot of radiative heat source term at chamber plane of symmetry. Blue dashed rectangle marks zone of local ortho-Cartesian mesh refinement.

6.3 Absorbing/emitting medium - 0.5 MW test rig

This section covers the modelling of pulverized coal combustion in a test rig in two atmospheres: air and a mixture of CO_2, O_2 and H_2O. The process was modelled using OpenFoam with implemented MCRT model. In one case ortho-Cartesian mesh is refined to show what is the impact on the results. The simulation results were confronted with experimental results of analogous test cases done in a test rig installed at Institute of Power Engineering in Warsaw. Moreover, the results for air case were compared with solution generated by Ansys Fluent with DO model.

Pulverized coal combustion

Modelling of pulverized fuels combustion is a challenging task involving a number of phenomena like turbulence, species transport, interaction of gaseous phase with particulate matter, convective and radiative heat transfer, evaporation, devolatilization, chemical reactions etc. The ability of modelling such systems gives an engineer a tool that plays an important role in design process of combustion chambers, furnaces, burners and emission reduction devices. In combustion chambers and furnaces, where high temperature levels are present, radiation heat transfer mode is of great importance as it becomes a dominant one. In most of furnaces exploited in power engineering, combustion processes are held in air atmosphere. As a consequence, radiation models were suited for application to heat exchange in air. However, new combustion technologies emerged due to the latest environmental policy of developed countries, accordingly to which CO_2 emissions are to be significantly reduced. One of such technologies is oxy-combustion in which fuel is combusted in atmosphere comprising of CO_2, O_2 and H_2O gases. Thus, there is also a need for a modelling tool that is capable of dealing with radiative properties of modified atmospheres. The current section presents MCRT model applied to radiation modelling of pulverized coal combustion in both air and oxy atmospheres.

6.3.1 Test rig

The test rig is installed at Institute of Power Engineering in Warsaw (Fig. 6.16). It has a maximum thermal input of 0.5 MW and allows to:

Figure 6.16: Overall view of 0.5 MW test rig installed at Institute of Power Engineering in Warsaw used to test fuel combustion in various atmospheres.

- test new designs of pulverized and gaseous fuel burners in order to determine the ranges of operational parameters,
- examine the behaviour of various fuels during the combustion and co-firing,
- examine the combustion process in modified atmospheres consisting of O_2, CO_2, N_2, H_2O, SO_2, NO,
- test technologies for reducing NO_x emissions: SCR, SNCR,
- examine processes of ash accretion and its influence on metal erosion.

A schematic view of the combustion chamber is shown in Fig. 6.17. First section of the chamber has cylindrical shape of diameter $0.64m$ and length of $Z = 3.61m$. Second section widens to the diameter of $0.40m$ at the outlet, which is positioned at $Z_{max} = 4.10m$ from the front wall. The burner is installed along the main symmetry axis in the center of the front wall.

Gas temperature is measured with thermocouples TC_1, TC_2, TC_3 located at $Z = 0.33$, $Z = 1.80$ and $Z = 3.92m$ respectively. Moreover, concentrations of O_2 and CO are measured in the last location near chamber exit by FTIR analyser.

The rig is equipped with two inspection windows which are cooled with air or, in the case of oxy-combustion, CO_2. The front wall is cooled down by water piping system. Side walls are insulated by a layer of mineral wool which

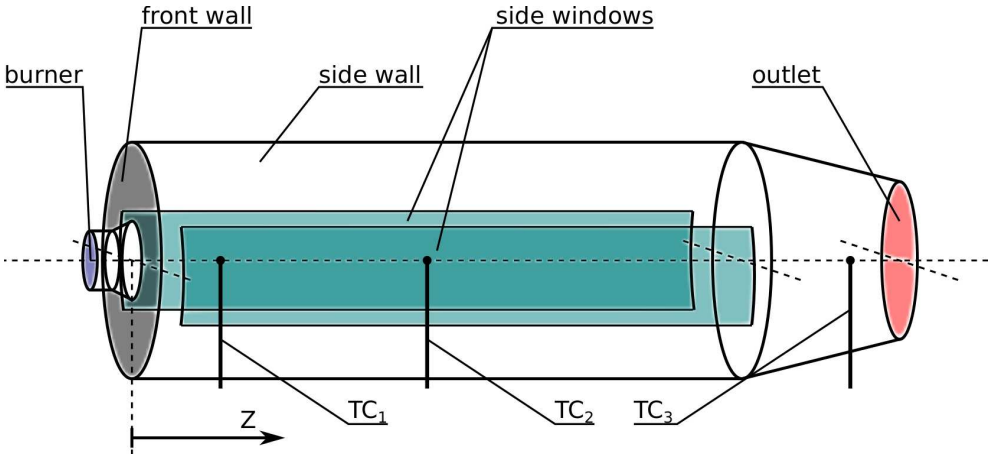

Figure 6.17: Schematic view of combustion chamber of 0.5 MW test rig equipped with two side windows for visual inspection and thermocouples TC_1, TC_2, TC_3.

is placed at a distance from the chamber outer shell. Thus, there exist a gap in between the chamber outer shell and insulation filled with air. In this way, side walls are also cooled by unmeasured amount of air from the room, where the rig is installed. It is known from experience that air escaping from the gap has temperature of $373 - 473K$.

Burner

During the tests a pulverized coal swirl burner designed in Institute of Power Engineering in Warsaw was used, a scheme and sub-model geometry of which are shown in Fig. 6.18 and Fig. 6.19.

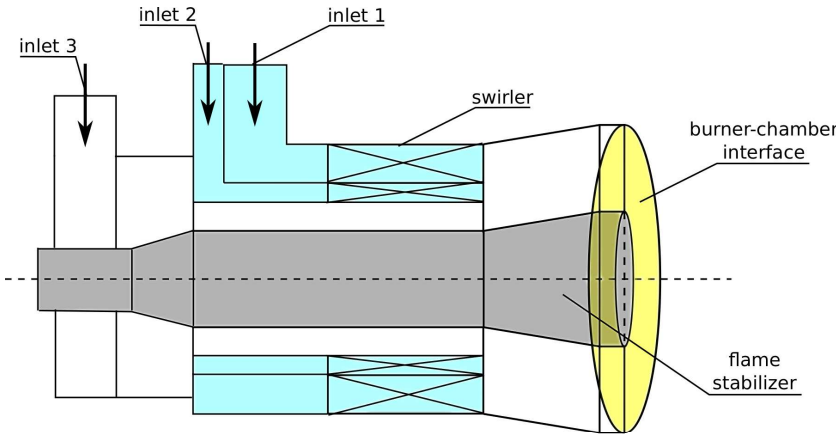

Figure 6.18: Schematic view of a swirl burner used in tests, design of Institute of Power Engineering in Warsaw. *inlet 3* - fuel supply, *inlet 1, inlet 2* - oxidant supply through swirlers having exit angle 50 degrees with respect to burner symmetry axis.

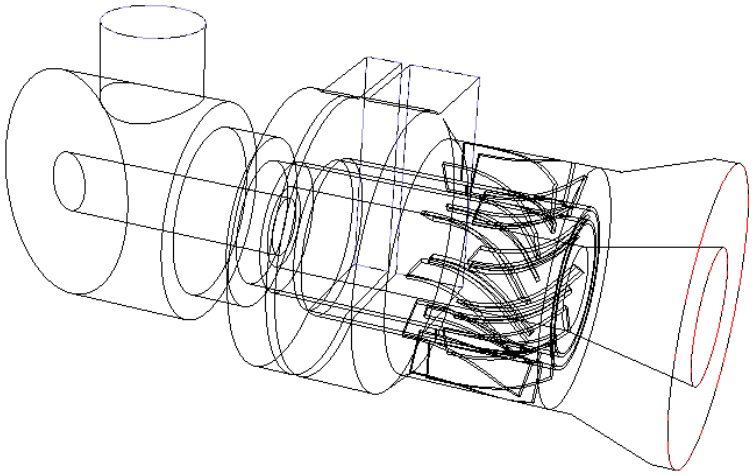

Figure 6.19: Sub-model of the burner.

Fuel is fed into the burner by *inlet 3*, while *inlet 1, inlet 2* are used to deliver oxidant - air or a mixture of O_2 and CO_2. The distribution of the flow between *inlet 1* and *inlet 2* is proportional to the inlet cross-section area. Oxidant passes through swirlers, after which its velocity forms an angle of 50 degrees with burner symmetry axis. High swirl results in large recirculation zone in the vicinity of the burner exit. Flame stability is ensured by the presence of a cone-shaped blunt body in the center of the burner. The sub-model of the burner is connected to the chamber by an interface.

6.3.2 Cases set-up

Cases

There are four cases of pulverized coal combustion analysed in the work, which are summarized in Tab. 6.6:

Table 6.6: Cases summary

Case Name	Atmosphere	CFD Package	Radiation Model
AIR-Fl	air	Fluent	Discrete Ordinates
AIR-OF	air	OpenFoam	MCRT
AIR-OFref	air	OpenFoam, refined mesh	MCRT
OXY-OF	$O_2 - CO_2$	OpenFoam	MCRT

Mesh

In order to account for a complex swirling flow with particles from a burner a sub-model has been used (Fig. 6.19). It allowed for significant reduction of the mesh size and computational time of the main model without compromising accuracy. The main model consisted of two meshes - CFD and uniform ortho-

Cartesian for ray-tracing. The *x-y-z* resolution of ortho-Cartesian mesh is 12 x 12 x 60. The summary of the meshes used in the simulation is given in Tab. 6.7.

Table 6.7: Mesh summary

Mesh	No. of cells	Avg. cell volume, m^3
Burner sub-model	433 k	6.7 e-9
Chamber, CFD	356 k	5.6 e-6
Chamber, ortho-Cart.	8640	1.5 e-4
Chamber, ortho-Cart. refined	9504	1.4 e-4

Case AIR-OFref used locally refined ortho-Cartesian mesh. The refinement region is located in the chamber in the visinity of burner exit, where the temperature gradients are expected to be the highest. It is bounded by a prism defined by two *x-y-z* points: $p_{min} = \{-0.16, -0.16, 0.05\}$, $p_{max} = \{0.16, 0.16, 0.28\}$, resulting in refinement of 6 x 6 x 3 cells. The cells marked for refinement are divided into eight smaller cells and yield 864 additional cells.

Coal Parameters

The test rig was fed with pulverized coal, a parameters of which are summarized in Tab. 6.8. The diameters of coal particles are sampled from Rosin-

Table 6.8: Proximate and ultimate coal analysis, test conditions

Parameter	Units	Value
Moisture	% wght.	4.2
Ash	% wght.	11.7
Volatiles	% wght.	33.7
HHV	kJ/kg	25619
LHV	kJ/kg	24582
C	% wght.	63.58
H	% wght.	4.28
O	% wght.	13.84
N	% wght.	1.03
S	% wght.	1.37

Rammler distribution. The parameters of the distribution were determined using data from sieve analysis: for mesh size 90 and 200 μm the retained mass of coal was 8.21% and 0.72% respectively.

In general, when a coal particle enters hot combustion chamber it is heated up and moisture evaporates. As the particle temperature increases, devolatilization occurs and finally char is oxidized. In the simulation evaporation is enabled, devolatilization rate is approximated by single kinetic rate model with pre-exponential constant $A = 2.0e5$ and activation energy $E = 4.9e7$. Coal

combustion is modelled using finite rate eddy dissipation model with a set of homogeneous and heterogeneous global reactions listed below.

R#1 $1.000Vol + 1.086O_2 \rightarrow 0.977CO + 1.890H_2O + 0.038SO_2 + 0.033N_2$,

R#2 $1.0CO + 0.5O_2 + 1.0H_2O \rightarrow 1.0CO_2 + 1.0H_2O$,

R#3 $1.0H_2 + 0.5O_2 \rightarrow 1.0H_2O$,

R#4 $1.0C + 0.5O_2 \rightarrow 1.0CO$,

R#5 $1.0C + 1.0H_2O \rightarrow 1.0CO + 1.0H_2$,

R#6 $1.0C + 1.0CO_2 \rightarrow 2.0CO$.

The exact definition of the reactions is possible together with parameters from Tab. 6.9. Data was taken from Toporov [118] and Chen [18] papers. Moreover,

Table 6.9: Parameters defining finite rate chemistry - coal combustion in air and oxy atmospheres [18, 118] A - pre-exponential constant, E - activation energy, β - temperature exponent

Reaction	A	E	β
R#1	1.60e6	5.06e7	1.00
R#2	5.42e9	1.26e8	0.75
R#3	5.00e12	1.00e7	1.0e7
R#4	0.00500	7.40e7	0.00
R#5	0.00192	1.47e8	0.00
R#6	0.00635	1.62e8	0.00

mass diffusion coefficients for reactions R#4, R#5, R#6 in air atmosphere are equal to 5.32e-12, 5.77e-12 and 1.72e-12 $s/K^{0.75}$ respectively [18]. In the case of oxy-combustion respective coefficients read 4.13e-12, 4.12e-12 and 1.69e-12.

Boundary Conditions

Tab. 6.10 presents the summary of the flows for two tested cases - AIR and OXY combustion conditions, while Tab. 6.11 scrutinizes boundary conditions for energy equation.

Total heat flux at *side wall* of the chamber has been estimated as a sum of contributions from convection and radiation at external surface of the wall:

$$q = q^r + q_c. \tag{6.5}$$

The temperature of the chamber outer shell and internal surface of the insulation are assumed to be 563 K and 440 K respectively. Emissivity of both

Table 6.10: Flows summary for test cases.

Flows	Units	AIR	OXY
Primary Oxidant	m_u^3/h	50	50
Secondary Oxidant	m_u^3/h	280	155
Side Windows Cooling	m_u^3/h	30	30
Coal	kg/h	47.9	47.9
Composition	Units	AIR	OXY
Primary Oxidant			
N_2	mole fr.	0.210	0.000
CO_2	mole fr.	0.000	0.800
O_2	mole fr.	0.790	0.200
H_2O	mole fr.	0.000	0.000
Secondary Oxidant			
N_2	mole fr.	0.762	0.000
CO_2	mole fr.	0.000	0.548
O_2	mole fr.	0.203	0.452
H_2O	mole fr.	0.036	0.000

Table 6.11: Temperature, heat flux boundary conditions.

BC Name	Units	AIR	OXY
inlet 1, 2	K	338	338
inlet 3	K	553	553
front wall	K	1000	1000
side wall	W/m^2	-4000	-4000
side windows	W/m^2	-55 500	-55 500

surfaces equals to 1.0. Thus, the radiative heat flux is:

$$q^r = \epsilon\sigma(T_{w1}^4 - T_{w2}^4) = 3571 W/m^2. \tag{6.6}$$

Air enters the gap between the insulation and outer shell of the chamber with temperature of 293 K and leaves having 493 K. The amount of air was not measured however, it is estimated to be 45 m_u^3/h. Having the necessary data, convective heat flux is

$$q_c = mc_p(T_{out} - T_{in}) = 441 W/m^2 \tag{6.7}$$

finally giving $q = 3571 + 441 W/m^2 = 4012 W/m^2$.

Total heat flux at *side windows* was difficult to assess, since there were no experimental data, that could explicitly be used. Therefore, the value of total heat flux has been found iteratively from the simulation. The value was modified to give the temperature at chamber exit close to the measurements,

with the condition, that values of other monitored parameters (eg. O_2 at exit, temperature at other measurement points) were also acceptable.

Radiation Model

In the case of MCRT model uniform ortho-Cartesian mesh of x-y-z resolution 12 x 12 x 60 is used. The number of rays traced from each surface and volume element is $N = 400$k.

DO model uses CFD mesh of size 356k elements. The angular discretization is $\phi = 4$, $\theta = 4$ yielding the order of the method equal to 16 (S_{16}).

The emissivity of coal particle surface is set to 0.9.

Surface emissivity of all chamber walls equals to 0.9 except for side windows, for which emissivity is 1.0. Walls are assumed to be diffuse and gray.

Radiative properties of gases in the case of air combustion are modelled by constant absorption coefficient of $1.0m^{-1}$. In oxy-combustion atmosphere the properties of gases filling-up the enclosure are spectral-dependent and are modelled using WSGG model with coefficients determined by G. Węcel [132].

6.3.3 Results

The results are organized in three sections. First section deals with pulverized coal combustion in air atmosphere computed by two models Fluent and OpenFoam - cases AIR-OF and AIR-Fl. Second section compares results of OpenFoam models for two atmospheres air and oxy $O_2 - CO_2$ - cases AIR-OF and OXY-OF. In the last part results of ortho-Cartesian mesh refinement are shown by comparison of AIR-OF and AIR-OFref cases.

Air Atmosphere

Tab. 6.12 shows comparison of the parameters measured during the test on the rig with the simulation results. Energy balance is summarized in Tab. 6.13.

Fig. 6.20 and Fig. 6.21 show plots of mean temperature at sections located at a distance from burner outlet and irradiation at centerline of the chamber respectively.

Contours of velocity magnitude, temperature, irradiation, O_2 and CO_2 mass fractions at the symmetry plane of the chamber are depicted in Figs 6.22, 6.23, 6.24, 6.25 and 6.26 respectively.

Table 6.12: Comparison of the parameters measured during the test with simulation results (cf Fig. 6.17).

Param.	Units	Rig Meas. AIR	Rig Meas. OXY	AIR-OF	AIR-Fl	OXY-OF	AIR-OFref
$T\|TC_1$	K	1618	1733	1650	1612	1689	1631
$T\|TC_2$	K	1550	1571	1553	1486	1525	1515
$T\|TC_3$	K	1273	1246	1280	1246	1208	1301
$O_2\|out$	vol.fr.	0.035	0.035	0.020	0.021	0.072	0.018
$CO\|out$	ppm	19	84	5	1	< 1	7

Table 6.13: Energy balance.

Name	Units	AIR-OF	AIR-Fl	OXY-OF	AIR-OFref
Heat of Reaction	kW	302.0	301.6	269.3	303.0
Side windows	kW	-84.4	-84.4	-83.0	-84.3
Radiative	kW	-80.4	-82.7	-80.8	-80.4
Convective	kW	-4.0	-1.7	-2.2	-3.9
Front wall	kW	-61.6	-68.2	-61.7	-62.5
Radiative	kW	-57.6	-65.4	-58.9	-58.4
Convective	kW	-4.0	-2.8	-2.8	-4.1
Side walls	kW	-25.5	-26.2	-25.2	-26.1
Convective	kW	-21.3	-23.3	-19.9	-21.5
Radiative	kW	-4.2	-2.9	-5.3	-4.6
Burner walls	kW	-1.3	0.0	-0.9	-1.8
Inlet 1	kW	0.03	1.3	0.2	-0.1
Inlet 2	kW	23.8	23.9	16.7	23.5
Outlet	kW	-150.3	-143.4	-111.2	-153.3
NET	kW	2.8	3.2	4.2	-1.6
NET/Heat of Rct.	%	0.9	1.1	1.6	-0.5

Temperatures predicted by both OF and Fluent models agree well with the rig measurements (cf. Tab. 6.12). The differences between measured and reported values are below 5%, with absolute differences being $\leq$ 32 K and $\leq$ 64 K for OF and Fluent respectively. Moreover, O_2 concentration at the outlet is close to the measured value for both models.

A good agreement between OF and Fluent models can be seen by comparing mean temperature at sections, shown in Fig. 6.20. The values corresponding to AIR-Fl are lower than those reported by AIR-OF by up to 5% excluding the close vicinity of the burner outlet, where the difference is higher. Also in this case, simulation results are close to the temperatures measured by thermocouples.

The values of irradiation along the chamber's main axis, shown in Fig. 6.21, correspond to the mean gas temperatures at sections. Here, the difference between models is 10% in the first part of the chamber located near the

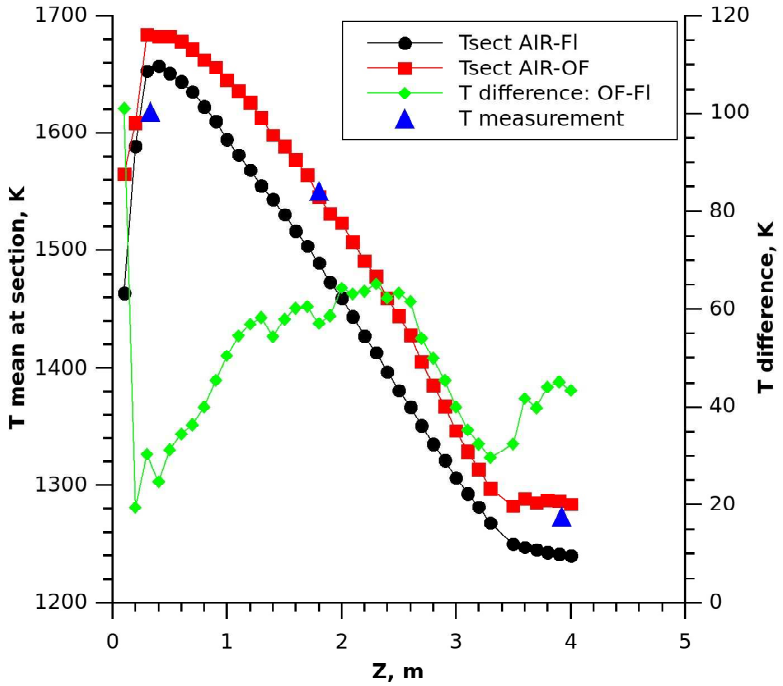

Figure 6.20: Mean temperature from chamber cross-sections located at distance Z from burner outlet and perpendicular to chamber axis compared to temperature measurements from the test rig.

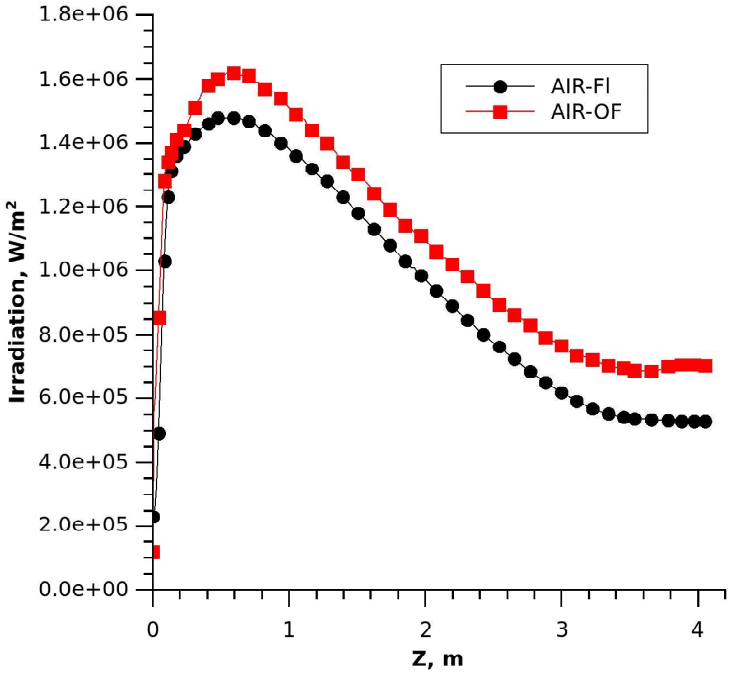

Figure 6.21: Irradiation distribution along the main axis of the rig.

burner and up-to 20% near the chamber outlet. This fact can explained by the discrepancies in both gas and wall temperatures. Average temperature of gas equals to 1496 K and 1447 K, and average wall temperature is 1472 K and

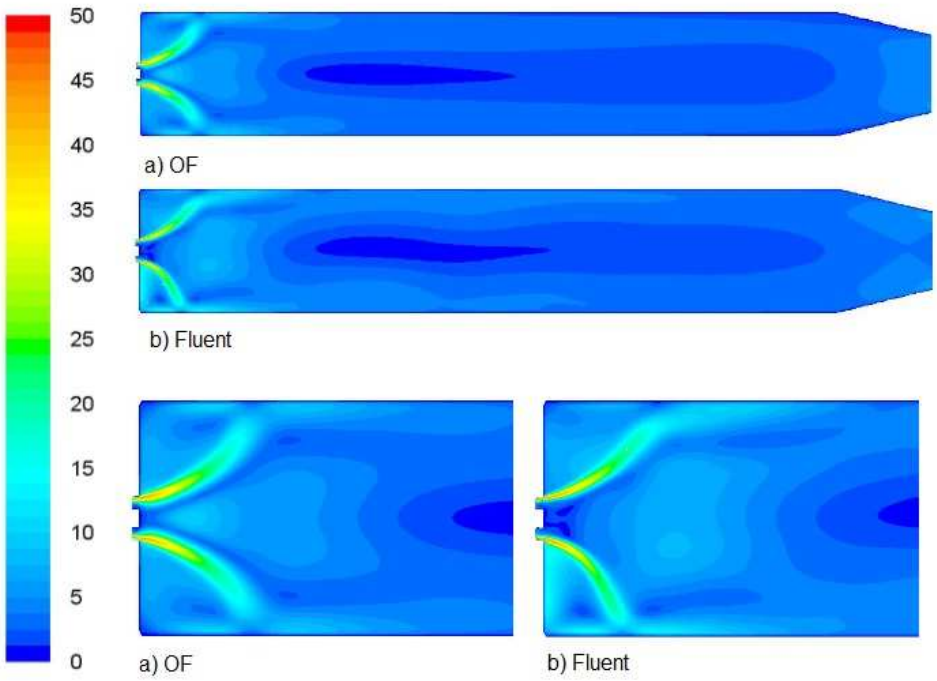

Figure 6.22: Comparison of velocity magnitude fields (m/s) for AIR-Fl and AIR-OF cases.

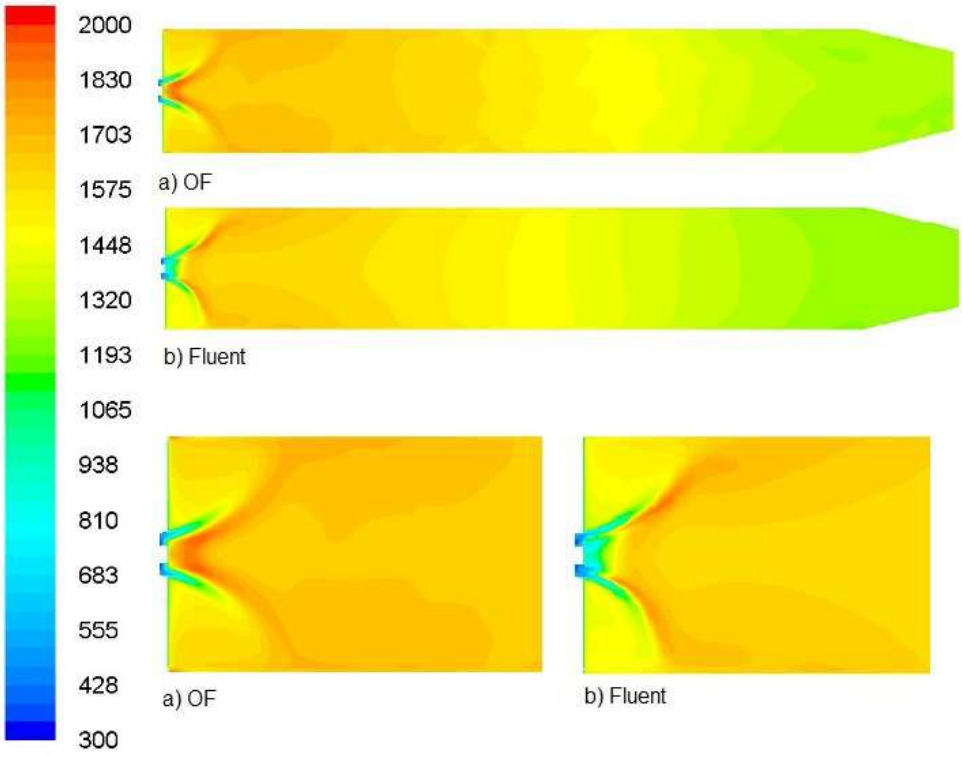

Figure 6.23: Comparison of temperature fields (K) for AIR-Fl and AIR-OF cases.

1410 K for AIR-OF and AIR-Fl respectively. Irradiation is proportional to T^4, thus 5% difference in temperatures can cause 20% difference in irradiation.

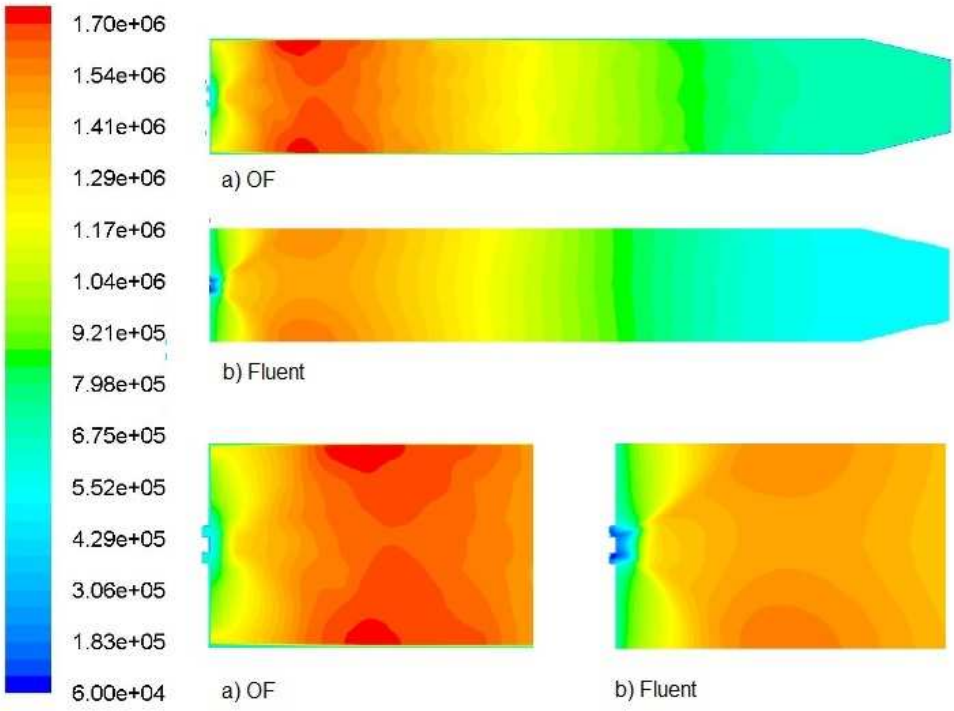

Figure 6.24: Comparison of irradiation fields (W/m^2) for AIR-Fl and AIR-OF cases.

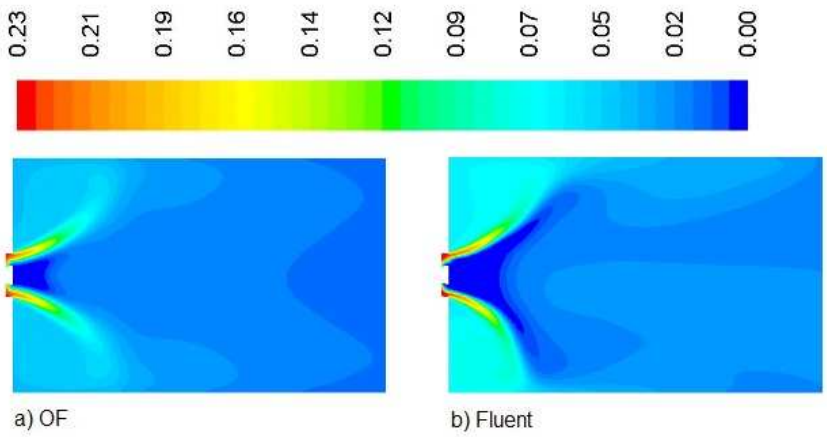

Figure 6.25: Comparison of O_2 mass fraction fields (-) for AIR-Fl and AIR-OF cases.

Heat of reaction yielded by both OF and Fluent models is the same to the accuracy of 0.2% (cf. Tab. 6.13). The values of total heat flux at individual surfaces of the chamber are also in good agreement. However, convective part of the heat flux calculated by AIR-OF model is higher than that of AIR-Fl for all considered surfaces.

An inspection of contour plots confirms the statement that the simulation results generated by OF and Fluent models are almost equivalent. The main differences between considered models can be seen in the vicinity of the burner.

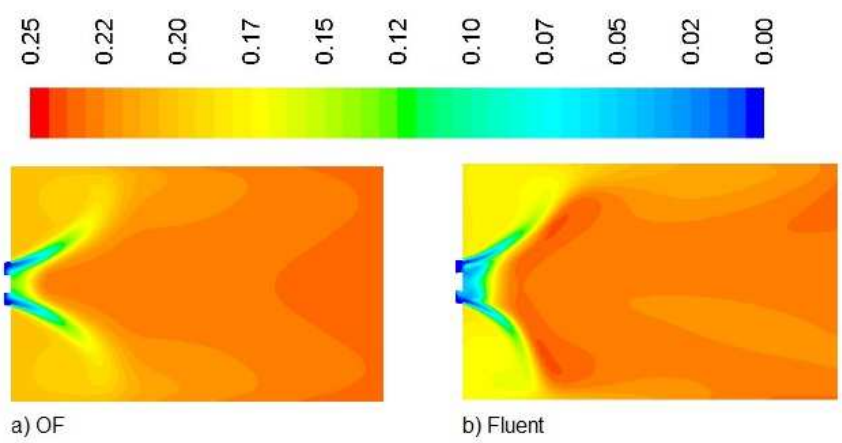

Figure 6.26: Comparison of CO_2 mass fraction fields (-) for AIR-Fl and AIR-OF cases.

In this region, the swirling flow coming out of the burner creates a recirculation zone, whose shape differs between OF and Fluent (cf. Fig 6.22). Not only the shape of this zone is a result of the flow pattern, but it is also influenced by other factors like devolatilization and evaporation rate, chemical reactions kinetics and turbulence. Thus the differences are also seen in contour plots of temperature, O_2 and CO_2 concentrations (Figs 6.23, 6.25, 6.26). Although special care has been put to set all the model parameters to be exactly the same in both models, there are some inherent differences between the models codes, that can create discrepancies. The detailed investigation of the differences between Fluent and OF codes, excluding radiation models, is outside the scope of the thesis.

Air and Oxy Atmospheres

This section covers comparison of OXY-OF and AIR-OF cases. Tab. 6.12 shows comparison of the parameters measured during the test on the rig with the simulation results. Energy balance is summarized in Tab. 6.13.

Fig. 6.27 and Fig. 6.28 show plots of mean temperature at sections located at a distance from burner outlet and irradiation at centerline of the chamber respectively.

Contours of velocity magnitude, temperature, irradiation, O_2 and CO_2 mass fractions at the symmetry plane of the chamber are depicted in Figs 6.29, 6.30, 6.31, 6.32 and 6.33 respectively.

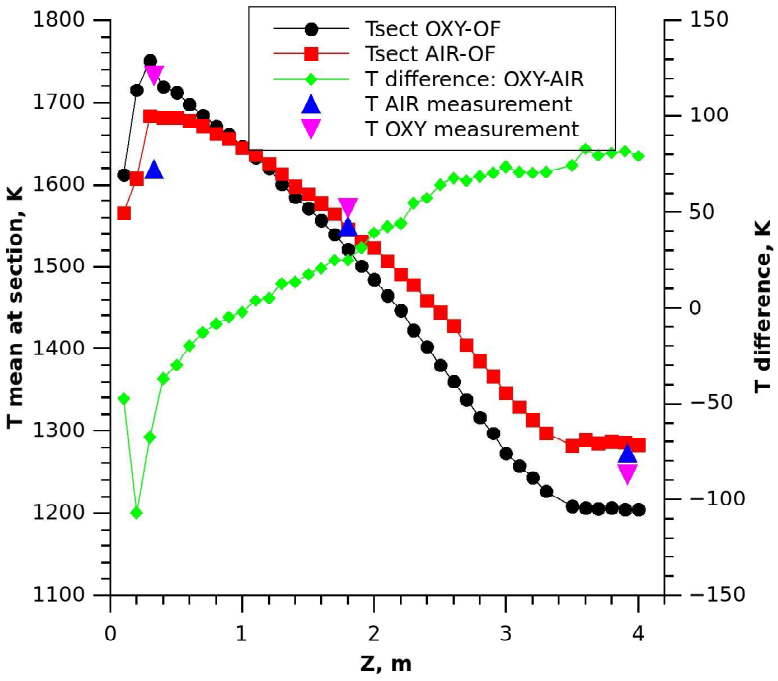

Figure 6.27: Mean temperature from chamber cross-sections located at distance Z from burner outlet and perpendicular to chamber axis compared to temperature measurements from the test rig.

Temperature reported by simulations in locations where thermocouples were installed shows very good agreement with measurements at the test rig in both AIR-OF and OXY-OF cases (cf. Tab. 6.12). The differences between measured and predicted values for respective cases are below 3%.

Due to the low amount of recirculated CO_2 in gases entering the combustion chamber and their higher density, the velocities at the burner exit are lower in the case of OXY-OF than in AIR-OF.

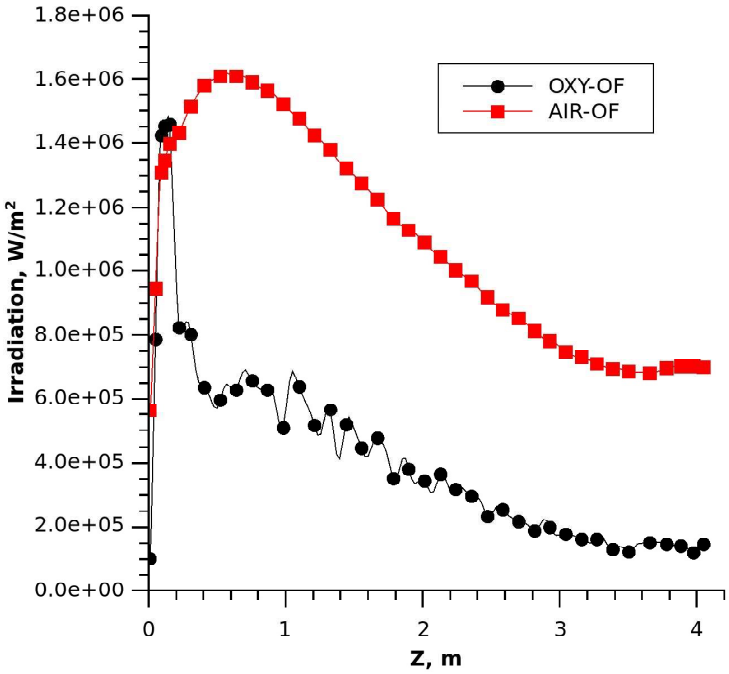

Figure 6.28: Irradiation distribution along the main axis of the rig.

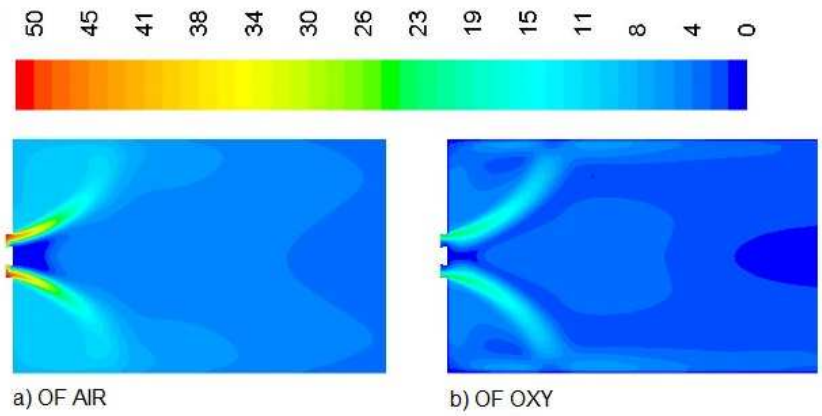

Figure 6.29: Comparison of velocity magnitude fields (m/s) for OXY-OF and AIR-OF cases.

In the case of OXY-OF mole fraction of O_2 resulting from simulation (7.2%) significantly differs from measured value of 3.5%. Reported value of CO in exhaust gases is ≤ 1 ppm (measured value 84 ppm), however there is unburned char in ash escaping the chamber. The fact that not all combustibles entering the chamber are completely burned is also seen in the value of heat of reaction (Tab. 6.13). The value of 269.3 kW is lower than for AIR-OF case by 32.7 kW. The discrepancies between O_2 values from OXY-OF and measurements are attributed to the kinetics of coal combustion chemistry. Constants for heterogeneous reactions were taken from open literature (cf. Tab. 6.9) for arbitrary

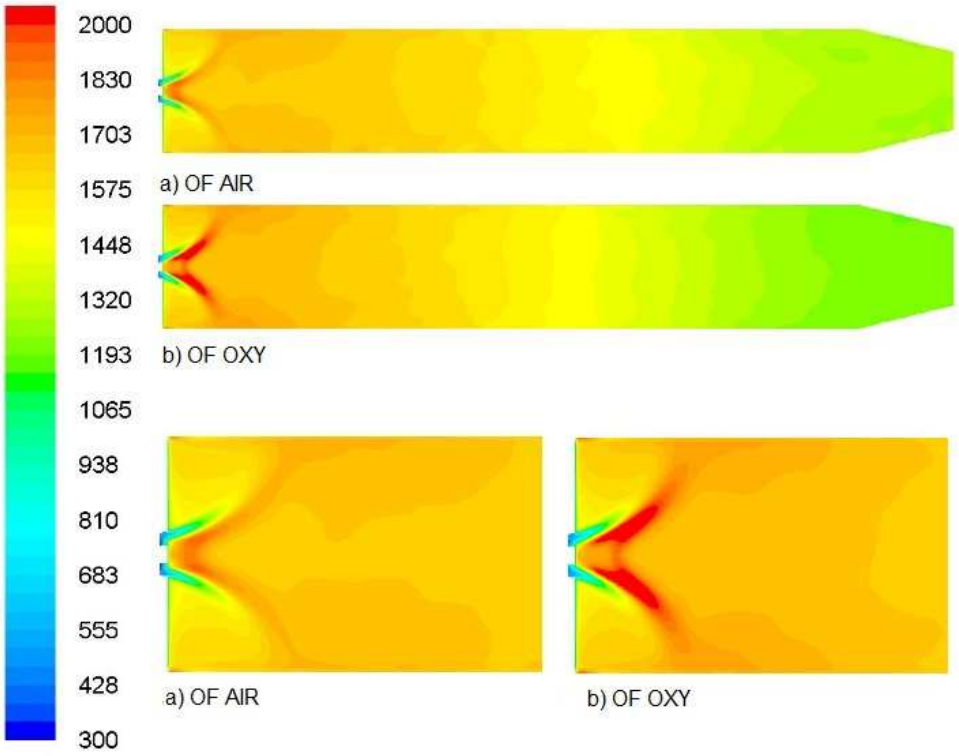

Figure 6.30: Comparison of temperature fields (K) for OXY-OF and AIR-OF cases.

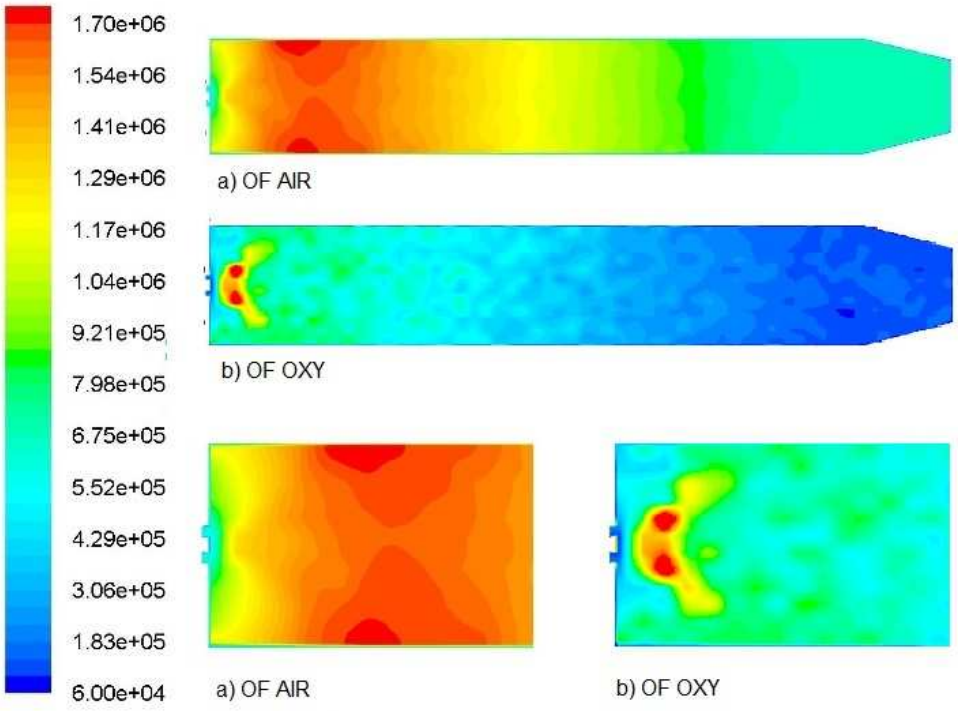

Figure 6.31: Comparison of irradiation fields (W/m^2) for OXY-OF and AIR-OF cases.

coal. Therefore, those values should be reconsidered and modified in order to achieve good agreement of simulation and test.

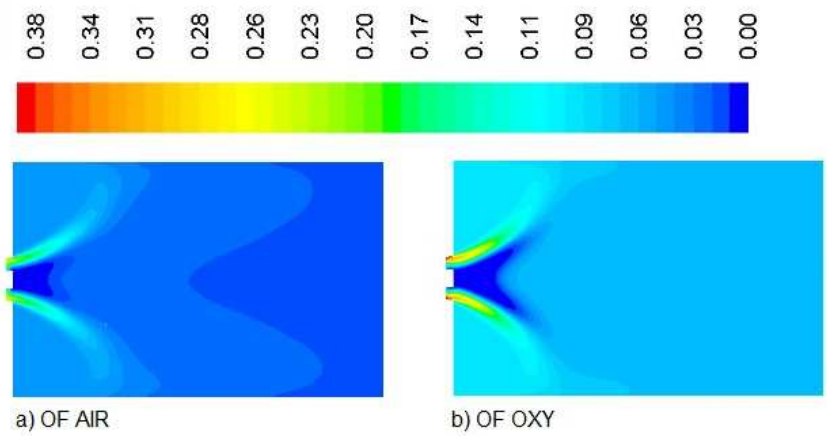

Figure 6.32: Comparison of O_2 mass fraction fields (-) for OXY-OF and AIR-OF cases.

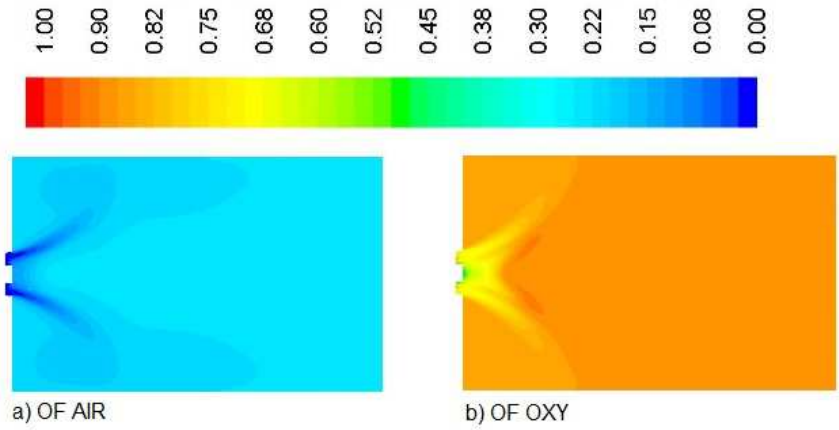

Figure 6.33: Comparison of CO_2 mass fraction fields (-) for OXY-OF and AIR-OF cases.

By comparing average temperature at sections (Fig. 6.27) it can be noted, that OXY-OF case has higher temperatures than AIR-OF case near the burner outlet and lower in the remaining part of the chamber. This observation is consistent with measurements and also can be seen in respective contourplots in Fig. 6.30. It should be noted that the values of temperature predicted by model for oxy-combustion are lower than measured values by up to 46 K (Tab. 6.12). This situation is expected to improve as soon as proper combustion kinetics is employed.

The values of irradiation along the centerline of the chamber (Fig. 6.28) are significantly lower in the case of OXY-OF than in AIR-OF. The reason behind such situation is that OXY-OF case has lower temperatures (cf. Fig. 6.27). Moreover, in OXY-OF case there should be higher equivalent absorption coefficient, however this is not evident, since in WSGG model the medium is

treated as a sum of gray gases. The full overview of the differences in irradiation fields is seen in Fig. 6.31. It can be noted that irradiation corresponds to the temperature field depicted in Fig. 6.30. For OXY-OF case the maximum values of irradiation occur in the vicinity of the burner, where the maximum temperature is also present.

It is also evident that OXY-OF case is much more sensitive to the statistical nature of Monte Carlo method, since the irradiation field has visible oscillations throughout the domain. In the case of OXY-OF, spectral properties of gases are modelled using WSGG approach, in which an irradiation field is a sum of irradiations resulting from each gray gas. In the equation describing irradiation for a specific gas there is a division by a sum of gas and particle equivalent absorption coefficients. Since not all of gases from a mixture have high absorption coefficient (a neutral gas has absorption coefficient equal to 0) and not all domain is covered by particles, there are cells in which there is a division by a close-to-zero term. In those cells, the value of irradiation is computed less accurately. The solution is to trace more energy bundles from a surface or volume element, reducing the variation in q_r and q_v terms also present in the equation. However by doing so, it is clear that the computational time quickly becomes a bottle-neck. In the present study 400k of bundles were traced for each of 5 gray gases considered in WSGG model, giving the total number of rays traced close to $16 \cdot 10^9$. The problem of the quality of the solution is a known issue. In the case of optically thin media (as it is the case for some of gray gases from WSGG model) the formulation of Monte Carlo model presented in the thesis is not optimal one. In the case of optically thin medium it is preferable to use energy-partitioning formulation to achieve good compromise between the solution quality and computational time (cf. Sec. 3.6). Besides the issue described above, the presented model is capable of generating results with good quality.

Air - Mesh Refinement

In the following the influence of ortho-Cartesian mesh refinement onto the results is investigated. Therefore, two cases of pulverized coal combustion in air are compared: AIR-OF and AIR-OFref, the second having the locally refined mesh.

The location of the mesh refinement zone corresponds to the region of high temperature gradients occuring in the vicinity of burner outlet. Higher resolution of the mesh allows for better accuracy of the model, because the

gas temperature, particle emission term and particle equivalent absorption coefficient in ortho-Cartesian cell are averaged from lower number of CFD cells.

Tab. 6.12 shows comparison of the parameters measured during the test on the rig with the simulation results. Energy balance is summarized in Tab. 6.13.

Fig. 6.34 and Fig. 6.35 show plots of mean temperature at sections located at a distance from burner outlet and irradiation at centerline of the chamber respectively. The mesh refinement region is marked with blue rectangle.

Contours of temperature and irradiation at the symmetry plane of the chamber are depicted in Figs 6.36 and 6.37 respectively.

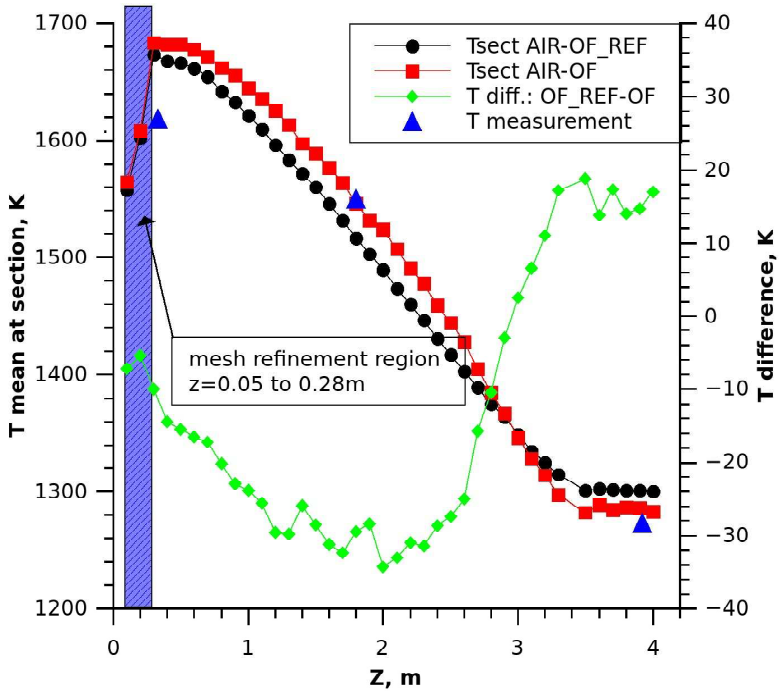

Figure 6.34: Mean temperature from chamber cross-sections located at distance Z from burner outlet and perpendicular to chamber axis compared to temperature measurements from the test rig.

The comparison of mean temperatures at chamber cross-sections between AIR-OF and AIR-OFref cases (cf. Fig. 6.34) shows the differences being $< 2\%$. Such differences are more attributed to the convergence of the model rather than mesh refinement. Moreover, looking at temperature contourplot (Fig. 6.36) local temperatures in the refined region do not differ significantly.

Analogously, the reported values of irradiation are almost identical (cf. Figs 6.35 and 6.37), the differences being $< 7\%$.

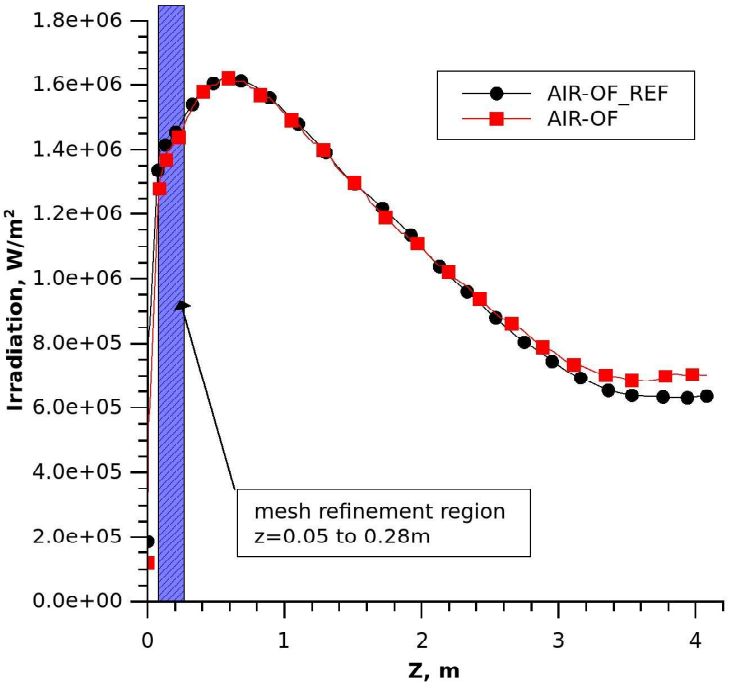

Figure 6.35: Irradiation distribution along the main axis of the rig.

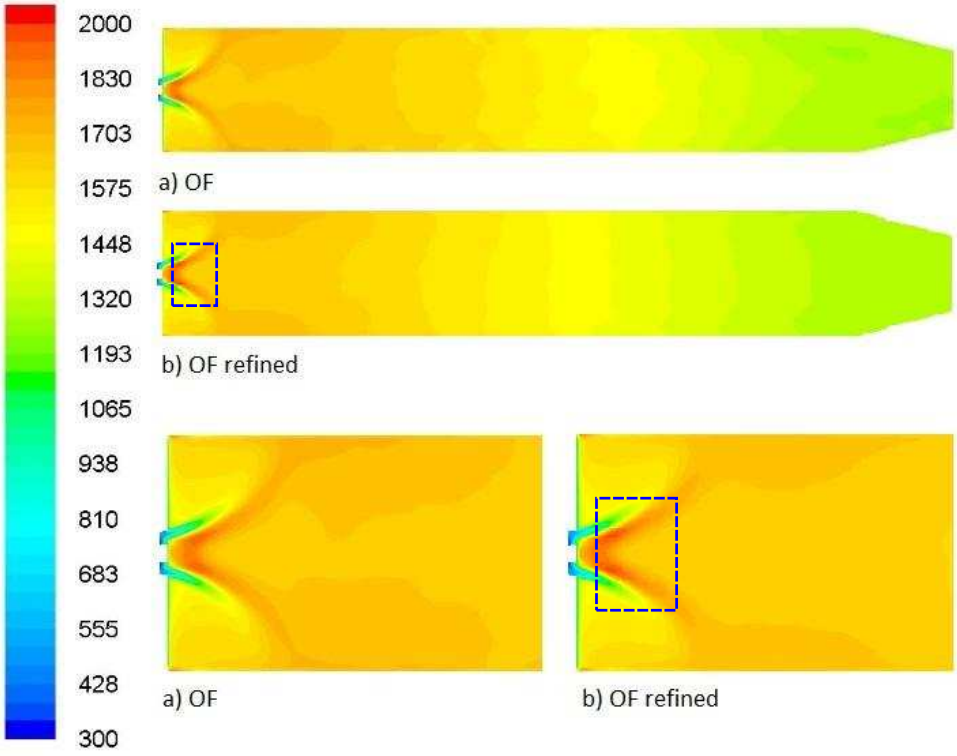

Figure 6.36: Comparison of temperature fields (K) for AIR-OF and AIR-OFref cases. Refinement region marked by blue rectangle.

In section 6.2.4 the mesh refinement showed significant impact on the results, however this is not the case for current example. The reason behind it is the nature of the temperature field. The temperature field for the case

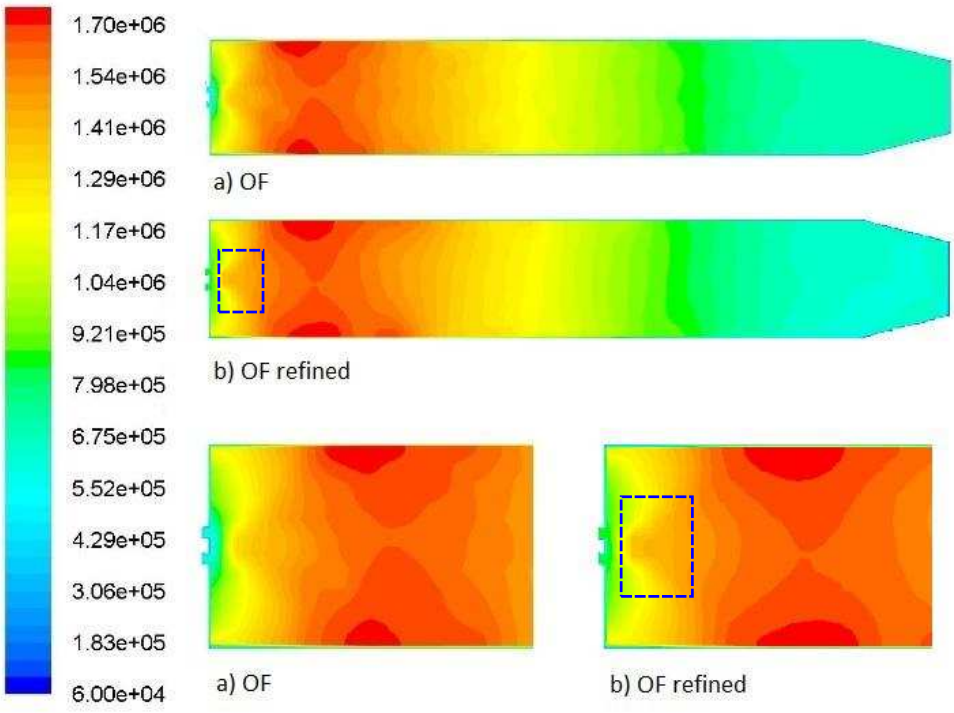

Figure 6.37: Comparison of irradiation fields (W/m^2) for AIR-OF and AIR-OFref cases. Refinement region marked by blue rectangle.

presented in section 6.2.4 was given by a function of position and was constant. In the case of 500kW combustion chamber, the temperature field is a result of iterative calculations of conjugated heat transfer problem. Thus, even if the zone of high temperature gradient is covered by mesh refinement, the temperature field can change after some iterations to the state similar to that before mesh refinement. Secondly, the case of pulverized coal combustion is much more complicated than non-isothermal combustion chamber, because of the presence of reacting particles. The radiative solution is affected not only by temperature, but also by particle absorption and emission terms. Therefore, even if the temperature field shows high local gradients, suggesting the location of mesh refinement, it can be desceptive because of the opposite gradient of particle emission terms. The presence of particles can cause more uniform solution of radiative analysis than expected judging just from the temperature field. In another words, the net radiative heat flux from a cell filled with cold gas and hot particles can be the same as from the cell filled with hot gas only (as is suspected to be the case in the vicinity of burner exit).

Since the cases with and without mesh refinement give results with only small differences, it can be concluded, that the ortho-Cartesian mesh resolution is adequate. It is also an evidence that the radiation problem can be solved on much coarser mesh than CFD mesh without significant impact on the results.

Chapter 7

Concluding remarks

7.1 Thesis summary

The thesis deals with development, validation and practical usage of Monte Carlo Ray Tracing model applied to radiative heat transfer in absorbing, emitting media.

MCRT technique in its application to radiative heat transfer has common features with Hottel's zonal method. In both methods the domain is subdivided into a finite number of surface and volume elements. Within each element the surface or medium parameters like temperature, surface emissivity or absorption coefficient of the medium have uniform distribution. In the case of formulation used in the thesis, the results of radiative heat transfer, radiative heat flux at walls and radiative heat source or sink in medium, are calculated using so called radiation distribution factors (RDFs). The computation of RDFs is the most time consuming part of MCRT. In the case of Monte Carlo in its standard ray tracing variant, values of RDFs are estimated by *tracing the rays*, i.e. emitting a large number of rays from a given element and registering the elements in which absorption takes place. Random sampling, a feature characteristic for Monte Carlo method, is used to determine the fate of each ray. Thus the parameters and events specific for the ray like its emission direction, absorption-free path, absorption at wall are determined by random sampling from known probability density functions.

Contrary to Discrete Ordinates, a method widely used in engineering applications, MCRT can deal with boundaries of special type (specular reflections, collimated beams) and complex material properties (non-diffusive surfaces, anisotropic radiation). This is the only method capable of dealing with radiative heat transfer problem of arbitrary level of complexity. Moreover, MCRT

is not prone to *ray effect* and *false scattering* as it is the case of DO and is capable of generating benchmark solutions. Stated above features make MCRT a promising tool for solving radiative heat transfer problems. However, the method has some drawbacks that limit its applicability.

The main drawback of MCRT is the need for computational resources. During the solution process, a huge number of rays (typically of order 10^5, 10^6) is emitted from each element and each of those rays has to be followed till absorption. In the case of conjugate heat transfer simulations, there is a need to simultaneously solve flow, turbulence, energy and radiation transfer equations. Thus, the mesh has to be dense enough to allow for dealing with small vortex structures characteristic for turbulent flow. Implementation of MCRT method to dense meshes used for CFD purposes, results in prohibitively long computational times. This fact is the reason why the method has not been used widely in engineering applications. Moreover, it is not present in commercial CFD packages, except for its basic version of surface-to-surface radiation model for determination of view factors.

The stated above reasons have driven the subject and goal of the thesis, i.e. to improve the performance of MCRT method, so that it would be capable of dealing with conjugate heat transfer problems in times acceptable from the engineering point of view.

The main outcome of the thesis was the development of an efficient system for ray tracing utilizing coarse, ortho-Cartesian, structured meshes, which are independent of CFD mesh and on which the radiation problem is solved. The idea of using coarse, structured meshes was based on research of G. Węcel and R. Białecki [128, 129, 131], who used them in their work on boundary element method. G. Wecel observed that BEM yields accurate results even for coarse discretization of the domain. This fact was explained by the long distance interactions occurring in radiative heat transfer, which tend to flatten temperature gradients making dense mesh not necessary. Within the current thesis, the solution of radiation heat transfer is interpolated from ortho-Cartesian mesh onto CFD mesh using tri-linear interpolation scheme. The code is written in C++ and is as an add-on to open-source CFD package OpenFOAM.

The ray tracing system developed within the current thesis incorporates parametric non-uniform rational basis spline surfaces for the description of boundaries. It can also deal with shadow zones. To the best knowledge of the author, there was no ray tracer using NURBS surfaces employed in the field of radiative heat transfer modelling. By using NURBS surfaces the domains of

complex shapes can be easily approximated and their mathematical description is compact, saving computer memory and transfer time. The main drawback of employing NURBS surfaces is the ray-surface intersection algorithm - much slower in comparison with the basic ray-triangle intersection. It was estimated that the speedup resulting from usage of ortho-Cartesian mesh is 40 to 90 depending on the case, without significant impact on the accuracy. However, it should be emphasized that the code is not professionally optimized, thus the reported values of speed-up are believed to be substantially higher. The higher the difference between ortho-Cartesian and CFD cells, the higher the speed-up.

An important step towards better efficiency of MCRT method was the implementation of parallel computing inside the code of ray tracer using OpenMP library. The logic behind employing the parallelization procedure is that tracing of a single ray does not need any information from other rays. In other words, rays can be traced independently. The code upgrade allows to run ray tracer procedure, the execution of which is the most time-consuming part of the whole code, on multiple threads on shared memory machines. In general, the speedup depends on the machine, however the test case run on eight-processor 2x4 Intel Xeon 2.33 GHz machine with eight threads showed speedup of 6.

Due to relatively simple mathematical description of MCRT model, the level of complexity of physics it describes can be gradually elevated with moderate programming effort. The model developed in the thesis has few versions, each of which can be chosen to suit a specific problem needs. Basic variant of the model, deals with radiative heat exchange between gray surfaces. Subsequently, it has been upgraded to account for the presence of optically active gray medium, solid particles suspended in the fluid and, finally, non-gray medium properties.

In the case of non-participating medium MCRT model developed within the thesis is capable of dealing with specular and diffuse surfaces. Additionally, it accounts for the presence of shadow zones i.e., when emitting and absorbing surfaces do not lay on their *line-of-sight*.

The presence of solid particles suspended in the medium is taken into account in MCRT model. The particles are assumed to be ideal spheres that emit and absorb radiation. However, during the tracing the ray can not be scattered by them. Instead, the particles are seen by the ray in the form of a gas having equivalent absorption coefficient. The equivalent absorption coefficient is proportional to the concentration and section area of the particulates and it is

being added to the gas absorption coefficient, resulting in higher ray absorption probability. The formulation allows the particles to have different temperature than surrounding medium, contrary to the approach found in literature [121]. This fact improves the accuracy of the model in the case of pulverized coal combustion, in which coal particles temperature significantly differs from the gas.

Non-gray medium properties are modelled using WSGG approach which guarantees accuracy and reasonable computing times needed in engineering applications. The coefficients of WSGG model has been determined by G. Wecel [130, 131, 132, 133] using HITEMP 2010 spectroscopic database to model properties of $O-2$ - CO_2 mixture encountered in oxy-combustion systems.

In order to be certain the developed model produces unbiased results it has been verified against available data. For non-participating medium, the verification of the model has been done using two cases. First, was to compute the value of a view factor and compare the result to the exact expression. Second - to calculate radiative heat fluxes at walls of the cube and confront the solution with S2S Fluent model. In both cases MCRT solution agreed very well with benchmarks. The version of MCRT model dealing with absorbing and emitting gray medium has been verfied against data generated by Radiarare Network of research institutions. Two benchmark problems have been solved. MCRT model results agreed to those obtained by other methods (MC, DO, DT, BEM), yielding the differences $\leqslant 1.5\%$. The last test has been conducted to prove the non-gray medium properties are implemented in proper manner. MCRT solution was found to follow benchmarks presented in G. Wecel paper [132]. The differences of reported radiative heat source term were $\leqslant 5\%$ while the predictions of radiative heat flux at wall were accurate to $\leqslant 9\%$. The main contributor to the discrepancies was different mesh resolution, causing flattening of the temperature profile peak.

The developed version of MCRT for non-participating medium has been demonstrated on the example of pit furnace conjugated heat transfer problem. The results were compared with Fluent S2S model showing very good agreement and proving the model can be successfully applied to geometries of complicated shapes with *shadow zones*.

The benefits of using MCRT model to gray participating medium has been shown on the example of cylindrical combustion chamber by comparison to Fluent DO model. Contrary to MCRT, DO is known to be prone to *ray* and *false scattering effects* due to angular and spatial discretization of RTE respec-

tively. It was shown, that to mitigate the solution deterioration due the the presence of those effects, both angular and spatial discretication orders have to be increased in DO model. The quality of the solution generated by the highest order DO model ($S_{16} - 2^{nd}O$) was similar to MCRT model with 100k rays emitted from one element.

In terms of performance, in the case the temperature field is given, DO $S_{16} - 2^{nd}O$ was 40 times faster than MCRT with 100k rays. Looking only at this result, one can conclude that DO is more efficient, however it is not always the case. For conjugate heat transfer problems, the temperature field is found in iterative procedure, which involves flow, energy and radiation transfer equations updates. The number of radiation field iterations can be very high ($10^2 - 10^4$), however it strongly depends on case. This fact reveals a field of application of MCRT model, in which it can be better in terms of performance than DO. The most time consuming part of MCRT is the determination of RDFs matrix. It is done in the pre-processing stage and needs to be run only once, provided the radiative properties of medium and walls are independent of temperature. Once determined, RDFs matrix is used to determine radiative heat fluxes at walls and heat sources in medium by substitution into equations. It was found that after 60 radiation iterations, the total computational time spend on MCRT model with 100k rays emitted from one element is less than computational time of DO $S_{16} - 2^{nd}O$. Thus, in application to conjugate heat transfer problems, MCRT can be an interesting alternative to DO. It should be emphasized here, that the code of MCRT model has not been optimized to give the best performance, as it is the case of Fluent commercial code. Thus, it can be expected, that there is a field for further improvement of the performance.

The concept of ortho-Cartesian mesh hierarchy was tested using this example. The mesh was locally refined in the region of highest temperature gradients. The reported differences in results were significant and $< 16\%$.

OpenFoam code together with MCRT radiation model has been applied to pulverized coal combustion in a test rig of maximum thermal input of 500 kW installed in Institute of Power Engineering in Warsaw. Simulations included combustion in air atmosphere, where the medium was treated as a gray gas of constant absorption coefficient. In this case the results of OF with MCRT model were validated against both Fluent DO solution and experimental results. The results shown very good agreement to analogous result generated by Fluent code and to measured parameters (temperature, O_2 at the outlet). The differences in temperature predictions were $\leqslant 5\%$. The version of MCRT

code with WSGG model allowed to take into account spectrally dependent gas properties in the simulation of coal combustion in $CO_2 - O_2$ mixture. The results were confronted with measurements on the test rig yielding very good temperature matching with differences $\leqslant 3.5\%$. The simulation predicted higher O_2 concentration in exhaust gases and higher unburned char content in ash escaping the chamber. The discrepancies were contributed to the kinetics of coal combustion chemistry. Reaction rates constants have been taken from open literature for coal of properties different from coal used during the test on 500 kW rig. An interesting observation is that in the case of WSGG model there is no need to recompute RDFs matrix, provided there is no significant changes in particles, H_2O and CO_2 concentrations throughout the domain. In WSGG model absorption coefficients of the gray gases comprising the model depend only on the H_2O and CO_2 concentrations. Temperature variations are taken into account in weighting coefficients, which can be updated independently. This observation can save a lot of time, since computing values of RDFs matrix is the most time-consuming part of the method.

In the case of combustion in air atmosphere, the ortho-Cartesian mesh was locally refined in the vicinity of the burner, where the temperature gradients are the highest. The comparison of the results shown no significant differences between models with and without mesh refinement. It is explained by the presence of hot coal particles in the relatively cold air coming from the burner. Thus, even if the mesh was refined, it did not appreciably influence the radiative energy emitted in each cell. In this case it has been proven, that using coarse mesh in radiation heat transfer problem is good assumption and it has not lowered the quality of the solution.

The thesis presented MCRT model, which at the current stage of development is a mature method that can be successfully used for modelling radiative transfer in engineering applications including conjugated heat transfer problems, spectral-dependent gas properties and presence of particles. The model improvements, namely coarse hierarchical ortho-Cartesian mesh with NURBS surfaces, resulted in almost 100 speed-up comparing to MCRT using dense CFD mesh. The efficiency of MCRT is still worse than Discrete Ordinates, however it has been shown that in conjugate heat transfer, MCRT can give comparable or even shorter computational time. MCRT does not suffer from ray and false scattering effects. In order to achieve reasonable computational time a generation of ortho-Cartesian mesh is necessary.

7.2 Suggestions for future work

Below, there is a list of ideas and problems that can be dealt with in the future:

- Read boundaries description directly from CAD file. This would greatly simplify and shorten the preprocessing stage of the radiation model. In the current version, every time the model is run it has to create NURBS surfaces describing the boundaries from the selected points lying on the boundary, which is a time consuming task.

- In the presented version of the radiation model, the boundary is described by a set of NURBS surfaces. Each boundary cell of the domain has at least one NURBS surface representing a fragment of the boundary. It is suggested to allow the boundary cells to share the same NURBS surface with other cells. In this way the mathematical description of the boundaries will be simplified and the number of bounding boxes crossed by the ray will be lowered.

- Adapt the code of MCRT radiation model to handle massively parallel computations. Now the code allows parallel computing of RDFs matrix only on shared memory computers. However, a step forward would be to take advantage of the distributed-memory multiprocessors and/or networks of workstations as they have huge computational power.

- MCRT radiation model can be upgraded to account for scattering on particles.

- A detailed models of gas radiative properties (k-distributions models) can be implemented within the framework of the current radiation model.

Appendix A

Surface to Surface method

The surface to surface (S2S) method was developed by Hottel [50] to deal with radiative heat transfer between surfaces, where the effects of participating medium are negligibly small or do not exist at all. It is also referred to as a *Net Exchange Method*.

The derivation of the equations for the method uses the concept of an *enclosure*, which is defined as an outer surface of the domain under the consideration. The enclosure may be composed of real and artificial surfaces, altogether forming a closed region.

The quantity of interest in the case of surface to surface radiation, when the boundary temperatures are known, is the net radiative heat flux q^r at any location on the boundaries of the enclosure. In the case, the radiative heat fluxes are specified, the unknowns are the surface temperatures T. In the following, it is assumed, that the surfaces are gray and diffuse.

The net radiative heat flux at the surface is obtained by making an energy balance, which in the absence of convection and conduction, is given by equation (see Fig. A.1)

$$q^r = b - i, \tag{A.1}$$

where q^r, b, i are respectively net, outgoing and incident radiative energy fluxes. i is also called *surface irradiation* and b *radiosity*.

The incident heat flux is calculated using the concept of *view factor*, the detailed derivation of which can be found in [81, 108]. The view factor $dF_{dA_i - dA_j}$ is defined as (cf. Fig. A.2)

$$dF_{dA_i - dA_j} = \frac{\cos\theta_i \cos\theta_j}{\pi |\mathbf{r}_i \mathbf{r}_j|^2} \, dA_j, \tag{A.2}$$

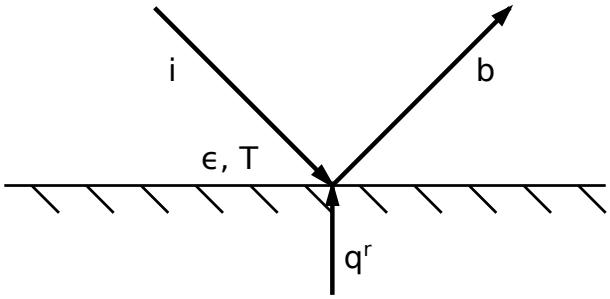

Figure A.1: Radiative energy balance for a surface.

where dA_i, dA_j are differential surfaces centred at points $\mathbf{r}_i$, $\mathbf{r}_j$ and having normal vectors $\mathbf{n}_i$, $\mathbf{n}_j$, $|\mathbf{r}_i\mathbf{r}_j|$ is the distance between surfaces and θ_i, θ_j are angles between surface normal vectors and the line connecting the surfaces. The view factor can also be interpreted as a diffuse energy leaving dA_i directly

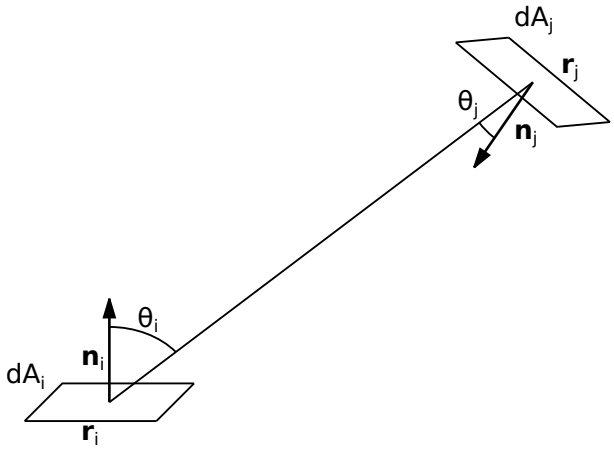

Figure A.2: Notation for radiative exchange between two diffuse differential areas.

towards and intercepted by dA_j to the total diffuse energy leaving dA_i.

In practical problems, the enclosure is subdivided into a finite number of areas. Over each area the following following assumptions are made:

i) the temperature is uniform,

ii) the surface properties ϵ, α, ρ are uniform and are independent of wavelength and direction,

iii) all the energy is emitted and reflected diffusely,

iv) the incident and reflected energy flux is uniform.

In the case of finite areas A_i and A_j the view factor F_{ij} is defined by

$$F_{ij} = \frac{1}{A_i} \int_{A_i} \int_{A_j} \frac{\cos\theta_i \cos\theta_j}{\pi |\mathbf{r}_i \mathbf{r}_j|^2} \, dA_j \, dA_i. \tag{A.3}$$

The view factors obey *reciprocity* and *summation* rules

$$A_i F_{ij} = A_j F_{ji}, \tag{A.4}$$

$$\sum_{j=1}^{N} F_{ij} = 1.0, \tag{A.5}$$

where N is the number of surfaces, which the enclosure was divided into.

Recalling equation (A.1), the surface net heat flux is a difference between irradiation and radiosity. The irradiation on a surface element i can be expressed by means of view factors as

$$i_i A_i = \sum_{j=1}^{N} b_j F_{ji} A_j, \quad 1 \leq i \leq N. \tag{A.6}$$

Using reciprocity rule (A.4) and dividing by A_i yields

$$i_i = \sum_{j=1}^{N} b_j F_{ij}, \quad 1 \leq i \leq N. \tag{A.7}$$

The radiosity from surface element i is a sum of emitted and reflected energy fluxes

$$b_i = (1 - \epsilon_i) i_i + \epsilon_i e_{b,i}, \quad 1 \leq i \leq N. \tag{A.8}$$

Substituting i from equation (A.1) into (A.8) yields

$$b_i = e_{b,i} - \left(\frac{1}{\epsilon_i} - 1 \right) q_i^r, \quad 1 \leq i \leq N. \tag{A.9}$$

Then, using equations (A.1), (A.7) and (A.9) and rearranging produces

$$\sum_{j=1}^{N} \left[\frac{\delta_{ij}}{\epsilon_j} - \left(\frac{1}{\epsilon_j} - 1 \right) F_{ij} \right] q_j^r = \sum_{j=1}^{N} \left[\delta_{ij} - F_{ij} \right] e_{b,j}, \quad 1 \leq i \leq N, \tag{A.10}$$

where δ_{ij} is Kronecker delta. In the case all temperatures are known, equation (A.10) may be presented in the matrix notation as

$$\mathbf{C} \cdot \mathbf{q^r} = \mathbf{e}, \tag{A.11}$$

and

$$\mathbf{e} = \mathbf{A} \cdot \mathbf{e_b}, \tag{A.12}$$

where $\mathbf{C}$, $\mathbf{A}$ are matrices with elements

$$C_{ij} = \frac{\delta_{ij}}{\epsilon_j} - \left(\frac{1}{\epsilon_j} - 1\right) F_{ij}, \tag{A.13}$$

$$A_{ij} = \delta_{ij} - F_{ij}, \tag{A.14}$$

for $1 \leq i, j \leq N$. Matrix $\mathbf{C}$ is generally fully populated, while $\mathbf{A}$ diagonal. $\mathbf{q^r}$ is the vector of unknown radiative heat fluxes and $\mathbf{e_b}$ denotes known surface emissive powers. Set of linear algebraic equations (A.11) and (A.12) is solved for unknown vector $\mathbf{q^r}$.

In the case the surface temperatures are not defined for all the surfaces, equation (A.11) can be rearranged into a similar equation containing all the unknowns. Moreover, if surface temperatures are not known they can be found by solving the heat conduction problem in the walls forming the enclosure assuming no radiation contribution in appropriate boundary conditions. The solution of heat radiation problem (A.11) yields then the radiative heat fluxes on the walls. Using their values, corrected temperatures of the radiating boundaries are produced by solving the heat conduction problem in the walls. Alternating solutions of radiation and conduction problems are continue until desired accuracy is achieved.

⋆ ⋆ ⋆

The crucial and the most time consuming part of the S2S method is the computation of view factors. According to equation (A.3), the calculation of the view factor between any two surfaces needs an evaluation of four dimensional integral, which is not a trivial task even for relatively simple geometries. Additional difficulty is associated with the singular bahvior of the integrand for the case of neighboring elements. A number of numerical methods can be utilised for evaluation of view factors. An extensive review of available methods is given in monographs [81, 108]. The methods include:

- Direct integration
  - surface integration,
  - contour integration,
- Monte Carlo sampling
- Special methods

- view factor algebra,
- crossed-strings method (2D only),
- unit sphere method,
- inside sphere method.

The description of the S2S model was based under the assumption that the surfaces are gray and diffuse. However, the model can be upgraded to include spectral variations of surface parameters. This can be done by implementing the model separately for each wavelength interval, for which the surface properties are assumed to be wavelength independent, and summing up the results. Moreover, the model has an extension to incorporate the specular reflections from surfaces. In this case, the solution is considerably more involved and time consuming.

Appendix B

Reciprocity equations

B.1 Absorbing and emitting medium without particles

This paragraph aims to derive the reciprocity equations (4.9 - 4.12) used in the formulation from section 4.1.1. In the case of absorbing and emitting medium without particles, there are four types of reciprocity equations for four different pairs of elements (cf. Fig B.1):

- surface - surface,
- surface - volume,
- volume - surface,
- volume - volume.

For each pair of elements, irrespectively of their type, the net heat exchanged between elements i and j due to radiation, $Q^r_{i\to j}$, is given by an equation

$$Q^r_{i\to j} = E^r_{ij} - E^r_{ji}. \tag{B.1}$$

Using the definition of radiation distribution factor - equation (4.1) - yields:

$$Q^r_{i\to j} = E^r_{e,i} D_{ij} - E^r_{e,j} D_{ji}. \tag{B.2}$$

Recall equation (4.2) for radiative energy emitted from surface and volume elements:

$$E^r_e = \begin{cases} \epsilon A e_b, & \text{(surface)}, \\ 4\pi\kappa V I_b, & \text{(volume)}. \end{cases} \tag{B.3}$$

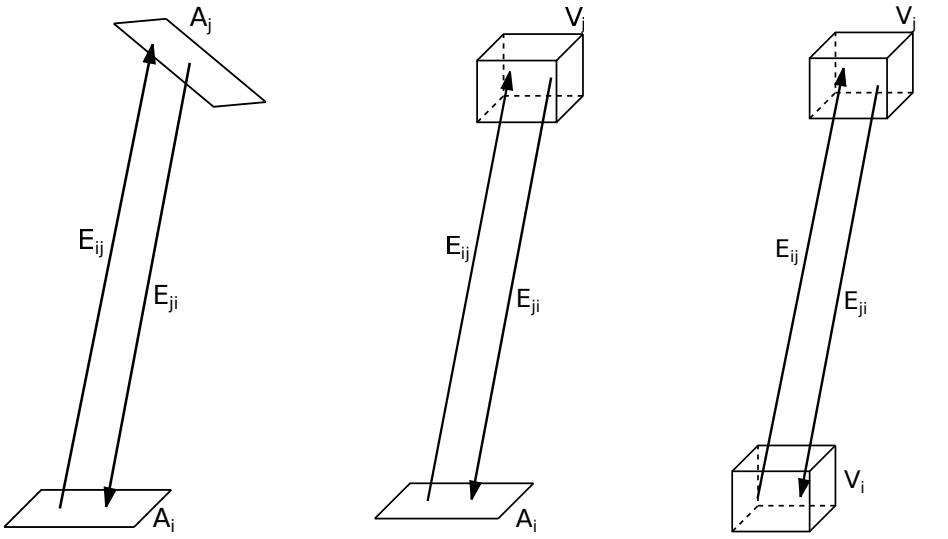

(a) Surface-Surface (b) Surface-Volume (c) Volume-Volume

Figure B.1: Radiative exchange between elements of different type.

Equation (B.1) should hold for every case. Therefore it should also be valid for a special case, when the temperatures of both elements i and j are equal:

$$T_i = T_j. \tag{B.4}$$

In this special case, due to the lack of temperature difference, there exists a thermal equilibrium state between elements and the net heat exchanged due to radiation $Q^r_{i\to j} = 0$. Therefore the following equation holds:

$$E^r_{e,i} D_{ij} = E^r_{e,j} D_{ji}. \tag{B.5}$$

Expanding equation (B.5) with the help of (B.3) and keeping in mind that $e_{b,i} = e_{b,j} = \sigma T_i^4 = \sigma T_j^4$ yields:

Surface-surface

$$\epsilon_i A_i e_{b,i} D_{ij} = \epsilon_j A_j e_{b,j} D_{ji}, \tag{B.6}$$

$$\epsilon_i A_i D_{ij} = \epsilon_j A_j D_{ji}, \tag{B.7}$$

Volume-surface

$$4\kappa_i V_i e_{b,i} D_{ij} = \epsilon_j A_j e_{b,j} D_{ji}, \tag{B.8}$$

$$4\kappa_i V_i D_{ij} = \epsilon_j A_j D_{ji}, \tag{B.9}$$

Surface-volume

$$\epsilon_i A_i e_{b,i} D_{ij} = 4\kappa_j V_j e_{b,j} D_{ji}, \tag{B.10}$$

$$\epsilon_i A_i D_{ij} = 4\kappa_j V_j D_{ji}, \tag{B.11}$$

Volume-volume

$$\epsilon_i A_i e_{b,i} D_{ij} = 4\kappa_j V_j e_{b,j} D_{ji}, \tag{B.12}$$

$$\kappa_i V_i D_{ij} = \kappa_j V_j D_{ji}, \tag{B.13}$$

where equations (B.7), (B.9), (B.11), (B.13) are called *reciprocity equations*.

B.2 Absorbing and emitting medium with particles

The reciprocity equations for the case of absorbing and emitting medium with the presence of particles are derived in the similar way, shown in section B.1.

There are four types of reciprocity equations for four different pairs of elements (cf. Fig. B.1):

- surface - surface,
- surface - volume,
- volume - surface,
- volume - volume.

Volume elements may include particles that also emit and absorb radiative energy. For each pair of elements, irrespectively of their type, the net heat exchanged between elements i and j due to radiation, $Q^r_{i\to j}$, is given by an equation

$$Q^r_{i\to j} = E^r_{ij} - E^r_{ji}. \tag{B.14}$$

Using the definition of radiation distribution factor - equation (4.20) - yields:

$$Q^r_{i\to j} = E^r_{e,i} D_{ij} - E^r_{e,j} D_{ji}. \tag{B.15}$$

Recall equation (4.21) for radiative energy emitted from surface and volume elements:

$$E^r_e = \begin{cases} \epsilon A e_b, & \text{(surface)}, \\ 4\pi\kappa V I_b + 4\pi V E_p, & \text{(volume)}. \end{cases} \tag{B.16}$$

Equation (B.14) should hold for every case. Therefore it should also be valid for a special case, when the thermal equilibrium between i and j elements exists. In this special case of thermal equilibrium, the net heat exchanged between elements due to radiation $Q^r_{i\to j} = 0$ and

$$E^r_{e,i} D_{ij} = E^r_{e,j} D_{ji}. \tag{B.17}$$

Due to the expansion of equation (B.17) with the help of (B.16):

Surface-surface

$$\epsilon_i A_i e_{b,i} D_{ij} = \epsilon_j A_j e_{b,j} D_{ji}. \tag{B.18}$$

Since the thermal equilibrium between elements holds:

$$T_i = T_j, \quad e_{b,i} = e_{b,j}, \tag{B.19}$$

$$\epsilon_i A_i D_{ij} = \epsilon_j A_j D_{ji}. \tag{B.20}$$

Volume-surface

$$\left(4\kappa_i V_i e_{b,i} + 4\pi V_i E_{p,i}\right) D_{ij} = \epsilon_j A_j e_{b,j} D_{ji}. \tag{B.21}$$

It should be noted that the equilibrium state can be fulfilled by infinite number of sets of temperatures $T_i, T_{p,i}, T_j$. It also should hold for the case when the temperature of particles, gas and surface are equal:

$$T_i = T_{p,i} = T_j. \tag{B.22}$$

Recall equation (4.22) which is

$$E_{p,i} = \sum_{m=1}^{M} \epsilon_{p,m} A_{pc,m} \frac{\sigma T_{p,m}^4}{\pi V_i} = \sum_{m=1}^{M} \epsilon_{p,m} \frac{\pi d_{p,m}^2}{4} \frac{\sigma T_{p,m}^4}{\pi V_i}. \tag{B.23}$$

It is assumed that the temperature of particles is uniform inside volume element i and equal to T_i, the particle temperature can be moved outside the summation over particles:

$$E_{p,i} = \frac{\sigma T_i^4}{\pi} \sum_{m=1}^{M} \epsilon_{p,m} \frac{\pi d_{p,m}^2}{4\, V_i}. \tag{B.24}$$

Now the so called particles equivalent absorption coefficient is defined as

$$\kappa_{p,i} = \sum_{m=1}^{M} \epsilon_{p,m} \frac{\pi d_{p,m}^2}{4\, V_i} \tag{B.25}$$

and used to give

$$E_{p,i} = \frac{\sigma T_i^4}{\pi} \kappa_{p,i} = \frac{e_{b,i}}{\pi} \kappa_{p,i}. \tag{B.26}$$

Thus, equation (B.21) can be written as

$$\left(4\kappa_i V_i e_{b,i} + 4\pi V_i \frac{e_{b,i}}{\pi} \kappa_{p,i}\right) D_{ij} = \epsilon_j A_j e_{b,j} D_{ji}, \tag{B.27}$$

$$4\left(\kappa_i + \kappa_{p,i}\right) V_i D_{ij} = \epsilon_j A_j D_{ji}. \tag{B.28}$$

Surface-volume

$$\epsilon_i A_i D_{ij} = 4\left(\kappa_j + \kappa_{p,j}\right) V_j D_{ji}. \tag{B.29}$$

Volume-volume

$$\left(4\kappa_i V_i e_{b,i} + 4\pi V_i E_{p,i}\right) D_{ij} = \left(4\kappa_j V_j e_{b,j} + 4\pi V_j E_{p,j}\right) D_{ji}. \tag{B.30}$$

It should be noted that the equilibrium state can be fulfilled by infinite number of sets of temperatures $T_i, T_{p,i}, T_j, T_{p,j}$. It also should hold for the case when the temperature of particles and gas are equal:

$$T_i = T_{p,i} = T_j = T_{p,j}. \tag{B.31}$$

Using equation (B.25), with the assumption that particle temperatures in volume elements i and j are uniform, equation (B.30) can be written as

$$\left(4\kappa_i V_i e_{b,i} + 4\pi V_i \frac{e_{b,i}}{\pi}\kappa_{p,i}\right) D_{ij} = \left(4\kappa_j V_i e_{b,j} + 4\pi V_j \frac{e_{b,j}}{\pi}\kappa_{p,j}\right) D_{ji}, \tag{B.32}$$

$$\left(\kappa_i + \kappa_{p,i}\right) V_i D_{ij} = \left(\kappa_j + \kappa_{p,j}\right) V_j D_{ji}. \tag{B.33}$$

The equations (B.20), (B.28), (B.29) and (B.33) are called *reciprocity equations.*

Appendix C

NURBS curves and surfaces

The purpose of this section is to provide a brief description of parametric non-uniform rational basis spline (NURBS) surfaces. More detailed information can be found in textbooks by Farin [31] and Piegl [96] and in surveys [32, 95]. Since the NURBS surfaces are represented as a cartesian product of NURBS curves, the latter are described in the first place.

C.1 Curves

A *NURBS curve* is a parametric vector-valued piecewise rational polynomial function of the form

$$\mathbf{C}(u) = \frac{\sum_{i=0}^{n} w_i \mathbf{P}_i N_{i,p}(u)}{\sum_{i=0}^{n} w_i N_{i,p}(u)}, \tag{C.1}$$

where u is a parameter, w_i are weights, $\mathbf{P}_i$ are control points and $N_{i,p}(u)$ are the normalized B-spline basis functions of degree p and order $p+1$, defined by *Cox-de Boor recursion formula*:

$$\begin{aligned} N_{i,0}(u) &= \begin{cases} 1 & \text{if} \quad u_i \leqslant u \leqslant u_{i+1}, \\ 0 & \text{otherwise}, \end{cases} \\ N_{i,p}(u) &= \frac{u - u_i}{u_{i+p} - u_i} N_{i,p-1}(u) + \frac{u_{i+p+1} - u}{u_{i+p+1} - u_{i+1}} N_{i+1,p-1}(u), \end{aligned} \tag{C.2}$$

where u_i are knots, forming a knot vector

$$\mathbf{U} = \{u_0, u_1, ..., u_m\}. \tag{C.3}$$

The degree, number of knots and number of control points are related by

$$m = n + p + 1. \tag{C.4}$$

In the case of non-uniform and non-periodic B-splines, the knot vector is given by

$$\mathbf{U} = \{\alpha, \alpha, ..., \alpha, u_{p+1}, ..., u_{m-p-1}, \beta, \beta, ..., \beta\}, \tag{C.5}$$

where the knots at the end α and β are repeated with multiplicity $p + 1$. In most practical problems $\alpha = 0$ and $\beta = 1$. The basis functions, given by (C.2), are defined over the parametric interval $u \in [0, 1]$.

The curve from equation (C.1) can be expressed as

$$\begin{aligned} \mathbf{C}(u) &= \sum_{i=0}^{n} \mathbf{P}_i R_{i,p}(u), \\ R_{i,p}(u) &= \frac{w_i N_{i,p}(u)}{\sum_{j=0}^{n} w_j N_{j,p}(u)}, \end{aligned} \tag{C.6}$$

where $R_{i,p}(u)$ are called *rational basis functions.*

Using four-dimensional homogeneous coordinate system, equation (C.1) can be rewritten as

$$\mathbf{C}^h(u) = \sum_{i=0}^{n} \mathbf{P}_i^h N_{i,p}(u), \tag{C.7}$$

where superscript h denotes homogeneous coordinates system (x, y, z, w). The fourth dimension w stores the weights of control points.

It can be noted, that in order to compute the coordinates of the point on the NURBS curve from equation (C.1), the values of basis functions $N_{i,p}(u)$ have to firstly determined. A basis function of a given degree p depends on basis functions of lower degree $p - 1$, with the exception for degree 0, which takes values 0 or 1. Thus, the higher the degree of a curve, the more expensive is its evaluation. The growing computational costs are better visible, when the basis functions are grouped in a triangular pattern:

$$\begin{array}{llll} N_{i,p} & & & \\ N_{i,p-1} & N_{i+1,p-1} & & \\ \vdots & & & \\ N_{i,0} & N_{i+1,0} & ... & N_{i+p-2,0} \end{array} \tag{C.8}$$

In general, NURBS curve can be viewed as a parametric interpolation curve created basing upon the control points. The influence of an individual control point $\mathbf{P}_i$ on the shape of NURBS curve can be adjusted by modifying the corresponding value of weight coefficient w_i. Setting the value of weight to 0 causes the control point to have no influence on the curve. By increasing the value of weight, the curve bends towards the control point. In theory it is possible to set negative values to the weights, however it may introduce some problems in the form of singularities, unpredictable curve shapes and convex hull property can be lost. Thus, in practice, the weights values are always $\geqslant 0$.

In order to to derive formulas for the curve derivative, equation (C.1) is rewritten to the form

$$\mathbf{C}(u) = \frac{n}{d}, \tag{C.9}$$

where n, d are nominator and denominator of equation (C.1). Using this notation, derivative of NURBS curve at a given point u is

$$\mathbf{C}'(u) = \frac{\partial \mathbf{C}(u)}{\partial u} = \frac{n'd - nd'}{d^2}, \tag{C.10}$$

where

$$n' = \sum_{i=0}^{n} w_i \mathbf{P}_i N'_{i,p}(u), \tag{C.11}$$

$$d' = \sum_{i=0}^{n} w_i N'_{i,p}(u). \tag{C.12}$$

The derivative of basis function are

$$N'_{i,p}(u) = \frac{N_{i,p-1}(u) + (u - u_i)N'_{i,p-1}(u)}{u_{i+p-1} - u_i} + \frac{(u_{i+p} - u)N'_{i+1,p-1}(u) - N_{i+1,p-1}(u)}{u_{i+p} - u_{i+1}}. \tag{C.13}$$

The derivatives of $N'_{i,0}(u) = 0$ for all u.

C.2 Surfaces

A *NURBS surface* of degree p in u direction and degree q in v direction in a bivariate vector-valued piecewise rational function of the form

$$\mathbf{S}(u, v) = \frac{\sum_{i=0}^{n} \sum_{j=0}^{m} w_{i,j} \mathbf{P}_{i,j} N_{i,p}(u) N_{j,q}(v)}{\sum_{i=0}^{n} \sum_{j=0}^{m} w_{i,j} N_{i,p}(u) N_{j,q}(v)}, \tag{C.14}$$

where u, v are parameters, $w_{i,j}$ are the weights, $\mathbf{P}_{i,j}$ are control points forming a control net, $N_{i,p}(u), N_{j,q}(v)$ are the normalized B-splines of degree p and q in the u and v directions respectively, defined over the knot vectors

$$\mathbf{U} = \{0, 0, ..., 0, u_{p+1}, ..., u_{r-p-1}, 1, 1, ..., 1\}, \tag{C.15}$$

$$\mathbf{V} = \{0, 0, ..., 0, v_{q+1}, ..., v_{s-q-1}, 1, 1, ..., 1\}, \tag{C.16}$$

where the end knots have multiplicities $p+1$ and $q+1$ respectively and $r = n+p+1$ and $s = m+q+1$ hold.

An evaluation of surface derivatives is an important topic, since they are frequently used in computation of surface normal vector and in the iterative Newton's procedure for finding ray-NURBS surface intersection. In practice, first order derivatives are of interest and therefore the discussion is limited to that case only. In the case of a surface defined in two dimensional parametric space, the partial derivatives are required. The partial derivative of a NURBS surface in u and v parametric directions are

$$\mathbf{S}_u = \frac{\partial \mathbf{S}(u,v)}{\partial u} = \frac{n}{d}\left(\frac{n_u}{n} - \frac{d_u}{d}\right), \tag{C.17}$$

$$\mathbf{S}_v = \frac{\partial \mathbf{S}(u,v)}{\partial v} = \frac{n}{d}\left(\frac{n_v}{n} - \frac{d_v}{d}\right), \tag{C.18}$$

where d, n denote denominator and nominator of equation (C.14) and

$$n_u = \sum_{i=0}^{n}\sum_{j=0}^{m} w_{i,j}\mathbf{P}_{i,j}N'_{i,p}(u)N_{j,q}(v), \tag{C.19}$$

$$d_u = \sum_{i=0}^{n}\sum_{j=0}^{m} w_{i,j}N'_{i,p}(u)N_{j,q}(v), \tag{C.20}$$

$$n_v = \sum_{i=0}^{n}\sum_{j=0}^{m} w_{i,j}\mathbf{P}_{i,j}N_{i,p}(u)N'_{j,q}(v), \tag{C.21}$$

$$d_v = \sum_{i=0}^{n}\sum_{j=0}^{m} w_{i,j}N_{i,p}(u)N'_{j,q}(v). \tag{C.22}$$

The derivatives N' are computed using equation (C.13). The physical meaning of directional derivatives $\mathbf{S}_u, \mathbf{S}_v$ is that they are tangent vectors to the underlying NURBS surface at a given point $\mathbf{P}_0 = \{u_0, v_0\}$ (cf. Fig. C.1). The surface

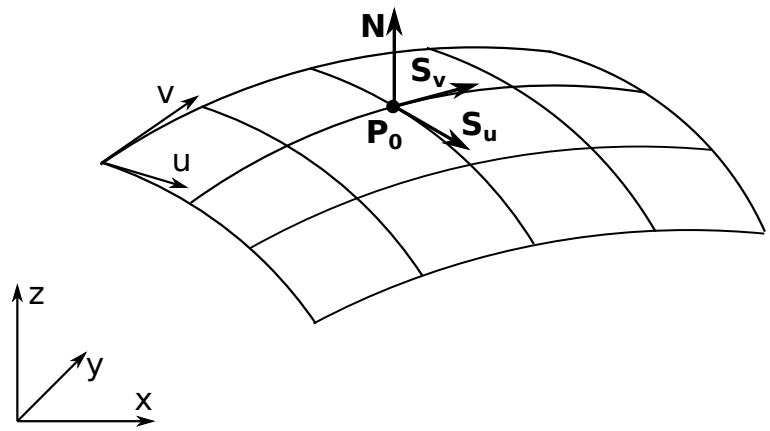

Figure C.1: NURBS surface tangent $\mathbf{S}_u, \mathbf{S}_v$ and normal $\mathbf{N}$ vectors at an arbitrary point $\mathbf{P}_0 = \{u_0, v_0\}$.

normal vector $\mathbf{N}$ and unit normal vector $\mathbf{n}$ can be determined from

$$\mathbf{N} = \mathbf{S}_u \times \mathbf{S}_v, \tag{C.23}$$

$$\mathbf{n} = \frac{\mathbf{N}}{|\mathbf{N}|}. \tag{C.24}$$

$\star \star \star$

NURBS curves and surfaces exhibit the following properties:

- All basis functions have values $\geqslant 0$.
- For any parameter u, the sum of all basis functions equals 1.
- The maximum order equals the number of control points in a given parametric direction.
- If the values of all weights are $\geqslant 0$, the curve or surface lies in the *convex hull*, formed by the union of $p + 1$ successive control points.

Convex hull property is one of the most important features of NURBS curves and surfaces, since it guarantees that the curve or surface lies inside the region bounded by control points.

C.3 Trimmed Surfaces

A *Trimmed NURBS Surface* is defined by underlying NURBS surface $\mathbf{S}(u, v)$ (C.14) of parametric domain $\Omega_p : \{0 \leqslant u \leqslant 1; 0 \leqslant v \leqslant 1\}$ and i sets of trimming curves $\mathbb{C}_i$ that define restrictions for Ω_p. Each set $\mathbb{C}_i$ is composed

of curves $C_{i,j}$ defined in $u - v$ space that form a closed loop. The direction of the loop is significant, since it defines which portion of the domain is to be discarded and which retained. If the trimming curves from set $\mathbb{C}_i$ form a countercolckwise loop (looking in the direction opposite to the surface normal vector $\mathbf{n}$) the part of the parametric domain lying outside of the loop is discarded and lying inside is retained (cf. Fig. C.2). The loops can be nested but can not intersect each other and the outermost loop must be defined in a counterclockwise direction.

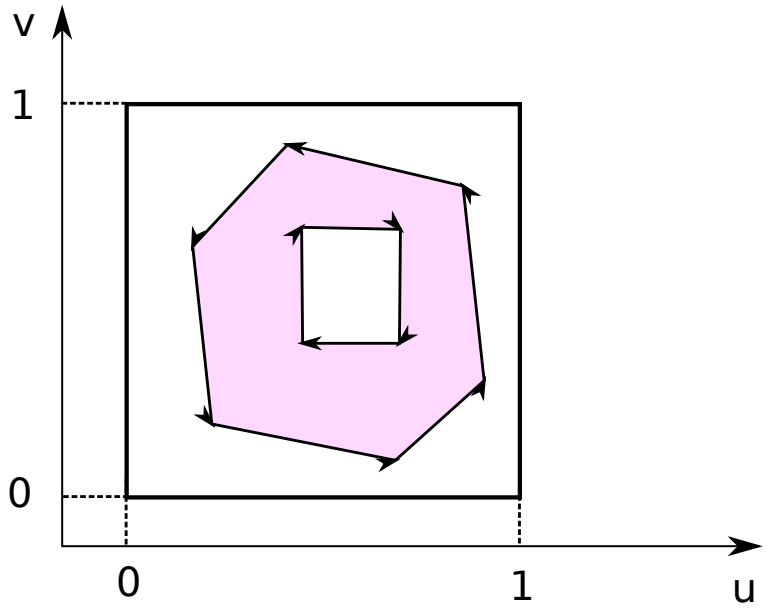

Figure C.2: NURBS Surface parametric domain trimmed by two sets of trimming curves. The resulting valid domain is marked by colour.

Appendix D

Newton's method of ray - NURBS surface intersection

The propagation of an energy bundle (ray) is described by a parametric vector equation

$$\mathbf{r}(t) = \mathbf{r}_0 + \mathbf{d} \cdot t, \tag{D.1}$$

where $\mathbf{r}_0$ is origin vector, $\mathbf{d}$ is direction vector of the energy bundle, t is the line parameter.

According to [61, 76] the ray equation can be rewritten as an intersection of two planes π_1 and π_2 (Fig. D.1)

$$\pi_i : \mathbf{P}_i^h \cdot (\mathbf{n}_i, d_i) = 0, \qquad i = 1, 2. \tag{D.2}$$

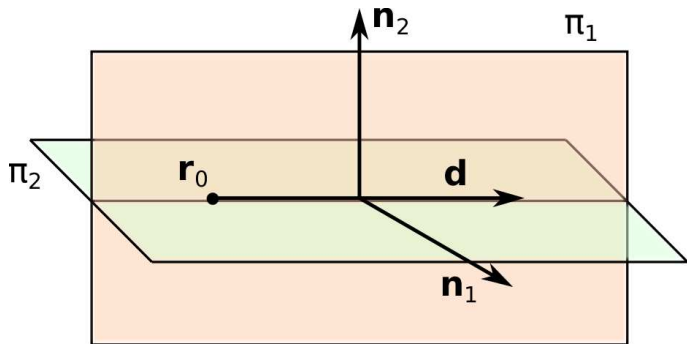

Figure D.1: A ray of origin $\mathbf{r}_0$ and direction d described by means of two arbitrary planes π_1, π_2 of normal vectors $\mathbf{n}_1$ and $\mathbf{n}_2$ respectively.

Vectors $\mathbf{P}_1^h$, $\mathbf{P}_2^h$ are defined in homogeneous coordinate system by arbitrary, perpendicular unit vectors $\mathbf{n}_1$, $\mathbf{n}_2$ and distances from the coordinate system

origin d_1, d_2:

$$\mathbf{P}_i^h = \{n_{x,i}, n_{y,i}, n_{z,i}, d_i\}, \quad i = 1, 2, \tag{D.3}$$

where

$$d_i = -\mathbf{n}_i \cdot \mathbf{r}_0, \quad i = 1, 2, \tag{D.4}$$

Ray-surface intersection point can be expressed by

$$\mathbf{P}_i^h \cdot (\mathbf{S}(u, v), d_i) = 0, \quad i = 1, 2. \tag{D.5}$$

Inserting equation (D.3) to (D.5) yields a system of equations

$$\mathbf{F}(u, v) = \begin{pmatrix} \mathbf{n}_1 \cdot \mathbf{S}(u, v) + d_1 \\ \mathbf{n}_2 \cdot \mathbf{S}(u, v) + d_2 \end{pmatrix}, \tag{D.6}$$

in which the parameters of the intersection point u^*, v^* are unknown. Newton's method uses truncated Taylor expansion for the function

$$\begin{pmatrix} u_{n+1} \\ v_{n+1} \end{pmatrix} = \begin{pmatrix} u_n \\ v_n \end{pmatrix} - \mathbf{J}^{-1}(u_n, v_n) \cdot \mathbf{F}(u_n, v_n), \tag{D.7}$$

where $\mathbf{J}$ is Jacobi matrix of system of equations $\mathbf{F}$ and is defined by

$$\mathbf{J} = (\mathbf{F}_u, \mathbf{F}_v) = \begin{pmatrix} \mathbf{n}_1 \cdot \mathbf{S}_u(u, v) \\ \mathbf{n}_2 \cdot \mathbf{S}_v(u, v) \end{pmatrix}. \tag{D.8}$$

Vectors $\mathbf{S}_u$, $\mathbf{S}_v$ are directional derivatives in u, v directions of parametric surface $\mathbf{S}(u, v)$, defined by equations (C.17) and (C.18). The exit conditions for Newton's iteration are

1. Convergence

$$||\mathbf{F}(u_n, v_n)|| < \epsilon, \tag{D.9}$$

   where ϵ is user specified threshold,

2. Divergence

$$||\mathbf{F}(u_{n+1}, v_{n+1})|| > ||\mathbf{F}(u_n, v_n)||, \tag{D.10}$$

3. Exceeding maximum number of iterations n_{max}

$$n > n_{max}. \tag{D.11}$$

According to [76] there is one more exit condition for Newton's iteration, i.e. when the solution is outside the valid parametric domain $u \notin [u_{min}, u_{max}), v \notin [v_{min}, v_{max})$. This condition was not taken into account, because the intersection point is subjected to further tests, described in section 4.5 which are more strict. In theory it can happen that the Jacobian is close to zero and its inverse tends to infinity. In this case either the surface is not regular or the ray is parallel to a tangent vector at this point. In such case authors of reference [76] suggest performing a jittered perturbation of the parametric point and initiate the next iteration. The model presented in this paper does not check for the singularity of Jacobian because of a few reasons. During the tests of the model the situation of singularity of Jacobian has never been encountered. Moreover, the aim is to make Newton's iteration as fast and simple as possible by removing unnecessary operations. Since the ray tracing procedure involves testing millions of rays against possible intersection with surfaces, the computational costs of addition of a new checking condition can be much higher than simply trace a new ray. The condition for checking the singularity of Jacobian was also omitted in the works of Abert [1, 2]. Finally, if the Jacobian is singular, the computed point is rejected or not found and a new ray is traced.

Bibliography

[1] Abert O. P.: *Interactive Ray Tracing of NURBS Surfaces by Using SIMD Instructions and the GPU in Parallel.* Master's Thesis. University of Koblenz-Landau, 2005.

[2] Abert O. P., Geimer M., Muller S.: *Direct and Fast Ray Tracing of NURBS Surfaces.* Interactive Ray Tracing 2006, IEEE Symposium. (2006), pp. 161-168.

[3] Almasi G.: *Research in highly parallel computer systems.* IEEE Electro Technology Review, **2** (1986).

[4] Amanatides J., Woo A.: *A Fast Voxel Traversal Algorithm for Ray Tracing.* In Eurographics Conference, (1987).

[5] ANSYS Inc. www.ansys.com

[6] Bayazitoglu Y., Higenyi J.: *The Higher-Oreder Differential Equations of Radiative Transfer: P_3 Approximation.* AIAA, **17** (1979), No. 4, pp. 424-431.

[7] Białecki R. A.: *Applying BEM to calculations of temperature field in bodies containing radiating enclosures.* In C. A. Brebbia and G. Maier, Boundary Elements VII, **2** (1985), pp. 35-50.

[8] Białecki R. A.: *Solving heat radiation problems using the boundary element method.* Computational Mechanics Publications, Topics in Engineering **15** (1993), Southampton UK and Boston USA.

[9] Białecki R. A., Grela Ł.: *Practical aspects of developing heat radiation BEM code.* Computational Mechanics Publications, In C. A. Brebbia and A. Kassab editors, Proc. 9th Int. Conf. on Boundary Element Technology (BETECH 94) (1994), pp. 29-39, Southampton UK and Boston USA.

[10] Białecki R. A., Grela Ł.: *Application of the boundary element method in radiation.* Journal of Theoretical and Applied Mechanics, **2** (1995), No. 36, pp. 351-364.

[11] Białecki R. A., Grela Ł., Węcel G.: *Coupled Field Problems,* chapter: Interaction of radiation with other heat transfer modes, WIT Press, (2001) pp. 39-78.

[12] Białecki R. A., Węcel G.: *Solution of conjugate radiation convection problems by a BEM FVM technique*. Journal for Quantitative Spectroscopy and Radiative Transfer, **84** (2004) pp. 539-550.

[13] Białecki R. A., Wecel G.: *BEM solution of the radiative heat transfer within natural gas fired combustion chamber.* Combustion Science and Technology, **178** (2006), No. 8, pp. 1413-1440.

[14] Baum M. M., Street P. J.: *Predicting the Combustion Behaviour of Coal Particles*, Combustion and Science Tech., **3** (1971), No. 5, pp. 231-243.

[15] Cengel Y. A.: *Heat Transfer: A Practical Approach, International Edition, 2nd Edition.* McGraw-Hill, 2003.

[16] Chandra R., Dagum L., Kohr D., Maydan R., McDonald J., Menon R.: *Paralell Programming in OpenMP.* Morgan Kaufmann Publishers, Academic Press, 2001.

[17] Chandrasekhar S.: *Radiative Transfer*, Dover Publications, 1960.

[18] Chen L., Zheng Yong Sze., Goniem A. F.: *Oxy-fuel combustion of pulverized coal: Characterization, fundamentals, stabilization and CFD modeling*, Progress in Energy and Combustion Science, **38** (2012) pp. 156-214.

[19] Cheng P.: *Study of the flow of a radiating gas by a differential approximation.* Ph.D. thesis, Stanford University, Stanford CA, USA, 1965.

[20] Chu K. H., Grief R.: *Theoretical determination of band absorption for non rigid rotation with applications to CO, NO, N2O and CO2.* ASME Journal of Heat Transfer, **100** (1978), pp. 230-234.

[21] Cleveland M. A.: *Radiative Heat Transfer in Combustion Applications: Parallel Efficiencies of Two Gas Models, Turbulent Radiation Interactionas in Particulate Laden Flows and Coarse Mesh Finite Difference Acceleration for Improved Temporal Accuracy.* Ph.D. dissertation, Oregon State University, 2012.

[22] Coelho P. J., Carvalho M. G.: *A conservative formulation of the discrete transfer method.* Journal of Heat Transfer, **119** (1997), No. 1, pp. 118-128.

[23] Coelho P. J.: *The role of ray effects and false scattering an the accuracy of the standard and modified discrete ordinates methods.* Journal of Quantitative Spectroscopy and Radiative Transfer, **73** (2002), No. 2-5, pp. 231-238.

[24] Cumber P. S.: *Improvements to the Discrete Transfer Method of calculating radiative heat transfer.* Int. J. Heat Mass Transfer, **38** (1995), No. 12, pp. 2251-2258.

[25] Daun K. J., Morton D. P., Howell J. R.: *Smoothing Monte Carlo Exchange Factors Through Constrained Maximum Likelihood Estimation.* Transaction of the ASME, **127** (2005), pp. 1124-1128.

[26] Deshmukh K. V., Modest M. F., Haworth D. C.: *Direct numerical simulation of turbulence-radiation interactions in a statistically one-dimensional nonpremixed system.* Journal of Quantitative Spectroscopy & Radiative Transfer, **109** (2008), pp. 2391-2400.

[27] Despres P., Rinkel J., Hasegawa B., Prevrhal S.: *Stream processors: A new platform for monte carlo calculations.* In Journal of Physics: Conference Series, IOP Publishing, **102** (2008) pp. 7-12.

[28] Edwards D. K., Menard W. A.: *Comparison of Models for Correlation of Total Band Absorption.* Applied Opt. **3**, (1964), No. 5, pp. 621-625.

[29] Edwards D. K., Balakrishnan A.: *Thermal radiation by combustion gases.* International Journal of Heat and Mass Transfer, **16** (1973), pp. 25-40.

[30] Efremov A., Havran V., Seidel H. P.: *Robust and Numerically Stable Bézier Clipping Method for Ray Tracing NURBS Surfaces.* Proceedings of

the 21st Spring Conference on Computer Graphics SCCG'05, (2005) pp. 127-135.

[31] Farin G.: *Curves and Surfaces for Computer Aided Geometric Design: A Practical Guide.* Academic Press Inc., New York, NY, USA, 1990.

[32] Farin G.: *From Conics to NURBS: A Tutorial and Survey.* IEEE Computer Graphics and Applications, (1992), pp. 78-86.

[33] Farmer J. T., Howell J. R.: *Comparison of Monte Carlo Strategies for Radiative Transfer in Participating Media.* Advances in Heat Transfer, **31** (1998) pp. 333-425.

[34] Field M. A.: *Rate of Combustion of Size-Graded Fractions of Char from a Low Rank Coal between 1200 - 2000 K.* Combustion and Flame, **13** (1969) pp. 237-252.

[35] Fiveland W. A.: *Discrete ordinates methods for radiative heat transfer in isotropically and anisotropically scattering media.* ASME Journal of Heat Transfer, **109** (1987), pp. 809-812.

[36] Fiveland W. A.: *Three-dimensional radiative heat transfer solutions by the discrete ordinates method.* Journal of Thermophysics and Heat Transfer, **2** (1989), No. 4, pp. 309-316.

[37] Fleck J.: *The calculation of non-linear radiation transport by a Monte Carlo method: statistical physics.* Methods in Computational Physics, **1** (1961), pp. 43-65.

[38] ANSYS Fluent. www.ansys.com

[39] Fujimoto A.: *Accelerated Ray Tracing.* Proc. Computer Graphics, Tokyo (1985), pp. 41-65.

[40] Fujimoto A., Tanaka T., Iwata K.: *ARTS: Accelerated Ray-Tracing System.* IEEE Computer Graphics and applications, **6** (1986), No. 4, pp. 16-26.

[41] Geimer M., Abert O. P.: *Interactive Ray Tracing of Trimmed Bicubic Bézier Surfaces without Triangulation.* WSCG 2005: The 13th International Conference in Central Europe on Computer Graphics, Visualization and Computer Vision, (2005), pp. 71-78.

[42] Glassner A. S.: *Space Subdivision for Fast Ray Tracing.* IEEE Computer Graphics and Applications, **4** (1984), No. 10, pp. 15-22.

[43] Goldsmith J., Salmon J.: *Automatic Creation of Object Hierarchies for Ray Tracing.* IEEE Computer Graphics and Applications, **7** (1987), No. 5, pp. 14-20.

[44] Goody R. M., Yung Y. L.: *Atmospheric Radiation - 2nd edition.* Oxford University Press, New York, 1989.

[45] Govaerts Y., Verstraete M.: *Raytran: A Monte Carlo ray-tracing model to compute light scattering in three-dimensional heterogeneous media.* IEEE Transaction Geoscience and Remote Sensing, **36** (2002), No. 2, pp. 493-505.

[46] Heirich A., Arvo J.: *A competitive analysis of load balancing strategies for parallel ray tracing.* The Journal of Supercomputing, **12** (1998), No. 1, pp. 57-68.

[47] Helbig K. P., Coelho P., Marakis J., Mbiock A., Weber R., Pasini S.: *Comparison of the radiative heat transfer methods using benchmark test cases.* Proceedings of the 3rd Int. Symposium on Radiation Transfer, Radiative Transfer III" 5-7, June 2001.

[48] Higenyi J.: *Higher Order Differential Approximation of Radiative Energy Transfer in a Cylindrical Gray Medium.* Ph.D. dissertation, Rice University, 1979.

[49] Hottel H. C., Cohen E. S.: *Radiant heat exchange in a gas-filled enclosure: Allowance for nonuniformity of gas temperature.* AIChE Journal, **4** (1958), pp. 3-14.

[50] Hottel H. C., Hoyt C.: *Radiant Heat Transmission.* in William H. McAdams (ed.), "Heat Transmission", 3rd ed., McGraw-Hill, New-York, 1954.

[51] Hottel H. C., Sarofim A. F.: *Radiative Transfer.* McGraw-Hill, 1967.

[52] Howell J., Perlmutter M.: *Radiant transfer through a gray gas between concentric cylinders using Monte Carlo.* Journal of Heat Transfer, **86** (1964), pp. 169-179.

[53] Howell J., Perlmutter M.: *Monte Carlo solution of thermal transfer in a nongray nonisothermal gas with temperature dependent properties.* AlChE Journal, **10** (1964), No. 4, pp. 562-567.

[54] Howell J.: *The Monte Carlo method in radiative heat transfer.* Transactions-American Society of Mechanical Eng., Journal of Heat Transfer, **120** (1998), pp. 547-560.

[55] Hsieh T. C, Grief R.: *Theoretical determination of the absorption coefficient and the total band absorptance including a specific application to carbon monoxide.* International Journal of Heat and Mass Transfer, **15** (1972), pp. 1477-1487.

[56] Hunsaker I. L.: *Parallel-distributed, reverse Monte-Carlo radiation in coupled, large eddy combustion simulations.* Ph.D. dissertation, The University of Utah, Chemical Engineering, Nov. 2013.

[57] Jansen F. W.: *Data structures for ray tracing.* Data structures for raster graphics. (1986), pp. 57-73.

[58] Jeans J. H.: *The equation of radiative transfer of energy.* Monthly Notices Royal Astronomical Society, **78** (1917), pp. 28-36.

[59] Jensen H. W., Christensen N. J.: *Photon maps in bidirectional Monte Carlo Ray Tracing of complex objects.* Comput. & Graphics, **19** (1995), No. 2, pp. 215-224.

[60] Jensen H. W.: *Monte Carlo Ray Tracing* SIGGRAPH, Course no. 44, July (2003).

[61] Kajiya J. T.: *Ray tracing parametric patches.* Computer Graphics (SIGGRAPH '82 Proceedings), **16** (1982), No. 3, pp. 245-254.

[62] Kalos M. H., Whitlock P. A.: *Monte Carlo Methods, Second, Revised and Enlarged Edition.* Wiley-Vch Verlag GmbH & Co. KGaA, Weinheim, 2008.

[63] Kay T. L., Kajiya J. T.: *Ray tracing complex scenes.* Computer Graphics (SIGGRAPH '86 Proceedings), **20** (1986), D. C. Evans and R. J. Athay, Eds., pp. 269-278.

[64] Knaus H., Schneider R., Han X., Strohle J., Schnell U., Hein K. R. G.: *Comparison of different radiative heat transfer models and their applicability to coal-fired utility boiler simulations.*

[65] Kopytov N. P., Mityushov E. A.: *Mathematical model of reinforcement of shells made of composite materials and problem of uniform distribution of points on surfaces.* Vestnik PGTU. Mechanika, **4** (2010), pp. 55-66.

[66] Kopytov N. P., Mityushov E. A.: *The Universal Algorithm of Uniform Distribution of Points on Arbitrary Analytic Surfaces in Three-Dimensional Space.* Fundamental Research, **4** (2013), p. 618-622.

[67] Lacis A. A., Oinas V.: *A description of the correlated-k distribution method for modelling nongray gaseous absorption, thermal emission and multiple scattering in vertically inhomogeneous atmospheres.* J. Geo. Res. **96** (1991) No. D5, pp. 9027-9063.

[68] Launder B. E., Spalding D. B.: *Lectures in Mathematical Models of Turbulence.* Academic Press, London, 1972.

[69] Lawson D. A.: *An improved method for smoothing approximate exchange areas.* Int. J. Heat Mass Transfer, **38** (1995), No. 16, pp. 3109-3110.

[70] Liu F., Swithenbank J., Garbett E. S.: *The Boundary Condition of the P_N-Approximation Used to Solve the Radiative Transfer Equation.* Int. J. Heat Mass Transfer, **35** (1992), No. 8, pp. 2043-2052.

[71] Liu F., Garbett E. S., Swithenbank J.: *Effects of Anisotropic Scattering on Radiative Heat Transfer Using the P_1-Approximation.* Int. J. Heat Mass Transfer, **35** (1992), No. 10, pp. 2491-2499.

[72] Lockwood F. C., Shah N. G.: *A new radiation solution method for incorporation in general combustion prediction procedures.* 18th International Combustion Symposium, Combustion Institute, (1981), pp. 1405-1414.

[73] Magnussen B., Hjertager B.: *On mathematical modelling of turbulent combustion with special emphasis on soot formation and combustion.* International Symposium on Combustion, **16** (1977).

[74] Mahan J. R.: *Radiation Heat Transfer: A Statistical Approach.* John Wiley & Sons, New York, 2002.

[75] Marrs R. E., Moss W. C., Whitlock B.: *Thermal Radiation from Nuclear Detonations in Urban Environments.* Lawrence Livermore National Laboratory, June 2007.

[76] Martin W., Cohen E., Fish R., Shirley P.: *Practical Ray Tracing of Trimmed NURBS Surfaces.* Journal of Graphical Tools, **5** (2000), No. 1, pp. 27-52.

[77] Mazumder S.: *Methods to Accelerate Ray Tracing in the Monte Carlo Method for Surface-to-Surface Radiation Transport.* Journal of Heat Transfer, **128** (2006), No. 9, pp. 945-952.

[78] Mbiock A., Weber R.: *Radiation in Enclosures: Elliptic Boundary Value Problem.* Springer Verlag, 2000.

[79] Mehta R. S.: *Detailed modeling of soot formation and turbulence-radiation interactions in turbulent jet flames.* Ph.D. dissertation, The Pennsylvania State University, Department of Mechanical Engineering, 2008.

[80] Menguc M., Viskanta R.: *Radiative transfer in three-dimensional rectangular enclosures containing inhomogeneous, anisotropically scattering media.* Journal of Quantitative Spectroscopy and Radiative Transfer, **33** (1985), No. 6, pp. 533-549.

[81] Modest M. F.: *Radiative Heat Transfer, Second Edition.* Academic Press An imprint of Elsevier Science, 2003.

[82] Modest M. F.: *The weighted-sum-of-gray-gases model for arbitrary solution methods in heat transfer.* Journal of Heat Transfer, Transactions of ASME **113** (1991), pp. 650-656.

[83] Modest M. F.: *Narrow band and full-spectrum k-distributions for radiative heat transfer – correlated-k vs. scaling approximation.* JQSRT **76** (2003), No. 1, pp. 69-83.

[84] Modest M. F., Riazzi R. J.: *Assembly of full-spectrum k-distributions from a narrow-band database; effects of mixing gases, gases and nongray absorbing particles, and mixtures with nongray scatterers in nongray enclosures.* JQSRT **90** (2004), No. 2, pp. 169-189.

[85] A Message-Passing Interface Standard, Version 3.0, September, 2012.

[86] Nishita T., Sederberg T. W., Kakimoto M.: *Ray Tracing Trimmed Rational Surface Patches.* Computer Graphics, **24** (1990), No. 4, pp. 337-345.

[87] Nevárez-Ayala F. J.: *A Monte Carlo Ray-Trace Environment for Optical and Thermal Radiative Design.* Ph.D. dissertation, Virginia Polytechnic Institute and State University, Department of Mechanical Engineering, 2002.

[88] Noble J. J.: *The zone method: explicit matrix relations for total exchange areas.* International Journal of Heat and Mass Transfer, **18** (1975), No. 2, pp. 261-269.

[89] nVidia CUDA zone. https://developer.nvidia.com/about-cuda

[90] OpenFOAM. www.openfoam.com

[91] Pabst H. F., Springer J. P., Schollmeyer A., Lenhart R., Lessig C., Froehlich B.: *Ray Casting of Trimmed NURBS Surfaces on the GPU.* Interactive Ray Tracing 2006, IEEE Symposium. (2006), pp. 151-160.

[92] Patankar S. V.: *Numerical Heat Transfer and Fluid Flow.* McGraw Hill, 1980.

[93] Point Cloud Library. http://pointclouds.org/

[94] Pegoraro V., Wald I., Parker S.: *Sequential Monte Carlo adaptation in low-anisotropy participating media.* In Computer Graphics Forum, **27** (2008), Wiley Online Library, pp. 1097-1104.

[95] Piegl L.: *On NURBS: A survey.* IEEE Computer Graphics and Applications, (1991) pp. 55-71.

[96] Piegl L., Tiller W.: *The NURBS Book, Monographs in Visual Communication, 2nd edition.* Springer-Verlag, Berlin Heidelberg, 1997.

[97] Porter R., Liu F., Pourkashanian M., Williams A., Smith D.: *Evaluation of solution methods for radiative heat transfer in gaseous oxy-fuel combustion environments.* JQRST **111** (2010), pp. 2084-2094.

[98] Rijkhorst E., Plewa T., Dubey A., Mellema G.: *Hybrid characteristics: 3D radiative transfer for parallel adaptive mesh refinement hydrodynamics.* Astronomy & Astrophysics, **452** (2006), pp. 907-920.

[99] Riviere P., Soufiani A., Taine J.: *Correlated-k and fictitious gas model for H2O infrared radiation in the Voigt regime.* Journal of Quantitative Spectroscopy and Radiative Transfer, **53** (1995), pp. 335-346.

[100] Rothman L. S., Gamache R. R., Tipping R. H., et.al: *The HITRAN Molecular Database: Editions of 1991 and 1992.* Journal of Quantitative Spectroscopy and Heat Transfer, **48**, (1992), pp. 469-507.

[101] Rothman L. S.: *HITRAN Newsletter.* **5**, (1996), No. 4, pp. 1-4.

[102] Rubin S. M., Whitted T.: *A 3-dimensional representation for fast rendering of complex scenes.* Computer Graphics, **14** (1980), No. 3, pp. 110-116.

[103] dos Santos A., Teixeira J., de Farias T., Teichrieb V., Kelner J.: *kd-tree traversal implementations for ray tracing on massive multiprocessors: A comparative study".* In Computer Architecture and High Performance Computing, 2009. SBAC-PAD'09. 21st Int. Symp on, IEEE, (2009) pp. 41-48.

[104] Schnell U., Schneider R., Magel H. C., Risio B., Lepper J., Hein K. R. G.: *Numerical simulation of advanced coal-fired combustion systems with in-furnace NOx control technologies.* 3rd Int. Conf. on Combustion Technologies for a Clean Environment, (1995), Lisbon, Portugal.

[105] Schuster A.: *Radiation through a foggy atmosphere*, Astrophys. J., **21** (1905), pp. 1-22.

[106] Schwarzschild K.: *Equilibrium of the Sun's Atmosphere.* Ges. Wiss. Gottingen Nachr., Math-Phys. Klasse, **1** (1906), pp. 41-53.

[107] Seco Warwick Poland: www.secowarwick.com/pl

[108] Siegel R., Howell J.: *Thermal Radiation Heat Transfer, 4th edition.* Taylor & Francis, New York, 2002.

[109] Smits B.: *Efficiency issues for ray-tracing.* Journal of Graphics Tools, **3** (1998), No. 2, pp. 1-14.

[110] Snegirev A. Y.: *Statistical modeling of thermal radiation transfer in buoyant turbulent diffusion flames.* Combustion and Flame, **136** (2004), pp. 51-71.

[111] Snegirev A. Y., Isaev S.: *Turbulent combustion and thermal radiation in a massive fire.* Advanced Combustion and Aerothermal Technologies, (2007), pp. 197-209.

[112] Soufiani A., Taine J.: *High temperature gas radiative property parameters of statistical narrow-band model for H2O, CO2 and CO, and correlated-k model for H2O and CO2.* International Journal of Heat and Mass Transfer, **40** (1997), no. 4, pp. 987-991.

[113] Stowell M. L., Fasenfest B. J., White D. A.: *Investigation of radar propagation in buildings: a 10-billion element cartesian-mesh fetd simulation.* Antennas and Propagation, IEEE Transactions on, **56** (2008), No. 8, pp. 2241-2250.

[114] Sun X., Smith P. J.: *A parametric case study in radiative heat transfer using the reverse Monte-Carlo ray-tracing with full-spectrum k-distribution method.* ASME Journal of Heat Transfer, **132** (2010), No. 2.

[115] Taniguchi H., Mochida A.: *Radiative Heat Transfer in the Mixture of Gas and Particle with Anisotropic Scattering Effect.* Proc. Pacific Rim Conf. on Environmental Control of Comb. Processes. (1994) pp. 13-31.

[116] Tashkun L. S., Perevalov V. I., Bykov A. D., Lavrentieva N. N., Teffo J. L.: *Carbon dioxide spectroscopic databank (CDSD).* Available from <ftp://ftp.iao.tu/pub/CDSD-1000>, 2002.

[117] Tesse L., Dupoirieux F., Taine J.: *Monte Carlo modeling of radiative transfer in a turbulent sooty flame.* Int. Journal of Heat and Mass Transfer **47** (2004), pp. 555-572.

[118] Toporov D., Bocian P., Heil P., Kellerman A., Stadler H., Tschunko S., Forster M., Kneer R.: *Detailed investigation of a pulverized fuel swirl flame in CO2/O2 atmosphere.* Combustion and Flame, **155** (2008), pp. 605-618.

[119] Toth D. L.: *On Ray Tracing Parametric Surfaces.* Computer Graphics (SIGGRAPH '85 Proceedings), **19** (1985), No. 3, pp. 171-179.

[120] Trivic D. N., Amon C. H.: *Modeling the 3-D radiation if anisotropically scattering media by two different numerical methods.* Int. Journal of Heat and Mass Transfer, **51** (2008), pp. 2711-2732.

[121] Trivic D. N.: *3-D radiation modeling of nongray gases-particles mixture by two different numerical methods.* Int. Journal of Heat and Mass Transfer, **70** (2014), pp. 298-312.

[122] Truelove J. S.: *Discrete-ordinates solutions of the radiation transport equation.* ASME Journal of Heat Transfer **109** (1987), No. 4, pp. 1048-1051.

[123] Truelove J. S.: *Three-dimensional radiation in absorbing-emitting-scattering media using the discrete-ordinates approximation.* Journal of Quantitative Spectroscopy and Radiative Transfer **39** (1988), No. 1, pp. 27-31.

[124] Walters D. V., Buckius R. O.: *Monte Carlo methods for radiative transfer in scattering media.* Annual Review of Heat Transfer, **5** (1992), pp. 131-176.

[125] Wang S. W., Shih Z. C., Chang R. C.: *An Efficient and Stable Ray Tracing Algorithm for Parametric Surfaces.* Journal of Information Science and Engineering, **18** (2001), pp. 541-561.

[126] Wang L., Modest M. F.: *Multi-scale full-spectrum k-distribution method for radiative transfer in inhomogeneous gas mixtures with wall emission.* In: Webb B. Modest M. F., editors. Proceedings of the ASME summer heat transfer conference, San Francisco, CA, 2005.

[127] Wang A.: *Investigation of turbulence-radiation interactions in turbulent flames using a hybrid finite volume/Monte Carlo approach.* Ph.D. dissertation, The Pennsylvania State University, Department of Mechanical Engineering, 2007.

[128] Węcel G., Białecki R. A., Nowak A. J., Fic A.: *BEM-FVM solution of conjugate heat transfer problems in Czochralski crystal growth process.* Boundary Element Technology XIV, Orlando, USA, Kassab A, Brebbia CA, (2001), pp. 67-76.

[129] Wecel G.: *BEM-FVM Solution of the Conjugate Radiative and Convective Heat Transfer Problem.* Archives of Computational Methods in Engineering, **13** (2006), No. 2, pp. 171-248.

[130] Wecel G., Ostrowski Z., Bialecki R.: *A novel approach of evaluating absorption line black body distribution function employing proper*

orthogonal decomposition. Journal of Quantitative Spectroscopy and Radiative Transfer, **111** (2010), No. 2, pp. 309-317.

[131] Węcel G.: *Mathematical modelling of coupled radiative and convective heat transfer.* Ph.D. Thesis. Silesian University of Technology, Institute of Thermal Technology, Gliwice 2003.

[132] Bordbar M. H., Wecel G., Hyppanen T.: *A line by line based weighted sum of gray gases model for inhomogeneous CO2-H2O mixture in oxy-fired combustion.* Combustion and Flame, **161** (2014), pp. 2435-2445.

[133] Wecel G., Ostrowski Z., Kozolub P.: *Absorption line black body distribution function evaluated with proper orthogonal decomposition for mixture of CO2 and H2O.* Int. Journal of Numerical Methods for Heat & Fluid Flow, **24** (2014) No. 4, pp. 932-948.

[134] Weiner M. M., Edwards D. K.: *Non-isothermal gas radiation in superposed vibration-rotation bands.* Journal of Quantitative Spectroscopy and Radiative Transfer, **8** (1968), pp. 1171-1183.

[135] Wise J. H., Abel T., Kim J., Wang P., Iannuci P.: *ENZO+MORAY: Radiation hydrodynamics adaptive mesh refinement simulations with adaptive ray tracing.* Monthly Notices of the Royal Astronomical Society, 2010.

[136] Whitted T.: *An improved illumination model for shaded display.* Communications of the ACM, **23** (1980), No. 6, pp. 343-349.

[137] Wu Y., Modest M. F., Haworth D. C.: *A high-order photon Monte Carlo method for radiative transfer in direct numerical simulation.* Journal of Computational Physics, **223** (2007), pp. 898-922.

[138] Zeeb C. N., Burns P. J., Branner K., Dolaghan J.: *User's manual for MONT3D-Version 2.4.* Department of Mechanical Engineering. Colorado State University, Fort Collins, CO, 1999.

[139] Zeeb C. N., Dolaghan J. S., Burns P. J.: *An Efficient Monte Carlo Particle Tracing Algorithm for Large, Arbitrary Geometries.* Numerical Heat Transfer, Part B, **39** (2001). No. 4, pp. 325-344.

[140] Zhang H., Modest M. F.: *A multi-scale full-spectrum correlated –k distribution for radiative heat transfer in inhomogeneous gas mixtures.* JQSRT **73** (2002) No. 2-5, pp. 349-360.

[141] Zhang J., Gicquel O., Veynante D., Taine J.: *Monte Carlo method of radiative transfer applied to a turbulent flame modeling with les.* Comptes Rendus Méchanique, **337** (2009), No. 6-7, pp. 539-549.

Enhancement of Monte Carlo Technique in Absorbing/Emitting Radiating Media for CFD applications

Paweł Kuczyński

Supervisor: **prof. dr hab. inż. Ryszard Białecki**

Institute of Thermal Technology
Silesian University of Technology, Konarskiego 22, 44-100 Gliwice, Poland
e-mail: pawelkuczy@yahoo.com

Abstract

The main objective of the thesis was to develop Monte Carlo Ray Tracing method able of sloving conjugate heat transfer problems in domains of arbitrary shapes, in the presence of non-gray gases and solid particles. The model uses coarse hierarchical ortho-Cartesian mesh with NURBS surfaces for boundary description, which is created based on CFD mesh. Ortho-Cartesian and CFD meshes exchange data. Thus, parameters of walls, medium and particles are averaged and serve as an input for radiation model solved on ortho-Cartesian mesh. The results being radiative heat flux and radiative heat source/sink are interpolated back onto CFD mesh. The code of the model is written in *C++*, uses multi-threading for parallelization and is designed to be an add-on to open-source CFD package OpenFoam.

It was shown that computational time of ray tracing on coarse ortho-Cartesian mesh and NURBS surfaces as boundaries can be 100 times faster than done on dense CFD mesh.

First part of the development consisted of model verification. The model has been sucessfully verified for a number of test cases including non-participating and participating medium wit gray gray and non-gray properties.

Subsequently, the model was employed to simulate the nitriding process of metal shaft in the pit furnace. The analysis allowed to determine the radiative power of electric heaters and temperature across the funace. The results showed excellent agreement with Ansys Fluent S2S model, proving applicability of MCRT to problems with non-participating medium.

MCRT model was also applied for simulation of non-isothermal chamber filled with gray gas. It was found that MC, contrary to DO, is not prone to false scattering and ray effects. It was also estimated that MC computing time can be comparable to that of DO for conjugate heat transfer problems, provided the radiative properties of walls and medium are temperature independent. The functionality of ortho-Cartesian mesh hierarchy was confirmed.

The final application of MCRT was simulation of conjugate heat transfer of pulverized coal combustion in air and oxygen-enriched atmospheres in the test rig of 500 kW maximum thermal input installed in Institute of Power Engineering in Warsaw. The results agreed very well with rig measurements for both air and oxy atmospheres. The results were also confronted with Fluent DO model and proven the capability of MCRT to solve problems with particles suspended in the medium and non-gray medium properties.

Usprawnienie Metody Monte Carlo w Ośrodkach Emitująco-Absorbujących w jej Zastosowaniach w Numerycznej Mechanice Płynów

Paweł Kuczyński

Promotor: **prof. dr hab. inż. Ryszard Białecki**

Instytut Techniki Cieplnej
Politechnika Śląska, Konarskiego 22, 44-100 Gliwice, Poland
e-mail: pawelkuczy@yahoo.com

Streszczenie

Głównym celem pracy było rozwinięcie modelu Śledzenia Promieni Monte Carlo, zdolnego do rozwiązywania sprzężonych zagadnień wymiany ciepła w obszarach o dowolnych kształtach, obecności gazów nieszarych oraz cząstek. Model używa rzadkiej hierarchicznej siatki ortokartezjańskiej z powierzchniami NURBS do opisu brzegów, która jest tworzona na podstawie siatki CFD. Pomiędzy siatkami zapewniono niezbędną wymianę informacji. Parametry ścian, ośrodka oraz cząstek są uśredniane i służą jako wartości wsadowe do modelu radiacji używającego siatkę ortokartezjańską. Wyniki, będące radiacyjnymi strumieniami ciepła na ścianach oraz radiacyjnymi objętościowymi źródłami energii są interpolowane na siatkę CFD. Kod napisany jest w *C++*, wykorzystuje wielowątkowość do zrównoleglenia obliczeń i jest zaprojektowany jako dodatek do pakietu OpenFoam z otwartym kodem źródłowym.

W pracy udowodniono, że czas śledzenia promieni na siatce ortokartezjańskiej z powierzchniami NURBS, może być 100 razy mniejszy niż na gęstej siatce CFD.

Pierwszą część w procesie rozwoju modelu była weryfikacja. Model został pozytywnie zweryfikowany na kilku przypadkach testowych włączając w nie ośrodki przezroczyste i aktywne z szarymi i nieszarymi własnościami gazów.

W kolejnej częsci pracy model zastosowano w symulacji procesu azotowania metalowego wału w piecu wgłębnym. Analiza pozwoliła określić radiacyjną moc elektrycznych grzałek oraz temperaturę w piecu. Wyniki wykazały bardzo dobrą zgodność z modelem S2S Ansys Fluent, potwierdzając możliwość zastosowania modelu MC do problemów w ośrodkach przezroczystych.

Model MC użyto w symulacji nieizotermicznej komory wypełnionej gazem szarym. Wykazano, że rozwiązanie MC, w przeciwieństwie do DO, nie jest narażone na efekty promienia oraz fałszywego rozpraszania. Oszacowano, że czas obliczeń MC możę być zbliżony do DO dla sprzężonych problemów wymiany ciepła, przy założeniu że własności radiacyjne ścian oraz ośrodka są niezależne od temperatury. Potwierdzono działanie hierarchiczności siatki ortokartezjańskiej.

W ostatnim przykładzie model MC użyto w symulacji spalania pyłu węglowego w atmosferach powietrznej oraz wzbogaconej tlenem na stanowisku testowym 500 kW Instytutu Energetyki w Warszawie. Wyniki wykazały bardzo dobrą zgodność z pomiarami dla obydwu atmosfer. Ponadto, wyniki były porównane z modelem DO Fluent i wykazały możliwość zastosowania MC do zagadnień sprzężonej wymiany ciepła z cząstkami oraz gazem nieszarym.